

QUANTITATIVE CHARACTERISATION OF THE GEOMETRY AND TOPOLOGY OF PORE SPACE IN 3D ROCK IMAGES

Zeyun Jiang

Submitted for the degree of Doctor of Philosophy

Heriot-Watt University

Institute of Petroleum Engineering

January 2008

This copy of the thesis has been supplied on condition that anyone who consults it is understood to recognise that the copyright rests with its author and that no quotation from the thesis and no information derived from it may be published without the prior written consent of the author or of the University (as may be appropriate).



IMAGING SERVICES NORTH

Boston Spa, Wetherby

West Yorkshire, LS23 7BQ

www.bl.uk

BEST COPY AVAILABLE.

VARIABLE PRINT QUALITY

ABSTRACT

In this thesis, a suite of techniques and algorithms is presented to tackle three main tasks. Firstly, many existing image-related approaches (processing or analysis) need to be extended from low-dimensional space (e.g. 2D) to a higher-dimensional space (3D). In addition, they often also need to be improved to achieve better accuracy and more efficiency to enable processing of massive volumetric images. Frequently new techniques or algorithms also need to be developed to cover the gap in these previous requirements. Based on these approaches, the second task is to extract the geometric and topological properties of the pore space directly from 3D images of rock samples. The third task is then to study and to establish the relationship between the microstructure and the macroscopic properties by constructing realistic network structures for network models or by conducting some numerical experiments such as mercury injection etc.

In the framework of the methodology presented in this thesis, many commonly used image processing and analysis approaches form the basis of the pore space quantification procedure. These primarily include 3D Euclidean distance transformations, 3D geodesic distance transformations, component labelling (clustering), and morphological operations. Among these techniques, some are either unavailable in 3D discrete space or are of too low-efficiency for handling the huge size of rock samples, and others simply did not exist prior to my work.

The next level of the methodology is to quantify the pore space. In order to process 3D images efficiently thus, firstly, the medial axis (skeleton) of the object (e.g. the pore space) is generated so that simple and compact basic information of the object remains while irrelevant redundant information is neglected in the resultant skeleton image. Having obtained the skeleton of an object, most of the geometric and topological quantities of this object can then be easily derived. After reviewing many existing algorithms, a more accurate and efficient thinning algorithm is presented to meet the specific requirements for the study of pore microstructure. Furthermore, general geometric and topological properties of the pore space are calculated and analysed, including pore size distribution, bond (or node) radii/length/volume, shape factor and

coordination number etc. As an important contribution, a novel algorithm to compute the Euler-Poincaré characteristic (Euler number) is presented and a new topological descriptor is introduced to overcome the limitations of the Euler number and the coordination number.

To validate the methodology and to carry out some basic analysis of the microstructure of porous media, I investigate the geometric and topologic features directly from 3D binary images of rock samples. The volumetric pore size distribution is obtained, and the frequency of pore inscribed radii (or diameter) is calculated, the shape of cross sections along pore channels is quantified as the shape factor and the corresponding algorithm is created. In this study, many quantities for describing the morphological properties of porous media have been successfully introduced.

To carry this novel methodology into the use of network models for the prediction of flow processes, three rock samples are selected and analysed. A new approach is developed for partitioning the pore space into the network of nodes and bonds. This partitioning differs from existing methods and it aims to solve some specific problems which often occur in unconsolidated (high porosity) porous media. Following this some single/multi-phase properties are calculated for these three rock samples, such as absolute permeabilities and relative permeabilities. A number of relations between pore size and the absolute permeability, or between pore connectivity and absolute permeability, are explored. The comprehensive relation between pore size, connectivity and absolute permeabilities is also studied and preliminary results are given.

This research has created new tools that will play important roles in the analysis of porous media.

ACKNOWLEDGEMENTS

This work would never have been accomplished without the unfailing patience and support of my supervisors Dr Gary Couple and Dr Kejian Wu. They have been a consistent source of support, knowledge and inspiration. Their special talent of radical thinking handed me the keys to unlock the gates of understanding and solve the difficult problems during the course of this study. They have always been readily available to discuss the research topics as well as to provide me with some personal help, and for this I am truly grateful.

I must express my deepest gratitude to Professor Ken Sorbie and Dr M.I.J. van Dijke for their marvellous ability to provide me with invaluable knowledge and technical guidance to clear the complexities and difficulties up systematically throughout this research work. Through serious moments of attending their lectures, reading their papers, discussing with them and writing my thesis guided by them, I have treasured their encouragement, kindness and advice throughout this study.

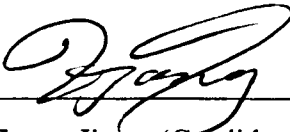
Special thanks also due to all my friends in the Institute and colleagues in the PRAMF group, for their and generous help and many useful suggestions, comments, as well as the friendly environment.

Financial support for this research was provided by the institute of Petroleum Engineering and British Research Council (EPSRC, EP/D00024351). This support is gratefully acknowledged.

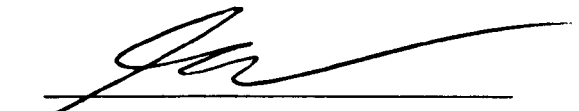
Finally, my sincere appreciation goes to my wife and lovely daughter for their constant interest, encouragement and love during these years.

DECLARATION STATEMENT


I hereby declare that the work presented in this thesis was carried out by myself over the last three years under the supervision of Dr Gary Couples, Dr Kejian Wu at Heriot-Watt University, Edinburgh, UK. It has not been submitted for any other degree.



Zeyun Jiang (Candidate)



Dr. Gary Couples (Supervisor)



Dr. Kejian Wu (Supervisor)

TABLE OF CONTENTS

CHAPTER 1	INTRODUCTION.....	1
1.1	BACKGROUND.....	1
1.2	CHALLENGES IN CHARACTERISATION OF THE PORE SPACE.....	8
1.3	MOTIVATION AND OBJECTIVE.....	11
1.4	OUTLINE OF THIS THESIS	12
CHAPTER 2	LITERATURE REVIEW	13
2.1	MORPHOLOGICAL IMAGE PROCESSING	13
2.1.1	<i>Digital Images</i>	13
2.1.2	<i>Mathematical Morphology</i>	14
2.2	THE STUDY OF TOPOLOGICAL PROPERTIES OF THE PORE SPACE	19
2.2.1	<i>Euler-Poincaré characteristic</i>	20
2.3	MEDIAL AXIS (SKELETON)	26
2.3.1	<i>Definitions of Medial Axis</i>	27
2.3.2	<i>Algorithms (skeletonization)</i>	29
2.3.3	<i>Medial Axis Properties</i>	40
2.4	QUANTITATIVE CHARACTERIZATION OF THE PORE SPACE.....	42
2.4.1	<i>Intuitive Definitions and Geometry Measurement</i>	43
2.4.2	<i>Rigorous Definitions and Non-Medial-Axis-based Approaches</i>	48
2.4.3	<i>Medial-Axis-based Approaches</i>	50
CHAPTER 3	IMAGE PROCESSING	56
3.1	BASIC DEFINITIONS AND NOTATIONS	56
3.2	DISTANCE TRANSFORMATIONS.....	61
3.2.1	<i>Distance Metrics</i>	62
3.2.2	<i>Geodesic and Chamfer Distances</i>	63
3.2.3	<i>The Relationship between Squared Euclidean and Chamfer Distances</i>	66
3.2.4	<i>New Distance Transformation algorithms</i>	68
3.2.5	<i>Geodesic Distant Transformation</i>	75
3.3	COMPONENT LABELLING ALGORITHM.....	81
3.3.1	<i>Previous Work</i>	81
3.3.2	<i>Extended Hoshen-Kopelman Algorithm</i>	83
3.3.3	<i>Explanation of the Extended HKA with examples</i>	84
3.4	EULER-POINCARÉ CHARACTERISTIC.....	88
3.4.1	<i>Previous Work</i>	88

3.4.2	<i>Theoretical Analysis</i>	94
3.4.3	<i>New descriptor of topological properties</i>	106
3.5	MEDIAL AXIS TRANSFORMATION (SKELETONISATION).....	108
3.5.1	<i>GT Network Consideration</i>	109
3.5.2	<i>Algorithm Description</i>	111
3.5.3	<i>Algorithm Implementation</i>	115
3.5.4	<i>Theoretical analysis</i>	117
3.5.5	<i>Examples of GT network</i>	122
3.6	CONCLUSION.....	125
CHAPTER 4 PORE STRUCTURE ANALYSIS TECHNIQUES		128
4.1	PARTITIONING THE PORE SPACE INTO A SET OF PORES	128
4.1.1	<i>Euclidean Distance Valued Skeleton</i>	130
4.1.2	<i>New Sphere-fitting Approach</i>	132
4.1.3	<i>Two Features and One Example</i>	135
4.2	CALCULATION OF SHAPE FACTOR	138
4.2.1	<i>Extraction of Cross Sections</i>	139
4.2.2	<i>Projection of Cross Section</i>	147
4.2.3	<i>Computation of Shape Factor of 2D Shapes</i>	150
4.3	CONSTRUCTION OF NETWORK STRUCTURE.....	157
4.3.1	<i>Partitioning the Pore Space into a Network</i>	157
4.3.2	<i>Characterising Network Elements</i>	166
4.4	CONCLUSION AND DISCUSSION.....	170
CHAPTER 5 APPLICATIONS		173
5.1	DATASET AND PRE-PROCESSING	173
5.1.1	<i>Sandstone Samples</i>	173
5.1.2	<i>Image Pre-processing</i>	176
5.2	GEOMETRIC PROPERTIES	178
5.2.1	<i>Sphere Equivalent Pore Size</i>	179
5.2.2	<i>Cross Sectional Pore Size</i>	181
5.2.3	<i>Cross Sectional Area and Shape Factor</i>	186
5.2.4	<i>Mercury Injection Simulation</i>	187
5.3	TOPOLOGICAL PROPERTIES	190
5.3.1	<i>Coordination Number</i>	190
5.3.2	<i>The Euler Number and its Limitation</i>	191
5.3.3	<i>Connectivity Coefficient</i>	194
5.4	EXTRACTED NETWORK FOR NETWORK FLOW MODEL.....	196
5.4.1	<i>IC Network Model</i>	196
5.4.2	<i>Analysis of Network Structure</i>	198
5.4.3	<i>Calculation of Conductance</i>	202
5.4.4	<i>The correlation between Absolute Permeability and Inscribed Diameter</i>	207

5.4.5	<i>The correlation between Absolute Permeability and Connectivity Coefficient</i>	210
5.4.6	<i>Comprehensive Correlation</i>	212
5.5	CONCLUSION.....	215
CHAPTER 6 DISCUSSION, CONCLUSIONS AND FUTURE RESEARCH		217
6.1	DISCUSSION	217
6.2	SUMMARY AND CONCLUSIONS	220
6.3	FUTURE RESEARCH.....	225

LIST OF TABLES

Table 3-1: Array *Lld* for labelling 8-components (left) and 4-components (right) of object pixels: The column numbers represent the entries of array *Lld*, i.e. labels, and the row numbers represent the scan order (see Figure 3-14(b)). 86

Table 4-1: Five smoothing schemes and their corresponding coefficients. 152

Table 4-2: The computation of shape factor of the 2D shape shown in Figure 4-26(a), the shape numbers $(N_p, N_e, N_v, N_c) = (17, 30, 13, 9)$ 152

Table 4-3: Shape factors of the cross section shown in Figure 4-31, where S_* is a new smoothing scheme by averaging their smoothing coefficients of S_1 and S_2 (i.e. $a = (0.125 + 0.0537)/2$ and $\rho = (0.2929 + 0.2146)/2$), G is the shape factor. 156

Table 4-4: Shape factors of the spatial cross section which is projected into the 2D shape shown in Figure 4-31 for three projecting coefficients (Figure 4-25). 156

Table 5-1: Basic (a) and quantified (b) morphological properties of the three sandstone samples shown in Figure 5-1 (L_d : average sphere equivalent pore diameter; I_d : average cross sectional pore diameter; G : average shape factor; C_n : average coordination number; ζ_v : connectivity coefficient; K : absolute permeability.).. 175

Table 5-2: Statistics of black 26-components (pores) and white 6-components (solid particles) from samples FS-A, FS-B and BS and the effect of pre-processing on porosity of the PS. In the column Original, R-Pore and R-Solid, three porosities are listed for each sample before and after removing isolated pores and removing floating solid particles. 177

Table 5-3: Statistics about the pore size of FS-A, FS-B and BS, where the pore size is described in terms of sphere equivalent size in diameter. 181

Table 5-4: Statistics of pore sizes of skeleton voxels for sample FS-A, FS-B and BS, where the pore size are described in terms of cross sectional diameter. 185

Table 5-5: Statistics of the Euler number and the number of pores sample FS-B and BS. 193

Table 5-6: Network structure properties. 199

Table 5-7: Creation of a series of images of different average pore size but the same topology ($\zeta_v = 687\text{mm}^{-3}$) from the original image of BS.....208

Table 5-8: The predicted absolute permeabilities for images of different connectivity but the same average pore size for BS.....211

Table 5-9: Triples of absolute permeability (K), connectivity coefficient (ζ_v) and cross sectional diameter (I_d).....213

LIST OF FIGURES

Figure 2-1: The representations of 2D or 3D image in terms of lattice of (a) squares – pixel or (b) cubes – voxels, respectively. 14

Figure 2-2: Some examples of grey level structuring elements used in morphological image processing. Here the intensity (grey level) is digitised in the range [0,255] (from black to white). Structuring element (a): $\pi(-1,0) = 240, \pi(0,-1) = 180, \pi(1,0) = 120, \pi(0,1) = 60, \pi(0,0) = 0$; (b): $\pi(0,0) = 240, \pi(1,-1) = 180, \pi(2,0) = 120, \pi(1,1) = 60, \pi(1,0) = 0$; (c): $\pi(0,0) = \pi(1,0) = \pi(2,0) = 0, \pi(0,-1) = \pi(1,-1) = 140, \pi(0,-2) = 230$; (d): $\pi(-1,-1) = \pi(1,-1) = \pi(-1,1) = \pi(1,1) = 230, \pi(0,-1) = \pi(1,0) = \pi(0,-1) = \pi(-1,0) = 130, \pi(0,0)=0$ 16

Figure 2-3: Illustration of dilation and erosion of \mathcal{A} by \mathcal{B} in 2/3D discrete space. \mathcal{A} is an active image and \mathcal{B} is a structuring element of circular or spherical shape. 18

Figure 2-4: An interpretation of opening and closing of \mathcal{A} by \mathcal{B} : opening breaks narrow passages and eliminates thin protrusions while closing fills the small non-convex shapes and bridges closed parts. 19

Figure 2-5: Computation of the Euler number for triangulation. (a) A 3D shape triangulated by two tetrahedra, $\chi_3 = 6 - 11 + 8 - 2$; (b) A triangulation of Spock’s head with 230k tetrahedra (www.lcg.ufrj.br). 21

Figure 2-6: Euler-Poincaré characteristic χ in 2/3D. h_0 = number of isolated components, h_1 = number of redundant connections (also called genus, or tunnels in 3D) and h_2 = number of completely enclosed cavities in 3D. 23

Figure 2-7: Three ways to represent 3D discrete object. (a) Lattice of points, (b) lattice of cubes and (c) lattice of surface patches. 23

Figure 2-8: Disector and its Euler number. (a) $\chi_2(X_1) = 1 - 1$; (b) $\chi_2(X_2) = 1 - 1$; (c) $\chi_2(X_1 \cap X_2) = 1 - 2$; thus $\chi_3(\mathcal{D}\mathcal{S}(X_1, X_2)) = 1$. Where grey region are object and white region are background of a section. 25

Figure 2-9: The medial axis in 2D (a, b) and the medial surface in 3D (c) and a few examples of inscribed disks in 2D and spheres (ball) in 3D. (b) The MA is

sensitive to boundary noise because noisy spurs remain in the skeleton due to the small variations on the boundary of the object.....	28
Figure 2-10: A wireframe torus with medial axis (the central curve).....	28
Figure 2-11: The skeleton of a 3D object with surfaces and curve arcs. (a) Without any cavities (from Pudney, 1998[132]) and (b) with a cavity. A cavity is a background component that is completely enclosed in an object.	29
Figure 2-12: The medial axis extracted from a sandstone image (a) with many spurious paths and (b) trimmed backbone of the PS.....	36
Figure 2-13: Four basic template cores of Ma and Sonke's parallel thinning algorithm which are used to generate deleting templates by reflecting and 90^0 rotating these template cores. Where a grey point is a "don't care" point which can be either an object point (black) or a background point (white).	39
Figure 2-14: Six Class A templates for deleting west, east, south, north, down, and up border points, respectively. Where black points are object points, white points are background points, and a grey point can be either object or a background point.	39
Figure 2-15: The concept of local aperture: (a) The local aperture $A(p)$ of p is defined as the diameter d (i.e. the length of the segment) of the maximal disk $B(c, d)$ (solid circle) centred at c including in the PS O . Note that the dotted circle centred at c_0 contains p but not the maximal, which means that the diameter of this disk cannot be defined as $A(p)$; (b) an illustration of local aperture map with different grey level representing different local aperture value.	44
Figure 2-16: Determination of pore-size distribution based on morphological operations. (a) The original 3D binary image of a sandstone sample of 1.4049 mm^3 the porosity is 20.2%; the size of a voxel is $5.6 \mu\text{m}$; (b) The PS of pore diameter $\geq 39.2 \mu\text{m}$; (c) The pore structure of pore diameters $\geq 61.6 \mu\text{m}$; (d) Cumulative morphological pore-size distribution of the sample shown in (a).....	46
Figure 2-17: A sandstone sample of volume 1.4049 mm^3 , the connectivity function is defined as the Euler number of the pore system with pores larger than the given pore diameter. It seems that the connectivity of the PS mainly depends on these pores of diameter between 28 and $50 \mu\text{m}$	47
Figure 2-18: The thirteen scanning orientations which yield planar serial sections. (a)-(c) The three orthogonal orientations including the directions (a) of physical serial	

sectioning; (d)-(g) The four corner-to-corner orientations; (h)-(m) The six diagonal orientations.....	49
Figure 2-19: The construction of triangular throat surface.....	51
Figure 2-20: Local or absolute minima along a pore path. Hydraulic radius of cross sections reach to local minima at three positions but only the middle one reach absolute minima.....	53
Figure 2-21: Cross sections through a geometry that will be mishandled by local pore merging rules. This whole object, being composed of overlapping maximal spheres, will be merged into a single pore.....	54
Figure 3-1: The direct neighbourhoods $\mathcal{N}(p)$ of a point p . (a) and (b) show different representations of the 2D direct (3×3) neighbourhoods, where $\mathcal{N}(p) = \{q_1, q_2, q_3, q_4, p, q_5, q_6, q_7, q_8\}$; (c) and (d) show two different representations of the 3D direct ($3 \times 3 \times 3$) neighbourhood, where $\mathcal{N}(p) = \{q_1, q_2 \dots q_{13}, p, q_{14}, q_{15} \dots q_{26}\}$	57
Figure 3-2: Examples of paths, curves and components. (a) A path $\{1, 2 \dots 9, 2, 10\}$ intersect itself; (b) a path $\{1, 2 \dots 10\}$ touches itself; (c) the set of grey pixels can be organised as a closed 8-curve, but not as a 4-curve; (d) the set of grey voxels is a 26-path, but not a 26-curve because voxel p has three 26-adjacent grey voxels. The set of grey pixels in (c) is an 8-component but not a 4-component, and the set of grey pixels in (d) is a 26-component but not an 18- or a 6-component. Note that in (a) ~ (d) all white (background) voxels are invisible for clarity. In (e) an example is shown of 4 26-components in 3D.....	60
Figure 3-3: Geodesic distance between p and q , $d_G(p, q)$, with respect to the constraint domain \mathcal{M} (the grey region) is defined as the length of the grey solid path. The length of the dotted line corresponds to the Euclidean distance between p and q ; $d_G(p, r) = \infty$ because no paths between p and r , with regard to the constraint domain \mathcal{M} , exist.	64
Figure 3-4: Moves and paths in 2D/3D: (a) a -move and b -move in 2D; (b) three paths of moves: the black consists of only a -moves and its length is $6a$, the grey consists of only b -moves and its length is $3b$, and the dashed consists of both a - and b -moves and its length is $2a + 3b$; (c) a -, b - or c -move in Z^3	66

Figure 3-5: Constraint domain \mathcal{M} (white) with 8-adjacency containing paths between p and r and between p and q with shortest chamfer distance. The constraint domain does not allow any paths between p and o 66

Figure 3-6: Examples illustrating two types of topological errors between the chamfer and the Euclidean distances..... 68

Figure 3-7: Relative coordinates vectors $R(p)$ and $R(q)$ to a background voxel o 71

Figure 3-8: a 2D squared Euclidean distance map of an image with 5 background pixels (red zeros). 73

Figure 3-9: An example of a 3D SED map for the image in the top left picture. The colours indicate the SED values of object voxels to the background, and range from grey (minimum SED 1) to deep blue (maximum SED 97)..... 74

Figure 3-10: 2D chamfer distance map with CD coefficients (3, 4) of an image with 5 background pixels (red zeros)..... 74

Figure 3-11: Illustration of the concept of an occlusion point p with respect to constraining domain \mathcal{M} (blank region): (a) in R^2 the dotted straight-line between o and p is partially located beyond \mathcal{M} , while the black straight-line between o and q is completely located within \mathcal{M} , in which $q \in B_\epsilon(p) = \{r: d_E(r, p) \leq \epsilon\}$ for sufficiently small $\epsilon > 0$ ($d_E(r, p)$ is the Euclidean distance between r and p); (b) in Z^2 the dotted straight-line between o and p is partially located beyond the constraining domain \mathcal{M} (white grids) and the black straight-line between o and q is located in \mathcal{M} , in which $q \in \mathcal{N}_8(p)$; (c) a shortest path of straight-lines included in \mathcal{M} from p_1 to p_6 76

Figure 3-12: Geodesic chamfer distance map with CDC of (3, 4)..... 80

Figure 3-13: Geodesic Euclidean distance map generated with the assistance of chamfer DT with CDC (3, 4). 80

Figure 3-14: 2D illustration for 8- and 4-component labelling: (a) original binary image; (b) forward scanning sequence order for object voxels (black). 85

Figure 3-15: Initial labels for labelling 8-components and 4-component after one-way scan (i.e. finishing accessing all the 25 object voxels shown in Figure 3-14(b)). 87

Figure 3-16: Final cluster image with sequential labels for 8-components and 4-components of object voxels. 87

Figure 3-17: Labelling of 3D object components using different patterns (background is transparent): (a) original image; (b) seven 6-components; (c) four 18-components; (d) two 26-components. 87

Figure 3-18: Illustration of a 26-transformation for adjacency pair (26, 6): (a) the closed 26-path $\gamma = \{p_1, p_2, p_3, r_2, r_1, p_4, p_5, p_1\}$ is an elementary 26-transformation of $\pi = \{p_1, p_2, p_3, q_1, q_2, q_3, q_4, p_4, p_5, p_1\}$, because $\gamma' = \{r_1, r_2\}$ and $\pi' = \{q_1, q_2, q_3, q_4\}$ are included in the same unit cube; (b) the closed 26-path $\gamma = \{p_1, p_2, p_3, r_1, r_2, r_3, p_4, p_5, p_6, p_7, p_8, p_9, p_1\}$ is not an elementary 26-transformation of $\pi = \{p_1, p_2, p_3, q_1, q_2, q_3, p_4, p_5, p_6, p_7, p_8, p_9, p_1\}$ because $\gamma' = \{r_1, r_2, r_3\}$ and $\pi' = \{q_1, q_2, q_3\}$ are not included in the same unit cube. 90

Figure 3-19: Illustration of Definition 3.5: (a) two closed α -paths within a double torus of two tunnels: π is shrinkable and γ is unshrinkable; (b) the black 18-path cannot be shrunk to a single black voxel, because the central voxel is white, thus revealing a tunnel..... 90

Figure 3-20: Geodesic neighbourhoods and topological numbers. (a) $G_{26}(p, \mathcal{B}) = \{\{q_1, q_2\}, \{r_1, r_2, r_3\}, \{o\}\}$, so $T_{26}(p, \mathcal{B}) = 3$; (b) $G_6(p, \mathcal{V} \setminus \mathcal{B}) = \{\{q_2, q_3\}\}$, so $T_6(p, \mathcal{V} \setminus \mathcal{B}) = 1$ 93

Figure 3-21: Illustration of opposite and link points. Point 1 is opposite to point 3, but not to point 2..... 95

Figure 3-22: Example of determination of $T_6(p)$. There are five white points in $\mathcal{N}(p)$ (p is the central point), $\mathcal{N}_{18}^*(p)$ contains 3 white points, but only one white component $\{p_3, p_4\}$ is 6-connected to p , therefore $T_6(p) = 1$ 96

Figure 3-23: Positions of the white 6-neighbours q and r of p (the central point) that are not 6-connected in $\mathcal{N}_{18}^*(p)$, corresponding to the two independent configurations when $T_6(p) = 2$. Under the condition of that q and r are not 6-connected in $\mathcal{N}_{18}^*(p)$, the colour of grey points can be black or white..... 97

Figure 3-24: Illustration of the three independent subclasses for case 2, with (a) four, (b) three and (c) two black points in $\{2, 4, 11, 5\}$ 98

Figure 3-25: Illustration of closed black 26-paths that cannot be transformed to a single point for the first subclass of case 2, shown in Figure 3-24(a): (a) two closed black 26-paths that are unshrinkable when 3 is black or 16 is black; two different closed black 26-paths when both points in (b) $\{9, 7\}$ or (c) $\{15, 13\}$ are black. Notice

that in each example both points in $\{6, 10\}$ can still be 6-connected to q and r , to ensure that $T_6(p) = 2$ 98

Figure 3-26: Demonstration of unshrinkable closed black 26-paths for the second subclass of case 2, shown in Figure 3-24(b), when points 12 and 16 are both white and, additionally, (a) point 8 is black, or (b) points 8 and 14 are both white, or (c) point 8 is white, point 14 is black and one of the points in $\{15, 9\}$ is black (indicated as dotted), or (d) point 8 is white, point 14 is black and both points in $\{15, 9\}$ are white. 99

Figure 3-27: Demonstration of unshrinkable closed black 26-paths for the third subclass of case 2, shown in Figure 3-24(c), when one of $\{4, 8\}$ is black we have a unshrinkable closed black path (a), otherwise each of $\{3, 7, 9\}$ must be black in corresponding to the consumption for this case, so a unshrinkable closed path can be found in (b). 100

Figure 3-28: All possible configurations for case 3 shown in Figure 3-24(c): (a) one point in $\{12, 16\}$ is black; (b) both 12 and 16 are white, and one point in $\{8, 14\}$ is black; (c) all points in $\{12, 16, 14, 8\}$ are white, and point 3 must be black; (d) points 12, 16 and 13 are white, and one point in $\{3, 8\}$ must be black; (e) all point in $\{12, 16, 3, 8\}$ are white, and 14 must be black, etc. For all these configurations, obviously, we can certainly find an unshrinkable closed 26-path. 100

Figure 3-29: Examples of objects with different EPCs: (a) $\chi = 2$, (b) $\chi = 1$, (c) $\chi = 0$, (d) $\chi = -1$, (e) $\chi = -2$, (f) $\chi = -3$. The EPC = the number of components – the number of redundant channels + the number of cavities. For the PS, the number of cavities (floating solid particles) should be zero, therefore, the number of redundant connections = the number of components – the Euler number. 102

Figure 3-30: (a) A 3D tomography sandstone image and the Euler number curve for a set of sub-images \mathcal{P}_i of the image, $i = 0, 1 \dots 98$. The dimensions of this image are 200^3 voxels, and the resolution is 5.6 micron. Black is the PS and grey is the solid matrix. (b) The relative Error between estimated (by Vogel's algorithm) and calculated (by my algorithm, HWU: Heriot-Watt University) the EPCs. Note that the relative error varies between 0 and 5% when the size of the sub-images is larger than 0.9 mm^3 105

Figure 3-31: Comparison of computation times using Vogel’s and our algorithm (i.e. HWU: Heriot-Watt University) for the calculation of 3D EPCs. Sub-images are cut from the rock image shown in Figure 3-30(a). 106

Figure 3-32: The specific Euler number against the volumes of a series of sub-images of the sandstone shown in Figure 3-30(a). It shows that the specific EPC could not be used as to describe the pore connectivity of an object..... 107

Figure 3-33: Structures with different topologies but the same Euler number (-1): (a) an object with two redundant connections; (b) a combination of two objects with three redundant connections. 108

Figure 3-34: Some instances of topology preservation: Considering an binary image $\mathcal{P} = (\mathcal{V}, 26, 6, \mathcal{B})$ where \mathcal{V} is the set of all voxels drawn in the figure and \mathcal{B} is set of all black voxels (object), p must be retained on the resultant skeleton, otherwise a tunnel will disappear; $\{q, r\}$ is a white 6-component which is completely enclosed, i.e. it is a cavity; removing any voxel of $\{o_1, o_2, o_3, o_4\}$ will destroy the cavity of $\{q, r\}$; removing t will create a tunnel..... 110

Figure 3-35: Skeleton of single voxel width except at the junction..... 110

Figure 3-36: Centredness of skeletons in 3D. The skeleton shown in (a) is derived by common DOHT approaches (Note that some recent thinning algorithms have improved on this by employing alternating direction schemes.) The locations of the skeletons depend on the scanning order within the region of same distance values. The skeleton depicted in (b) is generated by our algorithm with symmetry deletion, which is independent of scanning order. 111

Figure 3-37: Retaining boundary points: (a) and (b) Slice of the 3D squared Euclidean distance map on the inlet (and outlet). In each local maximum region one voxel is retained, which means that two boundary voxels in the two rectangle regions depicted in (a) are to be retained. Based on this criterion, an example of the skeleton with some boundary voxels (and boundary links) is shown in (c)..... 114

Figure 3-38: Skeletons with primary branches. (a) 2D example of a skeleton with a branch (dashed curve), where the grey area indicates has a geodesic distance to the pure topological MA (black curve), larger than a given threshold; (b) a pure topological GT network without any branches; (c) and (d) skeletons with some branches based on different thresholds..... 114

Figure 3-39: Topological network. (a) Original 3D image with only one 26-component, one cavity and three tunnels (Euler Characteristic is -1); (b) and (c) are two pure topological networks of the image shown in (a)..... 114

Figure 3-40: The Illustration of adjacent components and some examples of simple sets.

(a) An example of a local configuration of black and white circle voxels in the envelope of S (triangle voxels); (b) $\mathcal{E}_6(S)$ is the set of all black circle voxels; $\mathcal{E}_{16}(S)$ is the set of all square and diamond voxels, and $\mathcal{E}_{18}(S)$ is the set of all white circle voxels, note that grey voxels will be ignored according to definitions 6 and 7. Obviously there is only one black adjacent component of S , but two white adjacent components (set of squares and circular voxels, set of only diamond voxels). (c) The set of $\{1, 2, 3\}$ is a pure 6-component (definition 8) but not if including 4 because that 2 is 18-connected with 4; (d) All white 6-neighbours of triangle voxels are directly 6-connected ($\mathcal{E}_{18}(S)$ is empty). In (e) and (f), all object (pore) voxels are explicitly identified but all non-object (solid) voxels are omitted for simplicity: (e) the pure 6-components (set of grey voxels) can be simultaneously deleted because in their envelopes there is only one black adjacent component and one white adjacent component; (f) the pure 6-components (set of grey voxels) can not be identified as simple sets based on the theorem 1..... 119

Figure 3-41: A schematic illustration of the thinning process to extract the GT network of a sandstone sample. 123

Figure 3-42: The central location of the GT network (the PS is of transparency in grey colour and the GT network coded in black). 124

Figure 3-43: (a) Networks with many false links at the boundaries, when too many boundary points are retained; (b) networks after checking its 5×5 neighbourhood trying to find if there are any other border points which's distance value equal to or larger than current border point and they are not deletable points at current iteration. Doing so can ensure that as less as possible border points are retained, but some unwanted feature cannot be completely eliminated under the requirement of reasonable efficiency..... 124

Figure 3-44: GT network with cross sectional radii. The value is coded by the Rainbow colour system, in which the blue represents the smallest SED (i.e. 1) while the red represents the largest SED value. 125

Figure 4-1: Illustration of sphere-fitting partitioning of the pore space. (a) The PS in a porous medium; (b) three largest maximal inscribed spheres are fitted into at the very beginning; (c) many smaller maximal inscribed spheres are further fitted into; (d) the whole PS is occupied by a set of different spherical pores in the end. 129

Figure 4-2: The three discrete sphere-templates of radius 0, 1, 2 respectively..... 130

Figure 4-3: Some tiny spheres (filled) are fitted into the PS when large pores have been removed from the PS. 130

Figure 4-4: An example of coloured skeleton: (a) a 3D geometric object of regular shape; (b) its coloured skeleton, where the colours are used to code the SEDs; (c) a part of the coloured skeleton locating on the XY plane at the central point..... 131

Figure 4-5: Two steps of our sphere-fitting partitioning algorithm. (a) An Euclidean distance valued skeleton; (b) the corresponding modified skeleton associated with maximal inscribed spheres; (c) the set of individual pores. The different colours are used to represent the SEDs of individual pores. 133

Figure 4-6: 2D illustration of how backbones are extracted from the skeleton. (a) A skeleton with SED values; (b) a voxel p is found which has the maximum SED value (16); (c) all skeleton voxels which are connected to p and locate within the inscribed sphere (circle) are grouped as an individual backbone; (d) another voxel q of the maximum SED is found and the corresponding backbone is obtained. . 134

Figure 4-7: Pore voxels are clustered into individual pores of different sizes. A pore voxel p is clustered into an individual pore of size 16 because the distance to its backbone is the shortest one. 134

Figure 4-8: Two features. (a) The dead-end pore is not considered as an individual pore instead it is grouped into another pore because the dashed branch does not appear in the resultant skeleton (the black curve). (b) The size of the remaining part on the skeleton after removing two adjacent backbones depends on the inscribed radius (the length of the grey segment) rather than the radius of the inscribed sphere (black disc). 136

Figure 4-9: An example of our pore partitioning method. (a) The PS of a sandstone sample (porosity is 20.6%, resolution is 5.6 micron); (b): a subset of the PS shown in (a) is fitted in by a series of maximal inscribed spheres (different colours

represent different pore sizes); (c) the corresponding partitioned image of irregular and different size pores.....	136
Figure 4-10: Two PSDs of the sandstone sample shown in Figure 4-9(a).....	137
Figure 4-11: The definition of the shape factor and three regular shape factors (Valvatne and Blunt, 2004[170]).....	138
Figure 4-12: The computation of the shape factor. (a) Two CSs are extracted from the 3D PS; (b) a CS π is projected on XY plane and a 2D shape π' is then generated; (c) the cross sectional area A and perimeter P of π' is computed and transformed back to π	139
Figure 4-13: A cross section from p normal to the skeleton.	140
Figure 4-14: A discrete CS (i.e. the black region) is extracted using the plane of $y-2x = 0$. (a) The normal orientation (solid arrow) of the perpendicular plane through the origin of $(0, 0, 0)$ is $(-2, 1, 0)$ and the grey curve is the skeleton; (b) a part (the dashed line) of the perpendicular plane locating on the coordinate plane of $Z = 0$ will generate a disconnected discrete line.	140
Figure 4-15: The cross section consisting of grey voxels is not 26-connected. It suggests that the region including grey and black voxels should be the desired cross section.....	141
Figure 4-16: 2D illustration of a normal orientation and its approximated orientation. The direction (black arrow) in (a) will result in a disconnected CS, whereas its approximate direction (black arrow) in (b) leads to a connected CS.	141
Figure 4-17: Thirteen normal orientation and perpendicular planes (templates). (a) Three orthogonal orientations and their corresponding perpendicular planes; (b) Six diagonal orientations and one of such perpendicular planes; (c) Four corner-to-corner orientations and one of such perpendicular planes.	143
Figure 4-18: Thirteen orientations and their corresponding discrete perpendicular planes (templates) in the $3 \times 3 \times 3$ neighbourhoods of central points. Each grey arrow represents a normal orientation and each perpendicular plane consists of black voxels.....	144
Figure 4-19: Illustration of the process how to extract a CS. (a) A slice of the PS in a rock image (pore voxels are coloured in grey and solid voxels are coloured in white); (b) using the template shown in Figure 4-18, starting from the red point, blue voxels are firstly identified, and then green voxels etc.....	146

Figure 4-20: Illustration of the partition of individual CSs. (a) An orthogonal slice (green surface) intersected with the skeleton of a sphere-packed image; (b) the perpendicular plane (pore voxels in green, skeleton voxels in red and solid voxels in pink) at the corresponding position; (c) partition of individual CSs.....	146
Figure 4-21: The partition of individual cross sections: (a) a CS (the white region) going through two skeleton voxels; (b) Two desired individual CSs; (c) each pore voxel on the CS is clustered either blue CS or the black one based on the comparison of the geodesic distances to the two skeleton voxels.....	146
Figure 4-22: Three types of 3D discrete perpendicular planes. (a) Edge-edge; (b) face-face; (c) edge-face; (d) three kinds of spatial CSs (i.e. the grey surfaces).....	147
Figure 4-23: Projection of a spatial discrete plane consisting of only black voxels on XY-, XZ- or YZ-plane.....	148
Figure 4-24: Three types of spatial shapes and their corresponding projected shapes of a voxel. (a) A square on a face-face plane; (b) a rectangle on an edge-face plane; (c) a diamond on an edge-edge plane.....	149
Figure 4-25: Projecting coefficients for three different types of unit shapes.....	150
Figure 4-26: (a) A 2D shape on a coordinate plane; (b) four smoothing schemes.	150
Figure 4-27: A 2D shape of four pixels (squares) and its four shape numbers: $N_p = 4$, $N_e = 10$, $N_c = 2$ and $N_v = 6$	151
Figure 4-28: Geometrical explanation of the smoothing coefficients (a, ρ). S_{-} represents a general smoothing scheme.....	153
Figure 4-29: The selections of smoothing perimeter coefficients for approximating different regular shapes.	154
Figure 4-30: The 2x2 neighbourhood of a pixel p	154
Figure 4-31: A cross section extracted from a rock image.	155
Figure 4-32: Illustration of λ -adjacency. (a) Three λ -adjacencies between p and q , q and s , s and t ; (b) p is λ -adjacent to q because they are 18-adjacent and no 6-neighbours between them, however, p is not λ -adjacent to r even though they are 26-adjacent because of the existence of q between them; (c) a λ -adjacent path (Liang et al. 2000a[84]).	158
Figure 4-33: Illustration of partition issues. (a) Four pore channels (in 4 different patterns) which can not be distinguished by clustering the remaining skeleton	

voxels after removing the central voxel; (b) The backbone of a nodal pore should contain all skeleton voxels in the maximal inscribed sphere of the centre point.	159
Figure 4-34: Classification of skeleton voxels: (a) an isolated point (light green), three terminal points (grey), four link points (light blue) and four junction points (orange, junctions); (b) a skeleton of the PS of a sandstone sample with four colours representing four types (i.e. isolated, terminal, link and junction) of skeleton voxels.	160
Figure 4-35: Illustration of expanding node-skeleton voxels: (a) a skeleton, (b) an original node-skeleton voxel, (c) newly expanded node-skeleton voxels (in black).	160
Figure 4-36: (a) Merging all node-skeleton voxels within the two spheres (circles) into one node-backbone or (b) keeping them as two individual node-backbones.....	163
Figure 4-37: p is not 26-connected with q within the maximal inscribed spheres.....	163
Figure 4-38: Too many node-skeleton voxels are merged into a single node-backbone.	163
Figure 4-39: There is a tunnel (the central region) surrounded by four close original node-skeleton voxels.	163
Figure 4-40: Two original node-skeleton voxels p and q , two squared inscribed radii r_p and r_q and the squared Euclidean distance $d(p, q)$ between p and q	164
Figure 4-41: The node-skeleton voxels (in orange and red) in (a) are merged into one node-backbone (in red) in (b); and the remaining skeleton voxels (in blue) in (a) are clustered as six different bond-skeleton voxels (coded by different colours) because they are six components.....	165
Figure 4-42: The transformation from a realistic pore network to ideal pore network, where discs represent nodes and curves represent bonds.	167
Figure 5-1: Three CT scanned sandstone 3D images consisting of the PS (in black) and the solid matrix (in grey). FS-A and FS-B are two Fontainebleau sandstone samples, and BS is a Berea sandstone sample.....	174
Figure 5-2: Representative elementary volume of the three rock images (i.e. FS-A, FS-B and BS) with regard to their porosities.	175
Figure 5-3: The effect of floating solid particles and isolated pores on the extraction of pore skeleton (a) before and (b) after removing floating solid particles and isolated pores.....	178

Figure 5-4: Comparison between sphere equivalent size and cross sectional radii (size). Each pore voxel is assigned (grey level) a value corresponding to a sphere equivalent radius while each skeleton voxel is assigned a value corresponding to a radius of an inscribed circle within a CS.	179
Figure 5-5: Individual pores of different sizes (i.e. sphere equivalent size) coded by rainbow-inverted colour scheme: the maximal inscribed spheres (top) and extracted pores (bottom) for sub-images of SF-A, SF-B and BS, respectively...	180
Figure 5-6: Pore Size Distribution of rock samples FS-A, FS-B and BS.	181
Figure 5-7: Skeleton's central location for sub-images of FS-A, FS-B and BS, respectively.....	182
Figure 5-8: Small sub-images of the skeleton with SED values from FS-A, FS-B and BS, respectively. Voxels are supernova spectrum colour coded. Green represents skeleton pore voxels closest to the grain surface and yellow represents the skeleton voxels farthest from the grain surface.	182
Figure 5-9: 2D illustration of some configurations in the neighbourhood of a pore voxel of radius 1 (in voxel): All the pixels centred at each 3×3 square have the same radius of 1 in pixel (voxel) but have different configurations in its neighbourhood. The solid circle shows the sphere (circle) associated with the initial radius (e.g. 1) measured through the distance transformation while the dotted circle shows the ideal sphere (circle) for a more accurate radius. The ideal radius is showed right below each figure. Grey squares represent pore pixel and white square solid pixel.	183
Figure 5-10: The distribution of the number of 26-neighbours at a skeleton voxel with SED of 1 for sample FS-B.	185
Figure 5-11: The distributions of cross sectional diameter of sample FS-A, FS-B and BS.	185
Figure 5-12: The distributions of cross sectional area of skeleton voxels.	186
Figure 5-13: The distributions of shape factor of skeleton voxels for the three samples.	187
Figure 5-14: Illustration of invading process of mercury using our algorithm.....	190
Figure 5-15: Simulated mercury injection curves of FS-A, FS-B and BS.....	190
Figure 5-16: Distributions of the coordination number of pore networks extracted from FS-A, FS-B and BS.	191

Figure 5-17: Connectivity functions of sample FS-A, FS-B and BS.....	192
Figure 5-18: The stable trend of connectivity coefficients of FS-A, FS-B and BS as the volume of sub-images increase from about 0.1 mm ³ to 5.0 mm ³	195
Figure 5-19: Network structures of (100 ³) sub-samples of FS-A (left), FS-B (middle) and BS (right). The regions with volumes represent nodes and the grey lines bonds without volume. In IC network model, both of them are assigned with volume.	198
Figure 5-20: Node and bond size distributions of FS-A, FS-B and BS.	199
Figure 5-21: The correlation between node size (cross sectional diameter at the centre of each node) and the corresponding coordination number.....	200
Figure 5-22: The correlation between node size and the corresponding length of adjacent bonds.	201
Figure 5-23: The correlation between node and their adjacent node cross sectional diameter.	202
Figure 5-24: The stable trend of absolute permeabilities when the volume of sub-image becomes larger and larger.....	205
Figure 5-25: Relevance of the shape factor for the absolute permeability using the IC network model for sample FS-A. This result uses the same network for each experiment, with the difference being the assigned shape factor for all pores in that model.	206
Figure 5-26: Predicted oil/water relative permeabilities by IC network model for FS-A (top row), FS-B (middle row) and BS (bottom row). The primary drainage relative permeabilities illustrated in the left, secondary imbibition (waterflooding) relative permeabilities in the right.....	207
Figure 5-27: Measured data and their trend-lines of absolute permeability (K) against the average cross sectional inscribed diameter (I_d) for FS-A, FS-B and BS.	209
Figure 5-28: 2D schematic pictures demonstrate the idea for changing the topology by removing skeleton voxels.....	210
Figure 5-29: The correlation curves between absolute permeability K and connectivity coefficients ζ_v with trend-lines of slopes of 4.18, 6.38, and 3.39 for FS-A, FS-B and BS, respectively.	211
Figure 5-30: The correlation among absolute permeability (K), connectivity coefficient (ζ_v) and average cross sectional diameter (I_d) for sample FS-B.	214

Figure 5-31: Each curve corresponds to an array of reconstructed rock images with the same average pore size after removing amount of skeleton voxels. It shows the change of absolute permeability K against the connectivity coefficient ζ_v without changing the pore size.214

GLOSSARY

- A area, mm²
G shape factor
 I_d inscribed diameter, mm
K absolute permeability, mD
 K_r relative permeability
 K_{rw} wetting phase relative permeability
 K_m non-wetting phase relative permeability
P perimeter, mm

GREEK SYMBOL DESCRIPTIONS

- α black (foreground) adjacency
 β white (background) adjacency
 χ Euler number
 δ small increment
 ∇ gradient vector
 ε very small positive increment
 λ an adjacency
 μ viscosity of phase
 π a path
 ϕ porosity
 θ contact angle
 ρ smoothing perimeter coefficient
 σ standard variance
 ζ connectivity coefficient
 Δ small increment
 Σ summation

SUBSCRIPTS DESCRIPTION

c	chamfer distance of a unit shape or a corner
d	distance
e	an edge
x	x-direction
y	y-direction
z	z-direction
v	volume relevant or a vertex

NAME DESCRIPTION

CD	chamfer distance
CDC	chamfer distance coefficient
CS	cross section
DT	distance transformation
DM	distance map
EPC	Euler-Poincaré characteristic
GCD	geodesic chamfer distance
GD	geodesic distance
GED	geodesic Euclidean distance
GT	geometric and topological / geometry and topology
HKA	Hoshen-Kopelman algorithm
MA	medial axis
PAT	pore analysis tools
PC	personal computer
PS	pore space
PSD	pore size distribution
SED	squared Euclidean distance

LIST OF PUBLICATIONS

Jiang, Z., K. Wu, G. Couples, M. I. J. van Dijke, K. S. Sorbie, and J. Ma, 2007. “Efficient extraction of networks from three-dimensional porous media”, *Water Resour. Res.*, **43**, W12S03, doi:10.1029/2006WR005780.

Wu, K., van Dijke, M.I.J. Couples, G.D., **Jiang, Z.**, Ma, J., and Sorbie, K.S., 2006. “A New 3D Stochastic Model to Characterise Heterogeneous Porous Media, Applications to Reservoir Rocks”, *Transport in Porous Media* **65**, 443-467.

Wu, K., **Jiang, Z.**, Couples, G.D., van Dijke, M.I.J. and Sorbie, K.S., 2006. “Predicting 3-D structure of porous media and network extraction”, *The Gordon Conference on Flow and Transport in Permeable media*, July 30 - August 4, 2006 Proctor Academy, Andover, NH USA

Jiang, Z., Wu, K., Couples, G.D., van Dijke, M.I.J. and Sorbie, K.S., 2006. “Characterisation Of Pore Sizes and Connectivity in 3d Porous Media”, *CMWR XVI - Computational Methods in Water Resources, XVI International Conference*, Copenhagen, Denmark, June 19-22 2006

Wu, K., **Jiang, Z.**, Couples, G.D., Ma, J., van Dijke, M.I.J. and Sorbie, K.S., 2005. “Pore System Topology and the Prediction of Microscale Flow Properties”, *SIAM Conference on Mathematical and Computational Issues in the Geosciences*, June 7-10, 2005, in Avignon, France.

Wu, K., **Jiang, Z.**, Couples, G.D., van Dijke, M.I.J. and Sorbie, K.S., 2007. “Reconstruction of Multiscale Heterogeneous 3D Porous Media and The Flow Prediction”, *The 21st International Symposium of the Society of Core Analysts*, Calgary, Canada, 10-13 September 2007 (Oral Presentation).

Wu, K., **Jiang, Z.**, Ma, J., van Dijk, M.I.J., Couples, G.D., Sorbie, K.S., 2004. “A New 3-D Method to Characterise the Pore Structure of Deformed Rocks”, *EURO-Conference 2004 on Rock Physics and Geomechanics*, 20 – 23 September, Potsdam, Germany.

Chapter 1 Introduction

Fluid flows through porous media, and the thermal, electrical, and acoustic properties of these materials, are largely controlled by the geometry and topology of the pore systems. It is now well understood that these macroscopic properties cannot be derived theoretically without consideration of the micro-geometry and connectivity of the pore space through which transport takes place. The elucidation of the relationship between the microstructure and macroscopic flow behaviour in porous media is a fundamental problem of longstanding interest and of significant commercial importance. The major theme in this study is the representation of the pore space by a network of discrete “elements” and then predicting macroscopic properties across the network by applying certain fluid transport rules; this is referred to as pore-scale network modelling. In recent years, a large number of network models have been successfully used for this purpose, but the full power of the network approach depends strongly on the accurate and direct characterization of pore microstructure (i.e. the determination of geometric and topological features of the pore systems). Recent advances in high-resolution tomography have provided high quality 3D images necessary for the pore-scale characterization of porous media systems. The voxel representation (image) of the pore space makes it possible to quantify the microscopic characteristics. For the quantification of the pore space in 3D binary rock images, I have focused on extracting microscopic information of relevance to transport processes in a more accurate and systematic way by introducing a series of new approaches or by utilizing and refining existing techniques. These methods can be regarded as relating to the general fields of image processing/analysis, digital geometry/topology, and network modelling.

1.1 Background

The immediate motivation for this research is related to concerns associated with maximising recovery from hydrocarbon reservoirs. After a new oil field has been

discovered and primary conventional oil recovery has been carried out, a secondary or an enhanced recovery development plan may need to be implemented since as much as 60% of the original oil may otherwise be left in place (Macdonald et al., 1986[97]). Any such development depends on having a good understanding of the reservoir. That understanding will include issues related to the properties of the rocks.

Secondary and enhanced recovery processes usually involve the injection of various fluids or gas into the reservoir to displace the remaining oil. Although the length-scale of an oil field is measured in kilometres, the ultimate success of an oil recovery scheme is the net result of countless displacement events at a scale measured in microns. All recovery processes depend on the redistribution of reservoir fluids during production and injection, and the precise manner in which this occurs determines how much of the initial hydrocarbons will be recovered and how much will be left trapped (Silin and Patzek, 2006[157]). Traditional methods model multi-phase flows in this system using an averaging approach (e.g. Darcy's law). In fact, the effectiveness of the multi-phase flow oil displacement process is to a large extent determined by the pore-scale behaviour within the reservoir rock (Zhao et al., 1994[193]). The pore-scale behaviour in turn is governed by capillary displacements depending on the interfacial tensions, the wettability or phase contact angle at the pore surfaces and the pore sizes (van Dijke and Sorbie, 2003b[173]). The oil recovery is determined by the residual saturation – the volume fraction of the pore space (PS) occupied by oil which cannot be recovered because it is trapped or bypassed in the reservoir rock by the combined effects of capillarity or heterogeneity. Most of the existing methods for determining multi-phase macroscopic physical properties (e.g. residual saturation) and constitutive relations (e.g. capillary pressure-saturation, relative permeability) have either been measured experimentally or calculated using largely empirical approaches which are limited in their detail and applicability (Al-Raoush and Willson, 2005[7]). More recently alternative means of predicting fluid flow have been developed. For example, pore-scale modelling (e.g. network and Lattice Boltzmann) methods have been extensively explored to improve on our understanding of single-/multi-phase flow in porous media to obtain realistic estimations of residual saturations. Pore-scale modelling methods, particularly network models, offer a systematic approach to developing the relationship between microstructure and macroscopic properties. Recent advances in pore-level network modelling give researchers and engineers better insights

into pore-level displacement mechanisms, which play a profound role in influencing the mechanisms of secondary and enhanced oil recovery processes (Macdonald et al., 1986[97]). Furthermore, credible predictions of the impact of the rock wettability and fluid properties on the relative permeabilities and capillary pressures, as well as on the trapped oil and gas saturations, are now possible. Therefore, the study and use of network models makes it possible to design a physically based oil recovery development plan to pursue the goal of optimal reservoir development.

In the network modelling of flow through porous media, the pore structure is represented as a network of pore-bodies connected by pore-throats. The pore-bodies and pore-throats are often assigned some idealized geometry (e.g. spheres, cubes, or cylinders in 3D), and, by applying rules that govern the transport and arrangement of fluids in pore-bodies and pore-throats, macroscopic properties can then be predicted across the network (Lopez et al., 2003[93]). The prediction of physical properties of porous media from their microscopic origins usually involves three major steps (Øren and Bakke, 2003[119]): (i) the quantitative characterization of the microstructure; (ii) the characterization of wettability and the relevant pore-scale physics; (iii) an exact or approximate solution of the equations of motion that govern the transport phenomena of interest. To do so, two general approaches are commonly used. The first attempts to create an equivalent network using some statistical parameters (e.g. Vogel and Roth, 2001[185]; Delerue and Perrier, 2002[38]; Silin and Patzek, 2006[157]), and the second tries to directly map a specific porous medium onto a network structure in order to provide a one-to-one spatial correspondence between the porous medium and the network structure (e.g. Valvatne and Blunt, 2004[170]; Knackstedt et al., 2004[72]; Lindquist, 2006[86]; Van Dijke and Sorbie, 2006[174] and 2007[175]; Al-Kharusi and Blunt, 2007[3]).

Network models have successfully been used to study a wide range of single- and multi-phase flow processes. In the 1950s, Fatt (1956a[45], 1956b[46] and 1956c[47]) pioneered the network modelling approach for predicting relative permeability and capillary pressure. A number of studies following Fatt's approach appeared over the following decades (e.g. Larson et al., 1977[80]; Koplik, 1982[77]; Wilkinson and Willemsen, 1983[187]; Lenormand et al., 1983[82]; Kantzas and Chatzis, 1988[70]; Sahimi, 1988[142] and 1998[143]). Jerauld and Salter (1990[65]) investigated the effect of pore structure on relative permeability and capillary pressure hysteresis in two-phase

systems. Reeves and Celia (1996[134]) investigated the functional relationship between capillary pressure, saturation, and interfacial area using a pore network flow model. And Dillard and Blunt (2000[43]) modelled the fluid dissolution by tuning a network model to match the capillary pressure measured by dissolution experiments. Large scale computer simulations using pore network models of porous systems were carried out by Knackstedt et al. (2001[71]) who studied the effects of power-law fractal correlations on the pore-size distribution, and the effects of correlated heterogeneity on two-phase flow through porous media. Meanwhile the effect of variation of the wettability from pore to pore on three-phase flow was investigated by Van Dijke and Sorbie (2002[171]). And later they (van Dijke and Sorbie, 2003a[172]; 2003b[173]) developed a three-dimensional pore-scale network model for modelling capillary-dominated three-phase flow in porous media where the wettability varies from pore to pore, and the multi-cycle water-alternating-gas injection floods were simulated (Van Dijke and Sorbie, 2006[174]). The above rather selective summary of work indicates that pore network modelling has already become an effective tool to investigate or predict macroscopic properties from an understanding of fundamental pore-scale behaviour.

However, the difficulty of adequately describing the complex PS of real rock has substantially hampered network modelling of porous systems. According to Øren and Bakke (2003[119]), the quantification of pore structure combined with characterization of the wettability and the relevant pore-scale physics is essential for generating a network structure with genuine prediction capability. Particularly, quantitative characterisation of the pore microstructure of the porous medium is of utmost importance in the prediction of macroscopic fluid flow properties (Lindquist, 2006[86]). Blunt (2001[21]) emphasised: *“More research is needed to determine if we can characterize the pore space and wettability of reservoir rocks with sufficient ease and accuracy to make predictions of relative permeability and other properties a practical reality. If this is possible, then pore-scale modelling will have a huge impact on improved core analysis and characterization of multiphase flow properties”*. Therefore, in order to relate laboratory measurements conducted on core plugs to the larger scale (e.g. the field scale), much effort needs to be made to effectively characterise pore structure from the core scale down to the pore scale (Sheppard et al., 1999[151]). In other words, based on realistic and accurate morphological (i.e. geometrical and

topological, GT) information on the PS, the full power of the network approach may be realized to better understand macroscopic phenomena (Vogel, 2000[183]).

Quantitative characterisation of the GT of the PS includes (1) the determination of geometric/spatial features (e.g. pore size, pore shape, area, volume and physical locations), (2) the identification of pore connectivity (e.g. coordination number, specific Euler number and connectivity function), (3) the calculation of correlations between these quantities (e.g. two-point coordination function); and (4) the measurement of the statistical distributions (e.g. pore size distribution, coordination number distribution). With accurate and rich descriptors, we can then construct realistic network structures for the prediction of macroscopic properties using the network model approach. Moreover, we may then be able to explore single/multi-phase flow by establishing some analytical equations based on these characteristics.

In general, there are two kinds of methods which have been used extensively to characterise the pore microstructure. The first is to undertake experimental measurements of microscopic properties. For instance, the pore size distribution (PSD) of the PS can be obtained using experimental results such as water retention curves, mercury intrusion porosimetry, nitrogen adsorption isotherms or water desorption isotherms. But the accuracy of such measurements and the difficulty of unambiguously interpreting such laboratory experiments undermine the value of these kinds of methods. The second approach is to apply image processing and analysis techniques for extracting GT information directly from 2/3D rock images. Although some excellent methods, based on 2D thin sections (slices in 3D images), have been developed (e.g. Vogel, 1997a[181] and 1997b[182]), the results are not entirely accurate because all pairs of two parallel spatial close slices (i.e. disectors) do not provide sufficient information about the global connectivity and spatial variation of the 3D digital space (Kong et al., 1992[75]). Alternatively, using 3D images as the basis to quantify the pore microstructure has become a popular method in recent years.

There are various ways to obtain 3D images of porous media. For example, by directly simulating the actual sedimentary process, compaction and diagenesis, 3D rock images can be generated using numerical techniques (e.g. Øren and Bakke, 2003[119]). From 2D thin sections, 3D image reconstructions have been reported (Okabe and Blunt, 2005[117]; Wu et al., 2006[188]). Also micro-CT scanning of 3D images has been developed by several groups (Baldwin et al., 1996[13]; Lindquist and Venkatarangan,

1999[88]; Sok et al., 2000[160]; Delerue and Perrier, 2002[38]; Knackstedt et al., 2004[73]). In fact, recent advances in these techniques have allowed researchers to obtain 3D rock images at levels of the resolution down to $\sim 1 \mu\text{m}$ or even smaller (Sheppard et al., 2005[153]). The acquisition of these extremely rich data sets has motivated the development of algorithms for characterising the PS.

Quantitative characterisation of the PS from 3D rock images can be broadly categorised into two classes: medial-axis-based and non-medial-axis-based approaches.

For a porous medium, if we neglect the solid parts that “float” in the PS, the medial axis (skeleton) of the PS appears as a set of lines of voxels, which is located at or near the centre of the PS. The medial axis (MA) provides simple and compact (i.e. a lower dimensional representation) information about the GT of the PS and it is easier to analyse. Thus, several characterization approaches focus on the use of the pore skeleton. Additionally, the MA can be used as an embedded search structure to find specific sites (e.g. junctions) in the PS.

Based on the pore skeleton, Lindquist et al. (1999[88] and 2000[89]) developed algorithms to measure many morphological properties such as coordination number, pore channel length, pore volume, throat surface area, and pairwise correlations between these parameters. Recently, Prodanović et al. (2007[130]) presented an implementation to compute principal diameters for pores and throats, and surface areas and shape factors. Using a distance-ordered homotopic thinning algorithm (Pudney, 1998[132]), Knackstedt and co-workers (<http://www.rspysse.anu.edu.au/~col110/disord.html>) also built up a series of medial-axis-based algorithms to describe the microstructure of porous media, including effective throat/pore radii, coordination number, and pore channel lengths etc. In addition, some distributions, such as the correlation between throat-area and average pore volumes are also calculated and analysed extensively (Sok et al., 2000[160]). Ioannis and Ioannidis (2000[61]) utilised the template-based thinning algorithm (Ma and Sonka, 1996[96]) to extract the medial axis, and they then characterised many geometrical and topological parameters, such as pore volume, throat area, throat hydraulic radii, coordination number, effective pore size (radius) and throat size.

In non-medial-axis techniques, the general idea is to use mathematical morphology approaches to process the image and to quantify the disordered morphologies of porous media. Many researchers have made progress in the study of

these algorithms and applications. Delerue et al. (1999a[39] and 1999b[40]) introduced the concept of local pore size, which is defined as follows: At each point or voxel, the local pore size is the size of the maximum ball included in the PS and including the voxel. And they then developed a determination algorithm for the local size map. Based on the map, the PSD was straightforwardly calculated and a numerical simulation of mercury intrusion was carried out. Vogel and Roth (2001[185]) measured the morphological size distribution using morphological operations (e.g. erosion and dilation) and introduced the connectivity function which relates the specific Euler number to the corresponding pore size. However, inspired by the basic idea of pore skeleton, Silin and Patzek (2006[157]) analysed the GT of the PS based on a “maximal inscribed ball” algorithm. In their approach, a thinning image (skeleton-like) was used to distinguish between pore-bodies and pore-throats, and then the PSD and coordination number were easily obtained.

With high quality 3D images of porous media at hand, it is then possible for one to characterise the pore GT features, which are relevant to fluid flow and transport properties. However, the question is how to obtain accurate and sufficient quantities in a very efficient way. The answer is to establish a suite of comprehensive tools for image processing, feature description and statistical analysis. The quantification of the PS involves the application of several disciplines such as mathematical morphology, image processing, digital geometry and digital topology, and this is a complicated and demanding task. By doing so, we can construct a realistic network model directly mapped from 3D microstructure of the complex PS. This should retain the pore morphology and any inherent spatial correlations, and should make possible the predictions of macroscopic flow and transport properties. Most of the necessary microscopic properties have been successfully extracted from 3D images of porous media, good matches with experimental results have been reported, and reasonable predictions have also been reported through specific numerical experiments (e.g. Liang et al., 2000a[84] and 2000b[85]; Sok et al., 2000[160]; Vogel, 2000[183]; Van Dijke and Sorbie, 2002[171]; Okabe and Blunt, 2005[117]; Silin and Patzek, 2006[157]). However, an important question now arises: how can one fully capture the pore-scale GT characteristics with a network model? Such a question arises due to the inherent gap between often-used numerical representations and the complex morphology of the PS.

The accuracy and efficiency of algorithms are the main considerations of this thesis for the quantification of the PS.

1.2 Challenges in Characterisation of the Pore Space

For 3D rock images, I make the assumption that they are of high quality (e.g. appropriate resolution, noise-free), which means that they provide sufficient detailed information about the microscopic structure of the PS. The image itself may have originated from computer tomography (CT), image reconstruction from 2D thin sections, a computer model of rock deposition, or any other source. Instead of exploring the techniques to acquire such images and any artefacts related to the methods, I concentrate on the characterisation of the PS from 3D binary rock images, which is very useful for pore structure analysis, since this still poses challenging problems (Silin and Patzek, 2006[157]) in terms of (i) topological description, (ii) skeletonization and (iii) algorithm efficiency, as discussed in the following.

Topological description: The topology (connectivity) of the PS plays an important role in flow and transport in porous media. Unfortunately, a quantitative description of the connectivity of the complex porous structure is difficult (Vogel and Roth, 2001[185]). Most of the previous studies on this topic have focused on the determination of coordination number, i.e. the number of connections from one pore to others, which significantly depends on the definitions of pore-bodies and pore-throats and their corresponding partitioning algorithms. It is commonly recognised that the coordination number is a local topological property and is not sufficient for the statistical analysis of macroscopic fluid flow. Therefore, the Euler-Poincaré characteristic (EPC, or the Euler number) is regarded as an alternative descriptor, which is defined as the number of isolated components minus the number of redundant connections plus the number of completely enclosed cavities in the PS. For the EPC, there exist two problems that need to be solved: (a) the EPC is very sensitive to the image noise, and this highlights the importance of introducing a robust descriptor of the pore connectivity; (b) accurate computation of the EPC is still demanding. Vogel and Roth (2001[185]) presented an algorithm for obtaining the unbiased estimation of the EPC. They introduced the concept of connectivity function and applied it in their tunable network models. Apart from the exact computation of the EPC, counting

exactly how many pore components and how many redundant connections existing in the PS are also difficult problems.

Skeletonization (medial axis transformation): The concept of MA plays a pivotal role in subsequent investigations, such as partitioning the PS and measuring GT properties. Apart from morphology-based (e.g. Baldwin et al., 1996[13]) and Voronoi diagram-based (e.g. Delerue et al., 1999a[39]) approaches, many skeletonizations (i.e. the way to extract skeleton) are based on homotopic thinning (e.g. Lee and Kashyap, 1994[81]; Ma and Sonka, 1996[96]; Pudney, 1998[132]). The thinning algorithm relies on removing voxels layer by layer, while preserving certain GT properties of the object. This process continues until no more such voxels can be removed, and the remaining set of pore voxels becomes the medial axis of the PS.

However, intuitive extension of topological methods to digital images may be insufficient for rigorous analysis because it is difficult to transfer basic topological concepts to the discrete space (Vogel, 1997a[181]). Two of the unwanted side effects of thinning algorithms are pointed out by Silin and Patzek (2006[157]). One is that a refinement of the resolution can lead to less accurate results, and the other is that the result of thinning may be unstable with respect to the choice of the starting point. In addition, the sensitivity to the object boundaries always produces a large number of spurious branches in the MA and the check of the discrete topological invariants at each iteration or sub-iteration during the thinning process can be a daunting computational task. The essence of solving these problems lies in improving the robustness and efficiency of the thinning algorithm.

In obtaining the medial axis, the general requirement is topology preservation. Common morphological and Voronoi diagram-based algorithms cannot meet this demand. Another important geometrical constraint during the thinning process is that the MA should be located in the middle of the PS. Most of the existing algorithms either neglect this requirement or simply rely on additional trimming processes. Other features of the MA, including primary branches (related to the dead-end pore) and single voxel width, also need to be taken into account.

Therefore, much work involved in the skeletonization need to be done including comparison of thinning algorithms, determination of requirements about the MA and development of a robust as well as efficient thinning algorithm and extension of the applications of the medial axis.

Algorithm efficiency: Suppose we wish to analyse 3D binary images with large dimensions of 512^3 on a common PC within 1.5 hours (e.g. 1G RAM, 2.8GHz CPU). Developing appropriate algorithms to achieve this target without a high performance parallel computer is a very challenging task.

There are a lot of critical attributes of computer algorithms used in the measurement of GT properties and the pore partitioning, where the memory-consumption and computational complexity must be taken into account very carefully. It is well known that many quantities computed in discrete space may not retain the features of their continuous analogues. For instance, in the continuum space, a ball of radius r_1 centred at c_1 includes a ball of radius r_2 centred at c_2 if and only if $r_2 + \text{dist}(c_1, c_2) \leq r_1$, where $\text{dist}(c_1, c_2)$ is the Euclidean distance between the two centres c_1 and c_2 (Silin and Patzek, 2006[157]). But this criterion does not necessarily work in the corresponding discrete space. Such a paradox of discretisation imposes some additional complexity on the procedure of quantification and partitioning of the PS. Naturally, influenced by the original definition in the continuum space we could get the idea of doing something similar on the discrete space. For example, by dilating a described ball centred at a fixed voxel with radius addition of one voxel in each step until the ball touches the pore-solid boundary, the radius of the maximal described ball is then determined. In fact this method has no significant difference from one which directly computes the shortest distance from a pore voxel to the pore-solid boundary by comparing all the distances to the boundary voxels, and this kind of “algorithms” can be found in some literature. Therefore, in this study, the efficiency and accuracy of algorithms for measuring microscopic properties and statistically characterizing porous media have high priority.

For the construction of a network of pore-bodies and pore-throats, the PS needs to be partitioned into individual elements. Whether to partition the PS into pore-bodies and pore-throats, or just into pore-bodies, is a controversial issue in the network modelling literature. Some network models (e.g. Øren and Bakke, 2003[119]; Blunt, 2001[21]) appear to prefer some volume allocated to pore-throats in order to match experimentally observed residual saturations, while other models (e.g. Chang and Ioannidis, 2002[32]) perform adequately without this additional complexity. In this thesis, I have applied a different technique and used the resultant network structure to feed into the Imperial

College network model (Valvatne and Blunt, 2004[170]) for the prediction of macroscopic properties.

1.3 Motivation and Objective

It has been noted that the characterisation techniques for 3D porous media are still under development (Silin and Patzek, 2006[157]). The study of the digital topological attributes of porous media is essential to supply the relevant quantities for pore network modelling. We require a suite of accurate, efficient, robust and systematic tools for measuring GT properties of the PS or characterizing porous media in terms of various statistical quantities.

The main objective of this thesis is to develop a suite of algorithms and tools, which can be employed to quantify the PS, to conduct some basic analysis, and to construct a much more accurate and realistic network structure for predicting the flow properties of reservoir rocks. This general objective is achieved through the following steps:

- To intensively study the discrete topology of the PS by introducing effective topological invariants, developing algorithms for computing the EPC, and exploring the relationship between common topological quantities and the inherent connectivity of the PS.
- To analyse the advantages and disadvantages of previous skeletonization algorithms, and then develop a more robust and efficient thinning algorithm which will be suitable for generating the MA (implemented on a PC) in a reasonable time for a high resolution, large size and high porosity 3D rock image.
- To compare existing measurements and characterization techniques, find out the general demands for such approaches, and design more accurate and efficient algorithms to do the same task or an extended range of study.
- To extract the pore network structure that will be used as input for the network flow model to predict flow properties.
- A potential objective is to relate the functional relationship between macroscopic flow or transport properties and certain statistics, such as between absolute permeability and inscribed diameter, between absolute permeability and connectivity etc.

1.4 Outline of This Thesis

This thesis is structured as follows. Chapter 1 has given a brief introduction to the study of GT characterisation of porous media highlighting some recent research findings. Chapter 2 reviews the general topics of image processing and analysis techniques with emphasis on the current state of pore characterisation. In Chapter 3, I present the implementation and improvement of some important image processing algorithms including component labelling, morphological operations, the calculation of EPC and the extraction of skeleton from images. In Chapter 4, some pore structure analysis techniques are proposed of particular use for the study of multiphase fluid flow. In Chapter 5, some examples of applications of our methodology are given based on three rock sample datasets and some preliminary results on the analysis of pore structure are given. A summary of the main findings and the conclusion which I have achieved are given in Chapter 6.

Chapter 2 Literature Review

2.1 Morphological Image Processing

2.1.1 Digital Images

In general, the intensity (or grey level) of experimental images may be thought of as a continuous function of the position in the image, where the set of all positions in the Euclidean space is called the image space. In order to computationally handle and analyse images we first need to digitise them in order to obtain digital images. The digitisation is carried out by mapping the image onto a grid with quantization of the grey level. Usually, the image space of 2D (3D) digital images is represented by a lattice of squares or cubes shown in Figure 2-1. Each square (cube) is centred at a lattice point, corresponding to a pixel (2D) or a voxel (3D). Usually, the range of grey levels is divided into intervals and the grey level at any lattice point is required to take only one of these values. Binary images are just the special case of the grey level images when only two values are used, which are usually obtained by thresholding the range of grey level. However, in the study of digital geometry and topology (Kong and Rosenfeld, 1989[76]), an alternative definition of a binary image is given later which combines the identity of object and the adjacency of object points together.

To facilitate the discussion in the following, some mathematical definitions and notations are introduced in this section. Let \mathcal{P} be a grey level (or binary) image with image space \mathcal{V} in the d -dimensional discrete space Z^d . Often \mathcal{V} is chosen as a rectangular subset of Z^d , in other words, there are d positive integers $M_1 \dots M_d$ such that $\mathcal{V} = \{(p_1, p_2 \dots p_d) : 0 \leq p_j \leq M_j \text{ for } j = 1, 2 \dots d\}$. When $d = 3$, M_1 , M_2 and M_3 are the coordinates in the x , y , and z directions, respectively. For each lattice point $q \in \mathcal{V}$, hence, its coordinates can be simply written as (i, j, k) and the corresponding grey value at q of image \mathcal{P} is denoted by $\mathcal{P}(i, j, k)$. Usually, the intensity is digitised in the range $[0, 255]$, and with respect to the grey value all voxels (or pixels) in the image space are classified as either object (foreground) or non-object (background). In the following

discussion, I focus on introducing some basic concepts in mathematical morphology with emphasis on the morphological image processing of binary images.

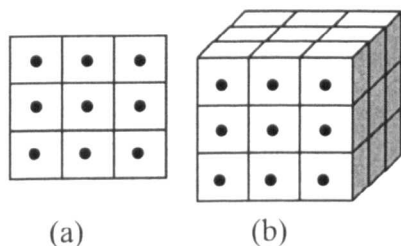


Figure 2-1: The representations of 2D or 3D image in terms of lattice of (a) squares – pixel or (b) cubes – voxels, respectively.

2.1.2 Mathematical Morphology

An ideal 2D or 3D digital image, such as computer-generated images (e.g. reconstructed images), is one that is free of noise and other artefacts which may affect the quantification of pore microstructures. Unfortunately, as is well known, genuine images obtained from CT (computed tomography), MRI (magnetic resonance imaging), or MRA (magnetic resonance angiograms) are certainly not perfect. Therefore, image pre-processing may be necessary before describing objects in such images in words or other quantities.

Digital image processing is very important for many industrial, medical and scientific applications. There is a vast amount of literature on this subject and a wealth of basic image processing techniques is available. As a branch of image processing, morphological image processing can be applied to enhance image quality or to extract image characteristics.

Mathematical morphology is essentially a set theory. By selecting a primitive shape as a probe (filter or template), set transformations may then be carried out to extract information about the shapes of objects in question. This approach was first investigated by Matheron (1975[104]) at the Paris School of Mines and extended by Meyer (1977[107]) and Serra (1982[149]). In the following, I summarise basic concepts in mathematical morphology in order to give a glimpse into the mathematical foundations and corresponding intuitive interpretations for describing objects (patterns, structures) in images.

Considering a point $p = (p_1, p_2 \dots p_d)$ and a set S in d -dimensional Euclidean space E^d , S_p denotes the translation of S by p , i.e. $S_p = \{p + b: b \in S\}$. The basic morphological operations are dilation and erosion, which can be extended to create many other morphological operations such as opening and closing.

The dilation of \mathcal{A} by \mathcal{B} is defined as the union of all translations of \mathcal{B} by every point in \mathcal{A} . Equivalently, this is a set that consists of all possible vector sums of pairs of elements, one coming from \mathcal{A} and the other from \mathcal{B} , i.e.

$$\mathcal{A} \oplus \mathcal{B} \equiv \cup_{b \in \mathcal{B}} \mathcal{A}_b = \{a + b: a \in \mathcal{A}, b \in \mathcal{B}\}. \quad (2.1)$$

The erosion is the morphological dual to the dilation. It combines two sets using vector subtraction of set elements. For two sets \mathcal{A} and \mathcal{B} in E^d , the erosion of \mathcal{A} by \mathcal{B} is the set of all elements x for which $x + b \in \mathcal{A}$ for every $b \in \mathcal{B}$, which is given by

$$\mathcal{A} \ominus \mathcal{B} \equiv \{x \in \mathcal{R}^d: \mathcal{B}_x \subseteq \mathcal{A}\}. \quad (2.2)$$

Obviously the roles of the sets \mathcal{A} and \mathcal{B} are symmetric in the dilation, i.e. $\mathcal{A} \oplus \mathcal{B} = \mathcal{B} \oplus \mathcal{A}$, but this is not true for the erosion. The dilation is identical to Minkowski addition (Michielsen et al., 2002[109]), however, one should be aware that the erosion is different from Minkowski subtraction, which is the intersection of all translations of \mathcal{A} by the elements $b \in \mathcal{B}$.

The basic morphological operations \oplus and \ominus can be used to construct other operations that perform more comprehensive filtering operations. Two of them are commonly used in pore structure analysis. They are opening \circ and closing \bullet operations, which play a very important role in morphological image processing and analysis. The opening and the closing are defined, respectively, as

$$\mathcal{A} \circ \mathcal{B} = (\mathcal{A} \ominus \mathcal{B}) \oplus \mathcal{B}, \quad (2.3)$$

and

$$\mathcal{A} \bullet \mathcal{B} = (\mathcal{A} \oplus \mathcal{B}) \ominus \mathcal{B}. \quad (2.4)$$

Both of them have the basic mathematical properties that are necessary for morphological image processing. For example, both opening and closing are

idempotent, i.e. $(\mathcal{A} \circ \mathcal{B}) \circ \mathcal{B} = \mathcal{A} \circ \mathcal{B}$ and $(\mathcal{A} \bullet \mathcal{B}) \bullet \mathcal{B} = \mathcal{A} \bullet \mathcal{B}$, which mean that it does not help to “open” or “close” an image twice or more using the same template.

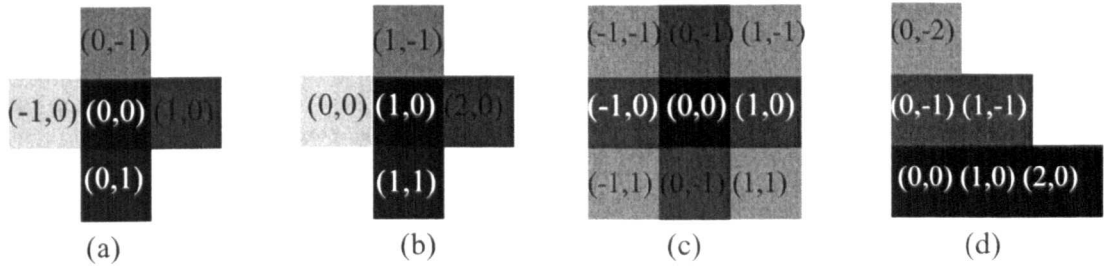


Figure 2-2: Some examples of grey level structuring elements used in morphological image processing. Here the intensity (grey level) is digitised in the range [0,255] (from black to white). Structuring element (a): $\mathcal{T}(-1,0) = 240$, $\mathcal{T}(0,-1) = 180$, $\mathcal{T}(1,0) = 120$, $\mathcal{T}(0,1) = 60$, $\mathcal{T}(0,0) = 0$; (b): $\mathcal{T}(0,0) = 240$, $\mathcal{T}(1,-1) = 180$, $\mathcal{T}(2,0) = 120$, $\mathcal{T}(1,1) = 60$, $\mathcal{T}(1,0) = 0$; (c): $\mathcal{T}(0,0) = \mathcal{T}(1,0) = \mathcal{T}(2,0) = 0$, $\mathcal{T}(0,-1) = \mathcal{T}(1,-1) = 140$, $\mathcal{T}(0,-2) = 230$; (d): $\mathcal{T}(-1,-1) = \mathcal{T}(1,-1) = \mathcal{T}(-1,1) = \mathcal{T}(1,1) = 230$, $\mathcal{T}(0,-1) = \mathcal{T}(1,0) = \mathcal{T}(0,-1) = \mathcal{T}(-1,0) = 130$, $\mathcal{T}(0,0)=0$.

In relation to digital images, the morphological operations can be visualized as working with two images and then creating another image for output. The image being processed is referred to as the active image, and the other image, a kernel (i.e. a template), is referred to as the structuring element. Each structuring element has a designed shape which can be thought of as a probe or filter of the active image. We can modify the active image by probing it with various structuring elements. Usually a symmetrical shape is chosen as a structuring element with its centre as its origin (although this is not necessary). For simplicity, in the following I focus on 2D to demonstrate the basic ideas of mathematical morphological operations. The extension to 3D is trivial theoretically and in practice as well.

The structuring element or template is a key concept in morphological image processing. A structuring element is a predetermined geometrical structure, which represents the viewer’s prior knowledge or expectation about the morphological content (e.g. shape and connectivity) of objects. There are two factors that are closely related to the use of the structuring element: one is its origin (0, 0), and the other is its shape (e.g. square, disc, star, sphere or cube etc.). For simplicity, we define a structuring element \mathcal{T} by specifying the displacement (k, l) relative to its origin together with the value $\mathcal{T}(k, l)$.

Some examples of structuring elements are shown in Figure 2-2. Very often the structuring element is chosen to be a symmetric shape (see Figure 2-2(a) ~ (c)).

Given two 2D grey level images \mathcal{P} and \mathcal{T} , according to Michielsen and Raedt (2001[108]), the dilation, erosion, opening and closing of \mathcal{P} by \mathcal{T} defined in (2.1~2.4) can be rewritten as:

$$\mathcal{P} \oplus \mathcal{T}(i, j) \equiv \text{Max}_{(k, l) \in \mathcal{V}}(\mathcal{P}(i - k, j - l) + \mathcal{T}(k, l)), \quad (2.5)$$

$$\mathcal{P} \ominus \mathcal{T}(i, j) \equiv \text{Min}_{(k, l) \in \mathcal{V}}(\mathcal{P}(i + k, j + l) - \mathcal{T}(k, l)), \quad (2.6)$$

$$\mathcal{P} \circ \mathcal{T} \equiv (\mathcal{P} \ominus \mathcal{T}) \oplus \mathcal{T}, \quad (2.7)$$

$$\mathcal{P} \bullet \mathcal{T} \equiv -((-\mathcal{P}) \circ (-\mathcal{T})). \quad (2.8)$$

Where the maximum in (2.5) and minimum in (2.6) are to be taken over all points in the image space \mathcal{V} of the structuring element \mathcal{T} ; and $-\mathcal{P}(\mathcal{T})$ is the image with the same image space \mathcal{V} as \mathcal{P} but with opposite grey level value with $\mathcal{P}(\mathcal{T})$. Note that a point (i, j) , $(i - k, j - l)$ or $(i + k, j + l)$ may go out of the image boundary of \mathcal{P} . It is convenient to assign minus infinity $(-\infty)$ to such pixels (i, j) which means that non value is given for these pixels at position (i, j) , called undefined pixels (voxels). Usually undefined pixels are considered as belonging to image's background.

In image processing, the two basic morphological operations \oplus and \ominus have local interpretations illustrated in Figure 2-3. For two images \mathcal{A} (square) and \mathcal{B} (disk), if we think of each point p of \mathcal{A} as a seed that grows the object \mathcal{B}_p (by placing the origin of \mathcal{B} at p), the union of all the grown objects is the dilation of \mathcal{A} by \mathcal{B} , i.e. $\mathcal{A} \oplus \mathcal{B} = \{x: \mathcal{B}_x \cap \mathcal{A} \neq \emptyset\}$; And the erosion of \mathcal{A} by \mathcal{B} can be interpreted as the locus of all centres c of \mathcal{B}_c if the translation \mathcal{B}_c of \mathcal{B} by c is entirely contained within \mathcal{A} . It is noted that the erosion of \mathcal{A} by \mathcal{B} may be empty if \mathcal{A} is smaller than \mathcal{B} .

As for the intuitive interpretation of opening and closing, if the structuring element is of convex shape such as a disk or sphere, a kind of simple interpretation of opening and closing is demonstrated in Figure 2-3. The opening of \mathcal{A} by \mathcal{B} is the region which is formed by moving \mathcal{B} within the interior of \mathcal{A} , while the closing of \mathcal{A} by \mathcal{B} can be referred to the locus of \mathcal{B} rotating along the exterior boundary of \mathcal{A} . Generally speaking, the opening smoothes the contour of an image, breaks narrow passages, and

eliminates thin protrusions, while the closing fills the small non-convex shapes and bridges closed parts.

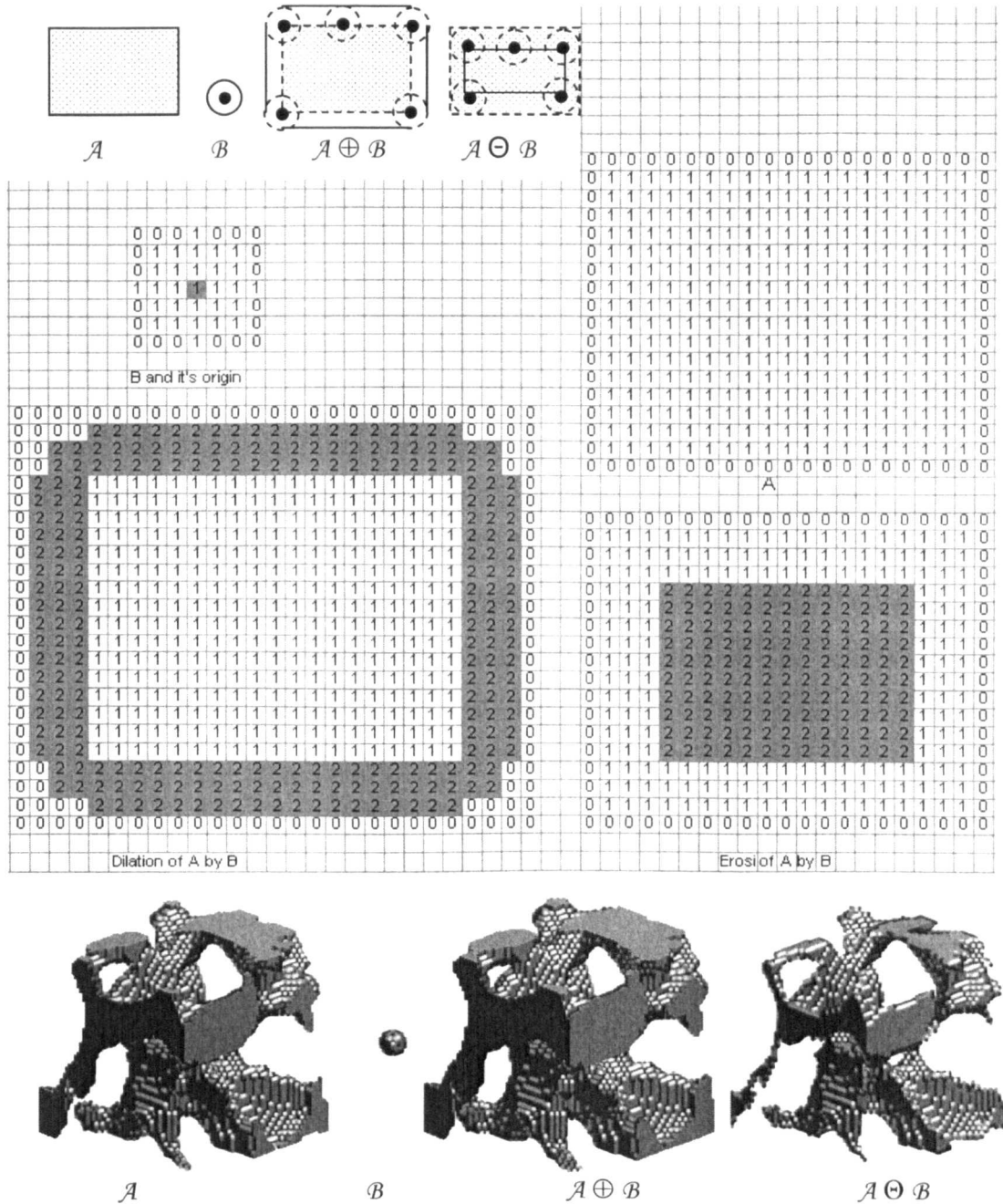


Figure 2-3: Illustration of dilation and erosion of A by B in 2/3D discrete space. A is an active image and B is a structuring element of circular or spherical shape.

In pore structure analysis, geometrical or topological information of the PS can be extracted by performing a number of morphological operations on 3D binary images of porous media.

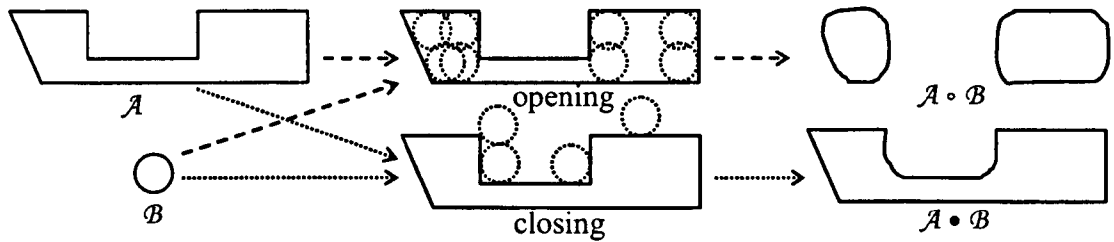


Figure 2-4: An interpretation of opening and closing of A by B : opening breaks narrow passages and eliminates thin protrusions while closing fills the small non-convex shapes and bridges closed parts.

2.2 The Study of Topological Properties of the Pore Space

The topology (connectivity) of the PS describes the way in which the pores are interconnected. The general framework for studying digital topological properties of objects from binary images has been developed by Kong and Rosenfeld (1989[76]). The topological properties of an object remain invariant under translation, rotation, scaling, and rubber-sheet transformation of the object (Gonzalez and Woods, 1993[53]), which include deformations, twisting, and stretching, but tearing is not allowed. From the topological point of view, there is no difference between a circle and an ellipse, or between a sphere and an ellipsoid. Hence, topological information is useful in object classification, thinning and skeletonization of objects, segmentation, and many other applications. In fact, for the study of fluid flow in porous media, Vogel and Kretschmar (1996[184]) proved that the pore connectivity may be more important than the pore size with respect to fluid transfer in porous media.

In the characterization of the topological properties of the PS, there are two types of approaches which are commonly used in the literature. The first is to directly extract the topological quantities (e.g. the Euler-Poincaré characteristic) by counting certain topological elements, such as isolated components, redundant connections (tunnels) or completely enclosed cavities, from 3D binary images of porous media. The second is to implicitly determine the topology by constructing net-like structures through the choice of network configuration, i.e. the arrangement of pore-bodies and pore-throats and certain correlations rules. In a classical pore-throat model, the pore structure is always partitioned into a network of pore-bodies connected by pore-throats. The number of pore-throats linked to a pore-body, i.e. the coordination number, is then used to quantify

the local connectivity of the pore structure. Apparently, the determination of coordination number totally depends on the pore partitioning, as will be discussed later.

2.2.1 Euler-Poincaré characteristic

The Euler-Poincaré characteristic (EPC), or Euler number for short, is a well-known topological descriptor to an object. In statistical physics and in material science, the Euler number is used as a characteristic describing the connectivity of the components of a composite material or of the PS of a porous medium (Ohser, et al., 2003[115]; Levitz, 2007[83]). In percolation theory (OKun, 1990[118]), the Euler number is used to describe the degree of connectivity of disordered (complex) systems (Zallen, 1983[192]) and to provide quantitative information in the determination of a percolation threshold (Stauffer,1985[161]). It belongs to the finite set of Minkowski functionals whose origin lies in the mathematics of convex bodies and integral geometry (Hadwiger, 1957[55]).

There are many equivalent ways for stating the definition of the EPC; see the books of Matheron (1975[104]), Schneider (1993[147]), and Serra (1982[149]). From the mathematical point of view, the EPC $\chi_d(X)$ of a set X in the d -dimensional Euclidean space E^d , is a basic quantity of integral geometry. In the case when X belongs to the convex ring (e.g. a polyhedral set in 3D), i.e. it can be represented as a finite union $X = \cup_{i=1,2 \dots m} X_i$ of compact convex sets X_i (e.g. convex polyhedra in 3D; i.e. for every open cover of a compact set S there exists a finite subcover of S in E^d) the EPC $\chi_d(X)$ can be defined using the inclusion-exclusion formula (Kong and Rosenfeld, 1989[76]) with the initial settings $\chi_d(\emptyset) = 0$ and $\chi_d(X_i) = 1$ for every compact convex set X_i for $i = 1, 2 \dots m$, i.e.

$$\begin{aligned} \chi_d(X) = & \sum_{i=1}^m \chi_d(X_i) - \sum_{i=1}^{m-1} \sum_{j=i+1}^m \chi_d(X_i \cap X_j) \\ & + \sum_{1 \leq i < j < k \leq m} \chi_d(X_i \cap X_j \cap X_k) + \dots + (-1)^{m+1} \chi_d\left(\bigcap_{i=1}^m X_i\right) \end{aligned} \quad (2.9)$$

For the EPC of a polytope, i.e. the convex hull of a finite set of points, there is an alternative definition in terms of the numbers of its lower-dimensional faces. Let $X \subset E^d$ be a polytope. For $k = 0, 1 \dots d$, denote by $\mathfrak{F}^k(X)$ the set of all k -faces of X , and let

$\#\mathfrak{T}^k(X)$ be the number of elements in $\mathfrak{T}^k(X)$ (i.e. cardinal number). Thus, the EPC is defined by

$$\chi_d(X) = \sum_{k=0 \dots d} (-1)^k \#\mathfrak{T}^k(X). \quad (2.10)$$

Most of the existing algorithms for computing the EPC of a digital image are based on counting the total number of k -faces in a polyhedral representation of the image. For example, for any arbitrary triangulation of a set X in 3-dimensional Euclidean space E^3 , which is illustrated in Figure 2-5, $\chi_3(X)$ is equal to the following sum:

$$\begin{aligned} \chi_3(X) = & \text{number of vertices in } X - \text{number of edges in } X \\ & + \text{number of faces (triangles) in } X - \text{number of tetrahedra in } X. \end{aligned}$$

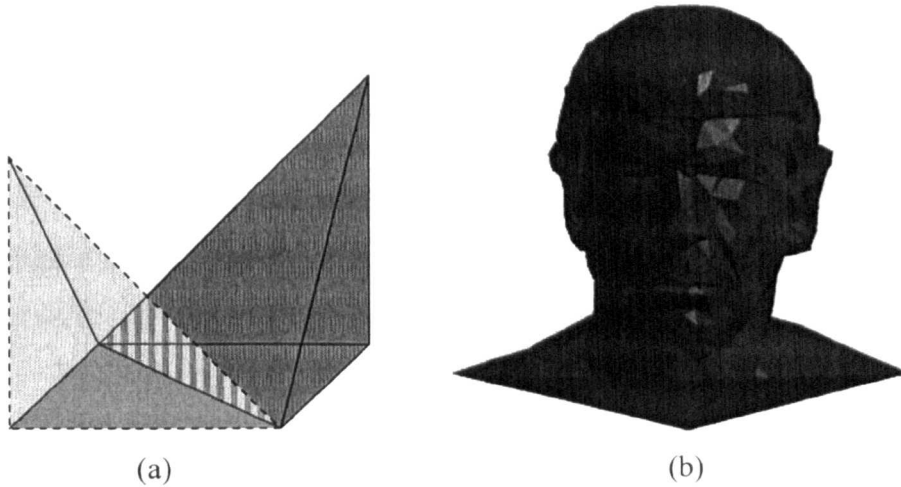


Figure 2-5: Computation of the Euler number for triangulation. (a) A 3D shape triangulated by two tetrahedra, $\chi_3 = 6 - 11 + 8 - 2$; (b) A triangulation of Spock's head with 230k tetrahedra (www.lcg.ufrj.br).

However, the recursive definition given by Hadwiger (1957[55]) is much more intuitive in different dimensional spaces, which is consistent with Kong and Rosenfeld's axioms (1989[76]). Considering a closed set X in d -dimensional Euclidean space E^d , the EPC $\chi_d(X)$ is defined as:

$$\chi_d(X) = \sum_{i=0}^{d-1} (-1)^i h_i(X), \quad (2.11)$$

where $h_i(X)$ is the i^{th} Betti number.

For the Betti numbers, in different spaces the interpretations are slightly different. In 1-dimensional space, $\chi_1(X)$ is the number of segments of X on a straight line. In 2D (see Figure 2-6(a)), $\chi_2(X)$ is the number $h_0(X)$ of separate components of X minus the number $h_1(X)$ of redundant connections (tunnels) within X where the latter equals to the number of holes in X :

$$\chi_2(X) = h_0(X) - h_1(X). \quad (2.12)$$

In 3D (see Figure 2-6(b)), $\chi_3(X)$ is the number $h_0(X)$ of isolated components minus the number of redundant connections $h_1(X)$ (also called the genus, or tunnels) plus the number $h_2(X)$ of completely enclosed cavities in X :

$$\chi_3(X) = h_0(X) - h_1(X) + h_2(X). \quad (2.13)$$

The number of redundant connections (genus, tunnels) h_1 of an object is the maximum number of ways an object may be cut by closed loops (e.g. the black ring in Figure 2-6(b)) without losing its initial connectivity. For example, $h_1 = 0$ for a ball and $h_1 = 1$ for a torus.

In the context of image processing and analysis it is usually assumed that the object set X (e.g. the PS) in the n -dimensional space is observed on a point lattice $L^n = cZ^n$ (where Z denotes the set of integers, $c > 0$ is called the resolution of image). The intersection $X \cap L^n$ is the mathematical expression for the observable information about X . In practical applications, the lattice L^n is restricted to a bounded window $W \subset E^n$. Let I_X denote the characteristic function X , i.e. $I_X(x) = 1$ if $x \in X$ otherwise $I_X(x) = 0$. The set $\{(x, I_X(x)) : x \in W \cap L^n\}$ is said to be the binary image of X observed in W . Usually in 3D, a set of cubic grid points is used as the observing window for 3D digital images. Then, according to the concept of continuous analog introduced by Kong et al. (1992[75]), a 3D digital image \mathcal{P} can be associated with a continuous analog $\mathcal{C}(\mathcal{P})$ (e.g. a polyhedral set), which corresponds to a kind of image representation. Thus the EPC $\chi_3(\mathcal{P})$ is then defined as $\chi_3(\mathcal{P}) = \chi_3(\mathcal{C}(\mathcal{P}))$ (Kong and Rosenfeld, 1989[76]).

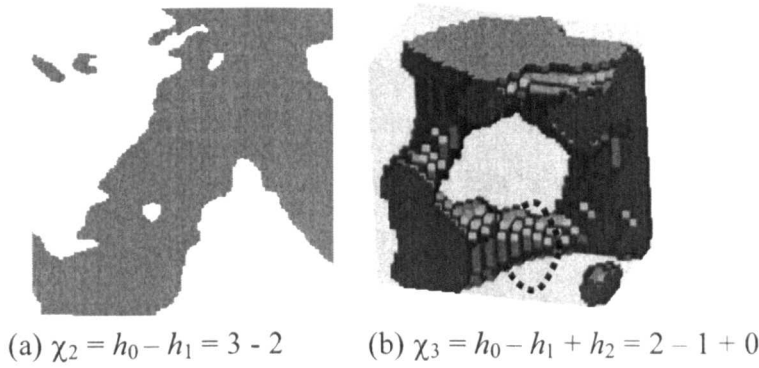


Figure 2-6: Euler-Poincaré characteristic χ in 2/3D. h_0 = number of isolated components, h_1 = number of redundant connections (also called genus, or tunnels in 3D) and h_2 = number of completely enclosed cavities in 3D.

At this stage of the topological analysis of a digital image, the remaining key problem is to compute the EPC based on different image representations. Generally there are three ways to represent the $3 \times 3 \times 3$ neighborhood of a voxel in 3D discrete space (see Figure 2-7).

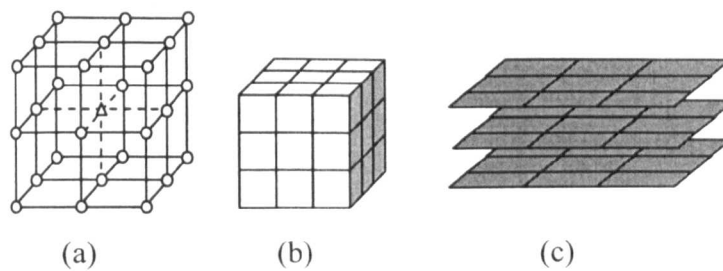


Figure 2-7: Three ways to represent 3D discrete object. (a) Lattice of points, (b) lattice of cubes and (c) lattice of surface patches.

A detailed review of previous presentation-based methods is given by Osher et al. (2003[115]). As stated by them, the computational complexity of the previous methods may be inadequate to meet the critical time requirements for large images, especially for large 3D images. Saha and Chaudhuri (1995[139]) proposed a new approach to tackle this problem. Based on computing the change in the number of black components, tunnels and cavities in a $3 \times 3 \times 3$ neighbourhood of an object point, they described an approach to compute the EPC of a 3D digital image from its lattice representation. Some much more efficient approximations of the EPC have also been investigated such as Vogel’s disector method and Ohser’s discretisation method.

A 3D binary image \mathcal{P} is regarded as the combination of serial parallel surfaces (or sections, see Figure 2-8(c)) X_i , i.e. $\mathcal{P} = \cup_{i=1} \dots m X_i$. Each pair of closely spaced 2D sections is called a disector, denoted by $\mathcal{D}\mathcal{S}(X_i, X_{i+1})$. Gundersen et al. (1993[54]) stated that an unbiased estimate of the 3D EPC can be obtained with the disector. Based on this idea, Vogel and Kretschmar (1996[184]) developed an estimate of $\chi_3(\mathcal{P})$. In contrast to the direct determination of the basic topological quantities h_0 , h_1 and h_2 in (2.13), for example, DeHoff et al. (1972[37]) presented a method for counting the basic topological quantities using serial sections. The estimation of $\chi_3(\mathcal{P})$ is a local measurement.

For a disector $\mathcal{D}\mathcal{S}(X_i, X_{i+1})$ of \mathcal{P} (see Figure 2-8(a) and (b)), the Euler number $\chi_3(\mathcal{D}\mathcal{S}(X_i, X_{i+1}))$ is calculated by

$$\chi_3(\mathcal{D}\mathcal{S}(X_i, X_{i+1})) = (\chi_2(X_i) + \chi_2(X_{i+1}) - 2\chi_2(X_i \cap X_{i+1})) / 2. \quad (2.14)$$

Where $X_i \cap X_{i+1}$ is obtained through the logical AND operator applied to these binary images and $\chi_2(X_i)$ can be easily obtained using Equation (2.12). The EPC $\chi_3(\mathcal{P})$ is then estimated by

$$\chi_3(\mathcal{P}) = \sum_{i=1} \dots m-1 \chi_3(\mathcal{D}\mathcal{S}(X_i, X_{i+1})). \quad (2.15)$$

Vogel and Roth (2001[185]) noted that this approach does not lead to an unequivocal description of the topology because the absolute values of h_0 , h_1 and h_2 are unknown. Principally, an exact determination of the topological quantities requires a global approach, i.e. the complete structure should be known. Consequently, this is the price which has to be paid for a local estimation of topological properties.

Osher et al. (2002[114]) also proposed four approaches to the estimation of the EPC of digital images which are observed in the points of a lattice (see Figure 2-7(b)). The key point is to introduce four versions of a discretisation that is based on different adjacency systems. By conducting comparisons of their four estimators, they found that the estimators, except for (26, 6) yield infinitely large systematic errors when the lattice spacing goes to zero.

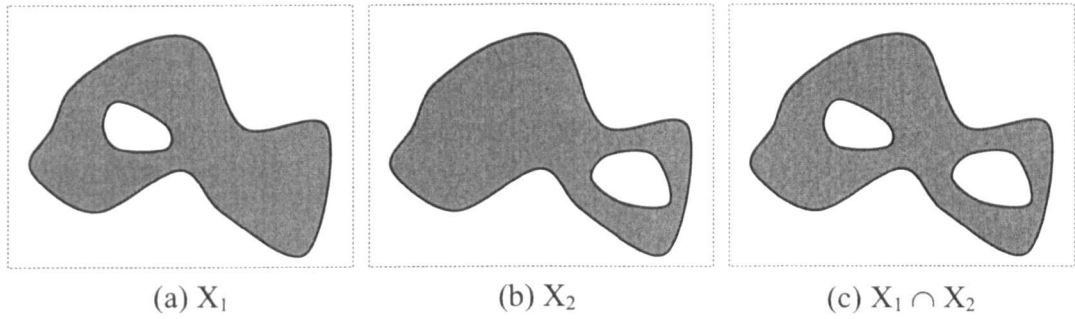


Figure 2-8: Disector and its Euler number. (a) $\chi_2(X_1) = 1 - 1$; (b) $\chi_2(X_2) = 1 - 1$; (c) $\chi_2(X_1 \cap X_2) = 1 - 2$; thus $\chi_3(\mathcal{DS}(X_1, X_2)) = 1$. Where grey region are object and white region are background of a section.

In the sense that the EPC of an object X in E^3 is defined as the EPC of its continuous analog $\mathcal{C}(X)$, $\chi_3(\mathcal{C}(X))$ is said to be the exact value of X . Along this research direction, Kong and Rosenfeld (1989[76]) presented an important localization axiom: the Euler number of a 3D digital image can be computed by calculating the change in the Euler number in $3 \times 3 \times 3$ neighborhood of object voxels. Based on this idea, Saha and Chaudhuri (1995[139]) described a new approach for computing the EPC of a 3D digital image, which is based on computing the change in numbers of isolated components, tunnels and cavities in the $3 \times 3 \times 3$ neighborhood of an object voxel due to its deletion. To do so, a look-up-table is built up by analyzing all configurations of a voxel.

The Euler number is an important topological quantity, however, its discrimination capabilities are limited since it is a single number derived from a linear combination of a certain number (i.e. Betti numbers) of topological elements. That is why many other quantities related to the EPC have been introduced in recent years. Vogel (1997b[182]) presented a connectivity function, which correlates the connectivity and pore size. In contrast to point-to-point correlations, which are most frequently used to introduce topological aspects into models of heterogeneous structure, the connectivity function provides information about the connectivity of the entire region of the model. Bykov et al. (1999[29]) define the concept of the index of a point in a 3D digital image. Based on this concept, an algorithm for computing the EPC was proposed. Ohser et al. (2003[115]) introduced the concept of the density of Euler number and gave an estimation of the EPC. However, currently available topological descriptions and

corresponding algorithms based on image analysis are limited by their inability to quantify the extent of the 3D connectivity of the PS in reservoir rocks.

2.3 Medial Axis (Skeleton)

Geometric analysis of an irregularly shaped object such as the PS of a rock is difficult due to the complicated morphology. This motivates us to reduce the object into a lower dimensional entity, which is called the skeleton of the object. In geometry, every object has a skeleton. The skeleton of an object is a subset of the object, which captures the geometric proximity of the boundary in a simple form. For a two-dimensional object the skeleton may consist at most of a union of curved arcs (see Figure 2-9(a) and (b)). For a three-dimensional object, the skeleton may be a network of surfaces and curved arcs (Figure 2-9(c)). However, if the object does not contain any interior cavities (i.e. the completely enclosed background components, or the floating solid particles), the surfaces in the 3D skeleton can be further reduced to a set of curved arcs. This resulting 3D skeleton is then called the MA if the skeleton only contains curves; otherwise, it is called the medial surface.

Besides the lower dimensional representation, the MA can also hold certain topological and geometrical properties, such as being topology preserving and central location etc. In this case, the MA of an object gives basic information on the topology and geometry; it is a simple and compact representation.

The MA can qualitatively describe how a complex object (e.g. the PS) is decomposed into simpler parts (e.g. nodes and bonds), how these parts bend (i.e. curvature, tortuosity or length of flow paths), and what is the shape and size of individual elements (e.g. pore channels, junctions) in the PS. Using the medial axis, we can clearly partition an object into individual portions and then measure their geometrical quantities. In fact, since the concept was first introduced, the medial axes have found many uses in areas of image processing and visualization. In the next section, I will focus on reviewing the quantification of pore microstructures, where some successful applications of MA are involved, for 3D binary images. In the following discussion, accurate definitions, existing algorithms and properties of the medial axes will be briefly discussed.

2.3.1 Definitions of Medial Axis

In 2D, the MA of an object is defined as the locus of the centres of the maximal inscribed disks (Blum, 1967[20]). In other words, in the continuum space it is the locus of points which are equidistant from at least two points on the boundary of the object. It has been proved that the MA of a 2D object must consist of a set of curves – a 1D representation. In 3D, the maximal inscribed spheres are used to define the corresponding concept although the problem becomes more complicated. The set of the centres of maximal inscribed spheres may contain surface patches in addition to a set of curves, which will then be called the medial surface rather than the medial axis. Figure 2-9 show a MA for a 2D object and a medial surface of a 3D object.

The definition of the medial surface can be formulated as follows (Kong and Rosenfeld, 1989[76]): let $X \subset E^3$ be a 3D object, a sphere of radius r centred at $x \in X$ is defined as $S_r(x) = \{y \in E^3: d(x, y) \leq r\}$, where $d(x, y)$ is the Euclidean distance between two points x and y in E^3 (i.e. $d(x, y) = [(x_1 - y_1)^2 + (x_2 - y_2)^2 + (x_3 - y_3)^2]^{1/2}$). A sphere $S_r(x) \subseteq X$ is maximal if it is not completely included in any other sphere included in X . The medial surface is then the set of centres of all maximal spheres included in X . A more illustrative definition of the medial axis or surface (skeleton) is given by the grass-fire analogy (Blum, 1967[20]), where the boundary of an object made entirely of dry grass is set on fire and the skeleton consists of the loci where the fire fronts meet and quench each other. The process of obtaining a skeleton is called skeletonization, and is also called the medial axis transformation (MAT) if the inscribed radii of each MA voxel are also recorded.

In the GT analysis of the PS, it is assumed that most of the flow paths in porous media have tubular-like shapes which will lead to a network of curves as the result of skeletonization. For example, the skeleton of a torus is a curved arc shown in Figure 2-10. In many applications, a concise representation of 3D objects with curved arcs or straight lines is desirable because of its simplicity. This line-like representation of a 3D object is also known as the centreline, curve-skeleton or the MA and is a simplified 1D representation of its medial surface, consisting only of curves. However, the definition of skeleton cannot directly lead to the generation of a curve-skeleton. In Figure 2-11 only such skeletons, which contain both curved arcs and surfaces, can be extracted based on the maximal inscribed spheres. So alternative definitions of 3D MA (curve-

skeleton) need to be further clarified and the corresponding skeletonizations also need to be reviewed.

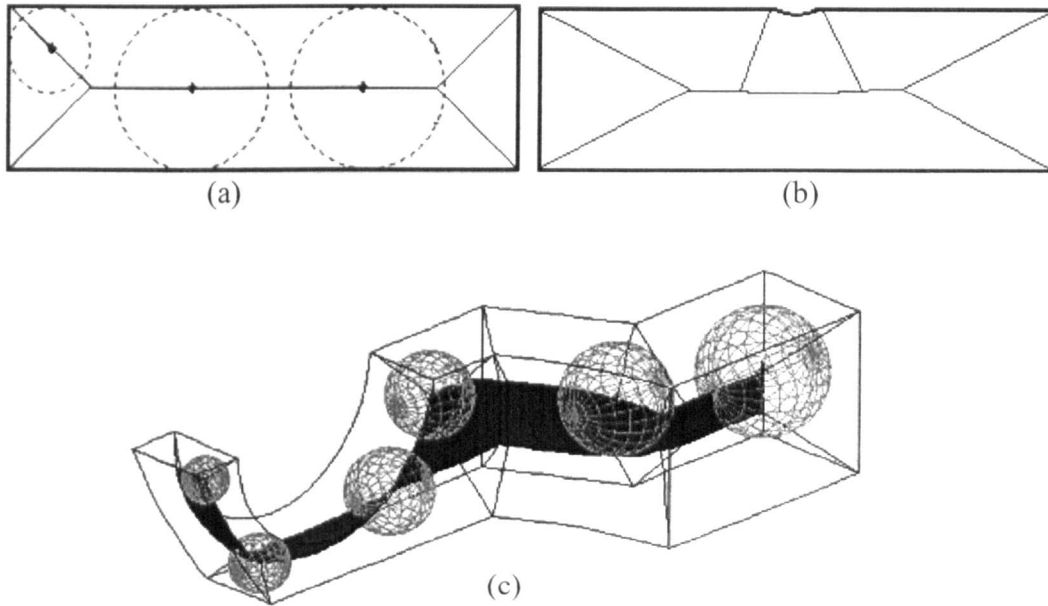


Figure 2-9: The medial axis in 2D (a, b) and the medial surface in 3D (c) and a few examples of inscribed disks in 2D and spheres (ball) in 3D. (b) The MA is sensitive to boundary noise because noisy spurs remain in the skeleton due to the small variations on the boundary of the object.



Figure 2-10: A wireframe torus with medial axis (the central curve).

The above definitions of skeleton were formulated in continuous space. In discrete space, the definitions are analogous to the continuous case. However, problems may occur because of discretisation. For example, a maximal sphere may touch the discrete boundary of an object at a single point rather than at least two points in the continuous space. As a result, in order to include all centres of maximal spheres, the discrete skeleton may be more than one image element (pixel or voxel) thick. Furthermore,

resolution can cause a loss of detail for certain objects. Some skeletonization algorithms work on geometric data (continuum), others deal with discrete objects only (distance field, thinning). In this section, I will focus on the discrete case.

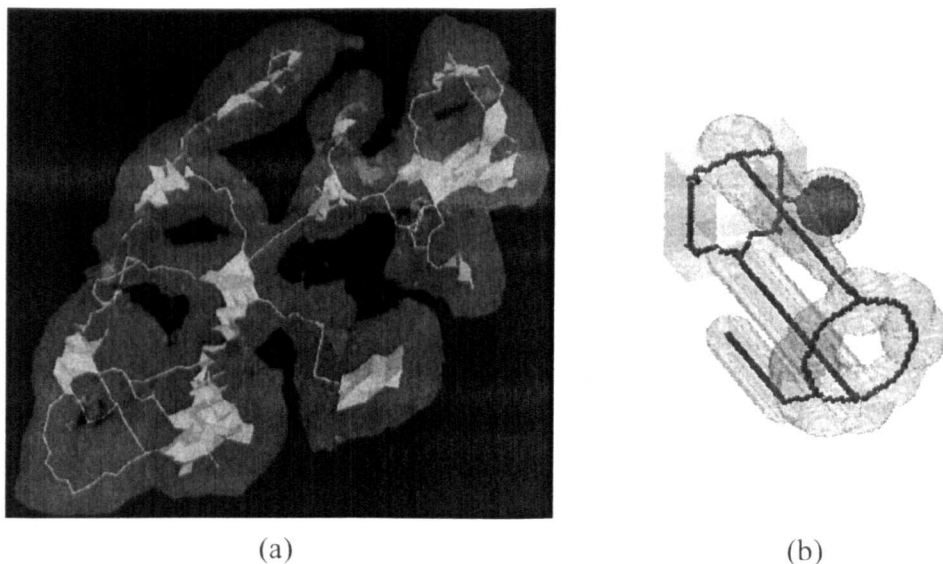


Figure 2-11: The skeleton of a 3D object with surfaces and curve arcs. (a) Without any cavities (from Pudney, 1998[132]) and (b) with a cavity. A cavity is a background component that is completely enclosed in an object.

2.3.2 Algorithms (skeletonization)

Since Calabi and Harnett (1968[30]) proposed the “grassfire” concept, many different MA extractions were developed targeting different materials and applications. Although some of the 2D algorithms are supposed to scale to 3D, I restrict my discussion only to algorithms explicitly designed for 3D. From the multiphase flow point of view, the line-like skeleton (the medial axis) of 3D objects plays a central role in pore analysis. The discussion below reviews general 3D curve-skeleton algorithms, i.e. the generation of a 1D curve-like representation for a 3D object. However, some medial surface algorithms will be included for the purpose of further reducing the medial surface into a medial axis (e.g. Borgfors et al., 1999[26]; Svensson et al., 2002[164]). Unless otherwise stated, in the following I consider 3D objects to be represented by voxels on a regular grid.

Most existing algorithms can be classified into three types: thinning methods, distance map based methods, and hybrid methods.

- **Thinning methods**

Thinning is described as a procedure for iteratively deleting object points while satisfying certain topological and geometric constraints, until no more points can be deleted (Kong and Rosenfeld, 1989[76]). The remaining subset of the object is then called the skeleton of the object. The thinning method can be imagined as peeling off the boundary of the object contained in an image layer by layer. The key aim is to remove the object points as efficiently (quickly) as possible without changing the topology of the original image. The basic topological quantities of a 3D object include the numbers of isolated components, tunnels and cavities. Therefore, during the thinning process no isolated components, no tunnels or no cavities are allowed to be created or deleted to fulfil the topological constraint.

Morgenthaler (1981[110]) introduced the notion of a simple point to localise the topological constraint in the $3 \times 3 \times 3$ neighbourhood. A simple point (Kong and Rosenfeld, 1989[76]; Bertrand and Aktouf, 1994[17]) is an object point which can be deleted without changing the topology of the object. The thinning process can then be described as starting from the object's boundary and continuing inward until no more simple points can be removed. In addition to the topological constraint, certain geometric conditions are used to prevent removal of some simple points (e.g. surface or curve endpoints) in order to maintain desired geometric properties of the object (for example, in order to ensure the desired width and location of the skeleton). These conditions are usually implemented as templates (or masks), of size $3 \times 3 \times 3$ or larger. Based on a counting approach, however, several local characterizations of simple points were proposed (e.g. Bertrand, 1994[14], 1995[15] and 1996[16]; Lohou and Bertrand, 2005[92]). The deletion of simple points is carried out either sequentially (Bertrand and Malandain, 1994[18]; Pudney, 1996[131] and 1998[132]; Saito and Toriwaki, 1994[144] and 1995[145] etc.) or in parallel (Lohou and Bertrand, 2004[91] and 2005[92]; Xie et al., 2003[189]; Palágyi and Kuba, 1997[120], 1998[121] and 199[122] 9; Manzanera et al., 1999[100]; Saha et al., 1997[141]; Ma and Sonka, 1996[96]; Gong and Bertrand, 1990[52] etc.) or with morphological operations (Jonker, 2000[69]). Of

the various parallel thinning algorithms, many of them are involved in the directional category. Directional thinning methods remove voxels only from one particular direction in each iteration (for example, North, South, Up, Down) using different numbers of directions and conditions to identify endpoints (Tsao and Fu, 1981[168]; Gong and Bertrand, 1990[52]; Bertrand and Aktouf, 1994[17]; Lee and Kashyap, 1994[81]; Saha et al., 1997[141]; Palágyi and Kuba, 1999[122]; Lohou and Bertrand, 2004[91]).

The main feature of thinning algorithms is topology-preservation and that the resultant skeleton is thin (no redundant points in the sense of topology-preservation, i.e. the topology of the original images will change if any point on the skeleton is further deleted), but the skeleton is not necessarily centred because of the explicit or implicit directional strategy.

- **Distance map based methods**

For a 3D binary image, its distance map is defined as another grey level image in which a distance value is assigned to each point in the image space. The distance of a point is defined as the smallest distance from that point to the boundary of the object, where different distance metrics (or functions) may be involved. Various distance functions can be chosen such as the Euclidean distance or its approximations (e.g. city-block, chessboard or chamfer distance metric). A distance map can also be approximated using fast marching methods (Sethian, 1999[150]; Telea and Vilanova, 2003[165]).

In distance map based methods, the idea is to find local maxima (ridge points, saddles) from the distance map of an object as potential candidates, and to prune these points to produce a 1D skeleton, and finally to connect these candidates using a path connection or minimum spanning tree approach (Zhou et al., 1998[194]; Wan et al., 2001[186]; Sundar et al., 2003[162]). Methods used to find candidate voxels include: distance ordered thinning (Pudney, 1998[132]; Gagvani and Silver, 2001[49]; Couprie and Zrou, 2005[35]), gradient searching (Bitter et al., 2001[19]), divergence computation (Bouix and Siddiqi, 2000[27]), geodesic front propagation (Perchet et al., 2004[126]), thresholding the bisector angle (Malandain and Vidal, 1998[99]) or

shrinking the surface along the gradient of the distance map (Schirmacher et al., 1998[146]).

After obtaining candidate voxels from the original object, these voxels are clustered and connected. For connectivity, most approaches use minimum spanning trees, shortest paths (He et al., 2001[56]) or other graph algorithms. In Zhou et al.'s paper (1998[194]), an "LM path" defines the connectivity of local maxima clusters. An alternative is provided by the fixed topology skeleton which is a set of a fixed number of connected active contours driven by the underlying distance map (Golland and Grimson, 2000[51]).

The principle of the MA transformation (MAT) is similar to the approach based on the distance map (Calabi and Harnett, 1968[30]; Malandain and Vidal, 1998[99]). The idea is to calculate the distance map of the object in an image, to find local maxima, and to reconnect the maxima. Delerue et al. (1999a[39]) used a ball-growing algorithm to extract the skeleton of the PS in a porous medium. The resulting skeleton based on MAT is centred in the local PS by construction, depending on the local maxima threshold. Unfortunately, this algorithm is not necessarily topology-preserving, as it depends on the path reconstruction and may produce redundant points on the skeleton.

In principle, the distance map based method can accurately extract the medial surface. However, it cannot extract a curve-skeleton from arbitrary objects without employing additional techniques to prune the medial surface. For example, for the shape in Figure 2-11(a), the voxels along the medial surface (in white) all have the same distance value. Therefore, some sort of pruning must be used to simplify these medial surfaces into central lines. The main advantage of the distance map based method is that computation of the distance map is very fast and it is widely used. In particular, for tubular objects (i.e. flow channels), the distance map approach works very well.

- **Hybrid methods**

To take advantage of both of the above approaches, hybrid methods have been introduced. One such method, called Distance Ordered Homotopic Thinning (DOHT Morgenthaler, 1981[110]), iteratively deletes object points in increasing distance map order without changing the topology of the original object. However, it imposes an

additive step, i.e. a distance transformation on its thinning process, and the resulting skeleton is still not truly in the central region. This is because in the region of points of the same distance value, the location of skeleton points depends on the scanning order.

During the thinning process, in which some object points are deleted (called deletable points), the deleting order determines the position of the resultant skeleton. For most of the MA applications, the “medialness” (i.e. central location) is an important property; however most of the existing thinning algorithms do not guarantee that the MA is located in the centre of the object. To minimise ordering effects and to ensure that the MA is as close to the geometric centre as possible, Saito and Toriwaki (1995[145]) proposed a Euclidean distance-based thinning method to produce a medial skeleton. Inspired by this approach, Pudney (1996[131] and 1998[132]) presented a similar algorithm. To meet the homotopic requirement (i.e. topological preservation), Pudney (1996[131]) used Kong and Rosenfeld’s (1989[76]) local definition of topology preservation. There are two conditions which should be tested for: (1) if there is only one connected component in the $3 \times 3 \times 3$ neighbourhood of a point; (2) if the Euler number is unchanged in the $3 \times 3 \times 3$ neighbourhoods before and after removing object points. An object point is called a simple point if its removal does not change the topology of the original object. These conditions have established a rough characterization for a simple point. Due to the difficulty of computing the 3D Euler characteristic, Pudney (1998[132]) used a much more efficient characterization of a simple point introduced by Bertrand and Malandain (1994[18]). As for the distance applied in Pudney’s algorithms, the chamfer metric is used as the distance function and the distance is defined as the length of the shortest chamfer distance from the object point to the background. The chamfer distance is a good approximation to the Euclidean distance. In fact, a chamfer distance with CDC (3, 4, 5) can minimise the upper bound on the difference between the chamfer and Euclidean distances (Borgefors, 1984[24]). In most contrast to the similar algorithms, the calculation of the chamfer distance is carried out on the fly rather than beforehand. Therefore, Pudney’s thinning process is controlled by the order of ascending distance, which can be efficiently implemented using ordered queues (Vincent, 1991[180]). To ensure that the resultant MA contains fewer spurious branches, Sheppard et al. (2004[151] and 2005[153]) modified Pudney’s (1998[132]) method by applying a Gaussian smoothing kernel to the Euclidean distance map, and using this as the ordering function for the thinning algorithm. Moreover, to

eliminate connections being formed across voxel corners or edges in the final 26-connectivity medial axis, they perform the first few steps of the homotopic thinning under the assumption that the object being thinned is 6-connected before switching to 26-connectivity for the remainder of the process.

- **Skeletonization algorithms used for pore structure analysis**

There are a number of published algorithms for pore structure analysis based on the MA of the PS. For thinning of the PS, two issues are widely discussed: topology-preservation and geometric constraints.

Lee and Kashyap (1994[81]) proposed a 6-directional parallel thinning, which has been used and improved by Lindquist et al. (2000[89]) later. They stated that their extracted MA should be topology-preserving, thin and at the central location. The topological constraints are satisfied by deriving an Euler table, counting objects using a labelling algorithm based on the octree representation of local configurations, and sequentially re-checking the connectivity before simultaneously removing simple points.

For a 3D binary image $\mathcal{P} = \{\mathcal{V}, \alpha, \beta, \mathcal{B}\}$ defined on a rectangular region $\mathcal{V} \subset Z^3$, where \mathcal{B} is the object set (e.g. the PS of a porous medium) and $(\alpha, \beta) = (6, 26)$ or $(26, 6)$, the EPC $\chi(\mathcal{B})$ is defined in (2.13). For a point (voxel) p of \mathcal{B} , the EPC of its $3 \times 3 \times 3$ neighbourhood $\mathcal{N}(p)$ of p is denoted by $\chi(\mathcal{B} \cap \mathcal{N}(p))$.

According to the definition and Proposition 1 introduced by Morgenthaler (1981[110]), Lee and Kashyap (1994[81]) described the topological thinning process as repetitively deleting one type of border points in \mathcal{B} one after another in parallel satisfying the following conditions until no more points can be removed:

$$(C_1) \chi(\mathcal{B} \cap \mathcal{N}(p)) = \chi(\mathcal{B} \cap \mathcal{N}(p) \setminus \{p\});$$

$$(C_2) h_0(\mathcal{B} \cap \mathcal{N}(p)) = 1;$$

(C₃) $h_0(\{S \cap \mathcal{N}(p)\} \cup \{(\mathcal{B} \setminus S) \cap \mathcal{N}(p)\}) = 1$, where S is the set of current simple points that satisfies (C₁) and (C₂).

For checking condition (C₁), the idea of Lobregt et al. (1980[90]) was used to calculate the EPC $\chi(\mathcal{B} \cap \mathcal{N}(p))$ based on a predefined Euler-table. To determine the connectivity (i.e. condition (C₂) and (C₃)), an octant-type data structure (i.e. octree) for

each point p is proposed to represent the local configuration in the $3 \times 3 \times 3$ neighbourhood $\mathcal{N}(p)$ of p . Taking advantage of the recursive nature of the octree, they implemented an efficient labelling algorithm to count the number of connected object in $\mathcal{N}(p)$.

As a parallel thinning algorithm, potential drawbacks of simultaneous removal of multiple simple points must be considered. To achieve parallel thinning without changing connectivity, 6 subiterations are introduced in each thinning iteration and a sequential re-checking procedure is used in Lee et al.'s algorithm. A border object point p is identified as of type N(North), S(south), W(west), E(east), U(up) or B(bottom) if the corresponding 6-neighbour (i.e. having common face with p in the direction) is a background point (e.g. belonging to solid phase), respectively. This strategy has been used by many researchers (e.g. Palágyi and Kuba, 1998[121]; Lohou and Bertrand, 2005[92]), but the major problem with this directional parallel thinning is that they cannot avoid destroying the original topological structure during the thinning process without additional checking. To solve this problem, Lee et al. sequentially re-examine each simple point p , which has already been labelled in the current subiteration, to determine if all simple points and the remaining points in the $3 \times 3 \times 3$ neighbourhood of p are still connected.

The topological preservation has been discussed briefly above. The remaining issue is how to decide the geometric constraints to ensure the thinness and the central location of the skeleton. Focusing on the skeleton consisting of only curved arcs (e.g. central lines), the concept of endpoint is needed which is defined as a point that has only one neighbour at a stage during homotopic thinning process. Taking account of this, all endpoints are to be retained even though they are also simple points. Using this algorithm, obviously the resultant skeleton of an object must be a MA which contains only curved arcs if the object has no cavities and the thinning process continues until no more voxels can be removed.

Lindquist et al. (1996[87]; 1999[88] and 2000[89]) used Lee et al.'s algorithm for geometric analysis of the PS in rock images. They found that their original algorithm is very sensitive to boundary noise (see Figure 2-12(a)). Boundary noise occurs for two reasons: inherent irregularities of the boundary between the pore and the solid phase, and disconnected components of pore voxels or dead end pores. The former should be avoided and the latter should be retained. However, distinguishing between spurious

paths which derive from boundary noise and genuine dead end pore channels is very difficult. To tackle this problem, Lindquist et al. (2000[89]) proposed criteria to trim all dead end paths from the medial axis, so that the remaining structure is the percolating backbone of the PS (see Figure 2-12(b)).

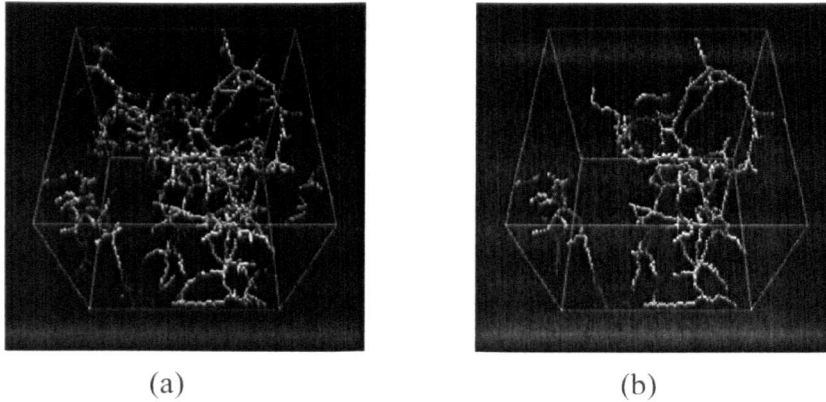


Figure 2-12: The medial axis extracted from a sandstone image (a) with many spurious paths and (b) trimmed backbone of the PS.

(http://www.ams.sunysb.edu/%7Elindquis/3dma/3dma_rock/3dma_rock.html).

Besides the sensitivity to boundary noise, Lee et al.'s algorithm leads to the systematic north-south, east-west, up-down biasing because the location of the MA depends on the thinning order. Lindquist and co-workers (1999[88] and 2000[89]) then introduced a rule to reorganize the thinning order according to the number of surface faces each border voxel has, in order to overcome this drawback of the original algorithm.

To achieve the central location of the medial axis, Pudney (1996[131]) implemented the thinning operation in the order of ascending distance. The distance of an object point is defined as the length of the shortest path from this point to the background. Instead of using the Euclidean distance metric, a chamfer metric with coefficients (n_1, n_2, n_3) is used as the approximation of the Euclidean distance between a pair of adjacent points such that $n_i/n_1 \approx \sqrt{i}$, $i = 2, 3$. To preserve the topology, Pudney apply Kong and Rosenfeld's (1989) definition of a simple point: let p be an object point in a 3D binary image $\mathcal{P} = (Z^3, \alpha, \beta, \mathcal{B})$, where $(\alpha, \beta) = (6, 26)$ or $(26, 6)$. p is a simple point if and only if the following conditions hold:

$$(C_1) p \text{ is } \alpha\text{-adjacent to just one connected component of } \mathcal{N}(p);$$

(C₂) $\chi(Z^3, \alpha, \beta, \mathcal{B} \cap \mathcal{N}(p)) = \chi(Z^3, \alpha, \beta, \{\mathcal{B} \setminus \{p\}\} \cap \mathcal{N}(p))$, where $\chi(\mathcal{P})$ is the EPC of a binary image \mathcal{P} .

An endpoint is defined an object point that has less than two object neighbours. The endpoint should be preserved and thus a point p is deletable if it is simple and has more than one object neighbour. The algorithm is implemented using ordered queues so that pre-calculation of the distance transform is not required.

Pudney (1998[132]) improved the above algorithm using a simplified characterisation of simple points (Bertrand and Malandain, 1994[14]) and using the chamfer metric with CDC (3, 4, 5). This localised characterisation does not involve calculation of the EPC but the counting of the number of components. Let p be an object point in a 3D binary image $(Z^3, \alpha, \beta, \mathcal{B})$, where $(\alpha, \beta) = (6, 26)$ or $(26, 6)$. Then p is a simple point if and only if the following conditions hold:

(C₁) p is α -adjacent to just one connected component of $\mathcal{N}_\alpha(p) \cap \mathcal{B}$;

(C₂) p is β -adjacent to just one connected component of $\mathcal{N}_\beta(p) \setminus \mathcal{B}$.

To implement the removal of multiple simple points in parallel, a technique called sequential rechecking (Lee and Kashyap, 1994[81]) is used to avoid changing the topology during the parallel thinning process.

Recently, Sheppard et al. (2005[153]) used Pudney's algorithm for the extraction of the MA of the PS with several minor changes. They found that by applying a Gaussian smoothing kernel to the Euclidean distance map, and using this as the ordering function for the thinning algorithm, the resultant MA contains fewer spurious features. They also suggested that it would be better to perform the first few steps of the thinning assuming that the object being thinned is 6-connected, before switching to 26-connectivity for the remainder of the process. Also the algorithm has been parallelised using a simulator. The problem with the above algorithms for parallel implementation is that additional measurements (i.e. sequential checking or simulator) substantially degrade the efficiency of the algorithms. Thus, Ma and Sonka (1996) designed a fully parallel thinning based on template matching to deal with this problem.

For a 3D image $\mathcal{P} = (\mathcal{V}, 26, 6, \mathcal{B})$, they used the following definition (Malandain and Bertrand, 1992[98]) to determine the simplicity of an object point.

(C₁) p is 26-adjacent to only one object in $\mathcal{N}(p) \setminus \{p\}$;

(C₂) p is 6-adjacent to only one background component in $\mathcal{N}_8(p)$.

Only when one simple point at a time is removed can we preserve connectivity. However, it is not true if more than one simple point has been deleted simultaneously in each iteration. As suggested by Kong (1993[74]), a set \mathcal{D} of points can be deleted in parallel if \mathcal{D} is a simple sequence, i.e. \mathcal{D} can be ordered as a sequence such that every point is simple after all its predecessors in the sequence are deleted. Such a set is called a simple set. Therefore a parallel thinning algorithm is said to preserve topology if it is only allowed to delete simple sets from the object region. Obviously this condition has theoretical value but is not easy to implement. Thus, Ma (1994[95]) proposed more general sufficient conditions and then used these to design deleting templates (i.e. configurations in the direct neighbourhood of a point). First, four basic templates (cores) were defined (see Figure 2-13); after reflecting and 90° rotating the template cores with some specific conditions, four classes (i.e. Class A, B, C and D) of deleting templates (for example, four Class A templates shown in Figure 2-14) were generated and then used to check whether an object can be identified as a candidate to be deleted.

To preserve the geometry of the original object, Ma and Sonka gave a definition of nontail points in order to retain end points. A tail point is either a line-end point or near-line-end point; any other points on a line are called nontail points. Applying this definition and the deleting templates, a MA are generated by the following algorithm:

Repeat

In parallel, delete every nontail object point which satisfies at least one deleting template;

Until no point can be deleted.

Furthermore, they provided an option for eliminating end points which resulted in removal of all “dangling ends” in the final medial axis. This algorithm is used by Liang et al. (2000a[84]) for partitioning the PS. However, this algorithm seems to neglect the central location of the medial axis, which would lead to inaccurate identification of pore necks.

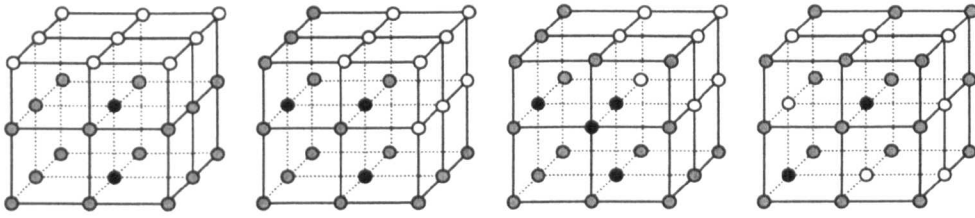


Figure 2-13: Four basic template cores of Ma and Sonke's parallel thinning algorithm which are used to generate deleting templates by reflecting and 90^0 rotating these template cores. Where a grey point is a "don't care" point which can be either an object point (black) or a background point (white).

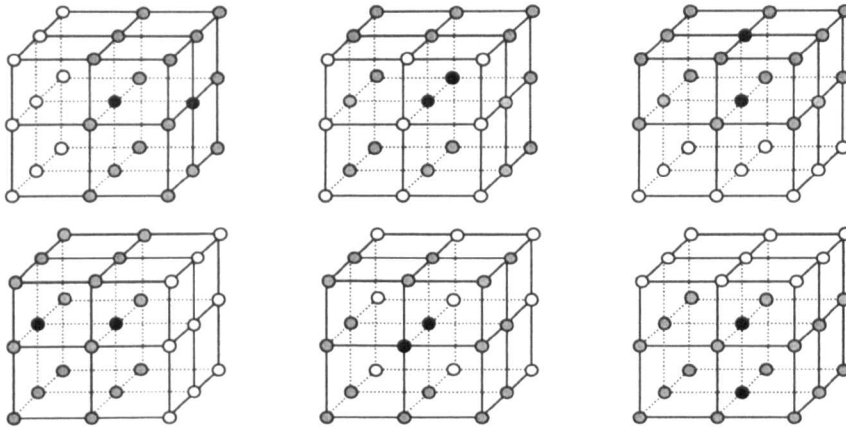


Figure 2-14: Six Class A templates for deleting west, east, south, north, down, and up border points, respectively. Where black points are object points, white points are background points, and a grey point can be either object or a background point.

In spite of the above thinning algorithms, some authors tried to find more efficient algorithms using morphological operations or other general image processing techniques. Baldwin et al. (1996[13]) developed a morphological thinning algorithm to obtain the "medial axis" of the PS. In the same year Lindquist and Lee (1996[87]) developed a "burn" algorithm motivated by the "grassfire" idea (Calabi and Harnett, 1968[30]). Delerue et al. (1999a[39]) developed another approach using geometric modelling where a ball growing algorithm using the Voronoi diagram was used to extract the skeleton of the PS (Delerue et al., 1999b[40]; Delerue and Perrier, 2002[38]). The major problem of these algorithms was that topology-preservation could not be satisfied or at least could not be proved, which is crucial for single-/multi-phase flow using network models.

2.3.3 Medial Axis Properties

The desirable properties of the MA depend on the applications for which it is required. For example, object recognition requires medial axes with primitive shape features to make similarity comparisons. On the other hand, statistical reconstruction of porous media (Thovert et al., 1993[167]) needs medial axes that contain detailed geometric information and are of the same connectivity to reduce the approximation error in the reconstruction process and to extract network structures for network models. Below, I briefly describe some important properties which may link to the pore analysis.

The connectivity of the MA faithfully represents the connectivity of the original object (i.e. the PS), has a strict geometric relationship to the object's surface and preserves important geometric properties.

Homotopic property (topology preservation): The homotopy of the MA requires us to faithfully represent the connectivity of the original object, which is closely related to the definition of connectivity. In three-dimensional discrete space Z^3 , two voxels are 6-adjacent if they share a face, 18-adjacent if they share a face or an edge and 26-adjacent if they share a face, an edge or a vertex. An α -path is a sequence of voxels $x_1, x_2 \dots x_m$ with x_i α -adjacent to x_{i+1} , where α is 6, 18 or 26. A α -component S is then a set of voxels such that each pair of voxels in S is connected by a α -path included in S . For a 3D binary image \mathcal{P} , in order to avoid topological paradoxes (Kong and Rosenfeld, 1989[76]), a pair of connectivities (α, β) must be chosen for the object and for the background, where α for the object connectivity and β for background connectivity. For the object \mathcal{B} in $(\mathcal{V}, \alpha, \beta, \mathcal{B})$, the MA of \mathcal{B} , denoted by $MA(\mathcal{B})$, is defined as a subset of the \mathcal{B} . According to Kong and Rosenfeld's definition, $MA(\mathcal{B})$ and \mathcal{B} have the same topology if they have the same number of α -components, tunnels and cavities. A cavity is a background β -components surrounded by an object component. Algorithms to count the number of connected components, tunnels and cavities in an object are given in (Saha and Chaudhuri, 1996[140]; Svensson, 2002[164]). Notice that a MA (only contains curve arcs) cannot be obtained from an object with cavities under the condition of topology preservation. To accommodate objects with cavities, we can either remove the cavities before generating the MA or relax the definition of topology preservation. This property is explicitly checked only by the thinning methods while

deleting points. None of the other methods provides any guarantees regarding homotopy.

Thin (Single voxel width): The medial axes should be one-dimensional, that is at most one voxel thick in all directions, except at junction points where the skeleton might become thicker to ensure connectivity between the different branches. So in this sense, the MA is a minimal deformation retraction of the object. Thus the points in the MA can be distinguished as three types: regular points, endpoints and junction points, which correspond to having exactly two neighbours, one neighbour, and more than two neighbours, respectively. The check of the thinness property can be easily done if the junction points are known in advance. Otherwise much more complicated methods may be involved. Obviously thinning algorithms can directly produce a single voxel width skeleton or further thin the medial surface to a 1D representation. The distance map based methods do not produce such a representation directly, which thus requires considerable post-processing.

Centred (central location): One important characteristic of a MA is its central location along the object (i.e. central placement with respect to the pore-grain surface, Lindquist et al., 2000[89]), which preserves the important geometrical features of the object. This is especially true for multi-phase flow where the central-line of a flow path is desired. Clearly the curve-skeleton should lie on the medial surface of the object, but this criterion alone does not guarantee centeredness. One possible way to quantify the centeredness of a curve-skeleton is to seed a number of uniformly distributed radial rays at each skeleton point and measure the distance to the boundary along each of these rays. The central location can be achieved in the first steps of methods using a distance map. However, once clustering and spanning trees are used, centeredness may be lost. Thinning methods do not guarantee centeredness. For example, for directional thinning the systematic north-south, east-west, up-down biasing cannot be avoided because the position of medial axes would depend on the order of the directions.

Robust: As shown in Figure 2-9(b), the MA is very sensitive to boundary noise, i.e. a small change on the boundary of an object can result in a drastic change in the medial axis. This means that many extraneous branches will occur in the resulting medial axis. This spurious branch formation makes it very difficult to quantitatively compare different instances of the same structure. A desirable property of the MA is to

exhibit weak sensitivity to noise and roughness on the boundary of the object. That is, the medial axes of a noise-free object and the same object with noise should be very similar. This can be done either smoothing the original image in advance or by pruning the resultant MA to distinguish between boundary noise and boundary irregularities.

Efficient to compute: Clearly, an algorithm should be efficient because many applications need real-time computations for high-resolution images. The Euclidean distance map of a 3D object can be computed in linear time using the algorithms of Saito and Toriwaki, 1994[144]; Meijster et al., 2000[106] and Maurer et al., 2003[105]). The subsequent steps of filtering and reconnecting the skeleton, however, may be more complex but they usually operate on a greatly reduced set of voxels. Thinning is also a linear process in the number of object voxels, which is mainly dependent on the checking of simplicity of object voxels.

2.4 Quantitative Characterization of the Pore Space

There are two steps in characterizing the PS. The first is to measure flow-relevant geometrical and topological properties such as pore/throat radius (volume), cross sectional/specific surface area, Euler-Poincaré characteristic and coordination number. Based on these basic quantities, the second step is to evaluate statistical quantities in the forms of distributions and correlations such as pore size distribution, coordination number distribution, spatial correlations and pore-body to pore-throat aspect ratios etc. Most of the existing characterizations involve both of these steps with some exceptions for computing simple statistical properties. With a good characterisation of the PS, either an equivalent network can be created or a realistic network structure can be mapped for a specific porous medium. Even more directly, numerical analysis can be done based on characterized data. The resulting network model may then be used to investigate or predict macroscopic flow and transport properties. From this point of view, the characterisation of the PS is of fundamental importance to many network models.

With a high-quality 3D binary image of a porous medium at hand, the first question is to decide which parameters are of interest. This depends on our understanding of the relationship between pore microstructure and macroscopic bulk properties as well as on the requirements of a specific network model. The second

question is how to quantify and to characterise the PS. Almost all pore structural parameters are closely related to the definitions of pore-bodies and pore-throats, which appear very complicated. Some definitions of pores may be intuitively clear, and other seem to be rigorous in the sense of mathematical representation, but no universal definition is available so far. For this reason, a large number of distinctive approaches have been presented and each has found some sort of successful application in the analysis of pore geometry. The practical value of partitioning PS into constituent smaller elements (i.e. pore-bodies and pore-throats) was first noted by Fatt (1956a[45]), who used a network model to describe drainage/imbibition processes in porous media. This view is also emphasised by Ioannidis and Chatzis (2000[61]): *'The most rigorous approach to quantitative characterization of the interior geometry of a porous medium is to partition the pore space into discrete and well-defined collection of individual pores.'* Partitioning PS can be done either based on the MA of the PS or by directly partitioning the PS from the original 3D binary images of the porous medium. The former is called the medial-axis-based approach and the latter is called the non-medial-axis-based approach in this thesis. In the following, some important methods for characterizing the PS, which are not related to identifying individual pore-bodies or pore-throats, will be selectively reviewed. Much effort will be given to the investigation of the methodologies that are involved in the partition of the PS. As a summary, I also review many important pore geometrical and topological properties that have already been quantified by other authors.

2.4.1 Intuitive Definitions and Geometry Measurement

Intuitively, in a fluid-bearing rock, pore-bodies are the larger openings where most of the fluid is stored. To a large extent, pore-bodies determine the rock porosity. Pore throats are the narrow gateways that connect the pore bodies and determine the rock permeability. Silin et al. (2004[154] and 2006[157]) expressed this view for capturing the natural features of pore microstructure. The algorithm proposed by Silin et al. consists of three steps: (i) calculating the radius of the maximal ball centred at each object voxel; (ii) removing the included balls to obtain the skeleton; (iii) distinguishing voxels into either master or slave voxels. As a direct result, a stick-and-ball representation of the PS can be developed to facilitate characterization of the PS. This

procedure can successfully measure many important microscopic morphological properties such as pore/throat size and coordination number.

Delerue et al (1999a[39] and 2002[38]) gave a definition of the pore where an individual pore is thought of as being a portion of the PS surrounded by the solid matrix with a homogeneous local aperture (in this definition no throats are involved). The local aperture $A(p)$ associated with a point p in the PS O is defined as the diameter d of the maximal ball $B(c, d)$ included in the PS and including the point p : $A(p) = \max\{d : p \in B(c, d) \text{ and } B(c, d) \subset O\}$, see Figure 2-15. The pore size is a mean of local apertures calculated at each point in the PS. Therefore the pore size distribution is straightforwardly obtained by computing the histogram of the local aperture over the whole image.

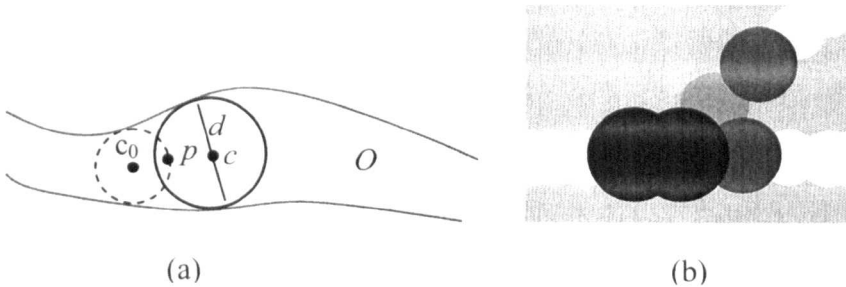


Figure 2-15: The concept of local aperture: (a) The local aperture $A(p)$ of p is defined as the diameter d (i.e. the length of the segment) of the maximal disk $B(c, d)$ (solid circle) centred at c including in the PS O . Note that the dotted circle centred at c_0 contains p but not the maximal, which means that the diameter of this disk cannot be defined as $A(p)$; (b) an illustration of local aperture map with different grey level representing different local aperture value.

From Vogel's point of view, the morphology of the PS can be interpreted in terms of processes of pore structure formation and hence, these processes may be directly related to flow and transport in the rock or soil. To simulate this process, morphological operations were used to measure pore size rather than identifying individual pores. In Figure 2-16, for a 3D binary image (Figure 2-16(a)) of a porous medium on a rectangular grid, Vogel and Roth (2001[185]) introduced a robust method to measure the pore-size distribution applying a set of morphological openings. To determine the cumulative pore-size distribution of a porous medium in the form of the proportion of pores larger than a given diameter, a series of discrete spheres of radius r is

approximated which is used as different structuring elements. The opening, i.e. erosion followed by dilation, removes all pores smaller than r , the volume of pores larger than the diameter $(2r+1)$ can be straightforwardly calculated based on this kind of PS partitioning. Using our dataset and my implementation of Vogel's algorithm, an example of pore structure and the pore-size distribution are demonstrated in Figure 2-16 . Note that in their approaches no attempt is made to partition the PS into individual pores. Instead, they directly determine the cumulative pore size distribution using morphological opening with structuring elements of increasing radii on the original binary image.

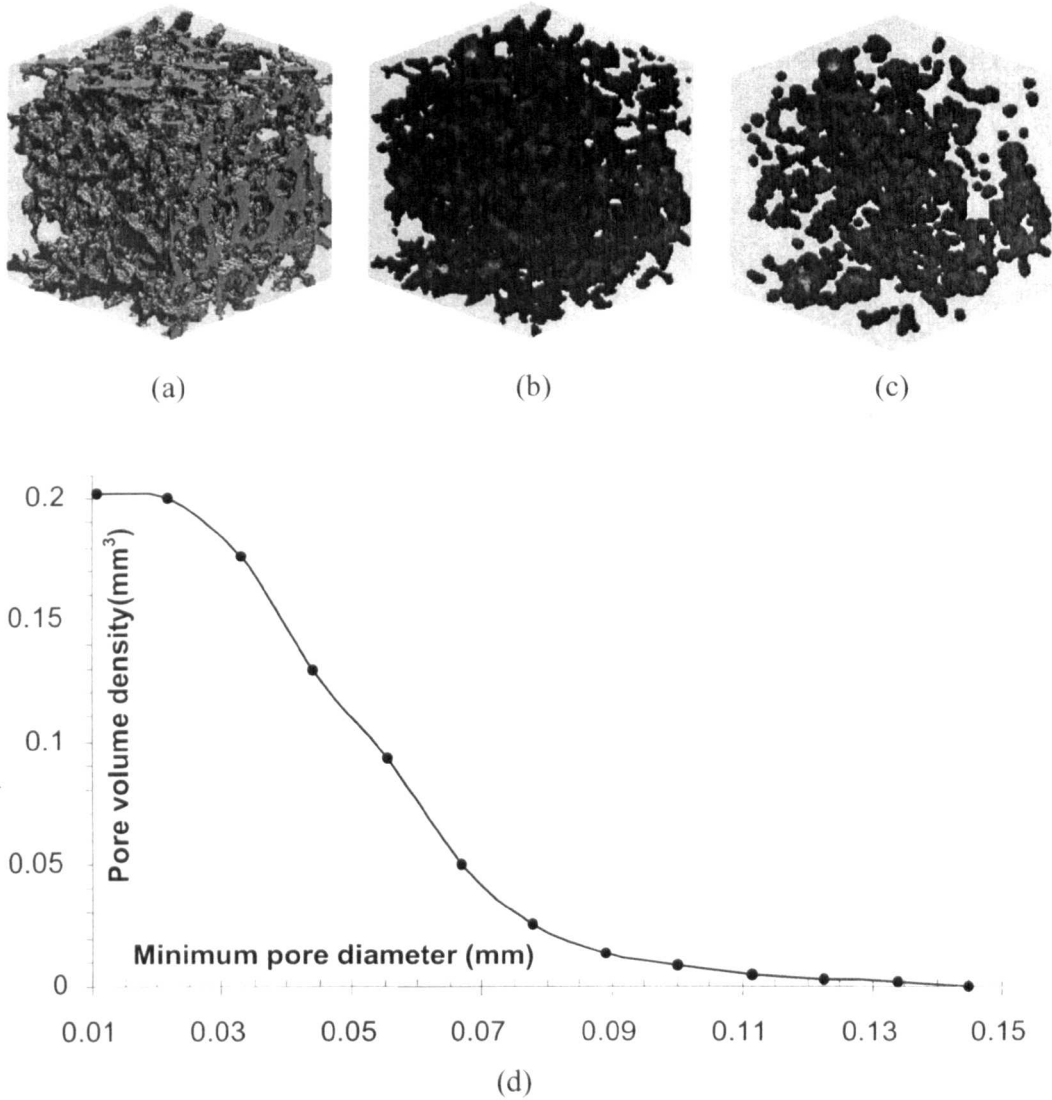


Figure 2-16: Determination of pore-size distribution based on morphological operations. (a) The original 3D binary image of a sandstone sample of 1.4049 mm³, the porosity is 20.2%; the size of a voxel is 5.6 μm; (b) The PS of pore diameter ≥ 39.2 μm; (c) The pore structure of pore diameters ≥ 61.6 μm; (d) Cumulative morphological pore-size distribution of the sample shown in (a).

Vogel (2000[183]) also noticed that combining the porosity and the pore-size distribution, the connectivity of the PS governs the transport of water, solutes and gases. The Euler-Poincaré characteristic (EPC) can be interpreted as a measure of connectivity, increasing positive value indicates decreasing connectivity of the pore structure, and decreasing negative values indicate increasing connectivity. Vogel and Kretzschmar (1996[184]) proposed an unbiased estimation of the EPC based on the dissector (i.e. a pair of parallel sections). Furthermore, the concept of connectivity function was introduced to overcome the shortcomings of the EPC (Vogel, 1997b[182]). The specific Euler number is defined as the EPC divided by the volume of the rock image, and the connectivity function $f(d)$ is then calculated by the specific Euler number of the pores of diameter larger than d (see Figure 2-17). In contrast to point-to-point correlations, which are most frequently used to introduce topological aspects into models of heterogeneous structure, the connectivity function provides information on the connectivity of the entire region of the model. Combining topological and geometrical information together, Vogel (2000[183]) proposed a method to generate a network model adaptable to the measured connectivity function, which is dependent on pore radius. In Figure 2-17, an example of connectivity function is given based on our data.

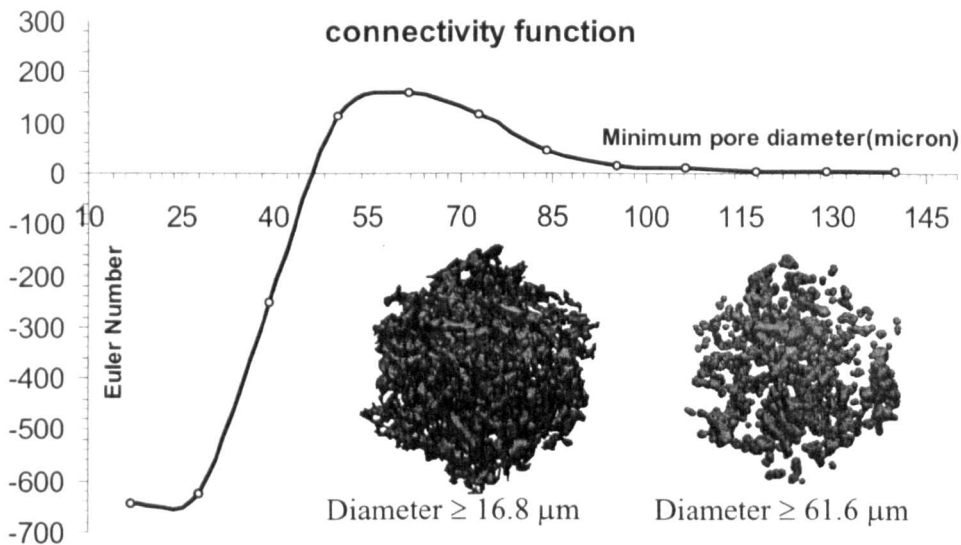


Figure 2-17: A sandstone sample of volume 1.4049 mm^3 , the connectivity function is defined as the Euler number of the pore system with pores larger than the given pore diameter. It seems that the connectivity of the PS mainly depends on these pores of diameter between 28 and $50 \mu\text{m}$.

In this category, no rigorous pore definitions are given because there is no clear boundary where a pore body ends and a pore throat begins. Apparently individual pores cannot be found using these kinds of methods, which means that more complex measures excluding pore size distribution, such as pore neck area and coordination number, cannot be obtained without further analysis. Another drawback of the above approach is that there is not a defined relationship between the topology of the PS network and that of the original PS because there is no guarantee that pore bodies will be simply connected.

2.4.2 Rigorous Definitions and Non-Medial-Axis-based Approaches

According to Dullien (1992[44]), the PS can be partitioned into two kinds of constituent elements – pore bodies and pore throats. The pore throats (or pore necks) are defined as volumeless constrictions between two pore bodies. When two non-miscible fluids are at equilibrium in the PS, the capillary forces at their interface can be modelled using the Laplace Law, which relates the capillary pressure to the curvature radius of the meniscus exhibited at the local boundary between the two fluids. The constrictions are then defined as the interfaces of minimal curvature radius, which is inversely proportional to the pressure required for an interface between two fluids to pass through the constriction.

Measuring the curvature radius of a meniscus is difficult because of the irregularity of the meniscus. So a normal cross section (CS) can be used as an approximate entity for the meniscus, and the hydraulic radius is taken to be an equivalent measure of curvature radius. The hydraulic radius, R_H , is defined as $R_H = A/P$, where A is the area of a normal CS and P is its perimeter. Therefore, a pore body can be defined as the region surrounded by solid phase and planes where the hydraulic radius of the PS exhibits local minima (Dullien, 1992[44]).

The above definition has been applied to a series of sections of rock images on the determination of pore characteristics by Kwiecien et al. (1990[79]), and Zhao et al. (1994[193]). Zhao et al. have used this definition and searched for pore necks directly by inspecting multiple slices, at up to 13 orientations (see Figure 2-18) within an image, for minima in the projection of the PS onto the scanning plane. As Zhao et al. discussed, many pore necks will be missed when using this neck finding approach,

while other regions can be mislabelled as necks. The latter can be improved using the nine-orientation scanning scheme introduced by Zhao et al. (1994[193]). However, this approach must always be a compromise relative to the complete unambiguous partitioning of the volume. Meanwhile, Lymberopoulos and Payatakes (1992[94]) presented an algorithm for identifying pore "chambers" and "throats". The throat has a volume and would be better represented as small capillaries rather than by defining pore necks as volumeless constrictions.

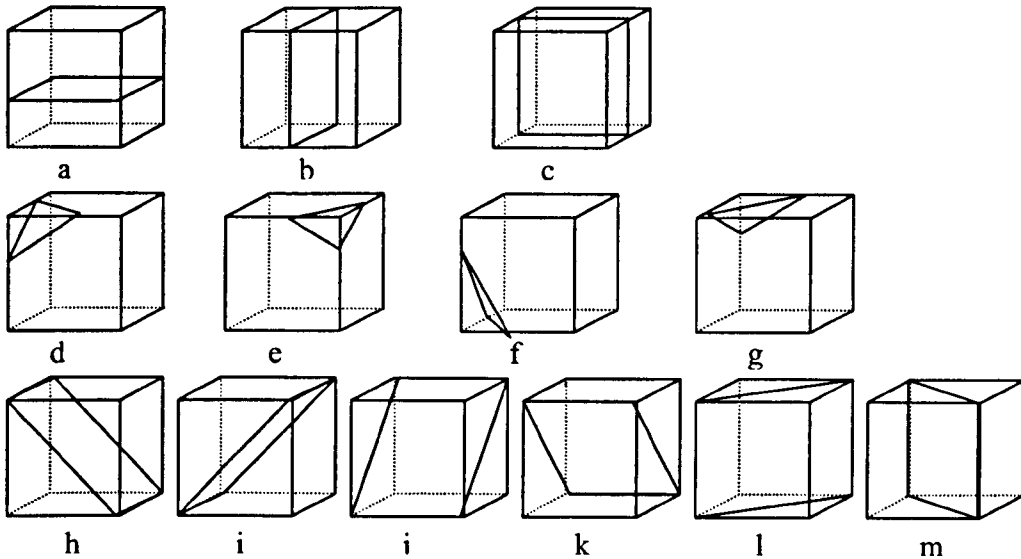


Figure 2-18: The thirteen scanning orientations which yield planar serial sections. (a)-(c) The three orthogonal orientations including the directions (a) of physical serial sectioning; (d)-(g) The four corner-to-corner orientations; (h)-(m) The six diagonal orientations.

Motivated by the above observations, Baldwin and co-workers (1996[13]) developed a morphological thinning algorithm to obtain a fully thinned image and to partition the PS into corresponding pores and throats. For a 3D binary image, the thinning proceeds in an iterative fashion; for each pass through the border voxels are identified and is eroded. This process continues until there are no more voxels remaining. During the thinning process, each voxel is labelled in order to relate it to the iteration at which this voxel is eroded. Thus a new thinned image is created after the morphological erosion is finished, which provides a natural starting point for identifying regions which are to become pores. Pores are identified as local maxima in intensity in the thinned image in which two voxels have a common corner are considered as being

connected (i.e. 26-connected). The algorithm proceeds by identifying local maxima at each level found in the thinned image. These local maxima are then grown to form pores by finding all connected voxels at levels that are the same or lower than the thinning level at which the local maximum was identified. This process is performed iteratively until all voxels, which were originally identified as belonging to the PS, are assigned to a pore. The thinning stage of the algorithm naturally partitions the PS into individual pores; necks are regions which thin at an earlier stage to the pores to which they are joined. For convenience, and to facilitate further analysis, a new image is produced where each pore is identified by a sequence number; all voxels belonging to a given pore are assigned the same integer value. At this stage, many statistics can then be readily determined such as pore-size distribution, coordination number distributions, and surface-to-volume ratios. However this approach leads to misidentification or less accurate partitioning of the PS because the thinning process is based on a segmentation algorithm.

2.4.3 Medial-Axis-based Approaches

The MA serves as a good basis for the characterisation of the PS. The MA of an object provides a one-dimensional representation of the object which is easier to analyse and has a strict geometrical relationship to the object's boundary and preserves important geometric properties of the object. Thus many geometric properties of the object can be taken directly from the object's skeleton, such as pore throat and pore body size distributions, pore body to pore throat size aspect ratios, coordination number, and spatial correlation with the porous system. Additionally, the MA can be utilized as an embedded search structure to find specific sites in the object or to construct a network structure. Many articles have appeared in recent years consistent with this view (Lindquist and Venkatarangan, 1999[88]). Existing approaches for partitioning the PS based on the MA can be broadly classified into two types, throat finding (e.g. Lindquist et al., 1999[88] and 2000[89]; Shin, 2002[159] and 2005[158]; Liang et al., 2000a[84]) and pore detecting (e.g. Al-Raoush et al., 2003[6], 2005[5] and 2006[4]; Sheppard et al., 2005[153]). Algorithms of the latter type locate pore bodies first and throats secondly. Throat finding algorithms consist of two steps, locating the throat position on the MA and constructing the throat surface.

Throat Finding Algorithms: From the flow point of view, a throat surface is a CS where maximum resistance is locally imposed on the fluid flowing through a pore channel.

Having improved Lee and Kashyap's (1994[81]) algorithm, Lindquist et al. (1999[88] and 2000[89]) successfully extract their desired medial axes from 3D images of consolidated systems. Venkatarangan (2000[177]) presented a dilation-based algorithm to construct a throat surface along a given MA path. During the dilation, the key point is for each voxel on the MA to obtain a closed loop of grain voxels, which is formed by detecting a change in the local Euler characteristic of the set of contacted grain voxels, and then constructing a triangulated surface (see Figure 2-19) to the closed loop by joining the centre or the face points of the MA voxel to the respective centres of the closed loop voxels. The area of the constructed triangular surfaces is then approximated by summing all respective triangle areas. The triangular surface having minimal area among all voxels on a MA path is defined as the throat surface of the path. A similar algorithm is also given by Shin (2002[159]), but Lindquist et al.'s algorithms do not suppose the throat surface as being planar. The throat surfaces are taken as triangulated interfaces; the set of voxels through which each triangulated throat surface pass defines a throat region.

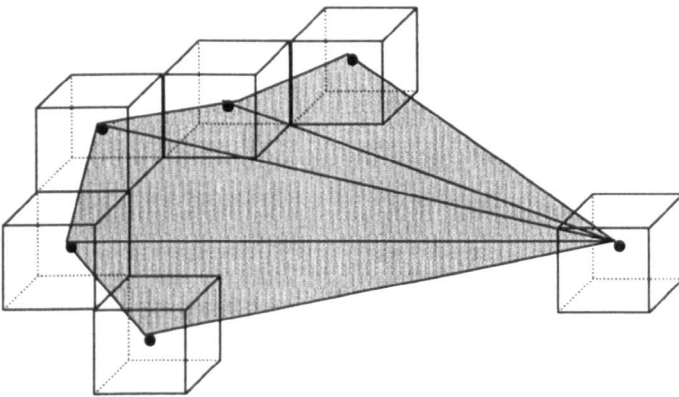


Figure 2-19: The construction of triangular throat surface.

Having located the throats, the PS can be partitioned into nodal pores separated by throat surfaces. This partitioning of the PS does not include an attempt to define channels connecting pores – rather two joining pores connect directly at the mutual throat surface. At this stage, the size of a nodal pore, defined as its volume, can be computed by considering partial volumes related to the corresponding throat surfaces.

To obtain the coordination number, Lindquist et al. (2000[89]) studied the relationship between the MA (percolating backbone) and node-channel structure in rock images. They found that there is not a one-to-one correspondence between them, and then they introduced a merge condition based on the shortest distance from the MA voxels to the solid phase. After merging nodal pores under this condition, the remaining paths and vertices of their modified MA then have a one-to-one correspondence with the pore channels and nodal pores of the image. Hence the coordination number distribution of the PS can be directly measured in terms of the coordination number of the vertices on the modified medial axis. Additionally, if removing all skeleton voxels which are located at multi-grain vertices (i.e. junctions on the medial axis), the remaining voxels on the MA can produce distinctive pore channels. Therefore the distance along the central portion of the pore channel connecting two nodal pores is defined as the length of the pore channel, which leads to the generation of the length distributions of the paths in the medial axis. An effective radius for a pore can also be computed using the sphere of equivalent volume. In a similar manner, three principal diameters (i.e. x, y and z) and an effective radius (from the circle of equivalent area) are produced for each planar or non-planar throat surface. Distributions of the principal diameters and the effective radius are produced for the pores and throats. They concluded that the throat surface area and the pore volume could be characterised as the log-normal-like distribution over an 18% porosity sample. Cross correlations between each pair of variables may also be of interest. Currently they produce cross correlation plots for a coordination number and pore volume and effective throat and pore radii.

Similar to Lindquist et al.'s approach (Lindquist et al., 1999[88] and 2000[89]), Liang et al. (2000a[84]) developed a PS partitioning method based on the skeletonization of Ma and Sonka (1996[96]) and their concept of λ -adjacency. Before partitioning the PS, they classify each skeleton voxel as either a link point if it has exactly two λ -adjacent neighbours, or a nodal point if it has three or more λ -adjacent neighbours. And then all nodal points are clustered into distinct vertices while the remaining link points are categorised as distinct pore paths. Using λ -adjacency rather than the commonly used 26(or 6)-adjacency leads to the identification of all intuitively correct vertices, which cannot be classified correctly via common adjacencies. The geometry of these pore paths are rigorously analysed by determining the cross sectional area and perimeter of their intersections with planes normal at each point of the path.

Using analytical geometry, they defined the tangent line at a MA point as the direction of the plane (i.e. cross section) normal at this point. And thus the area and the perimeter of each CS are readily determined. Local or absolute minima along each individual pore path (see Figure 2-20) can be further found by comparing the hydraulic radius (area or perimeter) of consecutive CSs.

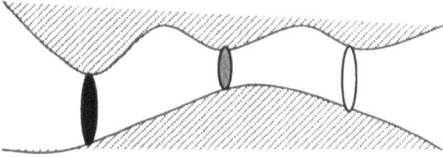


Figure 2-20: Local or absolute minima along a pore path. Hydraulic radius of cross sections reach to local minima at three positions but only the middle one reach absolute minima.

To partition the PS, Liang et al. (2000a[84]) argued that partitioning the PS into nodal pores separated by throat cross sectional surface would be better in the sense of the utility of the resulting pore and neck size distributions in network simulations (Ioannidis et al., 1999[62]). In other words, they identify pore necks with absolute minima rather than local minima in the hydraulic radius of individual pore paths. Pores are defined as the pore portions bounded by solid and neck voxels, which means the partition needs clustering pore voxels excluding neck voxels into individual pores. Unfortunately clustering according to the 26-adjacency rule would fail to assign the pore voxels on either side of the neck to different clusters. They then introduce a three-step approach to overcome this difficulty. First, the original image is clustered using a 6-adjacency rule, and all clusters connected with the MA are given the same label as the MA points. In a subsequent step, skeleton-6-connected clusters are partitioned into necks. Finally, all pore voxels clusters that are not 6-connected with the skeleton are reclustered using a 26-adjacency rule.

Once pores are correctly identified, their volume can be calculated by directly counting the number of voxels comprising each pore cluster. The coordination number of a pore can be easily determined by the number of pore throats connecting to the pore. It is also possible at this stage to examine a variety of possible correlations between pore and neck sizes, as well as the relationship between pore surface area and pore volume.

Pore detecting algorithms: To characterize the morphological structure of the PS, Sheppard et al. (2005[153]) used a skeletonization based on Pudeny's algorithm (1998[132]) to extract the MA of the PS. Rather than directly partitioning the PS, they first constructed a starting network by dividing the MA into clusters of voxels that are 26-adjacent to more than two other MA voxels, and chains of voxels that connect just two other MA voxels. Then a merging algorithm is developed with special consideration of two important issues: topology preservation and "snowballing" (see Figure 2-21). The direct result of the merging algorithm is a network of pore voxels and throat voxels on the medial axis.

Having identified all the pore bodies and throats in the medial axis, it remains to determine the geometry of these components, which means that one must partition the PS. Their algorithm first partitions the PS into pore bodies alone and then takes volume from the pore bodies to form pore throats. First, the PS is partitioned into pore bodies: a throat is defined as the surface where the regions surrounding two adjacent pores touch. This partitioning is achieved using the watershed transformation applied to the Euclidean distance map, in which the seed (starting) regions are determined by the MA voxels associated with each pore body. Then each of these pore bodies is taken and some of its volume is allocated to the pore throats that connect to it.

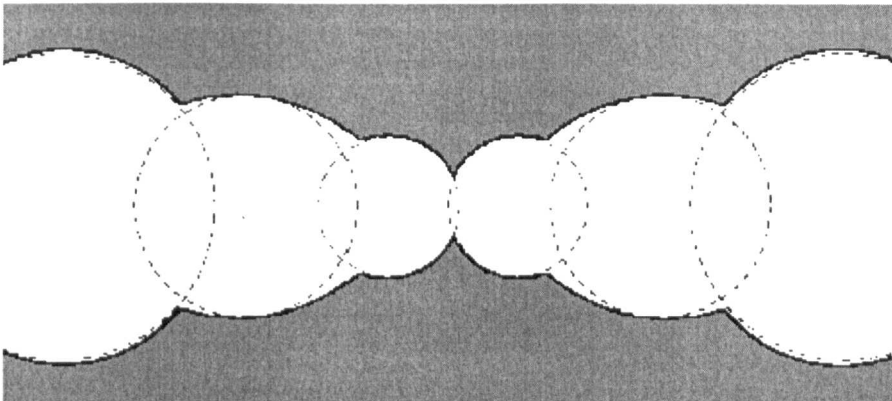


Figure 2-21: Cross sections through a geometry that will be mishandled by local pore merging rules. This whole object, being composed of overlapping maximal spheres, will be merged into a single pore.

With this partition of the PS, they computed many important quantities, such as the distribution of throat size, pore size, coordination number, pore length, correlations (e.g. between throat area and average the volumes of the two nodal pores, coordination

and pore volume, effective throat radius and the average effective radius of the two pores each throat separates etc.).

Once the morphological thinning MA is generated for the PS of a porous medium image, local maxima voxels on the MA are identified and are then grown to form pores by finding all connected voxels at the same or lower levels (Baldwin et al., 1996[13]). Necks are regions that are thinned at an earlier state to the pores they join. Over the whole PS, the pore size distribution, pore volume and throat area can be easily calculated.

With the MA of the PS extracted using Lindquist and Lee's (1996[87]) burning algorithm, a nodal point is then defined as a junction of three or more paths on the MA (Al-Raoush et al., 2003[6]). The centre of a nodal pore is chosen randomly among all connected nodal points, and the radius of the maximal sphere located at the nodal pore centre is considered as the radius of the nodal pore. A dilation algorithm is performed to find all spheres for all nodal pore centres in the PS, and a merging criterion is adopted to merge inscribed pore bodies if they overlap. Similarly, an inscribed throat radius can be calculated, in which the MA voxel with the minimum burn number along the path connecting two nodal pores is defined as the centre of the inscribed throat sphere. The smallest radius of inscribed spheres along a path is considered as the radius of the path (throat).

Chapter 3 Image Processing

In this chapter, a set of image processing techniques are presented by extending, improving existing approaches or developing new algorithms, aiming to provide a suite of robust, accurate and efficient image analysis tools for pore structure analysis. The tool (i.e. the pore analysis tools, PAT for short) mainly include distance transformation (Section 3.2), component labelling (Section 3.3), Euler number computing (Section 3.4) and medial axis transformation (Section 3.5). The commonly used definitions and notations through this thesis are presented in Section 3.1 in order to clarify basic topological concepts, which are closely associated with 3D binary images.

3.1 Basic Definitions and Notations

According to Kong and Rosenfeld (1989[76]), an n -dimensional binary image \mathcal{P} can be defined as a quadruple

$$\mathcal{P} \equiv (\mathcal{V}, \alpha, \beta, \mathcal{B}), \quad (3.1)$$

where \mathcal{V} is a finite subset of the rectilinear grid Z^n , called the image space of \mathcal{P} , (α, β) is a pair of adjacencies and $\mathcal{B} \subset \mathcal{V}$ is the set of object points. In particular, an image \mathcal{P} can simply be represented as a pair $(\mathcal{V}, \mathcal{B})$ if no adjacencies need to be considered.

A point p in $\mathcal{V} \subset Z^n$ is uniquely defined by a set of n integers $(c^1_p, c^2_p \dots c^n_p)$, where $c^1_p, c^2_p \dots c^n_p$ represent the Cartesian coordinates of a point p in Z^n . But in 2D or 3D discrete space it is more convenient to denote a point as (p_x, p_y) or (p_x, p_y, p_z) respectively, which is often called a pixel in 2D and a voxel in 3D. For digital image processing, a finite rectangular lattice \mathcal{V} is commonly used, that is $\mathcal{V} = \{(c^1_p, c^2_p \dots c^n_p) : 0 \leq c^j_p \leq L^j \text{ and } L^j \in Z^+, j = 1, 2 \dots n\}$. For example, in 3D \mathcal{V} is a set of all cubic grid points in a finite rectangular parallelepiped. Thus in \mathcal{V} all points can be classified as either interiors or border points.

Definition 3.1 (Interior and border points): For an image $\mathcal{P} = (\mathcal{V}, \mathcal{B})$, a point $p \in \mathcal{V}$ is said to be an interior point of \mathcal{P} if $0 < c_p^j < L^j$, for all $j \in \{1, 2 \dots n\}$, otherwise p is called a border point of \mathcal{P} .

Generally, a digital image \mathcal{P} can be considered as a function $\mathcal{P}: \mathcal{V} \subset \mathbb{Z}^n \rightarrow \mathcal{E} \subset \mathbb{Z}^d$ ($d = 1, 2 \dots$). In this dissertation, grey level images are considered occasionally, for which $\mathcal{E} = \{0, 1, 2 \dots 255\} \subset \mathbb{Z}^1$. In particular binary images are often used, for which \mathcal{V} is mapped into $\mathcal{E} = \{0, 1\}$. In other words, for each point $p \in \mathcal{V}$ there are only two possible integers, 0 or 1, which can be assigned to p , denoted by $\mathcal{P}(p)$.

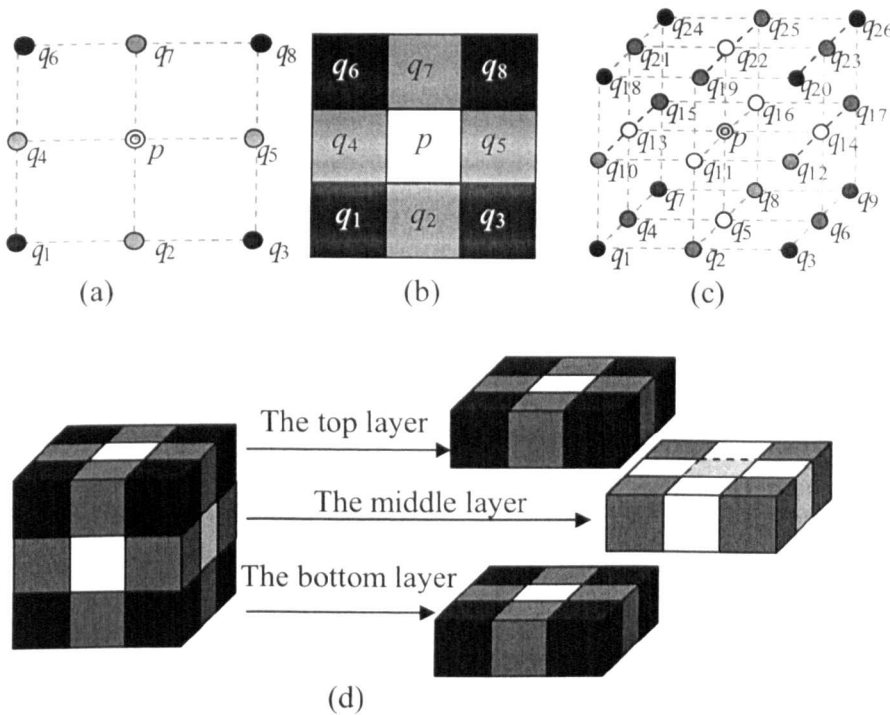


Figure 3-1: The direct neighbourhoods $\mathcal{N}(p)$ of a point p . (a) and (b) show different representations of the 2D direct (3×3) neighbourhoods, where $\mathcal{N}(p) = \{q_1, q_2, q_3, q_4, p, q_5, q_6, q_7, q_8\}$; (c) and (d) show two different representations of the 3D direct ($3 \times 3 \times 3$) neighbourhood, where $\mathcal{N}(p) = \{q_1, q_2 \dots q_{13}, p, q_{14}, q_{15} \dots q_{26}\}$.

In a binary image of interest, a point is called a black (foreground or object) point if it is assigned a value of 1. Otherwise, it is called a white (background or non-object) point. According to Definition 3.1, the set of all black points $\mathcal{B} \subset \mathcal{V}$ can be represented as $\mathcal{B} = \{p \in \mathcal{V}: \mathcal{P}(p) = 1\}$ and the set of all white points as $\mathcal{A}\mathcal{B} = \{p \in \mathcal{V}: \mathcal{P}(p) = 0\}$.

Commonly a discrete object can be represented as a lattice of points or as a lattice of squares (in 2D) or cubes (in 3D). Each point in the lattice has a direct neighbourhood, which is also called a 3×3 or a $3 \times 3 \times 3$ neighbourhood (see Figure 3-1) in 2D or 3D respectively.

Figure 3-1 shows two different representations of the direct neighbourhoods of a pixel and a voxel p . For a finite rectangular lattice \mathcal{V} the direct neighbourhood of a point $p \in \mathcal{V}$ in an image $\mathcal{P} = \{\mathcal{V}, \mathcal{B}\}$ is defined as

$$\mathcal{N}(p) = \{q \in \mathcal{V} : \max(|c_p^1 - c_q^1| \dots |c_p^n - c_q^n|) \leq 1\}. \quad (3.2)$$

This means that, for example, in 3D for an interior voxel p of \mathcal{P} the number of elements in $\mathcal{N}(p)$ is equal to 27, but for a border point this number is less than 27. Furthermore, we denote the set of points of $\mathcal{N}(p)$ excluding p , i.e. $\mathcal{N}(p) \setminus \{p\}$, as $\mathcal{N}^*(p)$, and each point in $\mathcal{N}^*(p)$ is called an adjacent point of p . Adjacency is defined more specifically in the following using the concept of α -neighbourhood introduced in the following.

Definition 3.2 (Adjacency): In 2D two distinct points p and q are said to be 8-adjacent if $q \in \mathcal{N}_8(p)$ (equivalently $p \in \mathcal{N}_8(q)$) and 4-adjacent if $q \in \mathcal{N}_4(p)$. In 3D two distinct points p and q are said to be 26-adjacent if $q \in \mathcal{N}_{26}(p)$ (i.e. $\{q \in \mathbb{Z}^3 : L_\infty(p, q) \leq 1\}$), 6-adjacent if $q \in \mathcal{N}_6(p)$ (i.e. $\{q \in \mathbb{Z}^3 : L_1(p, q) \leq 1\}$) and 18-adjacent if $q \in \mathcal{N}_{18}(p)$ (i.e. $\{q \in \mathbb{Z}^3 : L_1(p, q) \leq 2\} \cap \mathcal{N}_{26}(p)$).

In Figure 3-1(a) and (b), each grey pixel of $\mathcal{N}^*(p)$ is 4- and 8-adjacent to p , but each black pixel of $\mathcal{N}^*(p)$ is only 8-adjacent to p . In Figure 3-1(c) each white voxel of $\mathcal{N}^*(p)$ is 6-, 18- and 26-adjacent to p , each grey voxel of $\mathcal{N}^*(p)$ is 18- and 26-adjacent to p , and each black voxel of $\mathcal{N}^*(p)$ is only 26-adjacent to p . In the cubic model shown in Figure 3-1(d), two distinct voxels are 6-, 18- or 26-adjacent if they share at least one face, one edge, or one vertex, respectively.

For any point p in \mathbb{Z}^n , let $\mathcal{N}_\alpha^*(p)$ denote the set of all points in \mathbb{Z}^n that are α -adjacent to p excluding p and let $\mathcal{N}_\alpha(p)$, the α -neighbourhood of p be defined as $\mathcal{N}_\alpha(p) = \mathcal{N}_\alpha^*(p) \cup \{p\}$, where α is equal to the number of elements of $\mathcal{N}_\alpha^*(p)$ ($\alpha = 4, 8$ in 2D or $\alpha = 6, 18, 26$ in 3D). For example, the 4-neighbourhood $\mathcal{N}_4(p)$ of the central pixel p ,

shown in Figure 3-1(a) and (b), consists of 4 grey pixels q_1, q_4, q_5 and q_7 and the central pixel p . The 26-neighbourhood $\mathcal{N}_{26}(p)$ of the central voxel p , shown in Figure 3-1(c), contains 26 voxels (in white, grey and black) and the central voxel p . Consequently, we have $\mathcal{N}_{26}(p) = \mathcal{N}(p)$ and $\mathcal{N}_{26}^*(p) = \mathcal{N}^*(p)$ in 3D, while $\mathcal{N}_8(p) = \mathcal{N}(p)$ and $\mathcal{N}_8^*(p) = \mathcal{N}^*(p)$ in 2D.

According to Definition 3.2, we classify all voxels in $\mathcal{N}^*(p)$ as three different neighbours of p based on their adjacencies with p .

- (I) A 6-neighbour is 6-adjacent to p ;
- (II) A 18-neighbour is 18-adjacent but not 6-adjacent to p ;
- (III) A 26-neighbour is 26-adjacent but not 18-adjacent to p .

Similarly, in 2D two kinds of neighbours, 4- and 8-neighbours, can be identified according to the 4- and 8-adjacency.

The concept of α -neighbour is illustrated by the colours of the points in Figure 3-1. Each white voxel in Figure 3-1(c) is a 6-neighbour of p , each grey voxel is an 18-neighbour of p , and each black voxel is a 26-neighbour of p . The set of all α -neighbours of p is called the α -neighbour-set of p , denoted by $\tilde{\mathcal{N}}_\alpha(p)$. For example, in Figure 3-1(c), the 18-neighbour-set $\tilde{\mathcal{N}}_{18}(p)$ consists of all grey voxels (i.e. $q_2, q_4, q_6, q_8, q_{10}, q_{12}, q_{15}, q_{17}, q_{19}, q_{21}, q_{23}, q_{25}$).

The relation between the direct neighbourhood $\mathcal{N}(p)$, the α -neighbourhood $\mathcal{N}_\alpha(p)$ and the α -neighbour-set $\tilde{\mathcal{N}}_\alpha(p)$, $\alpha = 6, 18, 26$, of a voxel p is:

$$\begin{aligned}
 \mathcal{N}(p) &= \mathcal{N}_{26}(p); \\
 \mathcal{N}_\alpha(p) &= \mathcal{N}_\alpha^*(p) \cup \{p\}, \alpha = 6, 18, 26; \\
 \mathcal{N}_{26}^*(p) &= \tilde{\mathcal{N}}_{26}(p) \cup \tilde{\mathcal{N}}_{18}(p) \cup \tilde{\mathcal{N}}_6(p); \\
 \mathcal{N}_{18}^*(p) &= \tilde{\mathcal{N}}_{18}(p) \cup \tilde{\mathcal{N}}_6(p); \\
 \mathcal{N}_6^*(p) &= \tilde{\mathcal{N}}_6(p).
 \end{aligned} \tag{3.3}$$

Applying the definition of adjacency, connectedness of any two points can be defined. Two points p and q are said to be α -connected if there exists a sequence $\{p_1, p_2 \dots p_m\}$ between p and q such that p_i is α -adjacent to p_{i+1} for all $i = 1, 2 \dots m-1$ and $p_1 = p, p_m = q$. Such a sequence is called a α -path with end points p and q . A path with

the property of $p_0 = p_m$ is called a closed path. A closed path contains no end points. A α -path is called a α -curve or simply a curve if it does not intersect (Figure 3-2(a)) or touch (Figure 3-2(b)) itself, except at end points. Obviously, any point in a curve has exactly either one or two α -adjacent points. Some examples with regard to these concepts can be found in Figure 3-2.

Definition 3.3 (α -component): Let S be a subset of Z^n , then S is said to be a α -component if any two points in S are α -connected.

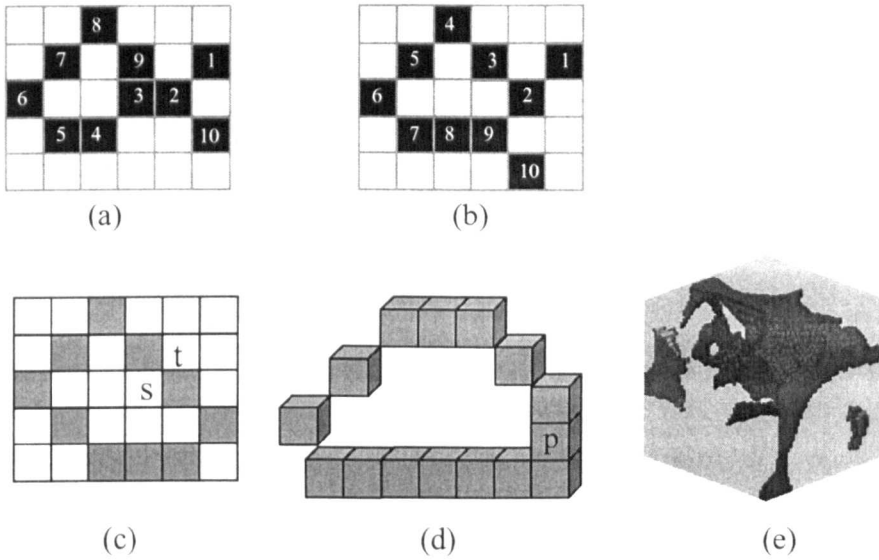


Figure 3-2: Examples of paths, curves and components. (a) A path $\{1, 2 \dots 9, 2, 10\}$ intersect itself; (b) a path $\{1, 2 \dots 10\}$ touches itself; (c) the set of grey pixels can be organised as a closed 8-curve, but not as a 4-curve; (d) the set of grey voxels is a 26-path, but not a 26-curve because voxel p has three 26-adjacent grey voxels. The set of grey pixels in (c) is an 8-component but not a 4-component, and the set of grey pixels in (d) is a 26-component but not an 18- or a 6-component. Note that in (a) ~ (d) all white (background) voxels are invisible for clarity. In (e) an example is shown of 4 26-components in 3D.

For instance, the set of grey pixels in Figure 3-2(c) is an 8-component but not a 4-component, and the set of grey voxels in Figure 3-2(d) is a 26-component, but it is neither an 18-component nor a 6-component.

For a binary image $\mathcal{P} = (\mathcal{V}, \alpha, \beta, \mathcal{B})$, the object set \mathcal{B} and background set $\mathcal{V} \setminus \mathcal{B}$ must satisfies different adjacencies (α, β) according to the requirement of the digital curve

and surface theorem. This theorem states that a simple closed curve or surface must separate the 2D or 3D space into two disconnected parts, i.e. the interior and exterior. In Figure 3-2(c), let \mathcal{B} be the set of grey pixels and its complement $\mathcal{V}\setminus\mathcal{B}$ be the set of white pixels. Since only 4- and 8-adjacencies are available in 2D, the only two adjacency pairs are (4, 8) and (8, 4) for \mathcal{B} and $\mathcal{V}\setminus\mathcal{B}$. For instance, points s and t , both belonging to $\mathcal{V}\setminus\mathcal{B}$, are 8-adjacent, so s and t cannot be separated by the 8-curve. Hence, $\mathcal{V}\setminus\mathcal{B}$ must have 4-adjacency in order to be separated by a black 8-curve in \mathcal{B} . Similar to the consideration in 2D, in 3D popular choices for (α, β) are four pairs of adjacencies: (6, 26), (6, 18), (26, 6), and (18, 6). Throughout this thesis, we use (26, 6), i.e. 26-adjacency for black points (\mathcal{B}) and 6-adjacency for white points ($\mathcal{V}\setminus\mathcal{B}$), because 26-adjacency for object voxels theoretically leads to smoother skeletons (Kong and Rosenfeld, 1989[76]).

3.2 Distance Transformations

Distance transformation (DT) converts a binary image into another grey level image, called a distance map (DM) of the original image, where the value of each object point corresponds to its shortest distance to all background points, 0 is simply assigned to background points. DMs are widely used in image processing and analysis. In this thesis, DMs will be mainly used to control the thinning process in the skeletonisation and to determine pore size (sphere equivalent or cross sectional sizes) in pore structure analysis.

Clearly such a simple and brute-force algorithm can be used for computation of the DM: for each object voxel, the distances to all background voxels are computed and the smallest one is stored. Despite its apparent simplicity, however, this approach is impractical, as it leads to prohibitively long computational times. Therefore, a major concern associated with DTs is the algorithm efficiency. One solution is to use a discrete distance metric (of integer values in discrete space), such as the city-block, chessboard or chamfer distance metric, which is easy to compute, to provide an approximation of the Euclidean distance.

In pore structure analysis, the exact Euclidean distance itself, rather than an approximation, is crucial for accurate measurement of the pore size in terms of sphere equivalent or cross sectional sizes, because the Euclidean distance is invariant under

rotation about any axis. Many authors have developed DT algorithms, such as vector distance transforms, fast marching methods and level set methods. A comprehensive review of DT can be found in Cuisenaire's PhD thesis (1999[36]) or Jones et al's article (2006[68]). According to Shih and Wu (2004a[154]), most techniques are either inefficient or complex to implement and understand. This has motivated me to extend and improve Shih and Wu's approach, aiming to handle large 3D images (e.g. volume of 1024^3 voxels) to facilitate the pore analysis and network construction.

The concept of Euclidean distance between two points implies that there must be a straight-line segment, linking these two points, in the Euclidean space (E^3) associated with a Euclidean distance value. In some applications, however, the straight-line segment between two voxels is required to be completely located within a constraint domain (a subset of E^3) rather than within the whole Euclidean space E^3 . This requirement leads to the introduction of geodesic distance (GD). For my application, this kind of distance will be employed to partition the PS or to determine individual spatial cross sections. In the following sections, the GD will be discussed, which is an extended squared Euclidean distance.

3.2.1 Distance Metrics

In n -dimensional Euclidean space E^n , the function d mapping from $E^n \times E^n$ to Z^+ (the set of nonnegative integers) is called a distance metric, if it satisfies the following distance metric criteria for any three points p , q and $r \in E^n$:

- (a) Positive: $d(p, q) \geq 0$,
- (b) Definite: $d(p, q) = 0 \Leftrightarrow p = q$,
- (c) Symmetric: $d(p, q) = d(q, p)$,
- (d) Triangular inequality: $d(p, r) \leq d(p, q) + d(q, r)$.

Let the n -dimensional vector $(c^1_p, c^2_p \dots c^n_p)$ represent the coordinates of a point p in E^n , or the vectors (p_x, p_y) and (p_x, p_y, p_z) in 2D and 3D, respectively. It is clear that the following function L_k , defined as

$$L_k(p, q) = (\sum_{i=1,2,\dots,n} |c^i_p - c^i_q|^k)^{1/k}, \quad (3.4)$$

is a distance metric for all nonnegative integers k .

Unlike the city-block (i.e. $L_1(p, q) = |p_1 - q_1| + \dots + |p_d - q_d|$) and chessboard distances (i.e. $L_\infty(p, q) = \max(|p_1 - q_1| \dots |p_d - q_d|)$), in the discrete space Z^n , the Euclidean distance d_E (i.e. L_2) is not integer-valued because it involves the square root operation. Consequently, in many applications, rather than using the ED, the SED is used. The SED between p and q is then defined as

$$d_{SE}(p, q) = [d_E(p, q)]^2. \quad (3.5)$$

Unfortunately, d_{SE} is not a distance metric because the triangular inequality is not satisfied, which limits the application of the SED. Based on the definition of the L_k , the direct neighbourhood, the α -neighbourhood and the α -neighbour-set of a voxel with $\alpha = 6, 18, 26$ in Equation (3.2) and (3.3) can be redefined as follows:

$$\begin{aligned} \mathcal{N}_6(p) &= \{q \in Z^3: L_1(p, q) \leq 1\}; \quad \tilde{\mathcal{N}}_6(p) = \{q \in Z^3: L_1(p, q) = 1\}, \\ \mathcal{N}_{26}(p) &= \{q \in Z^3: L_\infty(p, q) \leq 1\}; \quad \tilde{\mathcal{N}}_{26}(p) = \{q \in Z^3: L_\infty(p, q) = 1\}, \\ \mathcal{N}_{18}(p) &= \{q \in Z^3: d_{SE}(p, q) \leq 2\} \cap \mathcal{N}_{26}(p); \\ \tilde{\mathcal{N}}_{18}(p) &= \{q \in Z^3: d_{SE}(p, q) = 2\} \cap \mathcal{N}_{26}(p). \end{aligned}$$

3.2.2 Geodesic and Chamfer Distances

The definition of $d_E(p, q)$ is related to a segment linking p and q , which is called a path and is shown in Figure 3-3. The length of the segment equals to $d_E(p, q)$. If the straight segment (path) is required to be located totally within a constraint domain $\mathcal{M} \subset Z^n$, however, a single straight segment path between two points may not exist. In Figure 3-3, the dotted line is the path between p and q , but it is not entirely located within the constraint domain \mathcal{M} . (the bright grey region). If a path is allowed to consist of more than one straight-line segment, a so-called geodesic distance (GD) can be introduced. In Figure 3-3, between p and q there are two such paths, each of them contains a few straight-line segments, which totally are located within \mathcal{M} . In general, for any two points p and q in \mathcal{M} , we define the length of the shortest path which is totally located within \mathcal{M}

as geodesic distance between p and q , denoted by $d_G(p, q)$. Let $d_G(p, q) = \infty$ if there does not exist any path between p and q that is entirely located within \mathcal{M} .

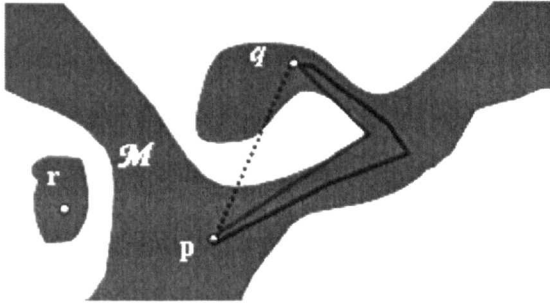


Figure 3-3: Geodesic distance between p and q , $d_G(p, q)$, with respect to the constraint domain \mathcal{M} (the grey region) is defined as the length of the grey solid path. The length of the dotted line corresponds to the Euclidean distance between p and q ; $d_G(p, r) = \infty$ because no paths between p and r , with regard to the constraint domain \mathcal{M} , exist.

Let $\mathcal{M} \subset E^n$ be a constraint domain, then $P = \{p_1, p_2 \dots p_n\}$ is a path in \mathcal{M} between p (p_1) and q (p_n), such that each pair of points p_i and p_{i+1} is linked by a straight-line segment, which is totally located within \mathcal{M} , for all $i = 1, 2 \dots n-1$. The length of the path P , $L(P)$, is calculated as

$$L(P) = \sum_{i=1}^{n-1} d(p_i, p_{i+1}), \quad (3.6)$$

where d is a distance metric. Thus the geodesic distance between p and q is defined as the length of the shortest path from p to q (e.g. the grey path in Figure 3-3). If the Euclidean distance is adopted in (3.6), the GD is often called the geodesic Euclidean distance, denoted by d_{GE} .

In Z^2 , a basic straight-line segment of a path is considered as the locus of one step move along horizontal, vertical or diagonal directions in the unit square of a pixel (Figure 3-4(a)). A horizontal move or a vertical move is called an a -move because both of them have the same moving length, and the diagonal move is called a b -move. Clearly, the length of a path, which consists of only a -moves (e.g. black path in Figure 3-4(b)), is the City-block distance (i.e. L_1 in (3.4)) if we assume that the length of a move is 1. In general, let a be the length of an a -move, and b be the length of a b -move. Given a path of moves between p and q in 2D, let \mathcal{K}_a and \mathcal{K}_b represent the numbers of a -moves and b -moves in the path, then the length of the path is defined as

$$d_{a,b}(p, q) = \mathcal{K}_a a + \mathcal{K}_b b. \quad (3.7)$$

In Z^3 , there are three kinds of moves shown in Figure 3-4(c), called a -, b - and c -move, respectively, as basic straight-line segments. Let a , b and c be the lengths of a -move, b -move and c -move, respectively, and \mathcal{K}_a , \mathcal{K}_b and \mathcal{K}_c represent the numbers of a -moves, b -moves and c -moves of a path between p and q in a path. Therefore, the length of the path is similarly defined as

$$d_{a,b,c}(p, q) = \mathcal{K}_a a + \mathcal{K}_b b + \mathcal{K}_c c. \quad (3.8)$$

Obviously, two points p and q in discrete space may be connected by an infinite number of paths. Among all these paths, there must exist a path with minimum length, which is called a shortest path. The length of the shortest path is defined as the chamfer distance (CD) between p and q , denoted by $d_{C(a,b)}(p, q)$ or $d_{C(a,b,c)}(p, q)$ in 2D or 3D, respectively. The coefficients (a, b) or (a, b, c) in (3.7) or (3.8) are referred to as the chamfer distance coefficients (CDC), or chamfer coefficients. For the two pixels p and q shown in Figure 3-4(b), for example, we can obtain many different CDs between p and q for different CDCs, such as,

- $d_{C(1, \sqrt{2})}(p, q) = 3\sqrt{2}$;
- $d_{C(1,2)}(p, q) = 6$;
- $d_{C(3,4)}(p, q) = 12$.

According to the four conditions for a distance metric (see Section 3.2.1), the CD may not be a distance metric if the CDC is not chosen properly. As stated by Marchand-Maillet and Sharaiha (1999[101]), the 2D chamfer distance $d_{C(a,b)}$ is a distance metric if

$$0 < a < b < 2a. \quad (3.9)$$

This condition ensures that the triangular inequality is met for $d_{C(a,b)}$. Moreover, the conditions on a , b , and c for $d_{C(a,b,c)}$ to be a distance metric is

$$3.10 \quad 0 < a < b < c, b < 2a \text{ and } c < b + a. \quad (3.10)$$

Considering the constraint domain \mathcal{M} in discrete space (see Figure 3-5) and applying the chamfer distance in (3.6) as the distance metric (i.e. $d(p, q)$) defines the geodesic chamfer distance.

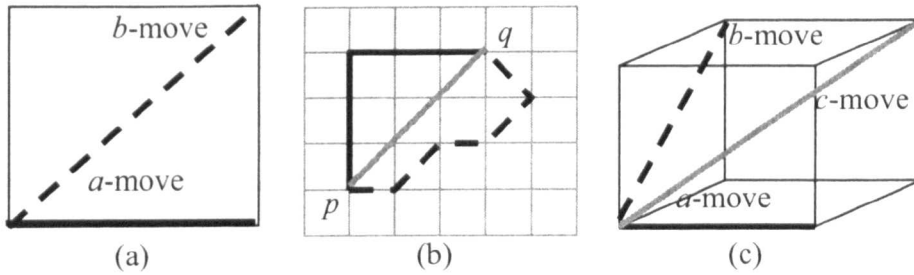


Figure 3-4: Moves and paths in 2D/3D: (a) a -move and b -move in 2D; (b) three paths of moves: the black consists of only a -moves and its length is $6a$, the grey consists of only b -moves and its length is $3b$, and the dashed consists of both a - and b -moves and its length is $2a + 3b$; (c) a -, b - or c -move in Z^3 .

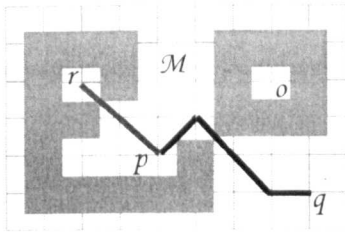


Figure 3-5: Constraint domain \mathcal{M} (white) with 8-adjacency containing paths between p and r and between p and q with shortest chamfer distance. The constraint domain does not allow any paths between p and o .

3.2.3 The Relationship between Squared Euclidean and Chamfer Distances

Given two pixels $p = (p_x, p_y)$ and $q = (q_x, q_y)$ in Z^2 , according to the definition of the chamfer distance (see (3.6) and (3.7)), the numbers of a -moves and b -moves ($\mathcal{K}_a, \mathcal{K}_b$) of the shortest path between p and q is computed as

$$\mathcal{K}_b = \min \{|p_x - q_x|, |p_y - q_y|\}, \mathcal{K}_a = \max \{|p_x - q_x|, |p_y - q_y|\} - \mathcal{K}_b. \quad (3.11)$$

Without loss of generality, we assume that $|p_x - q_x| \leq |p_y - q_y|$, Equation (3.11) is easy to prove using Dijkstra's shortest path theorem (1959[42]). Therefore, the SED ($|p_x - q_x|^2 + |p_y - q_y|^2$, see Equation (3.6)) between p and q in 2D can be calculated as

$$d_{SE}(p, q) = (\mathcal{K}_b)^2 + (\mathcal{K}_a + \mathcal{K}_b)^2 \quad (3.12)$$

In Z^3 the numbers of moves ($\mathcal{K}_a, \mathcal{K}_b, \mathcal{K}_c$) of a shortest path between p and q can similarly be computed as

$$\mathcal{K}_c = \min \{|p_x - q_x|, |p_y - q_y|, |p_z - q_z|\}, \quad (3.13a)$$

$$\begin{aligned} \mathcal{K}_b = \min \{ & |p_x - q_x| - \mathcal{K}_c, |p_y - q_y| - \mathcal{K}_c \} \\ & + \min \{|p_x - q_x| - \mathcal{K}_c, |p_z - q_z| - \mathcal{K}_c\} \\ & + \min \{|p_y - q_y| - \mathcal{K}_c, |p_z - q_z| - \mathcal{K}_c, \end{aligned} \quad (3.13b)$$

$$\mathcal{K}_a = \max \{|p_x - q_x|, |p_y - q_y|, |p_z - q_z|\} - \mathcal{K}_b - \mathcal{K}_c. \quad (3.13c)$$

Assuming that $|p_x - q_x| \leq |p_y - q_y| \leq |p_z - q_z|$, the 3D SED between p and q is given by

$$3.14 \quad d_{SE}(p, q) = (\mathcal{K}_c)^2 + (\mathcal{K}_b + \mathcal{K}_c)^2 + (\mathcal{K}_a + \mathcal{K}_b + \mathcal{K}_c)^2 \quad (3.14)$$

The chamfer distance is widely used as an approximation of the Euclidean distance to reduce the computational cost. A key issue in the study of the CD is to establish particular values of the chamfer coefficients as optimal. The latter refers to the criterion of minimizing the error resulting in the approximation of Euclidean distance values by chamfer distance values. The approximating error may be very large if the chamfer coefficients are not properly chosen. In contrast to other criteria (see, e.g., Verwer 1991[179]; Thiel and Montanvert, 1992[166]), Forchhammer's (1989[48]) topological inconsistencies or errors, as explained below, can be used to assess whether the CD calculations lead to the correct ordering of the Euclidean distances. This criterion is the basis of my geodesic Euclidean transformation algorithm (Algorithm 3.3).

Essentially, the ordering of the discrete distances does not match the ordering of the Euclidean distances. Consider the following 2D example (see Figure 3-6). Let the chamfer coefficients be $a = 3$ and $b = 4$, and consider the three pixels, $o = (0, 0)$, $s = (1, 2)$ and $t = (3, 3)$. According to Equation (3.11), we have $d_{C(3,4)}(o, s) = 3 \times 3 + 1 \times 4 = 13$,

$d_{SE}(o, s) = 1^2 + 4^2 = 17$, $d_{C(3,4)}(o, t) = 0 \times 3 + 3 \times 4 = 12$, $d_{SE}(o, t) = 3^2 + 3^2 = 18$, which means that the ordering of d_C is different from the ordering of the d_{SE} (or d_E).

To characterize optimal chamfer coefficients, Marchand-Mailler and Sharaiha (1999[101]) considered the criterion of topological ordering rather than the criterion of minimizing the error in the approximation of the Euclidean distance values (e.g. $\min_{(a,b)} |d_E(p, q) - d_{C(a,b)}(p, q)|$ for all pairs p and q).

Besides the incorrect ordering, another type of topological error concerns the inconsistency of equality of the two distances. For example, in Figure 3-6, the chamfer distance $d_{C(3,4)}(o, p)$ between o and p is equal to the chamfer distance $d_{C(3,4)}(o, q)$ between o and q but the SED $d_{SE}(o, p)$ between o and p is not equal to the SED $d_{SE}(o, q)$ between o and q . Marchand-Mailler and Sharaiha defined the optimal pair among all valid pairs (3.9) of CD coefficients as the smallest integer pair that guarantees the maximum achievable Euclidean distance limit. And they stated that for all pairs with $a \leq 10$, the pair (3, 4) is a local optimum, in the sense that it is the smallest pair of CD coefficients that leads to a (local) maximum Euclidean distance limit.

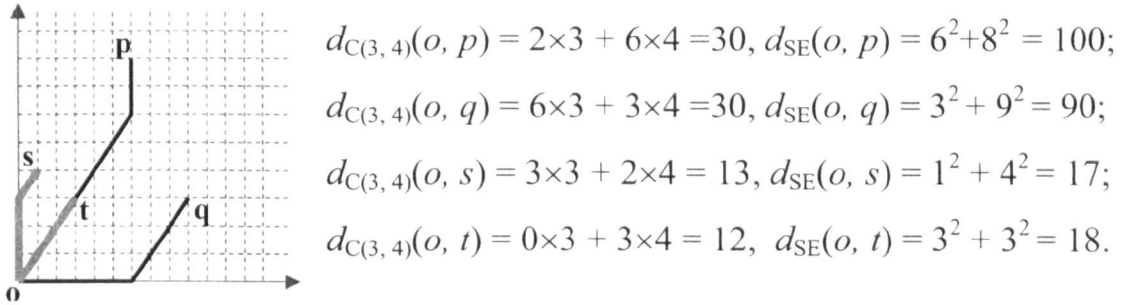


Figure 3-6: Examples illustrating two types of topological errors between the chamfer and the Euclidean distances.

Borgefors (1984[24]) has extended the chamfer distance in any arbitrary dimension and he proposed methods to optimize the approximation of the Euclidean distance. More recently, in addition to Marchand-Mailler and Sharaiha's 2D result, Borgefors (1996[25]) confirmed that the triple of 3D chamfer distance coefficients (3, 4, 5) minimizes the upper bound on the difference between the chamfer and the Euclidean distances.

3.2.4 New Distance Transformation algorithms

In the following, several algorithms are developed to obtain the SED and the CD transformations. When additionally taking a constraint domain into account, I propose to approximate the geodesic Euclidean distance by a geodesic chamfer distance with CDC (3, 4, 5) in 3D.

A 3D binary image $\mathcal{P}(\mathcal{V}, \mathcal{B})$ divides \mathcal{V} into foreground (object) \mathcal{B} and background $\mathcal{V} \setminus \mathcal{B}$ by assigning 0 to each voxel p in $\mathcal{V} \setminus \mathcal{B}$ and 1 to each voxel in \mathcal{B} , denoted by $\mathcal{P}(p) = 0$ or 1, respectively. A DT is used to convert an image into another grey level image, called the distance map (DM). DM has the same image space \mathcal{V} as its original image and for each voxel $q \in \mathcal{V}$, the value $DM(q)$ is assigned as the distance to the nearest background voxel, i.e.

$$DM(q) = \text{Min}\{d(q, r) : r \in \mathcal{V} \setminus \mathcal{B}\} \quad (3.15)$$

If the city-block (i.e. \mathcal{L}_1 in (3.4)) or the chessboard distance i.e. \mathcal{L}_∞ in (3.4)) is used in (3.15), the corresponding DMs are easy to compute as these distances can be recursively accumulated by considering only 6- and 26-neighbours, respectively. Unfortunately, this strategy cannot be directly applied to the computation of the SED map because the SED has no linear relation with the relative coordinates between two voxels.

Obtaining the distance map by directly applying Equation (3.15) is unpractical, as it is too time-consuming for 3D large images. Many SED algorithms have been proposed, which use morphological operators, filters, several paths on rows and columns, propagating vectors, or Voronoi diagrams. A comprehensive review of DT algorithms can be found in Cuisenaire's PhD thesis (1999[36]). In comparison with other techniques, the idea of propagating the relative coordinates between current point and its closest background point, in two scans of the original image, leads to a favourable algorithm that is less time-consuming than other schemes. Based on this idea, Shih and Wu (2004a[154]) presented a two-scan algorithm that uses 3×3 neighbourhoods to compute the exact 2D SED and they developed another two-scan algorithm to obtain the 3D SED map by decomposing the SED into different types of neighbourhoods. Motivated by these approaches, I present a similar algorithm to compute 2D and 3D SED maps which has three advantages, as it: (i) simplifies the

comparison of SED values in a $3 \times 3 \times 3$ neighbourhood, (ii) avoids any complex decomposition of the SED structure, (iii) is easy to implement and to understand.

The basic idea behind my algorithm is simple. When scanning a binary image, the zeros for background voxels are directly assigned as the values in the resultant DM. For a foreground voxel p , an extra scan needs to be applied within its $3 \times 3 \times 3$ neighbourhood (i.e. $\mathcal{N}(p)$), to obtain its current distance to the background as the shortest squared Euclidean distance is calculated using the distance of one of its 26-neighbours to the background. Simultaneously, for each object voxel (or relative coordinates between current object voxel and) the nearest background voxel is recorded during each scan.

The $3 \times 3 \times 3$ neighbourhood $\mathcal{N}(p)$ of voxel p is partitioned into two subsets, $\mathcal{N}_f(p)$ and $\mathcal{N}_b(p)$, which are used for a forward and a backward scan, respectively. As shown Figure 3-1(c), the $\mathcal{N}(p)$ is halved as $\mathcal{N}_f(p) = \{q_1, q_2 \dots q_{13}\}$ and $\mathcal{N}_b(p) = \{q_{14}, q_{15} \dots q_{26}\}$. For an image $\mathcal{P}(\mathcal{V}, \mathcal{B})$, notice that $\mathcal{N}_f(p)$ and $\mathcal{N}_b(p)$ may have less than 13 elements if p is a border voxel of \mathcal{P} (see Definition 3.1).

Let $R(p)$ record the relative coordinates vector $R(p) \equiv (R_x, R_y, R_z) = (p_x - o_x, p_y - o_y, p_z - o_z)$ of voxel p with respect to the coordinates of the nearest background voxel o (see Figure 3-7). The SED between p and o is defined via the distance between a voxel q in $\mathcal{N}(p)$ and o as

$$\begin{aligned}
 d_{SE}(p, o) &= (p_x - o_x)^2 + (p_y - o_y)^2 + (p_z - o_z)^2 \\
 &= (q_x - o_x)^2 + 2(p_x - q_x)(q_x - o_x) + (p_x - q_x)^2 + \\
 &\quad (q_y - o_y)^2 + 2(p_y - q_y)(q_y - o_y) + (p_y - q_y)^2 + \\
 &\quad (q_z - o_z)^2 + 2(p_z - q_z)(q_z - o_z) + (p_z - q_z)^2 \\
 3.16 &= d_{SE}(q, o) + C_f(p, q) + 2V(p, q) \times R(q)^T.
 \end{aligned} \tag{3.16}$$

Where $C_f(p, q) = (p_x - q_x)^2 + (p_y - q_y)^2 + (p_z - q_z)^2 = d_{SE}(p, q)$ denotes the SED value between a voxel and one of its 26-neighbours. Clearly, $C_f(p, q)$ is only related to their relative positions and independent of the absolute coordinates of p or q . The values of $C_f(p, q)$ are

$$C_f(p, q) = \begin{cases} 1 & \text{if } q \in N_6(p) \\ 2 & \text{if } q \in N_{18}(p) \\ 3 & \text{if } q \in N_{26}(p) \end{cases} \tag{3.17}$$

$V(p, q) = (p_x - q_x, p_y - q_y, p_z - q_z)$ in (3.16) is a vector that represents the difference between the coordinates of a voxel and one of its 26-neighbours, with

$$V(p, q) \in \{(1, 1, 1), (0, 1, 1) \dots (-1, -1, -1)\}. \quad (3.18)$$

The real vector of $V(p, q)$, that will be used in (3.16), is determined by the sequence number in (3.18) from 1 to 26 corresponding to $q_1, q_2 \dots q_{26}$ (see Figure 3-1(c)).

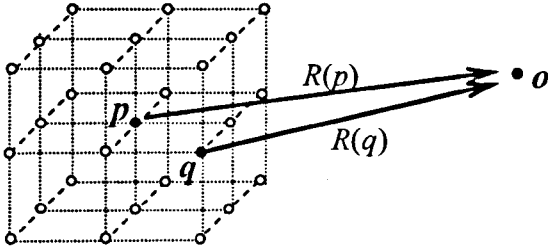


Figure 3-7: Relative coordinates vectors $R(p)$ and $R(q)$ to a background voxel o .

Algorithm 3.1: Two-way scan algorithm for squared Euclidean DT

Input: a 3D binary image $\mathcal{P}(\mathcal{V}, \mathcal{B})$, where \mathcal{B} is the set of foreground voxels in \mathcal{V} .

Output: the squared Euclidean distance map DM

1. *Forward Scan (left-to-right, near-to-far, bottom-to-top)*
 - If $p \in \mathcal{B}$ then { //foreground voxels
 - $DM(p) = \infty$
 - For each $q \in \mathcal{N}_f(p)$ // i.e. $\{q_1, q_2 \dots q_{13}\}$ in Figure 3-1(c)
 - $dist = DM(q) + C_f(p, q) + 2V(p, q) \times R(q)^T$
 - If $dist < DM(p)$ then {
 - $DM(p) = dist$ and
 - $R(p) = R(q) + V(p, q)$
 - }
 - } else { //background voxels
 - $DM(p) = 0$
 - $R(p) = (0, 0, 0)^T$
 - }
2. *Backward Scan (top-to-bottom, far-to-near, right-to-left)*
 - If $p \in \mathcal{B}$ then { //foreground voxels
 - For each $q \in \mathcal{N}_b(p)$ // i.e. $\{q_{14}, q_{15} \dots q_{26}\}$ in Figure 3-1(c)
 - $dist = DM(q) + C_b(p, q) + 2V(p, q) \times R(q)^T$

```

    if  $dist < DM(p)$  then {
         $DM(p) = dist$  and
         $R(p) = R(q) + V(p, q)$ 
    }

```

Algorithm 3.2: Two-way scan algorithm for the chamfer DT

Input: a 3D binary image $\mathcal{P}(\mathcal{V}, \mathcal{B})$, where \mathcal{B} is the set of object voxels in \mathcal{P} .

Output: the chamfer distance map DM for chamfer distance coefficients (a, b, c) .

Initialise:

$$Cf_{a,b,c}(p, q) = \begin{cases} a & \text{if } q \in N_6(p) \\ b & \text{if } q \in N_{18}(p) \\ c & \text{if } q \in N_{26}(p) \end{cases}$$

1. *Forward Scan (left-to-right, near-to-far, bottom-to-top):*

```

If  $p \in \mathcal{B}$  then {
     $DM(p) = \infty$ 
    For each  $q \in N_f(p)$ 
         $DM(p) = \min(DM(p), DM(q) + Cf_{a,b,c}(p, q))$ 
    } else {
         $DM(p) = 0$ 
    }

```

2. *Backward Scan (top-to-bottom, far-to-near, right-to-left):*

```

If  $p \in \mathcal{B}$  then {
    For each  $q \in N_b(p)$ 
         $DM(p) = \min(DM(p), DM(q) + Cf_{a,b,c}(p, q))$ 
    }

```

In the following, some examples are given of applications of the two-way scan SED and CD transformations.

Figure 3-8 shows a 2D SED map extracted by the two-way scan algorithm (Algorithm 3.1). The five red pixels form the background of the original image and all other pixels are the object. The SED of the background pixels are zeros, and the SED values of the object pixels are positive integers, which are the shortest SED to the background.

The colours of object pixels in Figure 3-8 are used to represent different nearest background pixels. In other words, two object pixels have the same colour if they have

the same nearest background pixel in the SED map. This feature can be used to cluster objects in many applications, such as partitioning the PS.

In Figure 3-9, a duct-network model is used to demonstrate the 3D SED map. In the original binary image, shown in the first picture of Figure 3-9, each duct has a square shaped CS with a constant size of 13x13 voxels. The 45968 object voxels are coloured grey and the background voxels are transparent. The image space is $\{(x, y, z): 0 \leq x \leq 39, 0 \leq y \leq 39, 0 \leq z \leq 39\}$. From left to right and top to bottom, starting at the second picture, the pictures show object voxels with SED values larger than 1, 2, 8, 20, 39, 48, 59, 79, and 97 respectively in the resultant SED map, and the corresponding numbers of object voxels are 37904, 36784, 27216, 11696, 3280, 1744, 969, 56, and 8, respectively.

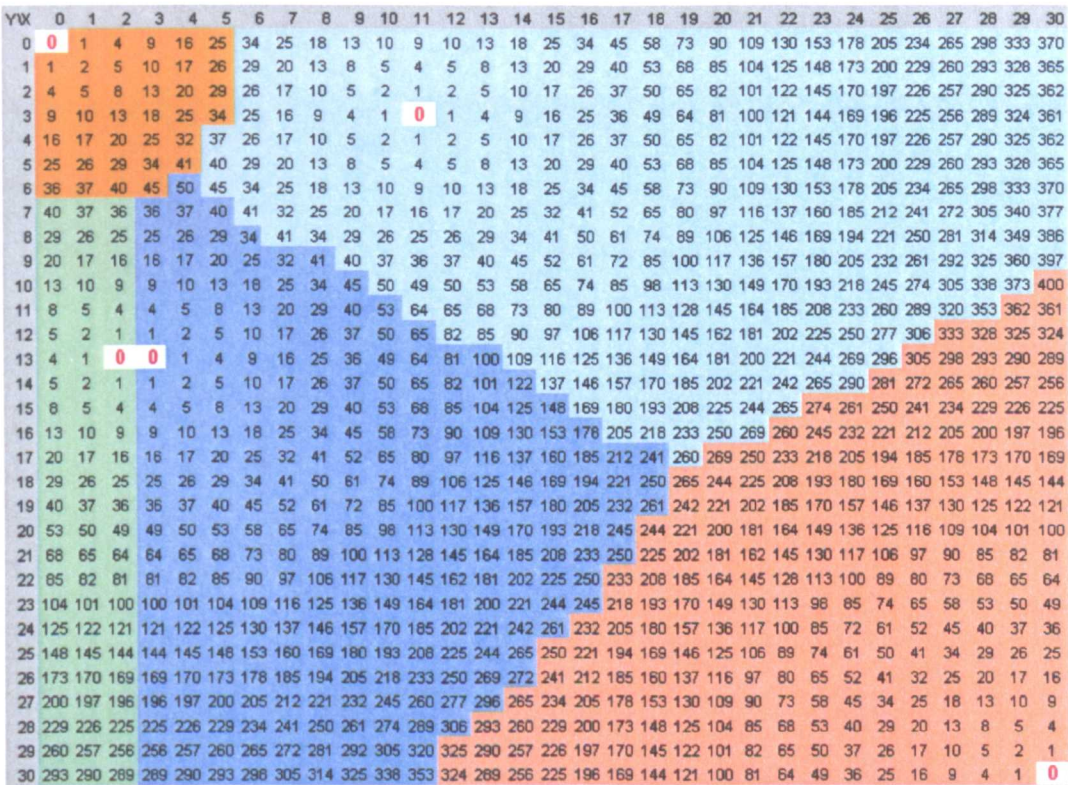


Figure 3-8: a 2D squared Euclidean distance map of an image with 5 background pixels (red zeros).

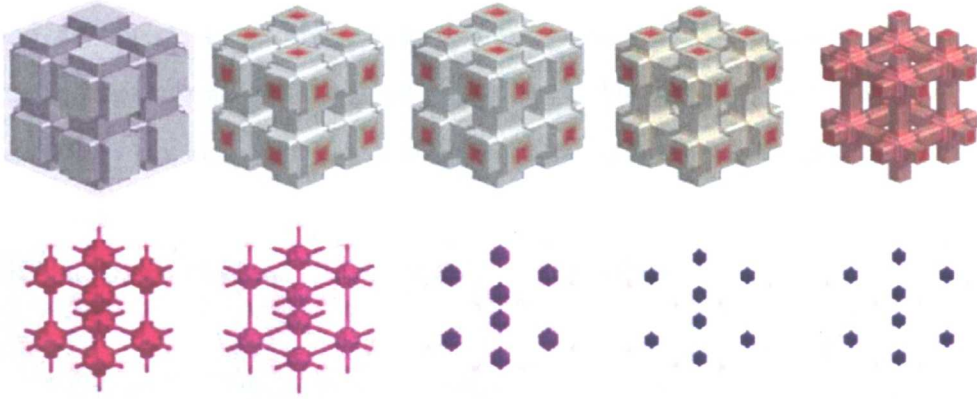


Figure 3-9: An example of a 3D SED map for the image in the top left picture. The colours indicate the SED values of object voxels to the background, and range from grey (minimum SED 1) to deep blue (maximum SED 97).

YX	0	1	2	3	4	5	6	7	8	9	10	11	12	13	14	15	16	17	18	19	20	21	22	23	24	25	26	27	28	29	30
0	0	3	6	9	12	15	18	15	12	11	10	9	10	11	12	15	18	21	24	27	30	33	36	39	42	45	48	51	54	57	60
1	3	4	7	10	13	16	17	14	11	8	7	6	7	8	11	14	17	20	23	26	29	32	35	38	41	44	47	50	53	56	59
2	6	7	8	11	14	17	16	13	10	7	4	3	4	7	10	13	16	19	22	25	28	31	34	37	40	43	46	49	52	55	58
3	9	10	11	12	15	18	15	12	9	6	3	0	3	6	9	12	15	18	21	24	27	30	33	36	39	42	45	48	51	54	57
4	12	13	14	15	16	19	16	13	10	7	4	3	4	7	10	13	16	19	22	25	28	31	34	37	40	43	46	49	52	55	58
5	15	16	17	18	19	20	17	14	11	8	7	6	7	8	11	14	17	20	23	26	29	32	35	38	41	44	47	50	53	56	59
6	18	19	20	21	22	21	18	15	12	11	10	9	10	11	12	15	18	21	24	27	30	33	36	39	42	45	48	51	54	57	60
7	20	19	18	18	19	20	19	16	15	14	13	12	13	14	15	16	19	22	25	28	31	34	37	40	43	46	49	52	55	58	61
8	17	16	15	15	16	17	18	19	18	17	16	15	16	17	18	19	20	23	26	29	32	35	38	41	44	47	50	53	56	59	62
9	14	13	12	12	13	14	15	16	19	20	19	18	19	20	21	22	23	24	27	30	33	36	39	42	45	48	51	54	57	60	63
10	11	10	9	9	10	11	12	15	18	21	22	21	22	23	24	25	26	27	28	31	34	37	40	43	46	49	52	55	58	61	60
11	8	7	6	6	7	8	11	14	17	20	23	24	25	26	27	28	29	30	31	32	35	38	41	44	47	50	53	56	59	58	57
12	7	4	3	3	4	7	10	13	16	19	22	25	28	29	30	31	32	33	34	35	36	39	42	45	48	51	54	57	56	55	54
13	6	3	0	0	3	6	9	12	15	18	21	24	27	30	33	34	35	36	37	38	39	40	43	46	49	52	55	54	53	52	51
14	7	4	3	3	4	7	10	13	16	19	22	25	28	31	34	37	38	39	40	41	42	43	44	47	50	53	52	51	50	49	48
15	8	7	6	6	7	8	11	14	17	20	23	26	29	32	35	38	41	42	43	44	45	46	47	48	51	50	49	48	47	46	45
16	11	10	9	9	10	11	12	15	18	21	24	27	30	33	36	39	42	45	46	47	48	49	50	49	48	47	46	45	44	43	42
17	14	13	12	12	13	14	15	16	19	22	25	28	31	34	37	40	43	46	49	50	49	48	47	46	45	44	43	42	41	40	39
18	17	16	15	15	16	17	18	19	20	23	26	29	32	35	38	41	44	47	48	47	46	45	44	43	42	41	40	39	38	37	36
19	20	19	18	18	19	20	21	22	23	24	27	30	33	36	39	42	45	48	47	44	43	42	41	40	39	38	37	36	35	34	33
20	23	22	21	21	22	23	24	25	26	27	28	31	34	37	40	43	46	49	46	43	40	39	38	37	36	35	34	33	32	31	30
21	26	25	24	24	25	26	27	28	29	30	31	32	35	38	41	44	47	48	45	42	39	36	35	34	33	32	31	30	29	28	27
22	29	28	27	27	28	29	30	31	32	33	34	35	36	39	42	45	48	47	44	41	38	35	32	31	30	29	28	27	26	25	24
23	32	31	30	30	31	32	33	34	35	36	37	38	39	40	43	46	49	46	43	40	37	34	31	28	27	26	25	24	23	22	21
24	35	34	33	33	34	35	36	37	38	39	40	41	42	43	44	47	48	45	42	39	36	33	30	27	24	23	22	21	20	19	18
25	38	37	36	36	37	38	39	40	41	42	43	44	45	46	47	48	47	44	41	38	35	32	29	26	23	20	19	18	17	16	15
26	41	40	39	39	40	41	42	43	44	45	46	47	48	49	50	49	46	43	40	37	34	31	28	25	22	19	16	15	14	13	12
27	44	43	42	42	43	44	45	46	47	48	49	50	51	52	51	48	45	42	39	36	33	30	27	24	21	18	15	12	11	10	9
28	47	46	45	45	46	47	48	49	50	51	52	53	54	53	50	47	44	41	38	35	32	29	26	23	20	17	14	11	8	7	6
29	50	49	48	48	49	50	51	52	53	54	55	56	55	52	49	46	43	40	37	34	31	28	25	22	19	16	13	10	7	4	3
30	53	52	51	51	52	53	54	55	56	57	58	57	54	51	48	45	42	39	36	33	30	27	24	21	18	15	12	9	6	3	0

Figure 3-10: 2D chamfer distance map with CD coefficients (3, 4) of an image with 5 background pixels (red zeros).

In Figure 3-10, the result is shown of using Algorithm 3.2, the chamfer DT, for the original image in Figure 3-8. Again, the five background voxels are coloured red and all object voxels are clustered into different classes depending on their nearest background voxels. For each pair of pixels p and q , $d_{C(3,4)}(p, q) = [Max(|p_x - q_x|, |p_y - q_y|) - Min(|p_x - q_x|, |p_y - q_y|)] \times 3 + Min(|p_x - q_x|, |p_y - q_y|) \times 4$. In pore structure analysis, 3D CD transformation with coefficients (3, 4, 5) will be used to guide the generation of the GED map, which in turn will be used to partition the PS.

3.2.5 Geodesic Distant Transformation

The geodesic distance defined in (3.6) has many applications, for example in route planning and object segmentation. In pore structure analysis it is useful to partition the PS into individual pore-bodies and pore-throats. Furthermore, the geodesic distance map can also be used to compute the length of flow paths or to find the major flow paths from inlet to outlet. The simplest implementation of the distance metric in (3.6) is the geodesic version of the city-block metric (i.e. \mathcal{L}_1 in (3.4)). Also other metrics, such as the chamfer distance, have been used but they are coarse approximations to the geodesic version of the Euclidean distance. In 1999[36], Cuisenaire gave a comprehensive review of DT algorithms, including the geodesic distance, in his PhD thesis. He concluded that the GED transformation is difficult to compute, because it requires much computer memory, exhausting floating-point arithmetic and floating-point comparisons. To simplify the transformation, he extended the methods of Piper and Granum (1987[127]) and Verwer et al. (1989[178]) for geodesic distance transformation. By generalizing the definition of the geodesic distance, Cuisenaire (1999[36]) proposed two algorithms (the bucket sorting algorithm and the circular propagation) to efficiently compute the new geodesic DT.

Cárdenes et al. (2003[31]) gave a definition of occlusion points and presented a local characterization of these points. An occlusion point p with respect to o in a constraining domain \mathcal{M} , illustrated in Figure 3-11(a), is defined as the point closest to o , for which for a given $\varepsilon > 0$, there exists no straight line included in \mathcal{M} that joins p and o , but there does exist a straight-line included in \mathcal{M} , between o and a point q such that $q \in B_\varepsilon(p)$, where $B_\varepsilon(p)$ is a ball centred at p of radius ε . In their algorithm for computation of

the geodesic Euclidean DT, occlusion points and distance information are propagated along the propagation forefront with increments of 1 after each step. Obviously, the determination of occlusion points depends on the accuracy of current floating-point distance values.

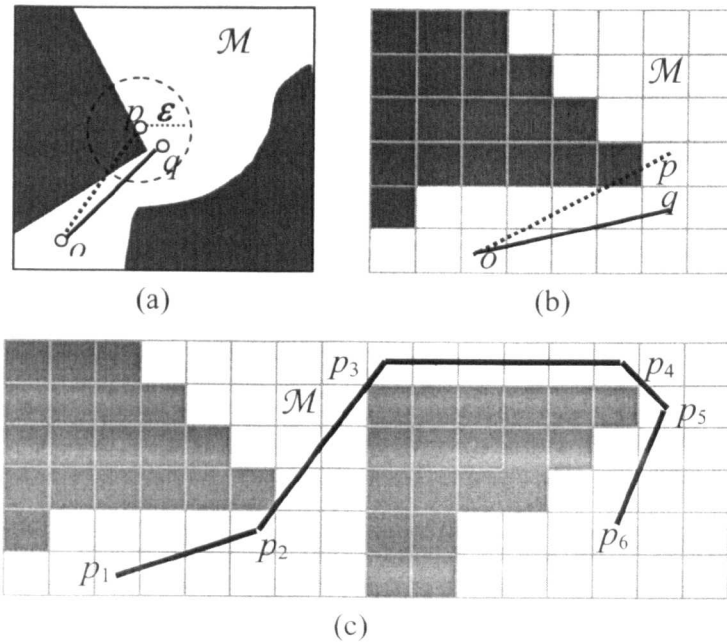


Figure 3-11: Illustration of the concept of an occlusion point p with respect to constraining domain \mathcal{M} (blank region): (a) in R^2 the dotted straight-line between o and p is partially located beyond \mathcal{M} , while the black straight-line between o and q is completely located within \mathcal{M} , in which $q \in B_\varepsilon(p) = \{r: d_E(r, p) \leq \varepsilon\}$ for sufficiently small $\varepsilon > 0$ ($d_E(r, p)$ is the Euclidean distance between r and p); (b) in Z^2 the dotted straight-line between o and p is partially located beyond the constraining domain \mathcal{M} (white grids) and the black straight-line between o and q is located in \mathcal{M} , in which $q \in \mathcal{N}_8(p)$; (c) a shortest path of straight-lines included in \mathcal{M} from p_1 to p_6 .

Among the various difficulties associated with the GED transformation, two issues have not yet been completely resolved. They are: (i) correctly and quickly finding the position of occlusion points and (ii) avoiding floating-point arithmetic.

Generally, the existing GED transformations are prohibited for large size 3D images (e.g. volume of more than 500^3 voxels), due to their huge memory- and computing time- requirements. Although I have not found any practical methods to

tackle the above two issues, a robust GED algorithm to tackle these issues should at least have the following properties:

- (a) The determination of occlusion points in discrete space should depend on the discrete visibility of the digital straight-line (Coeurjolly et al., 2004[34]);
- (b) The length of each segment, connecting two occlusion points, along a path should be integer-valued (e.g. the SED) rather than floating-point valued (e.g. the ED).

Bearing these two properties in mind, instead of directly computing the GED map, I develop an algorithm to obtain an approximation of the GED map. For two Euclidean paths $\{p_1, p_2 \dots p_m, o\}$ and $\{q_1, q_2 \dots q_n, o\}$, each straight segment in these two paths is located within the constraining domain. For these paths, the ordering of their Euclidean lengths is determined by the ordering of their chamfer lengths. In other words, we state that

$$\sum_{i=1}^{m-1} d_E(p_i, p_{i+1}) + d_E(p_m, o) \leq \sum_{i=1}^{n-1} d_E(q_i, q_{i+1}) + d_E(q_n, o) ,$$

if and only if

$$\sum_{i=1}^{m-1} d_{c(3,4,5)}(p_i, p_{i+1}) + d_{c(3,4,5)}(p_m, o) \leq \sum_{i=1}^{n-1} d_{c(3,4,5)}(q_i, q_{i+1}) + d_{c(3,4,5)}(q_n, o) .$$

The triple (3, 4, 5) of chamfer distance coefficients is often used because it leads to a local maximum Euclidean distance limit without topological errors (Marchand-Mailler and Sharaiha, 1999[101]) and it also minimizes the upper bound on the difference between the chamfer and the Euclidean distances (Borgefors, 1996[25]). Using the above rule, the floating-point comparison between two Euclidean values is avoided, but it comes at the expense of losing guaranteed accuracy for the Euclidean distances beyond this so-called local maximum Euclidean distance limit.

Algorithm 3.3: Geodesic chamfer distance transformation

Input: a 3D binary image $\mathcal{P} (\mathcal{V}, \mathcal{B}, \mathcal{M})$: \mathcal{B} is the foreground of \mathcal{V} , \mathcal{M} is a constraining domain with $\mathcal{B} \subset \mathcal{M} \subset \mathcal{V}$, $\mathcal{V} \setminus \mathcal{M}$ is the obstructing domain for which no distance can be obtained (-1 is commonly assigned in the distance map).

Output: chamfer distance map CDM , squared Euclidean distance map i.e. $SEDM$

Initialise: CDM and $SEDM$ are initialised as -1 for all voxels.

//List $TFront$ is used to track current propagation front

//List $CurobL$ is used to record obstructing voxels in a neighbourhood for

//determination of occlusion points.

//List $TNext$ is used to track next propagation front

For each $p \in \mathcal{B}$ {

$CDM(p) = 0$ and $SEDM(p) = 0$

For each $q \in \mathcal{N}(p)$ {

If $q \in \mathcal{M}$ and $CDM(q) = -1$ then put q into list $TFront$

// Use $CDM(q) = -1$ to ensure no replicated element exists in $TFront$

$CDM(q) = \infty$ and $SEDM(q) = \infty$

}

}

while $TFront$ is not empty {

while $TFront$ is not empty {

Take a voxel p from $TFront$ and $t = p$;

For each $q \in \mathcal{N}(p)$ {

If $q \in \mathcal{V} \setminus \mathcal{M}$ then put q into list of $CurobL$;

IF ($CDM(Q) = -1$) {

put q into list of $TNext$;

$CDM(q) = \infty$ and $SEDM(q) = \infty$ }

if $d_{(3,4,5)}(p, q) + CDM(q) < CDM(p)$ {

$CDM(p) = d_{(3,4,5)}(p, q) + CDM(q)$

$t = q$ }

// the end of For each $q \in \mathcal{N}(p)$

$SEDM(t) = d_{SE}(p, t)$ and $LimitVal = 25 \times SEDM(t)$

$a_1 = p_x - t_x, b_1 = p_y - t_y, c_1 = p_z - t_z$

For each s in $CurobL$ { //determining new occlusion points

$a_2 = p_x - s_x, b_2 = p_y - s_y, c_2 = p_z - s_z$

if $a_1 \times a_2 + b_1 \times b_2 + c_1 \times c_2 \geq 0$ then {

$a_0 = b_2 \times c_1 - c_2 \times b_1, b_0 = c_2 \times a_1 - a_2 \times c_1,$

$c_0 = a_2 \times b_1 - c_2 \times a_1, Dist = 100 \times [(a_0)^2 + (b_0)^2 + (c_0)^2]$

if $Dist < LimitVal$ then { // p is a new occlusion point,

let r is the 26-neighbour of p

such that r becomes the new predecessor of p in a path

$a_1 = p_x - r_x, b_1 = p_y - r_y, c_1 = p_z - r_z$

$SEDM(t) = (a_1)^2 + (b_1)^2 + (c_1)^2$ }

// the end of "if $a_1 \times a_2 + b_1 \times b_2 + c_1 \times c_2 \geq 0$ "

```
    } // the end of "For each s in CurobL"  
    Empty CurobL  
    } // the end of TFront is not empty  
    TFront = TNext and Empty TNext  
}
```

To illustrate Algorithm 3.3, the 2D binary image of Figure 3-10 is used, in which an obstructing domain is introduced, represented by the "wall" shown in Figure 3-12. The chamfer distances of the five foreground voxels are assigned as 0, the 2D CDC (3, 4) are used in this example. To all voxels in the constraining domain chamfer distances are assigned, as well as their corresponding closest object voxels, which are coded by different colours. Assisted by the chamfer distance value, a good approximation of the GED can be computed, which follows from comparison of chamfer distances, shown in Figure 3-13. In 3D, using the GED is very time-consuming because floating-point calculations are involved. Therefore in the partition of the PS, I will instead use the geodesic chamfer distance transformation unless higher accuracy is required.

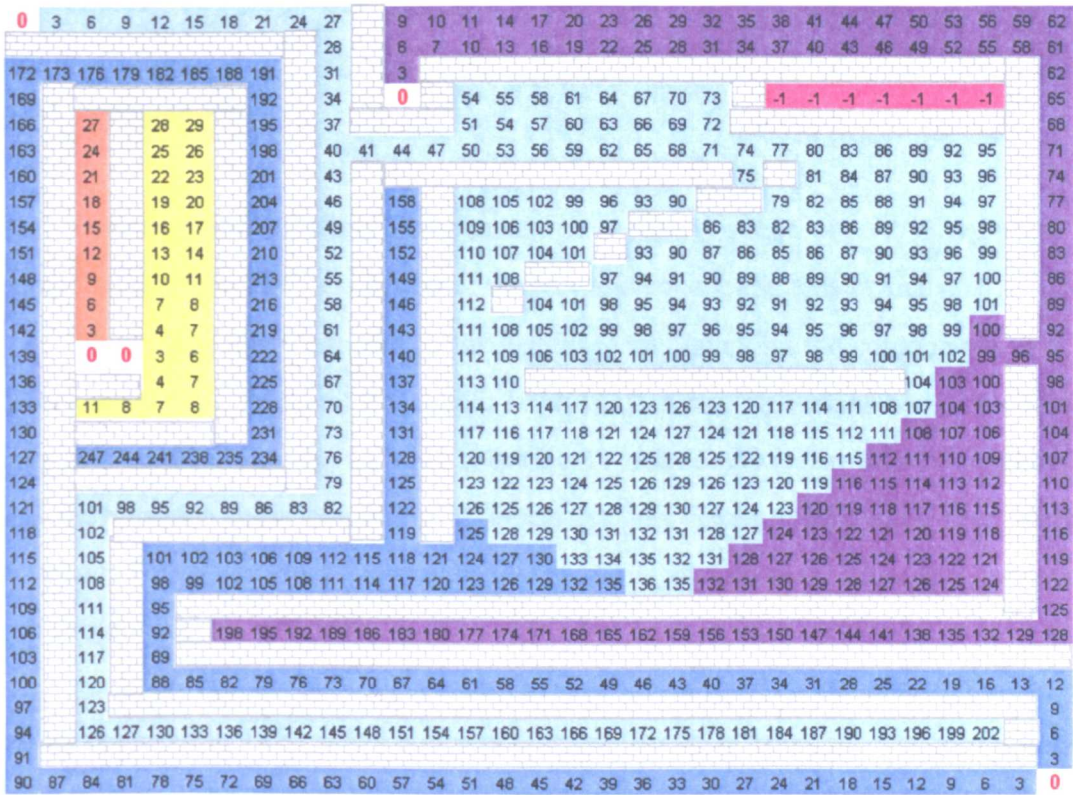


Figure 3-12: Geodesic chamfer distance map with CDC of (3, 4).

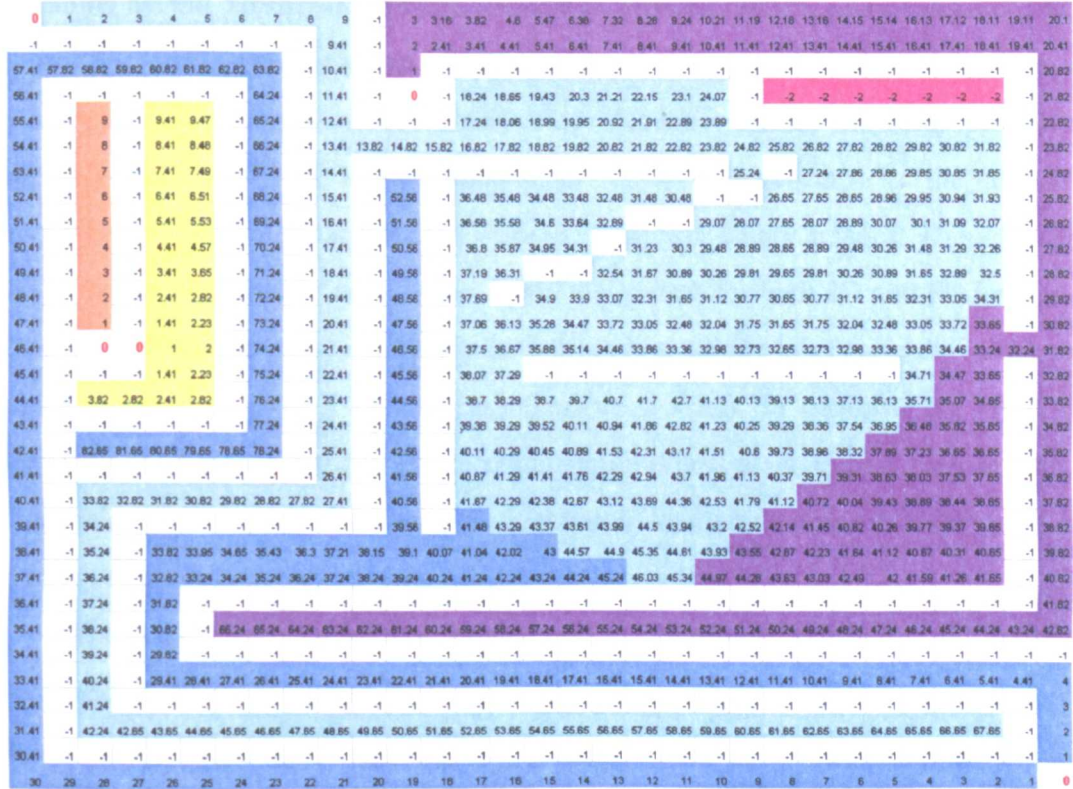


Figure 3-13: Geodesic Euclidean distance map generated with the assistance of chamfer DT with CDC (3, 4).

3.3 Component Labelling Algorithm

3.3.1 Previous Work

Counting and labelling components in a binary image are very important for computation of the EPC, extraction of the MA and conducting cluster analysis.

There exist many algorithms for searching and labelling the components in a 3D binary image (e.g. Park and Rosenfeld, 1971[123]). Many algorithms work by scanning only half neighbourhoods (i.e. only checking 13 neighbours rather than 26-neighbours) and they need a table consisting of labels for the voxels which have been already accessed. This table is used to manage the conflicts when a point belongs to more than one component.

An important breakthrough in the analysis of cluster size statistics in percolation theory occurred in 1976, when a cluster multiple labelling technique was introduced by Hoshen and Kopelman (1976[59] or <http://www.cs.utk.edu/~berry/parhk/node6.html>) for both 2D and 3D crystal structures. This algorithm is known in the statistical physics literature as the Hoshen-Kopelman algorithm (HKA), which revolutionized spatial cluster analysis in percolation theory. Only after the introduction of this algorithm did Monte-Carlo simulations of very large lattices become possible. In image processing, probably the most well known component labelling algorithms is the algorithm introduced by Rosenfeld and Pfalz (1966[138]) for 2D binary images. This algorithm led to the development of many other useful algorithms for both 2D and 3D images. In general, the target of these algorithms is to provide a unique label for each component, which is obtained after a second pass (backward scan). In contrast, the HKA can determine the number and the size of components in just a single pass (forward scan). The HKA's single and sequential pass through the lattice linearises the time and memory space requirement as a function of the lattice size.

The classic HKA on lattices focuses on the determination of sizes and the labels of individual clusters in a single pass (one-way scanning), with little attempt to improve the efficiency based on the specific use of different adjacencies. Usually three kinds of adjacencies (6-, 18- and 26-adjacencies) are used in Z^3 , which may lead to small ranges of accessed voxels when different data structures are utilized. For that reason, I extend

the HKA into 3D with the consideration of dealing with diverse adjacencies and efficiently counting of the components.

The main idea of this extension of the HKA can be simply described as follows. Consider a 3D binary image $\mathcal{P}(\mathcal{V}, \mathcal{B})$, where \mathcal{B} is the set of object voxels with α -adjacency. To label and count α -components in \mathcal{P} , each object voxel p is scanned in a certain order (e.g. Figure 3-14(b)) to find out the set $N_L(p)$ that consists of m α -adjacent voxels of p that have already been labelled, denoted as

$$N_L(p) = \{q_1, q_2 \dots q_m\}, \quad (3.19)$$

and the corresponding labels (i.e. positive integers) are represented by

$$L(q_1), L(q_2) \dots L(q_m). \quad (3.20)$$

Then p gets a new label if $N_L(p)$ is empty, otherwise p gets the minimum label in $N_L(p)$ i.e.

$$MinL = Min\{L(q_1), L(q_2) \dots L(q_s)\} \quad (3.21)$$

Meanwhile, the value of $-MinL$ is assigned to all elements of array Lld with entries $L(q_i)$ for $i = 1, 2 \dots m$, to represent that the current label $L(q_i)$ is a temporary label. Their proper labels ($MinL$) will only appear as the final labels. Note that the elements of the array Lld are either positive or negative, where the array indices denote the α -component labels.

Following the one-pass scan, a α -component in the image may have more than one distinct label, such as $\{L_1, L_2 \dots L_s\}$. The minimum of these labels, ML , is defined as the proper cluster label for which $Lld(ML) > 0$. For each other label L_j in $\{L_1, L_2 \dots L_s\}$ where $L_j \neq ML$, $Lld(L_j) < 0$, there exists a label $L_i \in \{L_1, L_2 \dots L_s\}$ such that $i = -Lld(L_j)$ ($i \neq j$). In Figure 3-15, for example, let us consider the 8-component identified by the set of labels $\{3, 4, 5\}$, for which the corresponding the array Lld is found as $\{Lld(3), Lld(4), Lld(5)\} = \{14, -3, -3\}$.

$Lld(3)$ denotes the component size and the labels of pixel 4 and 5 will be changed to $-Lld(4)$ and $-Lld(5)$ (see Figure 3-16). Therefore, the relationship among component labels can be represented by a tree graph. The root of the tree corresponds to the proper label. All other labels are nodes on the tree, which are connected directly or indirectly to

the root. After this brief introduction to the classic HKA, our extension of the HKA is outlined as follows.

3.3.2 Extended Hoshen-Kopelman Algorithm

Input: an image $\mathcal{A}(\mathcal{V}, \mathcal{B})$: \mathcal{B} is the set of object (foreground) voxels and $\mathcal{V} \setminus \mathcal{B}$ is the set of background voxels, α -adjacency is applied for object voxels.

Output:

- (1) Labelled image $LImg$, in which different α -components have different labels,
- (2) Number of α -components,
- (3) Size of each α -component.

Initialise:

$LImg$ is initialised as 0 for all voxels in \mathcal{V} ;

Array LId records the relationship between different component labels, LId is initialised as 0 for all entries;

Current available label $CurLbl$ is initialised as 0 (i.e. starting from 1);

Note that the number of α -components in the image is equal to the number of elements in Array LId with positive values (the size of the corresponding components) in the end of this algorithm. For example, in Table 3-1, the final result of LId is $\{1, 4, 14, -3, -3, 6, -6\}$. The number of elements with positive values in LId is 4, thus we know there are 4 8-components in the image shown in Figure 3-14(a).

```

//Scan the whole image in any order
For each  $p \in \mathcal{B}$  { //to find all labelled voxels
  For each  $q \in \mathcal{N}_8(p) \cap \mathcal{N}_8(p)$  {
    If  $LImg(q)$  is positive then { //labelled object voxels
      Put  $LImg(q)$  into the list  $NgLbl$ ; }
    //Record the label of  $q$  into temporary list  $NgLbl$ 
  }
  If  $NgLbl$  is empty then { //Newly found cluster
     $LId(++CurLbl) = 1$  //New labels  $CurLbl$ 
     $LImg(p) = CurLbl$  //Label current object voxel
  } else {
     $MinLbl = \infty$  //To find the minimum label in the list of  $NgLbl$ 
    While  $NgLbl$  is not empty {
      //The voxels, which are  $\alpha$ -adjacent to  $p$ ,

```

```

// have already been labelled prior to p.
//Get a label (lbl) from list NgLbl;
Newlbl = lbl and lbl = -Lld(lbl)
While ( lbl > 0 ) { //find its proper label
Newlbl = lbl and Lbl = -Lld(lbl) }
If Newlbl < MinLbl then {MinLbl = Newlbl; }
    //to find the minimum label
Put Newlbl into the list ProLbl;
} // the end for NgLbl is not empty
Sum = 0 //Accumulate the size of clusters
For each lbl ∈ ProLbl {
    If Lld(lbl) > 0 then Sum += Lld(lbl)
    Lld[lbl] = -MinLbl
}
Lld[MinLbl] = Sum //Current valid label
LImg(p) = MinLbl
Empty the list ProLbl;
} //end of "NgLbl is empty"
Empty lists of NgLbl;
} // end of "For each p ∈ B"
NumCom = #{i : Lld[i] > 0} //the number of entries of Lld with positive values
// Ouput sequence number for components if required
For each p ∈ B { //scanning all object voxels
    //Get a label (lbl) from list NgLbl;
    Lbl = LImg(p), Newlbl = lbl, lbl = -Lld(lbl)
    While lbl > 0 { //find its proper label
        Newlbl = lbl, Lbl = -Lld(lbl) }
    LImg(p) = Newlbl
}

```

3.3.3 Explanation of the Extended HKA with examples

Figure 3-14(a) shows a 2D binary image of dimensions 10×10 pixels, black pixels are foreground and white are background. To label and count all 8- and 4-components, the extended HKA is applied by scanning the image in a sequential order indicated in Figure 3-14(b). For simplicity, I use positive integers as labels (starting from 1). The data structure *Lld* is defined as a one-dimensional array with its entries representing the current labels, initialised as 0 for all entries, i.e. $Lld(m) = 0$, for labels $m = 1, 2, \dots$. This structure is used to record currently available labels and the relationship between all

already labelled pixels. The first block of Table 3-1 shows consecutive updates of Lld during the scanning process to label 8-components.

At the start, the pixel with scanning sequence number 1 in Figure 3-14(b) is accessed and all pixels in its direct neighbourhood are checked. Then, the first label (i.e. 1) is used and any others remain unchanged, i.e. $Lld(1) = 1$, but $Lld(m) = 0$ for $m > 1$, which is illustrated in the first row of Table 3-1. When pixel 2 is accessed, the new label 2 is used (see the second row in Table 3-1). However, when pixel 3 is scanned, no new label is needed, because pixels 2 and 3 are 8-adjacent and they must have the same final label. Instead, $Lld(2)$ is increased by 1 representing that one more pixel is found with label 2.

A complication occurs when pixel 12 in Figure 3-14(b) is accessed. In its neighbourhood, there exist pixels with labels 4 and 3. At this stage, we find the minimal label $MinLbl(3)$, which is then used as the label of pixel 12, while $Lld(MinLbl) = Lld(MinLbl) + Lld(4) + 1$ and $Lld(4) = -MinLbl$. $Lld(4) = -3$ means that label 4 is no longer a valid label and its pixels are absorbed in the 8-component with label 3.

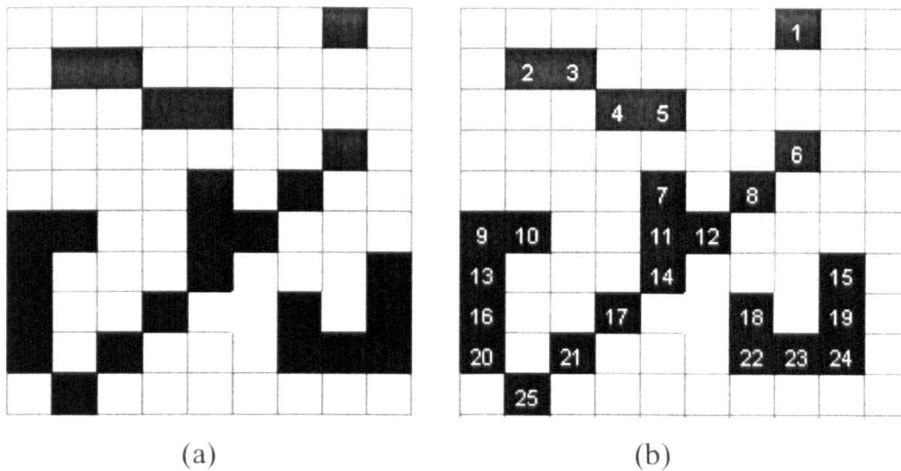


Figure 3-14: 2D illustration for 8- and 4-component labelling: (a) original binary image; (b) forward scanning sequence order for object voxels (black).

Following the one-way scan, the initial labels are shown in Figure 3-15. Seven different labels (i.e. 1, 2 ... 7) have been used, but not all labels are valid. In the last row of the left block of Table 3-1, the states of seven labels are listed. When $Lld(m) > 0$, m is a valid label, otherwise it points to its corresponding valid label. Thus labels 1, 2, 3, 6 are valid and 4, 5, 7 are temporary labels which point to label 3 ($Lld(4) = Lld(5) = -3$) or label 6 ($Lld(7) = -6$). In other words, for the original binary image shown in Figure

3-14(a), there are only four 8-components and the sizes (number of voxels in a component) of the four 8-components are 1, 4, 14 and 6, respectively.

Based on the *Lld* array, I adjust the labels to create a strictly sequential list which is convenient for some applications, as shown in Figure 3-15(a). Labelling of 4-component is demonstrated in the right block of Table 3-1 and Figure 3-15(b). For 3D image, a labelling example is given in Figure 3-17.

	1	2	3	4	5	6	7	8	9		1	2	3	4	5	6	7	8	9	10	11	12	
1	1	0	0	0	0	0	0	0	0	1	1	0	0	0	0	0	0	0	0	0	0	0	0
2	1	1	0	0	0	0	0	0	0	2	1	1	0	0	0	0	0	0	0	0	0	0	0
3	1	2	0	0	0	0	0	0	0	3	1	2	0	0	0	0	0	0	0	0	0	0	0
4	1	3	0	0	0	0	0	0	0	4	1	2	1	0	0	0	0	0	0	0	0	0	0
5	1	4	0	0	0	0	0	0	0	5	1	2	2	0	0	0	0	0	0	0	0	0	0
6	1	4	1	0	0	0	0	0	0	6	1	2	2	1	0	0	0	0	0	0	0	0	0
7	1	4	1	1	0	0	0	0	0	7	1	2	2	1	1	0	0	0	0	0	0	0	0
8	1	4	2	1	0	0	0	0	0	8	1	2	2	1	1	1	0	0	0	0	0	0	0
9	1	4	2	1	1	0	0	0	0	9	1	2	2	1	1	1	1	0	0	0	0	0	0
10	1	4	2	1	2	0	0	0	0	10	1	2	2	1	1	1	2	0	0	0	0	0	0
11	1	4	2	2	2	0	0	0	0	11	1	2	2	1	2	1	2	0	0	0	0	0	0
12	1	4	5	-3	2	0	0	0	0	12	1	2	2	1	3	1	2	0	0	0	0	0	0
13	1	4	5	-3	3	0	0	0	0	13	1	2	2	1	3	1	3	0	0	0	0	0	0
14	1	4	6	-3	3	0	0	0	0	14	1	2	2	1	4	1	3	0	0	0	0	0	0
15	1	4	6	-3	3	1	0	0	0	15	1	2	2	1	4	1	3	1	0	0	0	0	0
16	1	4	6	-3	4	1	0	0	0	16	1	2	2	1	4	1	4	1	0	0	0	0	0
17	1	4	7	-3	4	1	0	0	0	17	1	2	2	1	4	1	4	1	1	0	0	0	0
18	1	4	7	-3	4	1	1	0	0	18	1	2	2	1	4	1	4	1	1	1	0	0	0
19	1	4	7	-3	4	2	1	0	0	19	1	2	2	1	4	1	4	2	1	1	0	0	0
20	1	4	7	-3	5	2	1	0	0	20	1	2	2	1	4	1	5	2	1	1	0	0	0
21	1	4	8	-3	5	2	1	0	0	21	1	2	2	1	4	1	5	2	1	1	1	0	0
22	1	4	8	-3	5	2	2	0	0	22	1	2	2	1	4	1	5	2	1	2	1	0	0
23	1	4	8	-3	5	5	-6	0	0	23	1	2	2	1	4	1	5	2	1	3	1	0	0
24	1	4	8	-3	5	6	-6	0	0	24	1	2	2	1	4	1	5	6	1	-8	1	0	0
25	1	4	14	-3	-3	6	-6	0	0	25	1	2	2	1	4	1	5	6	1	-8	1	1	0

Table 3-1: Array *Lld* for labelling 8-components (left) and 4-components (right) of object pixels: The column numbers represent the entries of array *Lld*, i.e. labels, and the row numbers represent the scan order (see Figure 3-14(b)).

		8-adjacency		8-components				4-adjacency		4-components	
Y\X		0	1	2	3	4	5	6	7	8	9
0		0	0	0	0	0	0	0	1	0	0
1		0	2	2	0	0	0	0	0	0	0
2		0	0	0	2	2	0	0	0	0	0
3		0	0	0	0	0	0	0	3	0	0
4		0	0	0	0	4	0	3	0	0	0
5		5	5	0	0	4	3	0	0	0	0
6		5	0	0	0	3	0	0	0	6	0
7		5	0	0	3	0	0	7	0	6	0
8		5	0	3	0	0	0	7	6	6	0
9		0	3	0	0	0	0	0	0	0	0

		4-adjacency		4-components				4-adjacency		4-components	
Y\X		0	1	2	3	4	5	6	7	8	9
0		0	0	0	0	0	0	0	1	0	0
1		0	2	2	0	0	0	0	0	0	0
2		0	0	0	3	3	0	0	0	0	0
3		0	0	0	0	0	0	0	4	0	0
4		0	0	0	0	5	0	6	0	0	0
5		7	7	0	0	5	5	0	0	0	0
6		7	0	0	0	5	0	0	0	8	0
7		7	0	0	9	0	0	10	0	8	0
8		7	0	11	0	0	0	10	10	8	0
9		0	12	0	0	0	0	0	0	0	0

Figure 3-15: Initial labels for labelling 8-components and 4-component after one-way scan (i.e. finishing accessing all the 25 object voxels shown in Figure 3-14(b)).

		8-adjacency		8-components				4-adjacency		4-components	
Y\X		0	1	2	3	4	5	6	7	8	9
0		0	0	0	0	0	0	1	0	0	0
1		0	2	2	0	0	0	0	0	0	0
2		0	0	0	2	2	0	0	0	0	0
3		0	0	0	0	0	0	3	0	0	0
4		0	0	0	0	3	0	3	0	0	0
5		3	3	0	0	3	3	0	0	0	0
6		3	0	0	0	3	0	0	0	4	0
7		3	0	0	3	0	0	4	0	4	0
8		3	0	3	0	0	0	4	4	4	0
9		0	3	0	0	0	0	0	0	0	0

		4-adjacency		4-components				4-adjacency		4-components	
Y\X		0	1	2	3	4	5	6	7	8	9
0		0	0	0	0	0	0	0	1	0	0
1		0	2	2	0	0	0	0	0	0	0
2		0	0	0	3	3	0	0	0	0	0
3		0	0	0	0	0	0	0	4	0	0
4		0	0	0	0	5	0	6	0	0	0
5		7	7	0	0	5	5	0	0	0	0
6		7	0	0	0	5	0	0	0	8	0
7		7	0	0	9	0	0	8	0	8	0
8		7	0	10	0	0	0	8	8	8	0
9		0	11	0	0	0	0	0	0	0	0

Figure 3-16: Final cluster image with sequential labels for 8-components and 4-components of object voxels.

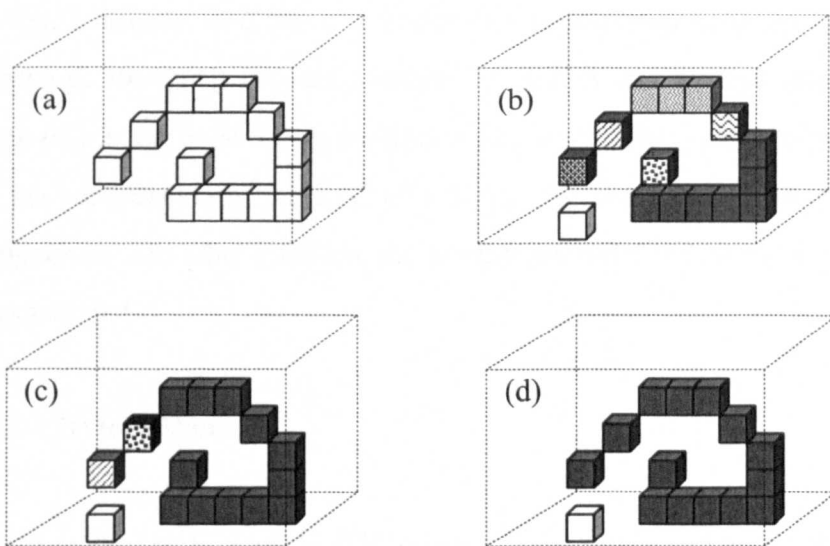


Figure 3-17: Labelling of 3D object components using different patterns (background is transparent): (a) original image; (b) seven 6-components; (c) four 18-components; (d) two 26-components.

3.4 Euler-Poincaré Characteristic

Digital topology is the study of the topological properties of objects in digital images. It provides an important mathematical basis for image processing applications such as image thinning (skeletonisation), border tracing and object counting. Among the topological descriptors, the Euler-Poincaré characteristic (EPC or the Euler number) has been proven to be an important quantity in image analysis which can be extended to form other descriptors (e.g. the connectivity function of Vogel and Roth, 2001[185]). The EPC describes the connectivity properties of the components of a composite material. It is used in such disparate applied areas as medicine, to characterise cancellous bone (Boyce et al. 1995[28]), statistical physics, to describe morphological properties of fluids (Ohser et al., 2002[114]), and material sciences, to analyse foams and other porous media (Levitz, 2007[83]). Estimation or computation of the EPC also plays an important role in the approximation of other intrinsic properties, like surface area, volume or curvature integrals (see Schneider and Weil, 1993[148]). Apart from obtaining an accurate result, fast computation of the EPC from a 3D image is also indispensable in pore structure analysis based on large amounts of 3D data.

In the previous chapter, I reviewed the relevant techniques to compute the EPC and some basic applications in digital topology and pore structure analysis. In this section, I describe and prove a finding - a relationship between topological numbers (Bertrand, 1994[14]) and the numbers of tunnels and cavities (Kong and Rosenfeld, 1989[76]) in the $3 \times 3 \times 3$ neighbourhood of a point. Then a new algorithm is presented for the computation of the EPC of a 3D binary image, based on this relationship. By comparison with other methods, the advantages and disadvantages of the algorithm are demonstrated.

3.4.1 Previous Work

Let $\mathcal{P} = (\mathcal{V}, 26, 6, \mathcal{B})$ be a 3D binary digital image and let $p \in \mathcal{B}$ be a black (object) point in \mathcal{V} . Following Saha and Chaudhuri (1995[139]) and Kong and Rosenfeld (1989[76]), I introduce the following definitions.

Definition 3.4 (Euler-Poincaré Characteristic, EPC): The EPC $\chi(\mathcal{P})$ of the image \mathcal{P} is equal to the number of black connected components minus the number of tunnels plus the number of cavities in \mathcal{P} .

As stated by Kong and Rosenfeld (1989[76]), this definition is only the specific 3D case of the n -dimensional EPC. In line with the review of the computation of the EPC in Section 2.2.1, the numbers of black (object) components, tunnels and cavities correspond to the 1st, 2nd and 3rd Betti numbers, (2.11), respectively. Consequently, for a 3D binary image \mathcal{P} , its EPC $\chi(\mathcal{P})$ is represented as

$$\chi(\mathcal{P}) = h_0(\mathcal{P}) - h_1(\mathcal{P}) + h_2(\mathcal{P}). \quad (3.22)$$

Note that the black components are 26-components defined in Definition 3.3. An example of 26-component is given in Figure 3-2(c). A cavity of \mathcal{P} is a white 6-component of \mathcal{P} that is completely surrounded by a 26-component of \mathcal{P} . Both can be easily identified and their numbers can be counted by applying the extended HKA.

The notion of a tunnel (hole, genus), which is closely related to the concept of handles, is not easy to define. Kong and Rosenfeld (1989[76]) gave a definition of a tunnel based on digital geometry, but this cannot be directly used to determine whether a white component in a digital image is a tunnel or not. Recently, based on convex deficiencies, Arcelli et al. (2005[8]) proposed a much more concrete definition for tunnels. For the computation of the EPC we are only interested in counting the number of tunnels in the whole range of a 3D image, or at least in a $3 \times 3 \times 3$ neighbourhood of a voxel. Thus neglecting the precise location of the tunnels, we concentrate on how to efficiently count the number of tunnels in a 3D binary image or in the direct neighbourhood of a voxel. The continuous transformation, proposed by Aktouf et al. (2002[1]), to determine the existence of a tunnel in an object, is crucial for the proof of the theorem that underpins the development of my algorithm.

Given two closed α -paths π and γ (see Section 3.1), with $\pi = \{p_1, p_2 \dots p_i, q_1, q_2 \dots q_m, p_{i+1} \dots p_k\} \equiv \pi_1 \bullet \pi' \bullet \pi_2$ and $\gamma = \{p_1, p_2 \dots p_i, r_1, r_2 \dots r_n, p_{i+1} \dots p_k\} \equiv \pi_1 \bullet \gamma' \bullet \pi_2$ ($m, n, k \geq 1$), π is said to be an elementary α -deformation of γ , denoted by $\pi \sim \gamma$, if both π' and γ' are included in the same unit square for the adjacency (6, 26) or in the same unit

cube for any other adjacencies (26,6), (18,6) or (6,18) which is demonstrated in Figure 3-18.

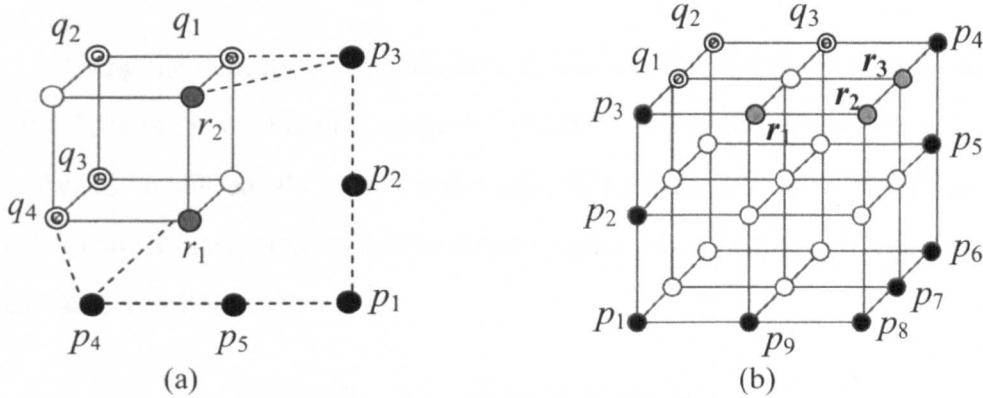


Figure 3-18: Illustration of a 26-transformation for adjacency pair (26, 6): (a) the closed 26-path $\gamma = \{p_1, p_2, p_3, r_2, r_1, p_4, p_5, p_1\}$ is an elementary 26-transformation of $\pi = \{p_1, p_2, p_3, q_1, q_2, q_3, q_4, p_4, p_5, p_1\}$, because $\gamma' = \{r_1, r_2\}$ and $\pi' = \{q_1, q_2, q_3, q_4\}$ are included in the same unit cube; (b) the closed 26-path $\gamma = \{p_1, p_2, p_3, r_1, r_2, r_3, p_4, p_5, p_6, p_7, p_8, p_9, p_1\}$ is not an elementary 26-transformation of $\pi = \{p_1, p_2, p_3, q_1, q_2, q_3, p_4, p_5, p_6, p_7, p_8, p_9, p_1\}$ because $\gamma' = \{r_1, r_2, r_3\}$ and $\pi' = \{q_1, q_2, q_3\}$ are not included in the same unit cube.



Figure 3-19: Illustration of Definition 3.5: (a) two closed α -paths within a double torus of two tunnels: π is shrinkable and γ is unshrinkable; (b) the black 18-path cannot be shrunk to a single black voxel, because the central voxel is white, thus revealing a tunnel.

Moreover, π' is defined as an α -deformation of π , denoted by $\pi \approx \pi'$, if there is a sequence of closed α -paths $\pi_0, \pi_1 \dots \pi_k$ such that $\pi = \pi_0, \pi' = \pi_k$ and $\pi_{i-1} \sim \pi_i$ for $i = 1, 2 \dots k$. Alternatively, π' is called homotopic to π with respect to α -deformation, or π can be α -transformed to π' .

Definition 3.5 (α -shrinkable): A closed α -path π is α -shrinkable (shrinkable for short) if π can be α -transformed to a single point, otherwise π is called unshrinkable or a handle (See Figure 2-18).

Using the concept of shrinkability, it follows from the discussion by Kong et al. (1992[75]) that if a 3D digital image $\mathcal{P} = (\mathcal{V}, 26, 6, \mathcal{B})$ contains no hollow torus, then the number of tunnels equals to the number of solid handles (related to unshrinkable paths). Considering a black voxel p and its direct neighbourhood $\mathcal{N}(p)$, two sub-images can be generated as follows.

$$\check{\mathcal{N}}(p) = (\mathcal{N}(p), 26, 6, \mathcal{N}(p) \cap \mathcal{B} \setminus \{p\}) \quad (3.23)$$

$$\hat{\mathcal{N}}(p) = (\mathcal{N}(p), 26, 6, \mathcal{N}(p) \cap \mathcal{B}) \quad (3.24)$$

Thus, $\check{\mathcal{N}}(p)$ and $\hat{\mathcal{N}}(p)$ are two 3D binary images with the same image space $\mathcal{N}(p)$. Moreover, p is always white (background) in $\check{\mathcal{N}}(p)$ while p is always black (foreground) in $\hat{\mathcal{N}}(p)$. For any other voxel of $\mathcal{N}(p)$, its colour in $\check{\mathcal{N}}(p)$ or $\hat{\mathcal{N}}(p)$ is the same as that of the corresponding voxel in \mathcal{P} . According to Kong and Rosenfeld (1989[76]), we have

Property 3.1: Let $\mathcal{P} = (\mathcal{V}, 26, 6, \mathcal{B})$ be a 3D binary image and let $p \in \mathcal{B}$ be a black voxel in \mathcal{P} . Then the EPC of $(\mathcal{V}, 26, 6, \mathcal{B})$ is equal to the EPC of $(\mathcal{V}, 26, 6, \mathcal{B} \setminus \{p\})$ plus the change in the EPC in $\mathcal{N}(p)$ due to the deletion of p .

Hence, the computation of the EPC of \mathcal{P} can be calculated using the following recursive relation (Kong and Rosenfeld, 1989[76]).

$$\chi(\mathcal{V}, 26, 6, \mathcal{B}) = 0 \text{ if } \mathcal{B} = \emptyset;$$

for any point $p \in \mathcal{B}$,

$$\chi(\mathcal{V}, 26, 6, \mathcal{B}) = \chi(\mathcal{V}, 26, 6, \mathcal{B} \setminus \{p\}) + \chi(\hat{\mathcal{N}}(p)) - \chi(\check{\mathcal{N}}(p)). \quad (3.25)$$

In (3.25) $\chi(\hat{\mathcal{N}}(p)) - \chi(\check{\mathcal{N}}(p))$ represents the change of the EPC in the $3 \times 3 \times 3$ neighbourhood of a black point p due to its deletion of p .

To compute $\chi(\hat{\mathcal{N}}(p))$, we use the following observations (Saha and Chaudhri (1995[139])):

$\hat{\mathcal{N}}(p)$ contains exactly one black component;

$\mathcal{N}(p)$ contains no cavities;

$\mathcal{N}(p)$ contains no tunnels.

In the sub-image $\mathcal{N}(p)$, p is 26-adjacent to any other black voxels in $\mathcal{N}(p)$ because p is the central black voxel in $\mathcal{N}(p)$. Therefore, there is exactly one black 26-components in $\mathcal{N}(p)$. Due to the fixed colour (i.e. black) of p it is not possible that $\mathcal{N}(p)$ contains an enclosed white 6-component. Also, there are no cavities in $\mathcal{N}(p)$. If the central voxel is black, any closed black 26-path in $\mathcal{N}(p)$ is certainly 26-shrinkable. Therefore, according to Definition 3.4, we have

$$\chi(\mathcal{N}(p)) = 1. \quad (3.26)$$

Thus the work boils down to the computation of the EPC of $\mathcal{N}(p)$ if the recursive relation (3.25) is used.

New Algorithm for Computing the Euler Characteristic

As mentioned in the literature review (Chapter 2), most of existing approaches to computing the EPC consider an n -dimensional digital object as a polyhedron composed of n -dimensional homogeneous structures. In those approaches the EPC of a binary image is defined in terms of numbers of k -dimensional elements in the polyhedral representation of the image (2.10).

Saha and Chaudhuri's (1995[139]) method is efficient for computing the EPC of a 3D binary image, if a look-up-table is well established in advance. However, it is not easy to build the look-up-table and the entries searching time is considerable. In this section I describe a different approach to compute the EPC of a 3D binary digital image from its digital representation.

Similar to Saha's approach, the algorithm is based on finding the change in numbers of black components, tunnels and cavities in the $3 \times 3 \times 3$ neighbourhood of a point after its deletion (i.e. changing to white). However, instead of using any kind of tables, I introduce a new analytical relationship between the topological numbers and the three Betti numbers in the $3 \times 3 \times 3$ neighbourhood of a voxel. Hence, the method only involves the counting of topological numbers and the recursive expression (3.25), which

is computationally efficient, because only a component-counting (cluster labelling) algorithm and a one-way scanning process are involved.

In 1994, Bertrand (1994[14]) introduced the concept of geodesic neighbourhood to define the topological numbers. In my approach, only two topological numbers are used as follows.

Definition 3.6 (Geodesic neighbourhood and Topological numbers): For a 3D binary image $\mathcal{P} = (\mathcal{V}, 26, 6, \mathcal{B})$ and a point $p \in \mathcal{V}$, let the geodesic neighbourhood $\mathcal{G}_{26}(p, \mathcal{B})$ be the set composed of all black 26-components of \mathcal{P} in $\mathcal{N}_{26}^*(p) = \mathcal{N}_{26}(p) \setminus \{p\}$. Then, the topological number $\mathcal{T}_{26}(p, \mathcal{B})$ is defined as $\mathcal{T}_{26}(p, \mathcal{B}) = \#\mathcal{G}_{26}(p, \mathcal{B}), \mathcal{T}_{26}(p)$ for short. $\#S$ denotes the number of elements in set S , i.e. its cardinal number. Moreover, let $\mathcal{G}_6(p, \mathcal{V} \setminus \mathcal{B})$ be the set of all white 6-components of \mathcal{P} in $\mathcal{N}_{18}(p) \setminus \{p\}$ such that each component \mathcal{E} in $\mathcal{G}_6(p, \mathcal{V} \setminus \mathcal{B})$ is 6-connected to p , i.e. there exists at least one point q in \mathcal{E} such that q is 6-connected to p , thus the topological number $\mathcal{T}_6(p, \mathcal{V} \setminus \mathcal{B})$ can be defined as $\mathcal{T}_6(p, \mathcal{V} \setminus \mathcal{B}) = \#\mathcal{G}_6(p, \mathcal{V} \setminus \mathcal{B}), \mathcal{T}_6(p)$ for short.

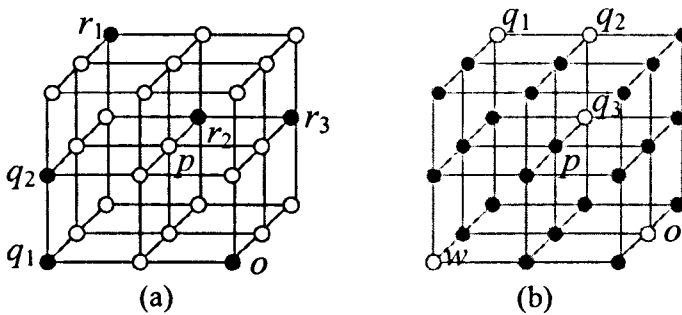


Figure 3-20: Geodesic neighbourhoods and topological numbers. (a) $\mathcal{G}_{26}(p, \mathcal{B}) = \{\{q_1, q_2\}, \{r_1, r_2, r_3\}, \{o\}\}$, so $\mathcal{T}_{26}(p, \mathcal{B}) = 3$; (b) $\mathcal{G}_6(p, \mathcal{V} \setminus \mathcal{B}) = \{\{q_2, q_3\}\}$, so $\mathcal{T}_6(p, \mathcal{V} \setminus \mathcal{B}) = 1$.

From the above definition, it is clear that the geodesic neighbourhood and the corresponding topological number are independent of the colour of p . Figure 3-20 illustrates configurations of black and white voxels in the $3 \times 3 \times 3$ neighbourhood of a voxel p . In the example of Figure 3-20(a), it is easy to understand that $\mathcal{G}_{26}(p, \mathcal{B})$ contains three black 26-components. But for $\mathcal{G}_6(p, \mathcal{V} \setminus \mathcal{B})$ and $\mathcal{T}_6(p, \mathcal{V} \setminus \mathcal{B})$, it should be noted that:

- 1) Each white 6-component in $\mathcal{G}_6(p, \mathcal{V} \setminus \mathcal{B})$ consists only of white voxels that are located within $\mathcal{N}_{18}^*(p) (\mathcal{N}_{18}(p) \setminus \{p\})$, so voxels w and q_1 do not belong to any set in $\mathcal{G}_6(p, \mathcal{V} \setminus \mathcal{B})$, because both voxels are only 26-neighbours of p ;

- 2) Each set S in $G_6(p, \mathcal{V} \setminus \mathcal{B})$ must be 6-connected to p , which means that at least one 6-neighbour of p must belong to S . Therefore, $G_6(p, \mathcal{V} \setminus \mathcal{B})$ does not contain the white 6-components $\{o\}$ even though $o \in \mathcal{N}_8^*(p)$.

Below I state the key result, which facilitates the computation of the EPC and the generation of many other topological quantities.

Let $\mathcal{P} = (\mathcal{V}, 26, 6, \mathcal{B})$ be a 3D binary image and let $p \in \mathcal{V}$ be a voxel in \mathcal{P} . Let $\check{\mathcal{N}}(p)$ be the sub-image $(\mathcal{N}(p), 26, 6, \mathcal{N}(p) \cap \mathcal{B} \setminus \{p\})$ of \mathcal{P} and let $h_1(p)$ and $h_2(p)$ be the number of tunnels and cavities in $\mathcal{N}(p)$ respectively. Then we have

$$\mathcal{T}_6(p) = h_1(p) - h_2(p) + 1. \quad (3.27)$$

Applied to Equation (2.11), the EPC of $\check{\mathcal{N}}(p)$ is then calculated as,

$$\chi(\check{\mathcal{N}}(p)) = h_0(p) - h_1(p) + h_2(p). \quad (3.28)$$

The number of black components $h_0(p)$ is obviously equal to the topological number $\mathcal{T}_{26}(p)$. Combing with Equation (3.25), the recursive algorithm for computing the EPC of \mathcal{P} can be stated as follows:

$$\chi(\mathcal{V}, 26, 6, \mathcal{B}) = 0 \text{ if } \mathcal{B} = \emptyset;$$

For any point $p \in \mathcal{B}$,

$$\chi(\mathcal{V}, 26, 6, \mathcal{B}) = \chi(\mathcal{V}, 26, 6, \mathcal{B} \setminus \{p\}) + \mathcal{T}_6(p) - \mathcal{T}_{26}(p). \quad (3.29)$$

3.4.2 Theoretical Analysis

For any point p in the image space of $\mathcal{P} = (\mathcal{V}, 26, 6, \mathcal{B})$, the number of cavities in the sub-image $\check{\mathcal{N}}(p)$ (3.23) is easy to count from the following lemma.

Lemma 3.1 (Saha and Chaudhuri, 1995[139]): The $\check{\mathcal{N}}(p)$ can contain at most one cavity (i.e. $h_1(p) \leq 1$), which occurs only when all 6-neighbours of p are black. Otherwise, the number of cavities in $\check{\mathcal{N}}(p)$ is zero.

On the other hand, it is difficult to determine the number of tunnels $h_1(p)$ of $\check{\mathcal{N}}(p)$. Kong and Rosenfeld (1989[76]) found that if a 3D digital image has no hollow torus,

then the number of tunnels in the image equals to the number of solid handles. It may be clear that $\check{\mathcal{N}}(p)$ cannot contain a hollow torus, otherwise at least one interior point must be black, but the only one interior point of $\check{\mathcal{N}}(p)$ is p , which is white by definition. Therefore, we have the following lemmas.

Lemma 3.2 (Aktouf et al. 2002[1]): $\check{\mathcal{N}}(p)$ contains at least one tunnel if there exists a closed black 26-path in $\mathcal{N}(p)$ that is unshrinkable.

In the proof of Equation (3.27) (i.e. Theorem 3.1 in the following), I will analyse all possible configurations of points in $\mathcal{N}_{18}^*(p)$, for which at least one unshrinkable closed black 26-path exists, in order to prove the existence of tunnels in $\check{\mathcal{N}}(p)$.

Lemma 3.3: Based on Saha and Chaudhuri's (1995[139]) Theorem 1, we have that $\check{\mathcal{N}}(p)$ contains no tunnels if and only if the set of all white 6-neighbours of p is 6-connected in $\mathcal{N}_{18}^*(p)$.

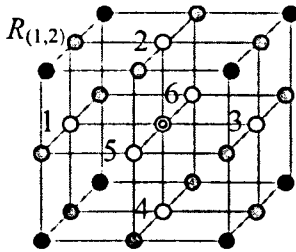


Figure 3-21: Illustration of opposite and link points. Point 1 is opposite to point 3, but not to point 2.

In $\mathcal{N}(p)$, two 6-neighbours of p are called opposite if they are not 26-adjacent (i.e. the pairs $\{1, 3\}$, $\{2, 4\}$ or $\{5, 6\}$ in Figure 3-21), otherwise they are called non-opposite 6-neighbours of p (i.e. $\{1, 2\}$, $\{2, 3\}$ etc. in Figure 3-21). Note that for any pair of non-opposite 6-neighbours $\{q, r\}$ of p , there exists only one 18-neighbour of p such that it is 6-connected to both q and r , denoted by $\mathcal{R}_{(q, r)}$, which is called a link-point between q and r (i.e. $\mathcal{R}_{(1,2)}$ is shown in Figure 3-21). According to Saha and Chaudhuri (1995[139]), we have the following lemma.

Lemma 3.4: If two non-opposite 6-neighbours $\{r, q\}$ of p in $\check{\mathcal{N}}(p)$ are not 6-connected in $\mathcal{N}_{18}^*(p)$ (i.e. $\mathcal{R}_{(r,q)}$ must be black), then the transformation of the link-point $\mathcal{R}_{(r,q)}$ to white removes exactly one tunnel from $\check{\mathcal{N}}(p)$.

The above lemmas (3.1-3.4) for computing the EPC of \mathcal{P} is based on the following theorem, which is an important result in this section.

Theorem 3.1: For a 3D binary digital image $\mathcal{P} = (\mathcal{V}, 26, 6, \mathcal{B})$ and any point $p \in \mathcal{B}$, the topological number $\mathcal{T}_6(p)$ is equal to the number of tunnels of $\check{\mathcal{N}}(p)$ minus the number of cavities plus 1 (3.27).

Proof: Recall that $\mathcal{T}_6(p)$ is the number of elements in the set (i.e. $\mathcal{G}_6(p)$) composed of all white components in $\mathcal{N}_{18}^*(p)$ that are 6-connected to p . In Figure 3-22, $\mathcal{N}_{18}^*(p)$ contains only two white components $\{p_2\}$ and $\{p_3, p_4\}$, but the first white component $\{p_2\}$ is not 6-connected to p , so there is only one white component $\{p_3, p_4\}$ in $\mathcal{G}_6(p)$ (i.e. $\mathcal{T}_6(p) = 1$). Thus, each white component C of $\mathcal{G}_6(p)$ must contain at least one 6-neighbour q of p such that $q \in C$. Furthermore, it is certain that $0 \leq \mathcal{T}_6(p) \leq 6$, because there are at most six 6-neighbours in $\mathcal{N}(p)$. Therefore we need to analyse the theorem in four cases: $\mathcal{T}_6(p) = 0$, $\mathcal{T}_6(p) = 1$, $\mathcal{T}_6(p) = 2$ and $\mathcal{T}_6(p) > 2$.

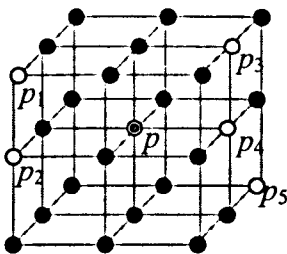


Figure 3-22: Example of determination of $\mathcal{T}_6(p)$. There are five white points in $\mathcal{N}(p)$ (p is the central point), $\mathcal{N}_{18}^*(p)$ contains 3 white points, but only one white component $\{p_3, p_4\}$ is 6-connected to p , therefore $\mathcal{T}_6(p) = 1$.

$\mathcal{T}_6(p) = 0$: All six 6-neighbours of p are black because $\mathcal{G}_6(p)$ is empty. According to Lemma 3.1 and Lemma 3.3, we have $h_2(p) = 1$ and $h_1(p) = 0$. Hence, Equation (3.27) is satisfied.

$\mathcal{T}_6(p) = 1$: There exists at least one white 6-neighbour q of p and any other white 6-neighbour of p is 6-connected to q in $\mathcal{N}_{18}^*(p)$. Lemma 3.3 states that $h_1(p) = 0$ and $h_2(p) = 0$ (see Lemma 3.1). Thus, Equation (3.27) is correct.

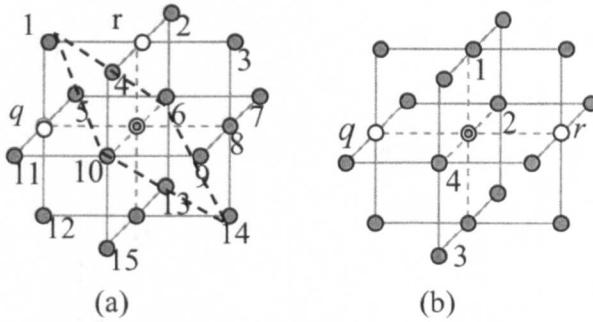


Figure 3-23: Positions of the white 6-neighbours q and r of p (the central point) that are not 6-connected in $\mathcal{N}_{18}^*(p)$, corresponding to the two independent configurations when $\mathcal{T}_6(p) = 2$. Under the condition of that q and r are not 6-connected in $\mathcal{N}_{18}^*(p)$, the colour of grey points can be black or white.

$\mathcal{T}_6(p) = 2$: There are exactly two white elements in $\mathcal{G}_6(p)$, so we can find two white 6-neighbours q and r of p such that q and r are not 6-connected in $\mathcal{N}_{18}^*(p)$. When allowing three-dimensional rotations in multiples of 90° about different axes, only two essentially different (independent) configurations exist, which are illustrated in Figure 3-23. Lemma 3.1 states that $h_2(p) = 0$, thus we need only to focus on the proof of $h_1(p) = 1$ when $\mathcal{T}_6(p) = 2$.

Firstly, let us discuss the configuration shown in Figure 3-23(a). Obviously point 1 is black, otherwise q and r are 6-connected in $\mathcal{N}_{18}^*(p)$. Then, there are three possibilities for the pair of points $\{6, 10\}$.

- Case 1: Both points in $\{6, 10\}$ are black;
- Case 2: Both points in $\{6, 10\}$ are white;
- Case 3: One of the points in $\{6, 10\}$ is white and the other is black.

For Case 1, of all points in $\{12, 16, 14, 8, 3\}$ shown in Figure 3-23(a) at least a point x must be black. Then a 26-closed black path can be formed (e.g. if $x = 14$, the black 26-path $\{1, 10, 14, 6, 1\}$ shown in Figure 3-23(a) appears) that cannot be transformed to a single point. According to Lemma 3.2, $\check{\mathcal{N}}(p)$ contains at least one tunnel, i.e. $h_1(p) \geq 1$. However, if we change point 1 to white (i.e. we remove point 1),

the two white 6-components in $G_6(p)$ will merge into one white component and the tunnel is destroyed (Lemma 3.3). Thus the number of tunnels in $\check{\mathcal{N}}(p)$ is equal to one, i.e. $h_1(p) = 1$.

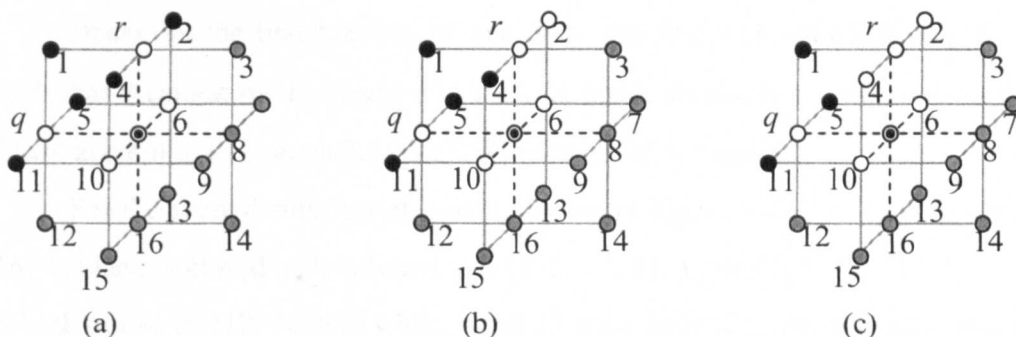


Figure 3-24: Illustration of the three independent subclasses for case 2, with (a) four, (b) three and (c) two black points in $\{2, 4, 11, 5\}$.

Case 2: Due to the symmetrical properties of configurations in $\mathcal{N}(p)$, there are only three independent subclasses for Case 2 (see Figure 3-24), i.e. four points, three point or two points in $\{2, 4, 11, 5\}$ are black.

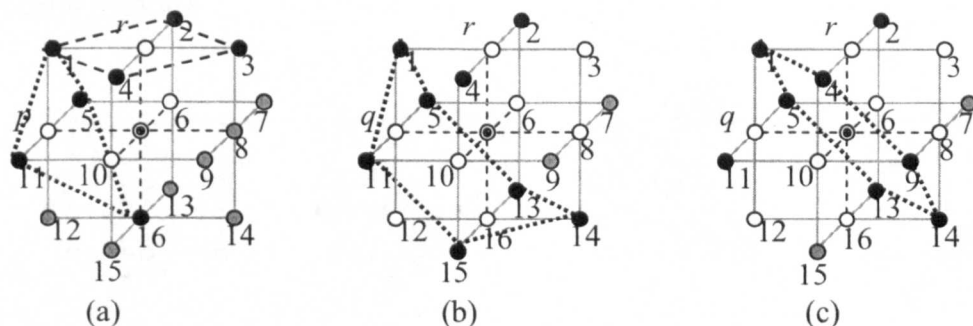


Figure 3-25: Illustration of closed black 26-paths that cannot be transformed to a single point for the first subclass of case 2, shown in Figure 3-24(a): (a) two closed black 26-paths that are unshrinkable when 3 is black or 16 is black; two different closed black 26-paths when both points in (b) $\{9, 7\}$ or (c) $\{15, 13\}$ are black. Notice that in each example both points in $\{6, 10\}$ can still be 6-connected to q and r , to ensure that $T_6(p) = 2$.

For the first subclass of Case 2, shown in Figure 3-24(a), it is easy to find a closed black 26-path that is unshrinkable if one of points 3 and 8 is black or one of points 12 and 16 is black, as shown in Figure 3-25(a). Conversely, if all points in $\{12, 16, 8, 3\}$

are white as depicted in Figure 3-25(b), point 14 must be black. Now, if points 15 and 13 are both black or points 7 and 9 are both black, a closed black 26-path can be found, as shown in Figure 3-25(b). Otherwise, if 13 and 9 or 15 and 7 are black, a closed black 26-path can be found, as illustrated in Figure 3-25(c).

Hence for the first subclass of case 2 we can find a closed black 26-path in $\mathcal{N}(p)$ such that it cannot be transformed to a single point, similar to the discussion of case 1. Then, according to Lemma 3.3, after removing point 1, $h_1(p) = 1$.

For the second subclass of case 2, shown in Figure 3-24(b), if one point in $\{12, 16\}$ is black, a closed path is found, i.e. $\{1, 5, 12, 11, 1\}$ or $\{1, 5, 16, 11, 1\}$; otherwise, if both points in $\{12, 16\}$ are white, point 13 must be black to avoid that q and r are 6-connected. Furthermore, this case can be discussed as follows:

- point 8 is black (see Figure 3-26(a));
- both points 8 and 14 are white (see Figure 3-26(b));
- point 8 is white, point 14 is black and one of the points in $\{15, 9\}$ is black (see Figure 3-26(c));
- point 8 is white, point 14 is black and both points in $\{15, 9\}$ are white (see Figure 3-26(d)).

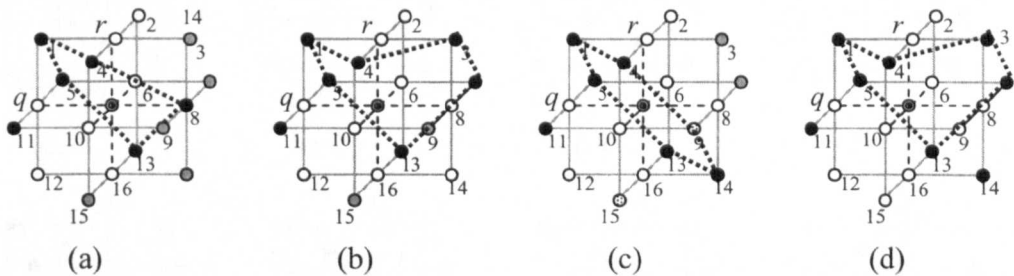


Figure 3-26: Demonstration of unshrinkable closed black 26-paths for the second subclass of case 2, shown in Figure 3-24(b), when points 12 and 16 are both white and, additionally, (a) point 8 is black, or (b) points 8 and 14 are both white, or (c) point 8 is white, point 14 is black and one of the points in $\{15, 9\}$ is black (indicated as dotted), or (d) point 8 is white, point 14 is black and both points in $\{15, 9\}$ are white.

From Figure 3-26, in all cases for the second subclass of Case 2 (Figure 3-24(b)) an unshrinkable closed 26-path can be found, which means that tunnels must exist. In addition, it is impossible to find any unshrinkable closed 26-path after removal of link-

points like point 1. Thus $h_1(p) = 1$. Similarly, for the third subclass of Case 2, shown in Figure 3-24(c), the same result can be obtained, as demonstrated in Figure 3-27.

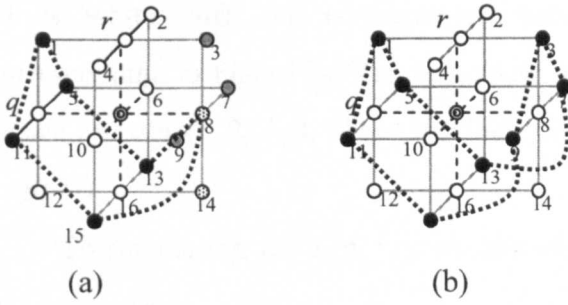


Figure 3-27: Demonstration of unshrinkable closed black 26-paths for the third subclass of case 2, shown in Figure 3-24(c), when one of $\{4, 8\}$ is black we have a unshrinkable closed black path (a), otherwise each of $\{3, 7, 9\}$ must be black in corresponding to the consumption for this case, so a unshrinkable closed path can be found in (b).

Case 3: All possible configurations are depicted in Figure 3-28. The proof is similar to the above method. I omit it here.

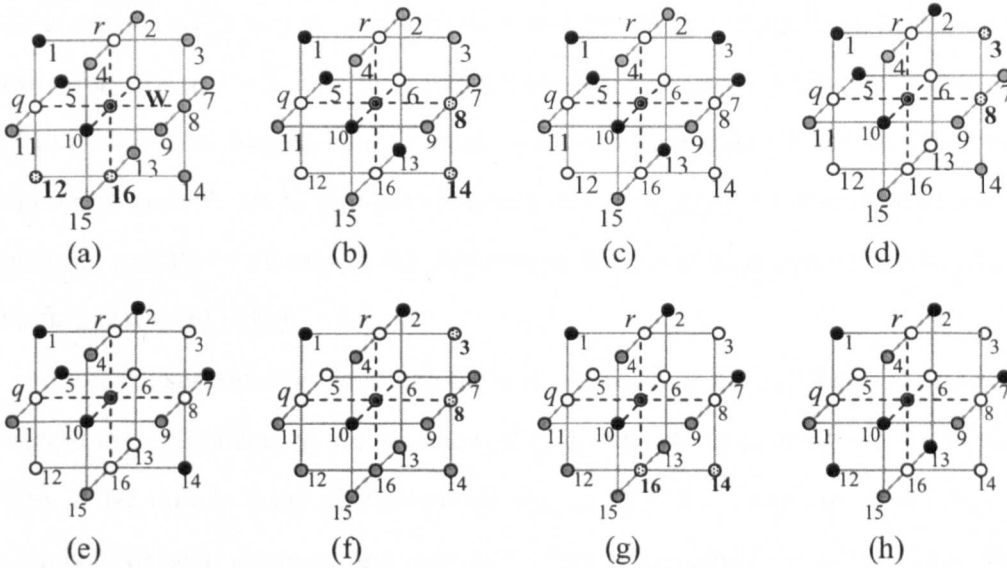


Figure 3-28: All possible configurations for case 3 shown in Figure 3-24(c): (a) one point in $\{12, 16\}$ is black; (b) both 12 and 16 are white, and one point in $\{8, 14\}$ is black; (c) all points in $\{12, 16, 14, 8\}$ are white, and point 3 must be black; (d) points 12, 16 and 13 are white, and one point in $\{3, 8\}$ must be black; (e) all point in $\{12, 16, 3, 8\}$ are white, and 14 must be black, etc. For all these configurations, obviously, we can certainly find an unshrinkable closed 26-path.

The second possibility for $\mathcal{T}_6(p) = 2$ arises when the two 6-neighbours of p are opposite, as shown in Figure 3-23(b). Suppose that at least one of the points in $\{1, 2, 3, 4\}$ is white, then the configuration becomes equivalent to one of the cases corresponding to Figure 3-23(a). Otherwise all points in $\{1, 2, 3, 4\}$ are black and the closed 26-path $\{1, 2, 3, 4, 1\}$ is unshrinkable. For both cases, the result is the same, i.e. $h_1(p) = 1$.

To summarise, for $\mathcal{T}_6(p) = 2$ we have $h_2(p) = 0$ and $h_1(p) = 1$, so Theorem 3.1 for this case is true.

$\mathcal{T}_6(p) > 2$: Each element of $\mathcal{G}_6(p)$ contains at least one white 6-neighbour of p , so we can arbitrarily pick one white 6-neighbour of p for each element of $\mathcal{G}_6(p)$, and obtain a set of $\mathfrak{R} \equiv \{q_1, q_2 \dots q_m\}$ where $m = \mathcal{T}_6(p) > 2$, in which each pair of points in \mathfrak{R} is not 6-connected in $\mathcal{N}_{18}^*(p)$. For q_1 , there is at most one point in \mathfrak{R} such that it is opposite to q_1 and any other point in \mathfrak{R} is non-opposite to q_1 . Therefore only two cases need to be considered.

For the first case, in which each point in $\mathfrak{R} \setminus \{q_1\}$ is non-opposite to q_1 , for all pairs of points (q_1, q_j) ($2 \leq j \leq m$) there exist $m-1$ link-points. After transformation of each link-point $\mathcal{R}_{(q_1, q_j)}$ ($j = 2, 3 \dots m$) to white, exactly one tunnel in $\check{\mathcal{N}}(p)$ is removed. When all link-points are transformed to white, only one component is left in $\mathcal{G}_6(p)$, therefore no tunnels are left due to the same reason as the case $\mathcal{T}_6(p) = 1$ discussed above. Hence, there are exactly m tunnels in the direct neighbourhood of p . According to Lemma 3.4 we find that $h_1(p) = \mathcal{T}_6(p) - 1$.

For the second case, in which there is one point in $\mathfrak{R} \setminus \{q_1\}$ that it is opposite to q_1 , without loss of generality, we assume that q_m is opposite to q_1 and there are \mathcal{N}_t tunnels in $\check{\mathcal{N}}(p)$. After transforming all link-points $\mathcal{R}_{(q_1, q_j)}$ ($j = 2 \dots m-1$) to white, $\mathcal{N}_t - (m - 2)$ tunnels have been removed and only two white components are left in $\mathcal{G}_6(p)$. From the above proof we know that there is only one tunnel for the $\mathcal{T}_6(p) = 2$, i.e. $\mathcal{N}_t - (m - 2) = 1$, hence $h_1(p) = \mathcal{T}_6(p) - 1$.

According to Theorem 3.1, the Euler number of a 3D binary image can then be easily computed using the recursive relationship (3.28) by removing object voxels one by one.

As a simple example, in Figure 3-29 a set of 3D objects are plotted and the corresponding Euler numbers are also computed. Two concepts (i.e. component, tunnels) are clearly demonstrated, no cavities exist in these objects. The number of tunnels is also explained as the number of redundant connections (channels). A connection is redundant, when it can be cut out without destroying the connectivity of the original object

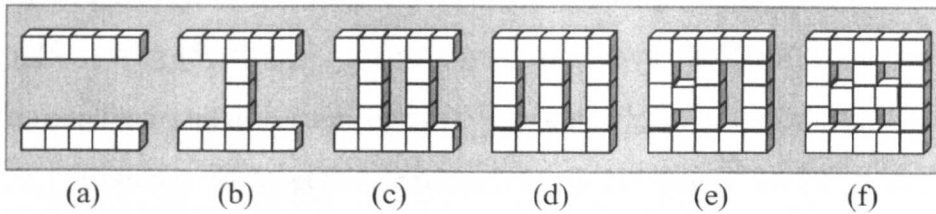


Figure 3-29: Examples of objects with different EPCs: (a) $\chi = 2$, (b) $\chi = 1$, (c) $\chi = 0$, (d) $\chi = -1$, (e) $\chi = -2$, (f) $\chi = -3$. The EPC = the number of components – the number of redundant channels + the number of cavities. For the PS, the number of cavities (floating solid particles) should be zero, therefore, the number of redundant connections = the number of components – the Euler number.

Algorithm Assessment and Comparison

In pore structure analysis, Vogel's algorithm (2000[183]) for estimating the EPC is used much more often than Saha and Chaudhuri's (1995[139]) exact computation. This is due to the fact that the error resulting from Vogel's approximation of the truth EPC can be ignored when the size of the targeted images is sufficiently large. The most attractive feature of Vogel's method is its simplicity and efficiency. In comparison, the algorithm for calculating the EPC developed by Saha and Chaudhuri is complex and time-consuming. They stated that in the worst case, the computation of the change in the EPC in a $3 \times 3 \times 3$ neighbourhood of a point p due to its deletion requires checking of all possible configurations of 26-neighbours of p . That means that a look-up-table with 2^{26} entries needs to be created. Consequently, if each entry of the look-up-table needs one byte, the complete table needs 64M bytes. For this reason, I only carry out a simple comparison between the accuracy of my algorithm and Vogel's method for a rock image.

Vogel's algorithm has already been explained in the previous chapter and the details can be also found in Vogel (1997a[181]). The general idea behind this algorithm is to convert a complicated 3D problem into a series of easier 2D problems by referring to a 3D binary image \mathcal{P} as a series of 2D slices S_i ($i = 1, 2 \dots m$). The 2D EPC of a slice can be directly obtained by counting the number of components and holes, which can be done by HKA. Considering two adjacent slices S_i and S_{i+1} , called a "dissector" denoted by $DS(S_i, S_{i+1})$, the 3D EPC of $DS(S_i, S_{i+1})$, is computed as $\chi_3(DS(S_i, S_{i+1})) = [\chi_2(S_i) + \chi_2(S_{i+1}) - 2\chi_2(S_i \cap S_{i+1})] / 2$ (see Figure 2-8). Then, the 3D EPC of \mathcal{P} can be estimated by combining all dissectors together, i.e. $\chi_3(\mathcal{P}) = \sum_{i=1}^{m-1} \chi_3(DS(S_i, S_{i+1}))$.

Contrary to Vogel's algorithm, for a 3D binary image \mathcal{P} , my approach for computing the 3D EPC of \mathcal{P} is based on the recursive relation (3.25). The local EPC change of p is calculated as

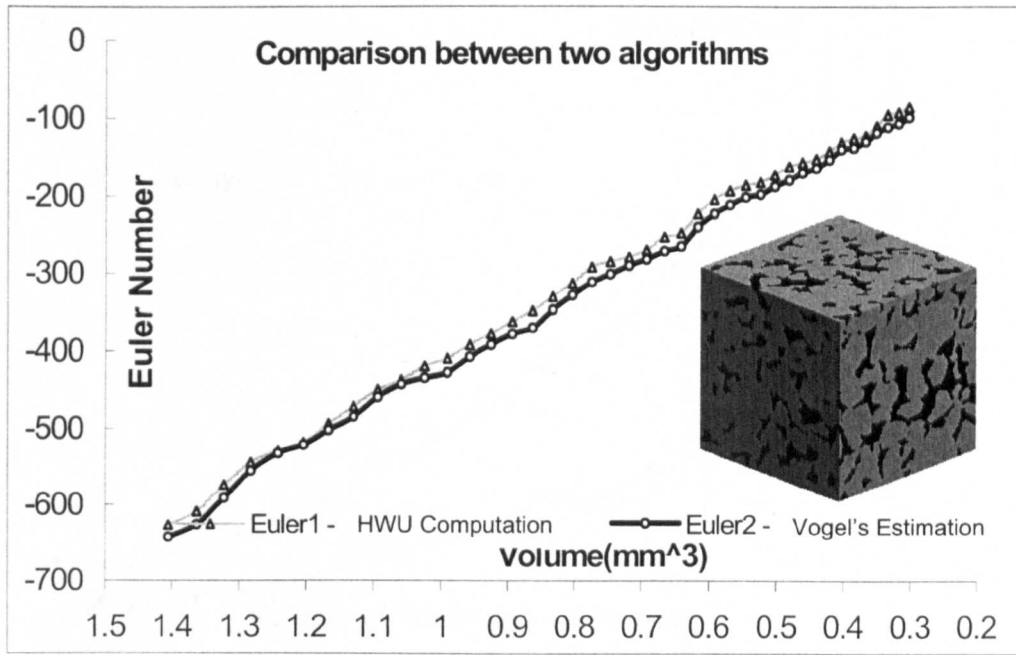
$$\chi(\mathcal{N}(p)) - \chi(\check{\mathcal{N}}(p)) = \mathcal{T}_6(p) - \mathcal{T}_{26}(p). \quad (3.30)$$

Therefore, the computation of the EPC involves only counting two topological numbers which can be easily obtained using the extended HKA.

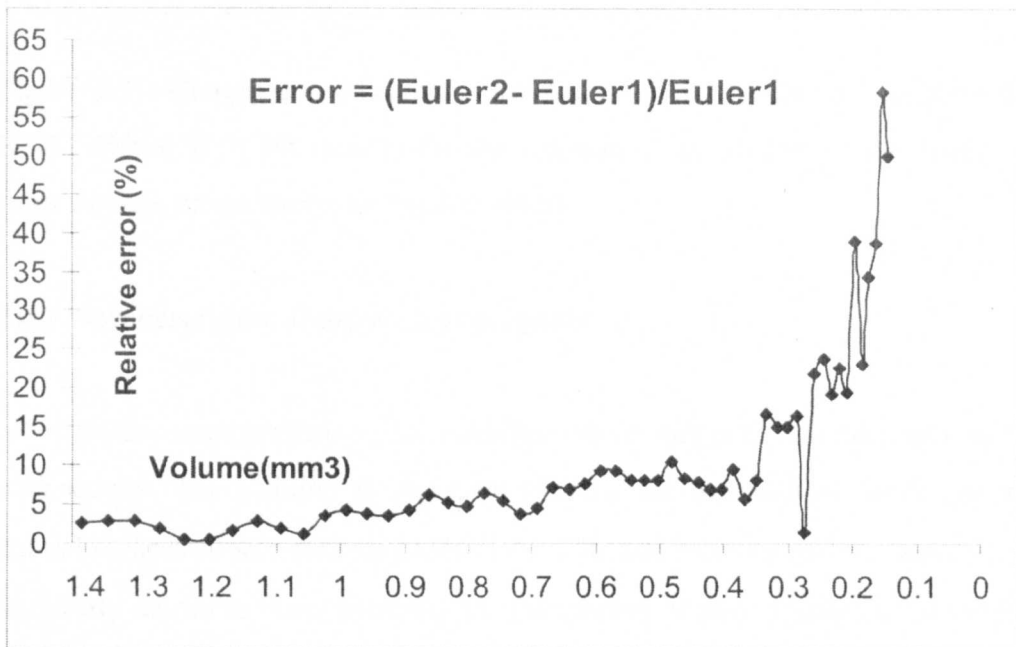
In Figure 3-30(a), a 3D tomography image \mathcal{P} of a sandstone is presented, which is used for the comparison with Vogel's algorithm in the following. The image space is a cubic matrix $\{(x, y, z): 0 \leq x \leq 199, 0 \leq y \leq 199, 0 \leq z \leq 199\}$ in Z^3 , and the PS shown in Figure 3-30(a) is coloured in black. The 3D EPC of \mathcal{P} are either estimated by Vogel's algorithm (Euler2), or calculated by my algorithm (Euler1), as -626 and -642, respectively. The relative EPC error between two methods (i.e. (Euler2-Euler1)/Euler1, see Figure 3-30(b)) can be very large when images are quite small and highly noisy. From a statistical point of view, the EPC error can be measured over a set of sub-images of different sizes or interior structures. Here we cut off a series of sub-images, denoted by $\mathcal{P}_0, \mathcal{P}_1 \dots$ from \mathcal{P} . For simplicity, let $\mathcal{P}_i = (\mathcal{V}_i, 26, 6, \mathcal{B}_i)$ where $\mathcal{V}_i = \{(x, y, z) \mid i \leq x \leq 199 - i, i \leq y \leq 199 - i, i \leq z \leq 199 - i\}$ and $\mathcal{B}_i = \mathcal{B} \cap \mathcal{V}_i, i = 0, 1 \dots 98$. For all sub-images I have calculated the EPC using both Vogel's and my algorithms, for which the results are presented in Figure 3-30(a) and (b).

According to the proof of Theorem 3.1 and the recursive algorithm (3.29), the computation of my algorithm leads to the exact Euler number rather than an approximation. For the sandstone image shown in Figure 3-30(a), the relative error

between Vogel's and my algorithm tends to be very large when small images or highly noisy images are used. In other words, the estimating error of Vogel's method applied to original small rock images cannot be neglected. This is the price of estimating the 3D EPC using a series of 2D EPCs. However, the significant advantage of Vogel's estimation is the algorithm efficiency. Figure 3-31 shows that Vogel's algorithm is significantly faster than mine.



(a)



(b)

Figure 3-30: (a) A 3D tomography sandstone image and the Euler number curve for a set of sub-images φ_i of the image, $i = 0, 1 \dots 98$. The dimensions of this image are 200^3 voxels, and the resolution is 5.6 micron. Black is the PS and grey is the solid matrix. (b) The relative Error between estimated (by Vogel's algorithm) and calculated (by my algorithm, HWU: Heriot-Watt University) the EPCs. Note that the relative error varies between 0 and 5% when the size of the sub-images is larger than 0.9 mm^3 .

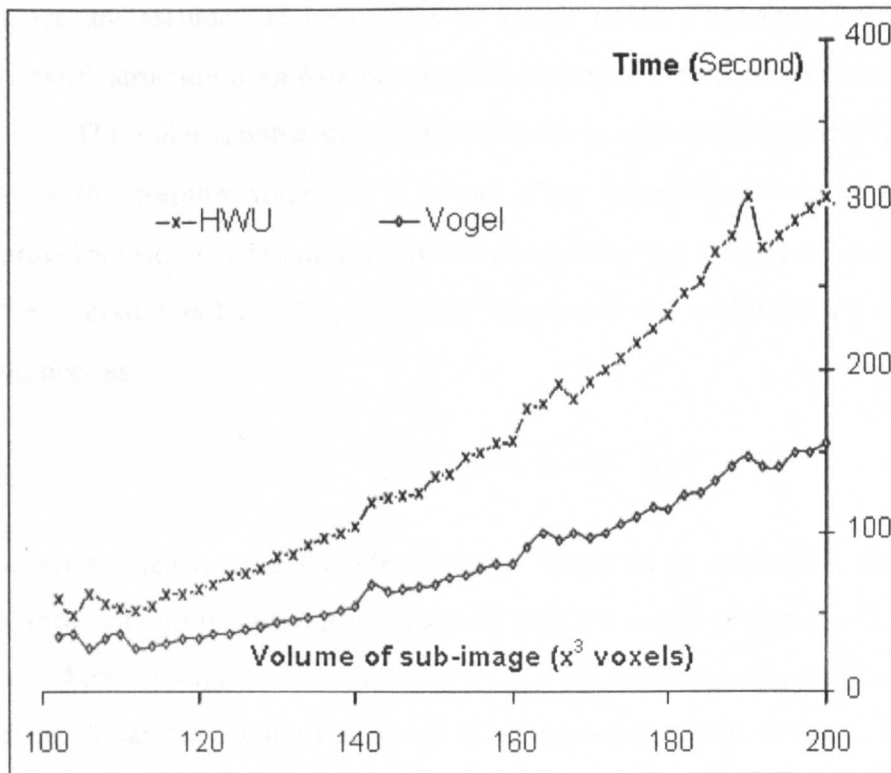


Figure 3-31: Comparison of computation times using Vogel's and our algorithm (i.e. HWU: Heriot-Watt University) for the calculation of 3D EPCs. Sub-images are cut from the rock image shown in Figure 3-30(a).

3.4.3 New descriptor of topological properties

As discussed previously, the coordination number is a local descriptor of the pore connectivity. The inability to represent globally the topology of the irregular PS of natural rocks has motivated me to study the EPC and its computation. The EPC χ (2.13) is directly related to three quantities i.e. the number \mathcal{N} of components, the number \mathcal{G} of tunnels and the number \mathcal{H} of cavities. \mathcal{N} and \mathcal{H} can be obtained by applying a component labelling (clustering) algorithm (e.g. HKA), and then the number \mathcal{G} of tunnels is given by

$$\mathcal{G} = \mathcal{N} - \chi + \mathcal{H}. \quad (3.31)$$

\mathcal{G} is also equivalent to the number of redundant connections. In pore structure analysis, cavities are commonly neglected, because solid particles floating in the void

space are assumed to be caused by image noise. Therefore, before extracting the network structure from rock images, it is necessary to remove all floating solid particles.

The Euler number does not lead to an unequivocal description of the topology, since the absolute values of \mathcal{N} , \mathcal{G} and \mathcal{H} are unknown. Moreover, the Euler number provides just a single number without considering the volume of objects for describing the overall topology. Vogel (1996) introduced the definition of the specific Euler number as

$$\chi_v = (\mathcal{N} - \mathcal{G} + \mathcal{H})/V, \quad (3.32)$$

where V is the volume of the image space. Based on this definition, the specific EPCs of a series of sub-images cut off from the original image (Figure 3-30(a)), are computed and shown in Figure 3-32. Note that the specific EPCs do not tend to become stationary, even though the volumes of image V_i are quite large. The reason is that many isolated tiny pores appear in the image because of image noise. These isolated tiny pores significantly degrade the ability of the EPC to describe object connectivity (i.e. \mathcal{N} is very large), but they do not contribute to fluid movement in single- or multi-phase flow.

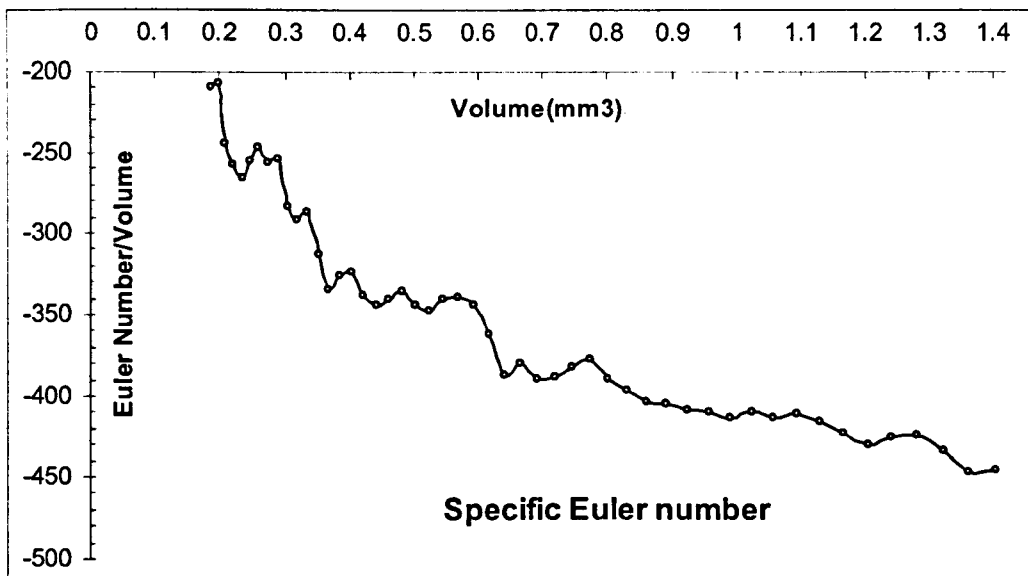


Figure 3-32: The specific Euler number against the volumes of a series of sub-images of the sandstone shown in Figure 3-30(a). It shows that the specific EPC could not be used as to describe the pore connectivity of an object.

Another issue related to the EPC is that it cannot distinguish a structure with the same Euler number but different numbers of components. In Figure 3-33, two different topological structures are presented that have the same Euler number.

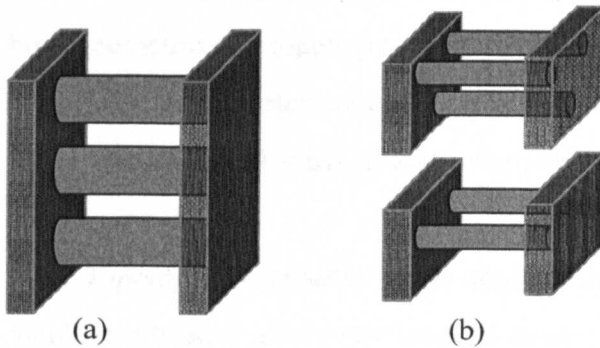


Figure 3-33: Structures with different topologies but the same Euler number (-1): (a) an object with two redundant connections; (b) a combination of two objects with three redundant connections.

For these reasons a new descriptor will be proposed, called the connectivity coefficient, which will be discussed in more detail in Chapter 5.

3.5 Medial Axis Transformation (skeletonisation)

For a given 3D image, it is common to study the object structure (e.g. the pore structure) by reducing the number of voxels as much as possible while preserving its intrinsic properties. The reduced 3D object may become 2D (i.e. surfaces) or even 1D entities (i.e. curves), which makes it much easier to explore its structure.

More precisely, a MA (skeleton or network) of the foreground of a 3D image is defined as a subset of the foreground that carries the necessary geometric and topological (GT) properties in a simple and compact (highly compressed) form. The first network extraction method (skeletonisation) applied to rock images was developed by Lindquist and Lee (1996[87]) and similar approaches have subsequently been presented by other authors, such as Vogel and Roth (2001[185]) and Knackstedt et al. (2004[73]). In Section 2.3, I have presented an extensive review of network extraction methods, which is also called MA transformation or skeletonization. In this section, I describe an new algorithm, which is designed for pore structure analysis, and the extracted skeleton is called a GT network.

3.5.1 GT Network Consideration

Based on the specific research needs, i.e. to predict multiphase flow properties, both geometric and topological features have to be included in the extracted network. Therefore, the skeletonisation focuses on: topology-preservation (homotopy), single voxel width, central location and integration of geometry. These issues are explained below.

Topology-preservation (homotopy): The GT network of the PS must be topologically equivalent to the original image. This means that all connected pores must remain connected after extracting the skeleton from the original images – no artificial false links should be added and no real links or pores should be removed. The objective is to ensure that the flow paths have not been changed in the resultant GT network. From a topological point of view, all components, tunnels and cavities in a skeleton image are kept the same as in its original image. Figure 3-34 shows some instances where this rule is broken.

Single voxel width (thinness): The GT network must be one voxel wide (i.e. each voxel on the skeleton has not more than two neighbours) except at points (e.g. at some junctions) where a thick skeleton is necessary to satisfy certain topological and geometrical criteria, where the connectivity condition may require several points. A single voxel width skeleton can easily be used to locate the centres and orientations of flow paths. It also makes it possible to properly identify the centres of nodes (pore bodies) and to accurately compute many other geometric properties. This rule is demonstrated in Figure 3-35.

Central location (centredness): It is crucial to ensure that the GT network is in the middle of the PS and invariant under the affine transformations including translation, rotation and scaling. In the study of fluid flow, the centred skeleton is important to calculate cross sectional areas normal to the central flow path and to calculate cross sectional radii etc. For general image processing, this consideration requires to capture the symmetry of a shape which is useful for object recognition. As mentioned above, the positions of skeleton voxels depend on the scanning order in which points are checked, and this order is often arbitrary. However, these methods

involve an additional time-consuming procedure and give no guarantee of the centredness of the equal distance domain in the 3D image, as illustrated in Figure 3-36.

Integration of geometry: In the application to the prediction of rock properties, the computation of shape factor G , and the inscribed radius of a pore CS, are critical. The shape factor is defined as $G = A/P^2$, where A is the cross sectional area and P is its perimeter (Mason and Morrow, 1991). The pore CS must be perpendicular to its medial line (skeleton) and independent of its scale, direction and position. In thinning algorithms, if all simple points are to be deleted without any constraints, then the resulting skeleton is called a pure topological network. In practical applications, however, some simple points should be retained to hold certain geometric features, which are often called endpoints. To create a network for flow prediction, it is necessary to recognize some boundary points (in the inlet/outlet faces), terminal points of major branches (called branch points) of dead-end pores, and anchor points (which are important, but cannot be described by any explicit rules) as endpoints.

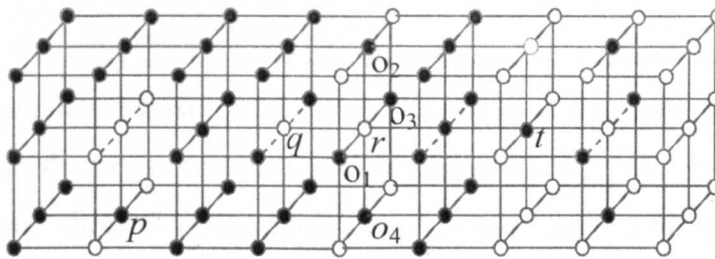


Figure 3-34: Some instances of topology preservation: Considering an binary image $\mathcal{P} = (\mathcal{V}, 26, 6, \mathcal{B})$ where \mathcal{V} is the set of all voxels drawn in the figure and \mathcal{B} is set of all black voxels (object), p must be retained on the resultant skeleton, otherwise a tunnel will disappear; $\{q, r\}$ is a white 6-component which is completely enclosed, i.e. it is a cavity; removing any voxel of $\{o_1, o_2, o_3, o_4\}$ will destroy the cavity of $\{q, r\}$; removing t will create a tunnel.

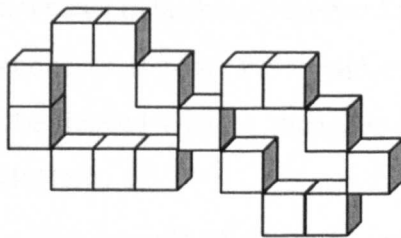


Figure 3-35: Skeleton of single voxel width except at the junction.

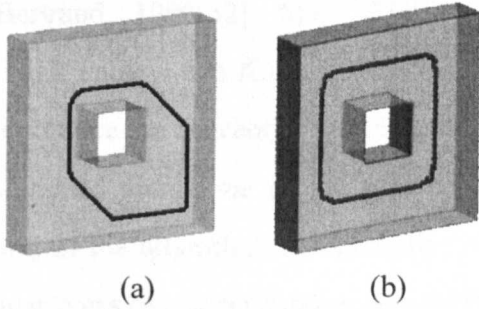


Figure 3-36: Centredness of skeletons in 3D. The skeleton shown in (a) is derived by common DOHT approaches (Note that some recent thinning algorithms have improved on this by employing alternating direction schemes.) The locations of the skeletons depend on the scanning order within the region of same distance values. The skeleton depicted in (b) is generated by our algorithm with symmetry deletion, which is independent of scanning order.

3.5.2 Algorithm Description

The GT network extraction algorithm combines a novel thinning technique and an improved version of the Euclidean distance transformation (EDT) to extract the network of the foreground (e.g. pore voxels) of an image. In other words, all foreground voxels are checked in ascending distance order (Saito and Toriwaki, 1995[145]; Lohou and Bertrand, 2005[92]) to determine whether they can be removed. The thinning technique aims at detecting and deleting as many points as possible at each iteration, rather than just one point, before invoking a clustering procedure (e.g. extended HKA, Hoshen and Kopelman, 1976[59]).

Usually, a clustering algorithm is utilised in the $3 \times 3 \times 3$ neighbourhood of an object point to determine the topological numbers of this point. As explained in Section 3.4, the topological numbers are defined as the number of 26-connected foreground components in the neighbourhood and the number of particular 6-connected background components. If both of the numbers are equal to one, the point is called “simple” and it can be deleted without changing the topology of an object (Bertrand and Malandain, 1994b[18]).

The concept of a simple point has been extended to that of a simple set (Ma, 1994[95]; Gau et al., 2003[50]), but so far no efficient algorithm exists to detect these simple sets (Lohou and Bertrand, 2004[91] and 2005[92]; Xie et al., 2003[189]; Gong

and Bertrand, 1990[52]; Ma, 1994[95]; Ma and Sonka, 1996[96]; Saha et al., 1997[141]; Palágyi and Kuba, 1997[120], 1998[121] and 1999[122]). To find a simple set, I introduce the concept of the foreground pure 6-component, a component of single width aligned along one of the grid coordinates, which is used as a candidate for checking in the algorithm. Additionally, in the envelope of a pure 6-component, two particular types of adjacencies are defined (for foreground and background components) analogous to the adjacencies in the neighbourhood of a point. In this Section I will prove Theorem 3.2, which states that if the pure 6-component has exactly one foreground and one background adjacent component, then the pure 6-component is simple. Consequently, in the thinning algorithm all voxels in a simple pure 6-component can be totally deleted together at a time. Note that the theorem only provides a sufficient condition for the “simplicity” of a pure 6-component. In other words, if it does not have exactly one foreground or one background adjacent component, then the pure 6-component needs to be checked in the way of point by point. In the numerical experiments, clustering of voxels in the neighbourhood of a single point is almost as time-consuming as clustering voxels in the envelope of a set (about 2.45 voxels per set for the sandstone samples). Therefore, the total number of times to invoke the clustering procedure is reduced in the whole thinning process, greatly improving the efficiency of the thinning algorithm.

Another advantage of the new thinning algorithm is that, because it checks within the envelope of a pure 6-component, simple set detection can be carried out in parallel at alternating rows or columns of the image. This interval detection strategy also ensures that most foreground points are checked only once.

The thinning algorithm guarantees homotopy and thinness, but it does not necessarily produce central-aligned skeletons. Unlike other thinning algorithms that attempt to achieve centredness by scanning in 6 or 12 directions (Palágyi and Kuba, 1997,1998), my thinning algorithm achieves centredness through scanning in only 2 directions (forwards and backwards). The Euclidean distance map is used to control the main order of scanning (i.e. voxels of small distances are checked first). Then, in a given layer of the distance map (containing voxels of equal distance), the order of scanning is controlled by symmetry detection. In other words, rather than removing points during each scan, I keep all removable points until the end of a full iteration

involving the two scans. This ensures that each point in the layer of the same distance has an equal probability of being detected and subsequently removed.

Because of the nature of thinning algorithms, only topological information of the pore system is preserved, yielding the so-called pure topological skeleton. Generally a lot of geometrical information is lost, such as boundary features, dead end pores etc., which may also be important in the prediction of flow properties. Below I explain (in outline) how I preserve the important geometrical information related to so-called endpoints.

Boundary points: For the study of flow properties, it is important to identify inlet and outlet pores (links), whereas the normal thinning process tends to remove most of the points at inlets and outlets. I introduce a region-constraining rule to retain one voxel in a local maximum SED (squared Euclidean distance) region at the corresponding boundaries, even if this voxel is a simple point. In Figure 3-37, the preservation of two boundary points, as endpoints of the resultant GT network, is illustrated.

Branch points: For some flow calculations, for example involving a diffusion process, the medial lines of dead-end pores should be kept in the resulting GT network. In Figure 3-38(a) a 2D dead-end pore is shown. To retain the branch (dashed curve) its length should be larger than a specified threshold. To achieve this, I calculate the geodesic distance map from the pure topological medial line (black line in Figure 3-38(a)), similar to the 2D calculation of Cárdenes et al. (2003[31]). A branch of the MA is kept in dead-end regions (grey in Figure 3-38(a)) that has a geodesic distance larger than a threshold. A voxel in this region (a branch point) is retained if it has only one 26-neighbour, and so is the medial line connecting it to the pure topological MA through the thinning.

Anchor points: To process large 3D images, the images must be divided into sub-images in which boundary link points must be retained to preserve a specific property. These so-called anchor points are located on the boundary of a sub-image to integrate the various sub-skeletons into a global skeleton.

Based on the criteria for thinning, different extracted skeletons are shown in Figure 3-38(b) ~ (d) and in Figure 3-39. The further explanation will be given later.

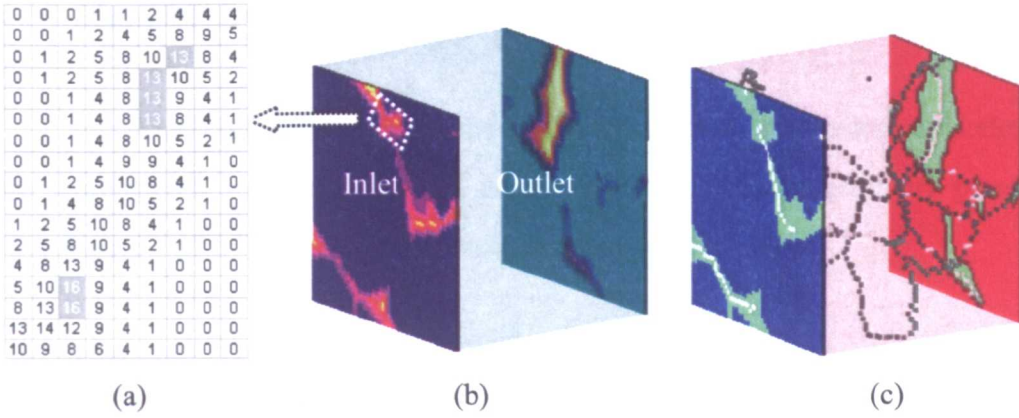


Figure 3-37: Retaining boundary points: (a) and (b) Slice of the 3D squared Euclidean distance map on the inlet (and outlet). In each local maximum region one voxel is retained, which means that two boundary voxels in the two rectangle regions depicted in (a) are to be retained. Based on this criterion, an example of the skeleton with some boundary voxels (and boundary links) is shown in (c).

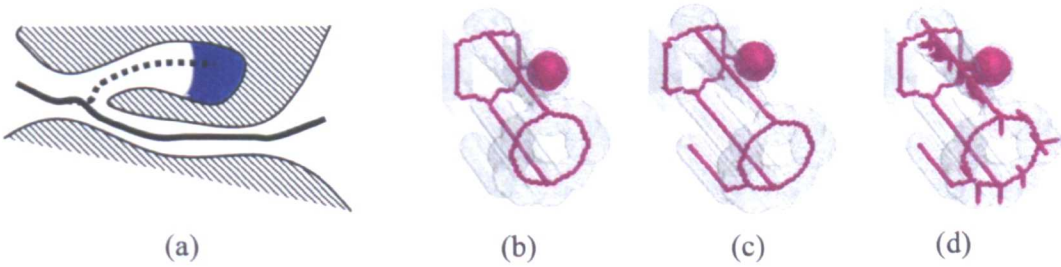


Figure 3-38: Skeletons with primary branches. (a) 2D example of a skeleton with a branch (dashed curve), where the grey area indicates has a geodesic distance to the pure topological MA (black curve), larger than a given threshold; (b) a pure topological GT network without any branches; (c) and (d) skeletons with some branches based on different thresholds.

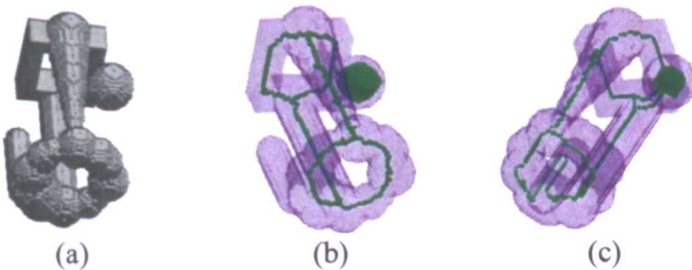


Figure 3-39: Topological network. (a) Original 3D image with only one 26-component, one cavity and three tunnels (Euler Characteristic is -1); (b) and (c) are two pure topological networks of the image shown in (a).

3.5.3 Algorithm Implementation

For simplicity, I first explain the extraction of the pure topological skeleton, i.e. the topologically representative and centred skeleton, without geometry preservation (See Figure 3-39). Then I take account of geometry preservation.

Extraction without Geometry Preservation

For a 3D binary image \mathcal{P} , the thinning operation is carried out as follows:

Computation of the Squared Euclidean Distance Map: First, the SED Map of an image \mathcal{P} , a grey-scale image denoted by $\text{Map}(\mathcal{P})$, is calculated as described in Section 3.4, in which the value $\text{Map}(p)$ of a foreground voxel p is the shortest squared Euclidean distance from this voxel to the background of \mathcal{P} , while the value of any background voxel is zero. The distance map is used for controlling the thinning order to assure centeredness of the GT network. During the thinning operation $\text{Map}(\mathcal{P})$ is updated when points are deleted, i.e. removed from the foreground.

Two queues of object voxels, denoted by Q_1 and Q_2 , are used in the algorithm. All candidate voxels are stored in Q_1 at the beginning. These voxels comprise the (layer of) foreground voxels with current minimum SED. In Q_2 all voxels are stored that are marked for deletion at the end of current iteration. Such points p in Map are assigned as infinite, i.e. $\text{Map}(p) = \infty$.

Initialisation: At the start of the thinning process, Q_1 contains all voxels of current minimum SED (usually 1) in $\text{Map}(\mathcal{P})$, and Q_2 is empty.

Thinning iteration steps: The thinning consists of the following steps:

Step 1: If Q_1 is empty, the thinning process is stopped, otherwise go to Step 2.

Step 2: Using our extended HKA, all voxels in Q_1 are clustered into a family $F(Q_1)$ of all 6-components. Each 6-component in $F(Q_1)$ is divided into several pure 6-components.

Step 3: For each pure 6-component \mathcal{S} , check if (a) it is 26-connected to a marked voxel in \mathcal{P} (i.e. interval detection) or (b) it cannot be determined as a simple set based on

Theorem 3.2. Under these conditions, go to Step 5. Otherwise all voxels in S are marked and all voxels in the black adjacent component are pushed into Q_2 .

Step 4: After processing all 6-components in $F(Q_1)$, all marked voxels in \mathcal{P} are deleted (symmetrical deletion), which finishes one iteration. All voxels in Q_2 having the new minimum distance value are pushed into Q_1 (which should obviously be emptied before this operation), then go to Step 1.

Step 5: For each voxel p in a pure 6-component S , check if (a) p is 26-connected to a marked voxel, or (b) not a simple point. If these conditions are not satisfied, p is marked and all black 26-adjacent voxels of p are pushed into Q_2 . Then go to Step 3.

Examples of extracted GT networks without endpoints (i.e. without geometry preservation) are shown in Figure 3-38(b) and Figure 3-39(b) and (c).

Extraction with Geometry Preservation

For the end application, a GT network with geometry preservation (i.e. with endpoints) is necessary. In addition to the above algorithm for extracting the general network, the GT network must also include geometrical properties.

Removing isolated pores and cavities (pre-processing): Isolated pores and floating solid particles (cavities) do not contribute to fluid flow and should be removed before a network structure is constructed for a specific model. An isolated pore is a black 26-component in porous images, and is usually thinned into a single voxel by homotopic thinning. A cavity is a white (solid) 6-component in rock images, i.e. an isolated solid particle floating in the PS, which produces a surface skeleton rather than a curve skeleton. An example of a surface skeleton (spherical surface) is shown in Figure 3-39(b). Firstly, a $3 \times 3 \times 3$ constructing element is chosen and a morphological opening (dilating after eroding) is conducted in order to smooth rock images. Secondly, the extended HKA is used to determine isolated pores in a rock image, and all the isolated pores which do not link to image boundaries are then removed (i.e. replaced by solid). A similar operation is performed to determine all isolated solid parts (cavities) and to replace them by pores.

Computing SEDM near boundaries: In order to retain boundary points on the inlet and outlet, for calculation of the distance map I suppose that all voxels beyond the boundaries are pore voxels.

Retaining endpoints: In Step 4 above, marked voxels are checked to determine whether they occur on a boundary. If a marked voxel occurs on a boundary without any other 26-adjacent voxels of larger or equal distance value, then it is retained as a boundary point. Similarly, to retain branch points, all voxels with distance value larger than the threshold are checked. If a marked voxel has no 26-connected pore voxels with larger or equal distance value, then it becomes a branch point. Examples of extracted GT networks with endpoints are shown in Figure 3-39(c) and (d).

3.5.4 Theoretical analysis

In the following, some basic definitions and notions which are closely related to the study of digital topology are presented, and then I give the proof of the theorem.

(1) Basic definitions and notions

According to Kong and Rosenfeld (1989[76]), a 3D binary image \mathcal{P} is defined as a quadruple $\mathcal{P} = (\mathcal{V}, \alpha, \beta, \mathcal{B})$, where $\mathcal{V} \subset Z^3$ is a subset of the integer space Z^3 in which a point p is defined as a triple (p_1, p_2, p_3) with integer coordinates. A point p is assigned a value of 0 if it belong to background (white point $p \in \mathcal{V} \setminus \mathcal{B}$, i.e. $\mathcal{P}(p) = 0$) or 1 (foreground or black point: $p \in \mathcal{B}$, i.e. $\mathcal{P}(p) = 1$), denoted by $\mathcal{P}(p)$ or $\mathcal{P}(p_1, p_2, p_3)$. During the following image processing, a finite cubic lattice $\mathcal{V} = \{(x_1, x_2, x_3): L_{0i} \leq x_i \leq L_{1i}, x_i \in Z, i = 1, 2, 3\}$ is used. \mathcal{B} is the set of all black points (or object points), and (α, β) is a pair of adjacencies for foreground and background, respectively. (26, 6), (6, 26), (18, 6), and (6, 18) are commonly used adjacency pairs, which are constrained by the Digital Jordan's Curve/Surface Theorem (Rosenfeld, 1979[137]). We use 26-adjacency for black points (in \mathcal{B}) and 6-adjacency for white points ($\mathcal{V} \setminus \mathcal{B}$) because the adoption of such a scheme generally leads to smoother skeletons (Kong and Rosenfeld, 1989[76]). More details of the associated topology can also be found in the previous sections of this thesis.

Definition 1 – Adjacency and neighbourhood: For any two distinct voxels p and q , three adjacencies (6-, 18- and 26-adjacencies) have been defined and discussed in Chapter 3 (see Definition 3.3 and Equation (3.3)). The corresponding neighbourhoods of a point p are denoted as $\mathcal{N}_\alpha(p)$ ($\alpha = 6, 18, 26$). For a set of points $S \subset Z^3$, $\mathcal{E}_\alpha(S) = \cup_{p \in S} \mathcal{N}_\alpha(p)$ is called the α -envelope of S .

Definition 2 – Path and component: A sequence of distinct points $\langle x_0, x_1 \dots x_n \rangle$ is said to be an α -path from point x_0 to point x_n if x_i is α -adjacent to x_{i-1} for each $1 \leq i \leq n$ ($\alpha = 6, 18, 26$). Let S be a subset of Z^3 , then two points p and q are α -connected in the set S if there exists a α -path in S between p and q , i.e. $x_0 = p$, $x_n = q$, and $x_i \in S$ for each $0 \leq i \leq n$. A set S is α -connected if any two points in S are α -connected in S , in which S is also called a α -component. For a 3D image $\mathcal{P} = (\mathcal{V}, \alpha, \beta, \mathcal{B})$, a α -component of \mathcal{B} is often called a black component, a β -component of $\mathcal{V} \setminus \mathcal{B}$ is called a white component of \mathcal{P} .

Definition 3 – Topological number (Bertrand, 1994[14]): For any voxel p , $\mathcal{T}_{26}(p, \mathcal{B})$ is the number of black 26-components of $\mathcal{N}_{26}(p) \cap \mathcal{B} \setminus \{p\}$ and $\mathcal{T}_6(p, \mathcal{V} \setminus \mathcal{B})$ is the number of white 6-components in $\mathcal{N}_{18}^*(p)$, in which each component contains at least one white 6-neighbour of p (see Definition 3.6). The set of such white points is denoted by $\mathcal{G}_6(p)$ called the geodesic neighbourhood.

Definition 4 - Simple Point: Bertrand (1994[14]) presented the following local characterization of a simple point. Let $p \in \mathcal{B}$ be a black point in a 3D image \mathcal{P} . Then, p is a 26-simple point (a simple point for short) if and only if $\mathcal{T}_{26}(p, \mathcal{B}) = 1$ and $\mathcal{T}_6(p, \mathcal{V} \setminus \mathcal{B}) = 1$.

Definition 5 - Simple Set: A set S of points is said to be simple in the 3D image \mathcal{P} if the points of S can be arranged in a sequence in which each point is simple after all of its predecessors in the sequence have been removed from \mathcal{P} (Ma, 1994[95]; Gau et al. 2003[50]).

The above definition is not quite useful for identifying a simple set directly from original images, and we have not yet found a practical algorithm to identify a simple set

even though some progress in this research has lately been made by Lohou and Bertrand, (2004[91] and 2005[92]). In our algorithm, if a set cannot be recognized as simple, each point in the set must be checked individually in the way of one point after another in our algorithm. There are three additional concepts needed which are defined below.

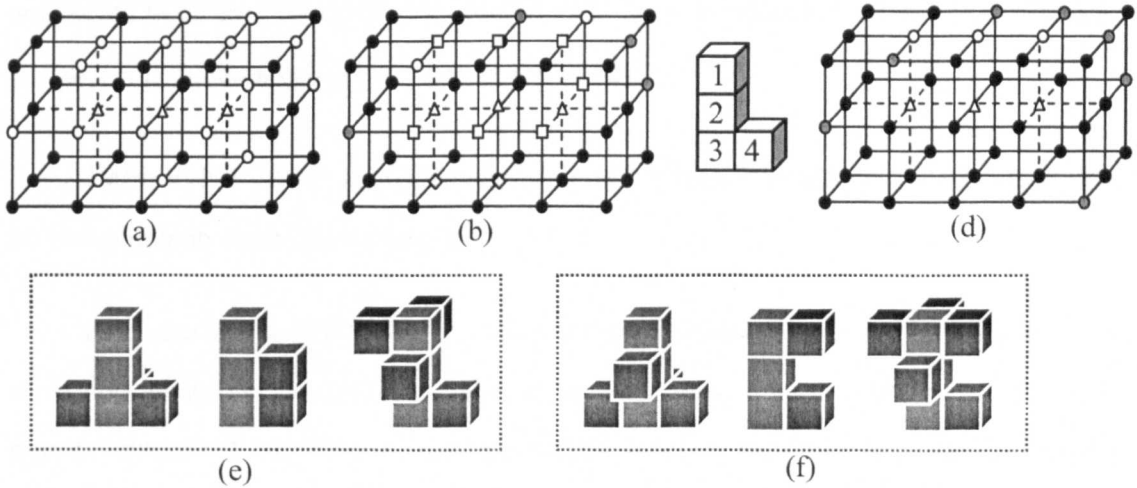


Figure 3-40: The Illustration of adjacent components and some examples of simple sets. (a) An example of a local configuration of black and white circle voxels in the envelope of S (triangle voxels); (b) $E_B(S)$ is the set of all black circle voxels; $E_{WB}(S)$ is the set of all square and diamond voxels, and $E_{W8}(S)$ is the set of all white circle voxels, note that grey voxels will be ignored according to definitions 6 and 7. Obviously there is only one black adjacent component of S , but two white adjacent components (set of squares and circular voxels, set of only diamond voxels). (c) The set of $\{1, 2, 3\}$ is a pure 6-component (definition 8) but not if including 4 because that 2 is 18-connected with 4; (d) All white 6-neighbours of triangle voxels are directly 6-connected ($E_{W8}(S)$ is empty). In (e) and (f), all object (pore) voxels are explicitly identified but all non-object (solid) voxels are omitted for simplicity: (e) the pure 6-components (set of grey voxels) can be simultaneously deleted because in their envelopes there is only one black adjacent component and one white adjacent component; (f) the pure 6-components (set of grey voxels) can not be identified as simple sets based on the theorem 1.

Definition 6 - Adjacent black component: Let $S \subset \mathcal{V}$ and $E_B(S) = (E_{26}(S) \cap \mathcal{B}) \setminus S$ be the set of black points excluding elements of S in the 26-envelope of S . Each 26-connected subset of $E_B(S)$ is called an adjacent black component of S .

Definition 7 - Adjacent white component (see Figure 3-40): Let $S \subset \mathcal{V}$ and $\mathcal{E}_{w6}(S) = (\mathcal{E}_6(S) \cap (\mathcal{V} \setminus \mathcal{B})) \setminus S$ be the set of white points in the 6-envelope of S , but excluding elements of S . Further, let $\mathcal{E}_{w18}(S) = ((\mathcal{E}_{18}(S) \setminus \mathcal{E}_6(S)) \cap (\mathcal{V} \setminus \mathcal{B})) \setminus S$ be the set of white points in the 18-envelope, of S , but excluding elements of S , and let each point in $\mathcal{E}_{w18}(S)$ be 6-connected to at least two points in $\mathcal{E}_{w6}(S)$. Then each 6-connected set of $\mathcal{E}_w(S) = \mathcal{E}_{w6}(S) \cup \mathcal{E}_{w18}(S)$ is called an adjacent white component of S .

Definition 8 - Pure 6-component: Let $S \subset \mathcal{V}$ be a 6-component, then S is pure if no two points in S are 18-connected.

From the above definition, it is apparent that S looks like a “straight segment” in three coordinate directions of the discrete space Z^3 (see Figure 3-40(c)). So, for each pure 6-component, there are exactly two terminal voxels and any other voxel is called a non-terminal voxel.

(2) Sufficiency condition for a simple set

Theorem 3.2 - Sufficiency condition of simple set: Let $S \subset \mathcal{B}$ be a pure 6-component in an image $\mathcal{P} = (\mathcal{V}, 26, 6, \mathcal{B})$. S is simple if the number of black adjacent components of S is 1 and the number of white adjacent components of S is also 1.

Proof: From definition 8 for the black pure 6-component S , if an order, in which all voxels in S can be deleted one after another without changing the topology of \mathcal{P} , can be found, then this theorem will be proved, i.e. S is a simple set. Firstly, I will prove that there always exists a simple point p in S , and then the remaining set $S \setminus \{p\}$ consists of either only one black pure 6-component S_1 or two black pure 6-components S_1 and S_2 . Secondly, I will prove that if both S_1 and S_2 exist, the condition of theorem 3.2 will be met.

Existence of a simple point p in S : From definition 6 above, there exists at least one point p in S such that the number of white 6-neighbors of p is larger than 0, denoted by $\mathcal{T}_6(p)$. Otherwise, $\mathcal{E}_{w6}(S)$ is empty, and hence $\mathcal{E}_{w18}(S)$ is also empty, which disagrees with the condition (i.e. the number of adjacent white components of S is 1). If there is not any point p in S such that $\mathcal{T}_6(p) > 1$, then, based on this condition, all white 6-

neighbours of such voxels of $\mathcal{T}_6(p)=1$ in S must be directly 6-connected (shown in Figure 3-44(d)), and obviously it must be a simple set (Ma, 1994[95]). Suppose that there is no such point of $\mathcal{T}_d(\cdot) > 1$ in S such that it is a simple point. Having a point p in S with $\mathcal{T}_d(p) > 1$ means that the number of white 6-neighbours of p is larger than 1, and hence the number of elements in $\mathcal{E}_{w6}(S)$ is larger than 1. If $\mathcal{E}_{w18}(S)$ is empty, then all elements in $\mathcal{E}_{w6}(S)$ cannot be 6-connected becoming only one white component. Thus, $\mathcal{E}_{w18}(S)$ is not empty and, according to definitions 6 and 7, for each point in $\mathcal{E}_{w18}(S)$ there are at least two 6-neighbors in $\mathcal{E}_{w6}(S)$. Therefore, we have at least one point p in $\mathcal{E}_{w6}(S)$ such that all its white 6-neighbours are 6-connected through some of the elements in $\mathcal{E}_{w18}(S)$, thus p is a simple point by definition 4 above.

All 6-components in $S \setminus \{p\}$ are pure and meet the conditions of Theorem 3.2: The remaining set $S \setminus \{p\}$ may be either one pure 6-component S_1 (when p is a terminal voxel) or two pure 6-components S_1, S_2 (when p is a non-terminal voxel), if the number of elements of S is larger than 1. For the first case, according to definitions 6 and 7, we have that $\mathcal{E}_B(S) = \mathcal{E}_B(S_1)$ and the number of white adjacent components of S_1 must be 1 because p is a simple point and p is also a 6-neighbour of one voxel in S_1 . For the second case, there are only two possibilities that $\mathcal{E}_B(S) = \mathcal{E}_B(S_1) = \mathcal{E}_B(S_2)$ or one of S_1, S_2 , denoted by S_{n1} , which has the same adjacent black set as S (i.e. $\mathcal{E}_B(S_{n1}) = \mathcal{E}_B(S)$), meanwhile the other one, denoted by S_{n2} , has an empty black adjacent set (i.e. $\mathcal{E}_B(S_{n2}) = \emptyset$). For S_{n2} , the deletion sequence can be easily determined by starting from a terminal voxel, so $S_{n2} \cup \{p\}$ is a simple set (Ma, 1994[95]). For the same reason, the number of white adjacent components of S_{n1} must also be 1.

It is straightforward to prove that when S contains only one black voxel, this theorem is equivalent to the definition of simple point (definition 4) and therefore the theorem has been proved. Therefore, this theorem can be considered as being the extension of local characterization of a simple point, but here only a sufficient condition for the identification of simple set of a special set (pure 6-component) is given.

(3) Thinning based on theorem 3.2

Based on this theorem, in the GT network extraction, for a given candidate set S , all black 6-components in S will be firstly clustered using the HKA (Hoshen and

Kopelman, 1976[59]). These clusters might be removed simultaneously rather than as single points, depending on the following detection result. To determine black/white adjacent components of the black 6-component, the algorithm starts scanning the envelope of each black 6-component S' ; if one voxel in S' is 18-connected to any other scanned voxel in S' , then the scanning process stops, and a pure 6-component is found. Later, the number of black/white components can also be counted using the extended HKA again. If this is a simple set, it will be labelled as a deletable set, otherwise each voxel of this black 6-component will be checked for its simplicity.

In addition to the above improvement (i.e. checking the simplicity of a set rather than a point), a further increase in efficiency is possible if other features of thinning are taken into account. Because the simple point/set is only related to its neighbourhood or envelope, i.e. the change of any point beyond the neighbourhood or envelope does not affect the deletability. Thus, after an iteration of thinning, only those neighbouring voxels are taken as a candidate set, which are 26-connected to a simple voxel or one voxel in a simple pure 6-component, so the number of detections for deletability can significantly be reduced.

3.5.5 Examples of GT network

Illustration of the thinning processing: In the pore structure analysis, the GT network (skeleton) of the PS of a 3D rock image is extracted, starting from the outside of the PS, according to the squared Euclidean distances and certain rules to remove pore voxels layer by layer. In Figure 3-41, this process is illustrated for a sandstone image.

Central location of the GT network: Using the same rock image, the GT network of the PS is plotted in Figure 3-42. Visually the central location can be recognised immediately.

GT network with adjustable branches: To retain the links to inlet and outlet, some simple points on the border of an image should be kept. But improper rules could lead to a lot of false links appearing in the resultant GT network. In Figure 3-43, the first column shows two examples of this problem which is a side-effect of the retention of border points. To tackle this problem, in the thinning algorithm, local maxima are regarded as the candidates for retaining, but a check in the larger (e.g. $5 \times 5 \times 5$) neighbourhood rather than the $3 \times 3 \times 3$ neighbourhood is carried out. During an iteration,

all border voxels, that have local maxima in the corresponding SED map and have no other candidates in their $5 \times 5 \times 5$ neighbourhoods, will be retained in the resultant GT network. The result is shown in the second column in Figure 3-43.

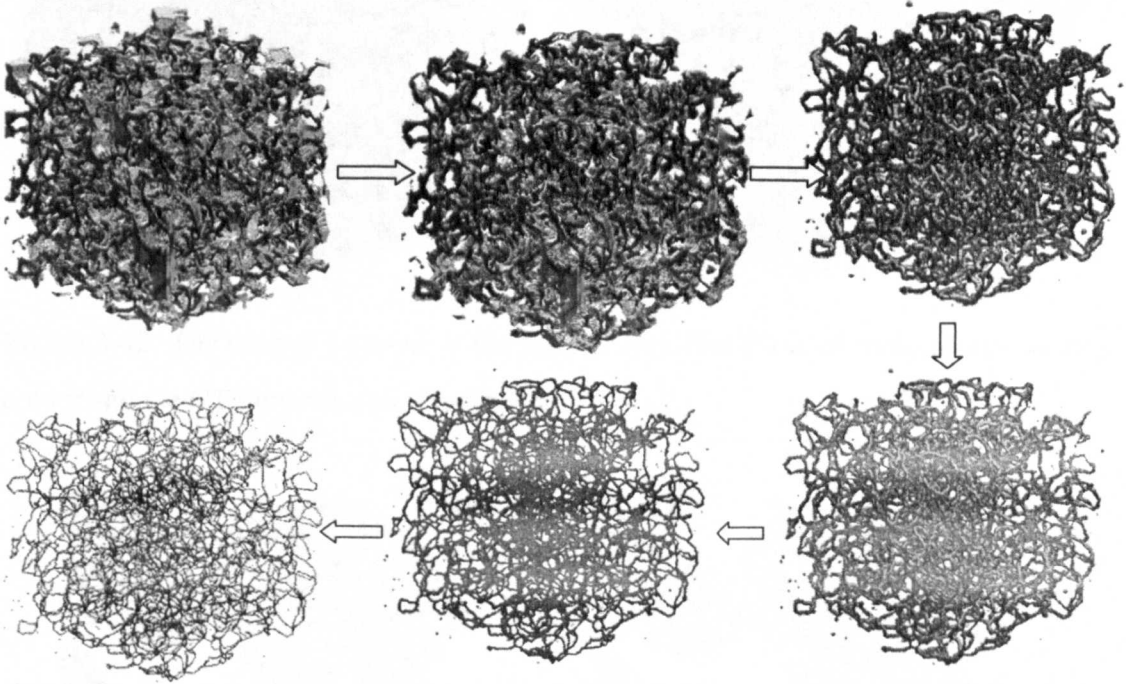


Figure 3-41: A schematic illustration of the thinning process to extract the GT network of a sandstone sample.

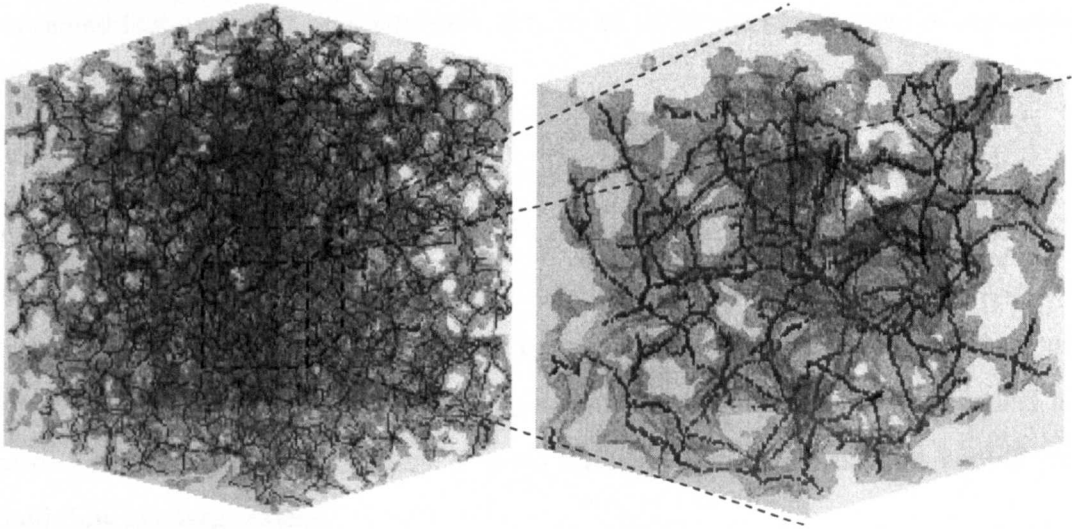


Figure 3-42: The central location of the GT network (the PS is of transparency in grey colour and the GT network coded in black).

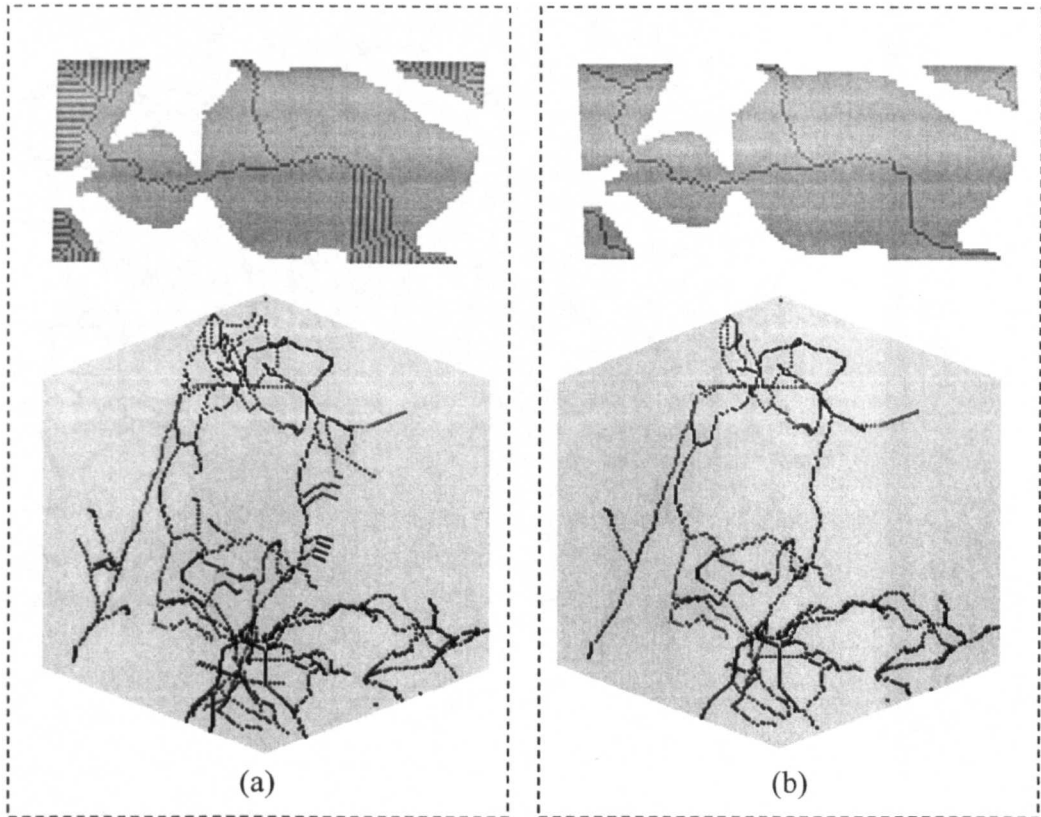


Figure 3-43: (a) Networks with many false links at the boundaries, when too many boundary points are retained; (b) networks after checking its $5 \times 5 \times 5$ neighbourhood trying to find if there are any other border points which's distance value equal to or larger than current border point and they are not deletable points at current iteration. Doing so can ensure that as less as possible border points are retained, but some

unwanted feature cannot be completely eliminated under the requirement of reasonable efficiency.

GT network with cross sectional radii: The thinning order in the algorithm is guided (controlled) by the SED map. This ensures the central location of the GT network and it also provides information about the cross sectional radii at each skeleton point (see Figure 3-44). The latter is very useful when numerical simulation of mercury injection and computation of fluid transport properties through the network model are carried out, because the distribution of cross sectional radii on the skeleton controls the fluid flow to a large extent.

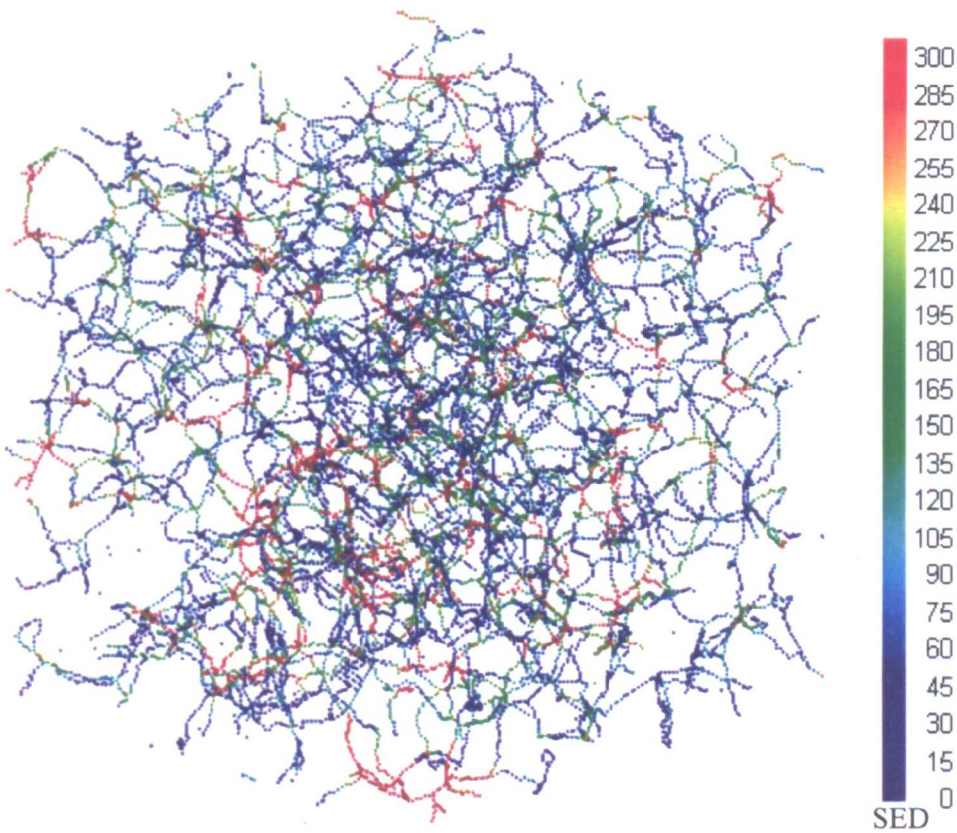


Figure 3-44: GT network with cross sectional radii. The value is coded by the Rainbow colour system, in which the blue represents the smallest SED (i.e. 1) while the red represents the largest SED value.

3.6 Conclusion

The Euclidean distance transformation developed by Shih and Wu (2004a[154]) is extended to 3D with several improvements including (1) simplifying the comparison of SED values in a $3 \times 3 \times 3$ neighbourhood, (2) avoiding complex decomposition of the SED structure and (3) being easy to implement and to understand. These features in my algorithm are achieved by introducing a simple SED relationship (3.16) between neighbouring voxels and pre-calculating the distance coefficient (see (3.17) and (3.18)). Also, the efficiency is improved by only computing the new distance for the current voxel through its already-accessed neighbours in the current scan, rather than through the whole $3 \times 3 \times 3$ neighbourhood. Moreover, I have explored other distance transformations such as geodesic chamfer or Euclidean DT, which can be used to compute the length of flow paths and to partition the pore space. Using geodesic chamfer distance with CDC of (3, 4, 5), the upper bound on the difference between chamfer and Euclidean distances is minimized (Borgefors, 1984[24]), and the maximum achievable Euclidean distance limit without topological errors is guaranteed (Marchand-Mailler, 1999[101]). For the geodesic Euclidean transformation, however, only an approximation algorithm is given and more work needs to be done in pursuit of an efficient implementation of the GED transformation.

The first very successful clustering algorithm was developed by Hoshen and Kopelman ([59]) in 1976, which was extended into 3D later by themselves and other researchers. This algorithm can produce both the clustering label and the number of clusters after two-pass scans (forward and backward). If only the number of clusters is required, only a single pass scan is necessary. In the pore structure analysis, different adjacencies (26-, 18-, 6- and λ -adjacencies) need to be considered for either foreground or background or for different rocks (e.g. sandstone and siltstone). Thus, I have extended the HKA for varying adjacencies and I have further improved its efficiency by introducing a new data structure for storing temporary labels and its searching algorithm with an object-oriented implementation.

To quantify pore connectivity, the basic features of the Euler number have been intensively analysed and a new computation method has been introduced. The Euler number is a single number describing the overall topology, i.e. decreasing negative values indicate increasing connectivity. In Chapter 5, I explore its sensitivity to imaging noise on three sandstone samples, which reveals instabilities (Figure 3-32). This indicates that the Euler number cannot be simply used as a topological descriptor.

Compared to Saha and Chaudhuri's approach (1995[139][139]), the computation of the change in the Euler number in $3 \times 3 \times 3$ neighbourhood is improved by establishing a relationship (3.27) between topological numbers (they can be easily calculated by invoking the extended HKA) and numbers of tunnels and cavities, rather than by building up a look-up-table with 2^{26} entries. To tackle the side-effect of tiny isolated pores and floating solid particles on the Euler number, a more effective topological descriptor will be presented in Chapter 5.

Taking into account topology-preservation, central location, thinness and integration of geometry (e.g. primary branches, dead-end links and boundary links), I have developed an efficient and robust homotopic thinning algorithm to generate the pore GT-network (skeleton). Using the new strategy of symmetric delay deletion and new data structures, the thinning process in my approach is controlled by descending Euclidean distance order. The simplicity of a set or a point is checked using the extended HKA. Compared to other thinning algorithms, in addition to topology-preservation and thinness the significant different features of our skeletonization can be stated as follows:

(1) Central location: Using the exact SED to guard the thinning process ensures, to a large extent that the resultant GT-network is located in the central flow path of pore channels. Besides, symmetric delay deletion and avoiding checking neighbours or envelopes push the GT-network further near or at the central lines, even within equal-distance regions.

(2) Efficiency: Checking the simplicity of sets rather than only points significantly increases the number of deletable voxels at each iteration. And avoiding the checking of the envelope of a simple set or the neighbourhood of a simple point within an iteration reduces the number of detections for deletable voxels.

(3) Adjustable primary branches and boundary links: Using the pure topological skeleton as central lines, a geodesic chamfer distance map can be computed in which zeros are assigned to solid voxels, and the GCD value of pore voxels relative to the pure skeleton are assigned to the pore voxel. Selecting a percentage of the maximal GCD value in the distance map, voxels that have large enough GCD values and the corresponding branches are retained in the resultant skeleton. Similarly, for each region in the inlet or outlet (boundaries), only one voxel is retained leading to a boundary links satisfying the $5 \times 5 \times 5$ checking rule.

Chapter 4 Pore Structure Analysis

Techniques

From the geometric point of view, the total pore space of a porous medium is considered as a set of connected pores. Pore structure analysis then consists of the study of geometric properties such as the pore size distribution. Taking topological features into account, the pore space can be referred to as a network of pore elements, often partitioned into nodes (pore-bodies) and bonds (pore-throats), with the nodes being linked by bonds. Furthermore, to each network element (a node or bond) we can attach a range of geometric attributes (e.g. shape factor, size, volume, coordination number etc) based on a series of image processing operations conducted on 3D rock images. With such a realistic pore network representation, we can idealise the pore space into a network flow model that allows the prediction of transport properties. In this chapter, I focus on three issues: (1) to partition the pore space into a set of pore elements; (2) to compute the shape factor of each pore element; and (3) to construct a pore network representation.

4.1 Partitioning the Pore Space into a Set of Pores

According to Dullien (1992[44]), pores can be defined as those portions of the pore space (PS) confined by solid surfaces and planes erected where the hydraulic radius of the PS exhibits local minima. Although this definition can lead to a good partitioning of the PS using a multi-orientation scanning algorithm, apparently it can result in the identification of too many false pore-throats (Zhao et al., 1994[193]), and the definition does not provide a robust way to separate pore bodies from pore-connection elements. This definition is also very time-consuming to implement in discrete space (Liang et al., 2000a[84]).

If each pore in a porous medium is regarded as being of approximately spherical shape, then the PS can be partitioned into a set of sphere-equivalent pores (plus or

minus connection elements). This kind of approaches to partitioning of the PS into a set of individual pores is often classified as a sphere-fitting technique in the literature. The basic idea is simple (see Figure 4-1): a series of maximal inscribed spheres are fitted into the PS, and then the PS is partitioned into the set of spherical pores represented by those spheres.

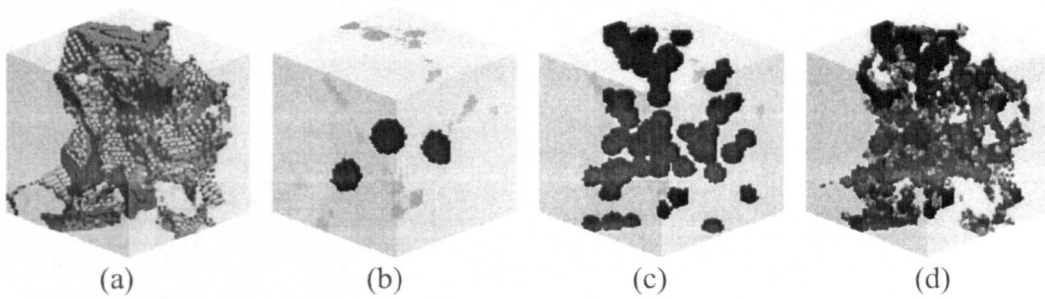


Figure 4-1: Illustration of sphere-fitting partitioning of the pore space. (a) The PS in a porous medium; (b) three largest maximal inscribed spheres are fitted into at the very beginning; (c) many smaller maximal inscribed spheres are further fitted into; (d) the whole PS is occupied by a set of different spherical pores in the end.

Unfortunately, two major problems are bound to appear when the sphere-fitting method is used to partition the PS. Firstly, the discrete spheres used in sphere-fitting methods are quite coarse due to the nature of discrete space. In Figure 4-2, for example, three discrete spheres (with radius of 0, 1, and 2, respectively) are used as three basic sphere-like templates to be fitted into the PS. It is clear that this scheme could result in a vague partition of the PS, because just a few small sphere-templates cover a very large range of sizes of the PS. The three sphere-templates shown in Figure 4-2 contain 1, 7 and 33 voxels, respectively. And the number of voxels between the two spheres of radii 1 and 2 is 26. In general, any local region in the PS that consists of more than 7 but less than 34 voxels will be classified as a pore of radius 2. In fact, a reasonable partition could be chosen such that a local pore region consisting of more than 15 but less than 45 voxels is considered as a pore of radius 2. For this reason, i.e. that there may be a large number of differently-sized pores that occur between two discrete spheres of radii r and $r + 1$, the general sphere-fitting method produces a coarse partitioning of the PS, and the pore size determined by this partition may have little value for pore structure analysis when the imaging resolution is quite low.

Secondly, too many false, tiny spherical pores are typically created. According to Dullien (1992[44]), a pore should be surrounded by a ring (or a path) composed of the solid. Otherwise, it should be regarded as a false pore. In Figure 4-3, some spheres (discs in the drawing) are fitted into the remaining PS which is generated by removing the two larger pores. These spheres are not surrounded by any rings within the solid region in 3D. Such false pores are usually very small and may be composed of one single voxel.

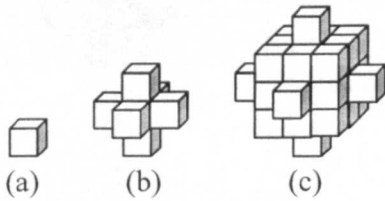


Figure 4-2: The three discrete sphere-templates of radius 0, 1, 2 respectively.

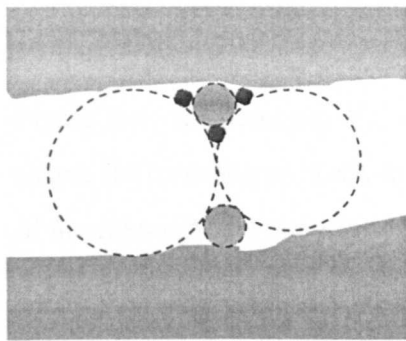


Figure 4-3: Some tiny spheres (filled) are fitted into the PS when large pores have been removed from the PS.

To overcome these major drawbacks and to improve the algorithm efficiency, I present a new version of the sphere-fitting method based on the skeleton and distance map derived from 3D rock images. In this method, no predefined sphere-templates are needed and the issues important to fluid flow through the PS are taken into account. The latter consideration means that dead-end pores may not be regarded as individual pores because no fluid flows through them. The partitioned PS is clustered into a set of irregular-shaped large pores of distinct sizes rather than into spherical pores, and the method avoids identifying a large number of false tiny pores.

4.1.1 Euclidean Distance Valued Skeleton

Instead of directly operating on the original binary images of porous media, the presented sphere-fitting partitioning method in this subsection is based on a composite image which is generated by combining together two images – the skeleton (i.e. GT network or MA) and the distance map.

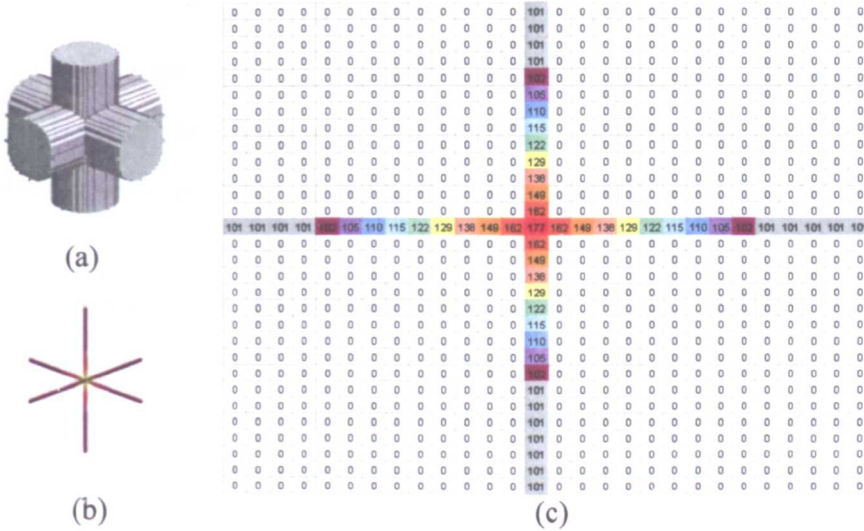


Figure 4-4: An example of coloured skeleton: (a) a 3D geometric object of regular shape; (b) its coloured skeleton, where the colours are used to code the SEDs; (c) a part of the coloured skeleton locating on the XY plane at the central point.

A pore skeleton is a 1D entity that retains the pore topology, and it is used to represent the central-lines of flow paths. Using skeletons rather than the original images, many image operations can be implemented in a much easier and more efficient way. In addition, the distance value at each skeleton voxel coincides with the radius of the corresponding inscribed sphere, which makes the calculation of the inscribed radius easy. Combining the skeleton and the distance map of a porous image together, the new image is called the Euclidean distance valued skeleton, or coloured skeleton for simplicity. For example, the skeleton of the geometric object shown in Figure 4-4(a) is composed of three central-lines (Figure 4-4(b)), and to each voxel on the skeleton a distance value is assigned based on the distance map. In a distance map, for each background (solid) voxel its distance is zero and for any other object (pore) voxel the distance is defined as the SED to its closest background voxel. The colours in Figure 4-4(b) are used to represent different distance values along the skeleton, and a part of the coloured skeleton on the XY plane is illustrated in Figure 4-4(c) where the SED values are also given.

4.1.2 New Sphere-fitting Approach

There are two steps involved in the new sphere-fitting approach. Firstly, the Euclidean distance valued skeleton is partitioned into various regions of different sizes based on the SED map. Such a region of skeleton voxels is a 26-connected component and its equivalent pore size is determined by the maximum SED in the region. In the algorithm, after identifying all such regions the original coloured skeleton is modified to another skeleton in which each voxel in a partitioned region has the same SED value. Secondly, each region on the modified skeleton is expanded within the PS into an individual pore, and the corresponding region on the skeleton is then called the backbone of the individual pore. For example, the coloured skeleton (the central-line) in Figure 4-5(a) is partitioned into three regions (segments) shown in Figure 4-5(b), and an algorithm of volumetric partitioning is then used to expand the three regions into three individual pores shown in Figure 4-5(c). In this method, pore sizes are determined by the distance values and pore boundaries are formed by the normal planes and the surfaces of inscribed spheres centred on the skeleton. The sphere-fitting process is guided by a descending size order and a non-overlapping restriction. In other words, larger pores are extracted before smaller pores and no overlapping between inscribed spheres is allowed. These two features ensure that rigorous pores are extracted and no false tiny pores appear in the resultant partitioning. This algorithm can be described as two steps:

Step 1: Fitting and cutting out backbones of individual pores. Scanning the coloured skeleton, a skeleton voxel can be found which has the maximum SED value. Among all the skeleton voxels in Figure 4-6(a), the voxel p shown in Figure 4-6(b) has the maximum SED value (i.e. 16), i.e. the inscribed radius at p is $\sqrt{16}$. Starting from this voxel, a backbone can be generated by grouping in all skeleton voxels: (1) which are connected with that voxel; and (2) whose distances d_{SE} (i.e. $d_{SE}(p, q) = (q_x - p_x)^2 + (q_y - p_y)^2 + (q_z - p_z)^2$) to the voxel are equal or less than the maximum SED value. In Figure 4-6(b), all skeleton voxels within the maximal inscribed sphere (dotted circle) of radius 4 centred at p are grouped as an individual backbone. Hence a modified skeleton (Figure 4-6(c)) is obtained by assigning the SED value of p to all voxels in the backbone. Scanning the skeleton but skipping all skeleton voxels which have already

been grouped into backbones, another voxel (e.g. q in Figure 4-6(d)) having maximum SED value can be found and a backbone is then grouped. This process repeats until all skeleton voxels are grouped into different backbones.

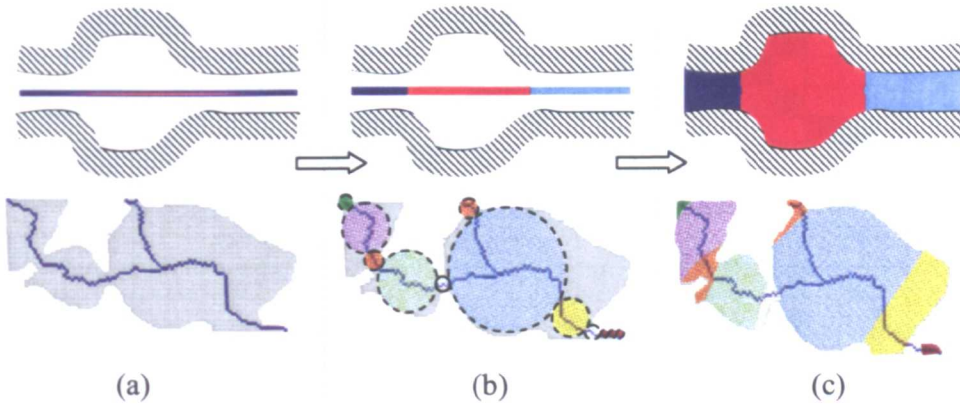


Figure 4-5: Two steps of our sphere-fitting partitioning algorithm. (a) An Euclidean distance valued skeleton; (b) the corresponding modified skeleton associated with maximal inscribed spheres; (c) the set of individual pores. The different colours are used to represent the SEDs of individual pores.

Step 2: Partitioning the PS into a set of individual pores. For each extracted backbone on the modified coloured skeleton, some of its nearby pore voxels in PS are further clustered as an individual pore if each of these pore voxels has the shortest distance to the considered backbone than to any other backbone segment. In Figure 4-7, the original coloured skeleton shown in Figure 4-6 is converted into a modified skeleton of four backbones. These four backbones can then be expanded within the PS into four individual pores by grouping the pore voxels one by one, and the sizes of these four individual pores are determined by the labelling values (i.e. 16, 16, 13 and 4) on the modified skeleton. Using the squared Euclidean distance, the pore voxel p shown in Figure 4-7 is clustered as belonging to an individual pore of size 16 because its distance (25) to the backbone of label 16 reaches to the minimum among the four distances (25, 36, 41 and 61). In the algorithm, the geodesic chamfer distance (see Equation (3.8)) and Figure 3-3) is used to approximate the geodesic Euclidean distance. Doing so ensures that much higher efficiency can be achieved without losing necessary accuracy for pore structure analysis. This is why I selected the geodesic chamfer distance transformation (see Algorithm 3.3 in Chapter 3) to implement the grouping process.

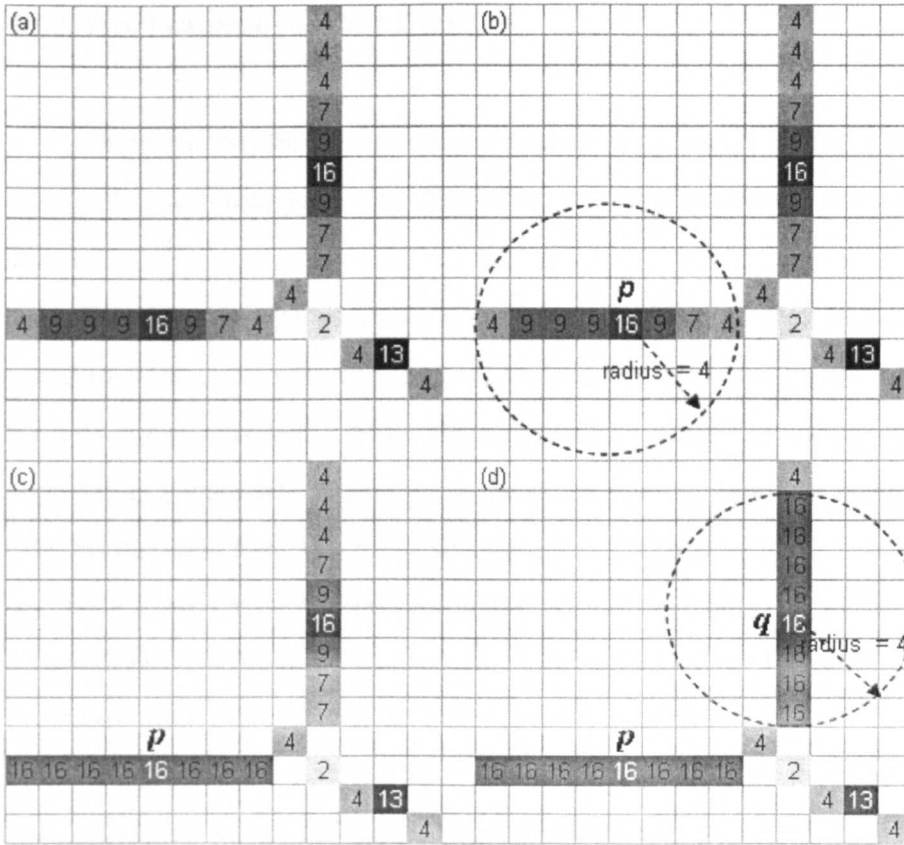


Figure 4-6: 2D illustration of how backbones are extracted from the skeleton. (a) A skeleton with SED values; (b) a voxel p is found which has the maximum SED value (16); (c) all skeleton voxels which are connected to p and locate within the inscribed sphere (circle) are grouped as an individual backbone; (d) another voxel q of the maximum SED is found and the corresponding backbone is obtained.

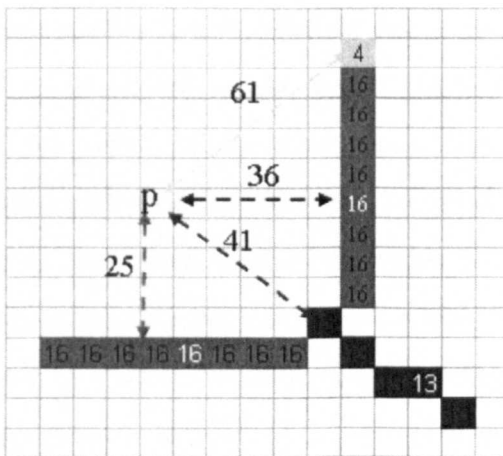


Figure 4-7: Pore voxels are clustered into individual pores of different sizes. A pore voxel p is clustered into an individual pore of size 16 because the distance to its backbone is the shortest one.

4.1.3 Two Features and One Example

There are two features of the pore partitioning which are significantly different to other published methods: being fluid flow relevant and accurate measurement of pore size.

Based on the Euclidean distance valued skeleton of rock images, the PS can be partitioned into a set of irregular pores of different sizes (see Figure 4-6(c)) by applying the GD transformation. Unlike the approach presented by Baldwin (1996[13]), my approach extracts pores starting from the skeleton rather than just anywhere in the PS. A clear relationship between pore partitioning and fluid flow paths is obtained. In fact, in my method, only such regions on the main fluid flow paths (i.e. on the skeleton) can be grouped into individual pores and any other regions in the PS can be either ignored or combined into other pores. In other words, dead-end pores are not considered as individual pores even though they are large. In Figure 4-8(a), the dead-end pore has not been identified as an individual pore because the corresponding branch (the dotted curve) does not appear in the resultant skeleton using the GT network algorithm, which means that there is no fluid flowing through the dead-end pore. Using a network flow model, we will see that the dead-end pores have of little effect on the prediction of macroscopic transport properties, such as absolute permeability or conductivity.

More accurate pore size can be obtained using my algorithm. In Figure 4-8(b), along the skeleton the region between the two maximal inscribed spheres can be filled in by a smaller inscribed sphere (black disc). In general sphere-fitting methods, the size of the corresponding pore at that position is usually labelled by a very small number (i.e. the radius of the black disc). Obviously it is more reasonable if the size is determined by the larger one (the length of the grey segment). In my algorithm, the pore size is determined by the SED value at a skeleton voxel, i.e. the squared Euclidean distance to its closest solid voxel, rather than by the radius of a real maximal inscribed sphere. In addition, no discrete sphere-templates are used in the algorithm, which avoids using discrete radii (1, 2) as pore sizes. This scheme coincides with Thovert's (1993[167]) instinct concept about pores, and also it finds a successful application in the computation of pore size distribution.

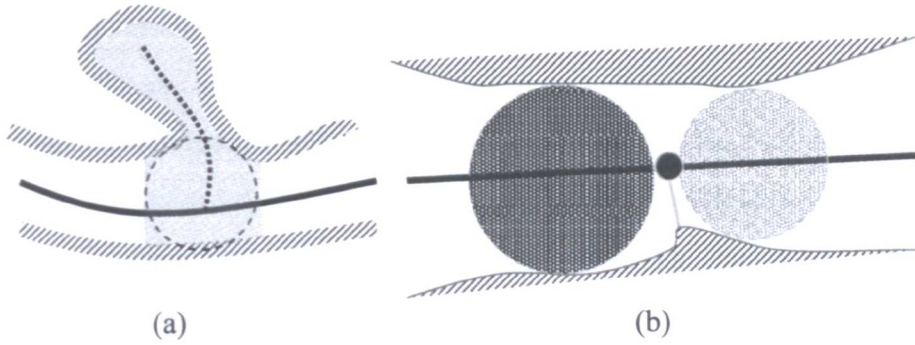


Figure 4-8: Two features. (a) The dead-end pore is not considered as an individual pore instead it is grouped into another pore because the dashed branch does not appear in the resultant skeleton (the black curve). (b) The size of the remaining part on the skeleton after removing two adjacent backbones depends on the inscribed radius (the length of the grey segment) rather than the radius of the inscribed sphere (black disc).

As for an application of the partitioning method, a sandstone sample is used to compute the pore size distribution. Figure 4-9(a) shows a 3D sandstone image where the PS is visible and the solid matrix is transparent for simplicity. To highlight the idea of the algorithm, Figure 4-9(b) illustrates that a subset of the PS is fitted in by a series of maximal inscribed spheres. The green corresponds to the maximum pore size and the red corresponds to the minimum. These inscribed spheres become the central parts (including backbones) of irregular pores demonstrated in Figure 4-9(c), the irregular pores are generated by expanding the central parts using the geodesic chamfer DT with coefficients (3,4,5).

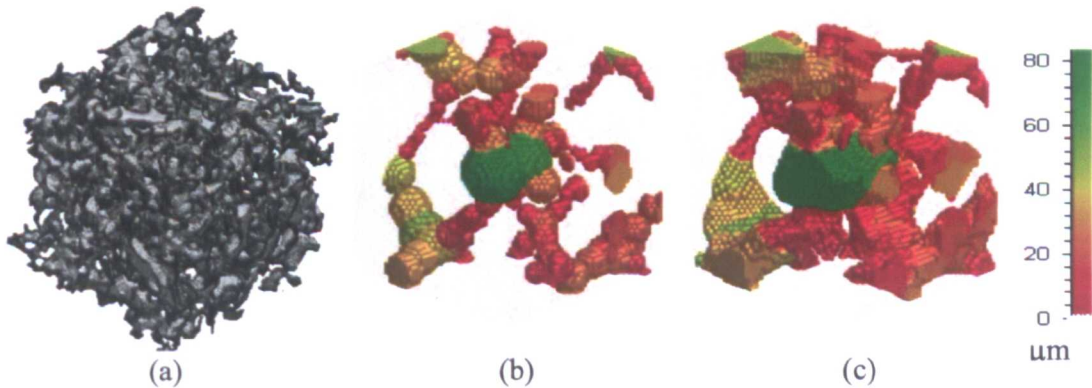


Figure 4-9: An example of our pore partitioning method. (a) The PS of a sandstone sample (porosity is 20.6%, resolution is 5.6 micron); (b): a subset of the PS shown in (a) is fitted in by a series of maximal inscribed spheres (different colours represent different pore sizes); (c) the corresponding partitioned image of irregular and different size pores.

As discussed above, the partitioning approach uses the skeleton to locate the main flow paths and obtains a set of fluid-flow-relevant pores as its output. It also uses the squared Euclidean distance on the coloured skeleton as the pore size rather than the radii of discrete spheres (see Figure 4-2). This second feature leads to finer detail for relevant geometric quantities, such as the pore size distribution. The pore size distribution (PSD) contains the information about how different size pores occur in a porous medium, which has been proved by Vogel and Roth (2001[185]) to be an important geometric descriptor for better understanding of single-/multi-phase flow in porous media. For a partitioned PS B in a rock image \mathcal{P} (e.g. Figure 4-9(c)), the PSD of \mathcal{P} is defined as

$$PSD(r) = \#\{q \in B : r - \Delta_r \leq \mathcal{P}(q) \leq r + \Delta_r\} / \#\{q \in B\} \quad (4.1)$$

where r represents the radius (size) of an individual pore and $\#$ denotes the operation of counting the number in a set. In the resultant partitioned image \mathcal{P} , a pore voxel q is said to belong to a pore of radius r if $r - \Delta_r < \mathcal{P}(q) \leq r + \Delta_r$ for an $\Delta_r > 0$.

Figure 4-10 gives two PSDs of the sandstone sample shown in Figure 4-9(a). Using a series of discrete spheres (see Figure 4-2), the general sphere-fitting obtains a coarse PSD (the black curve shown in

Figure 4-10). It is clear that my algorithm gives much more detail about the PSD.

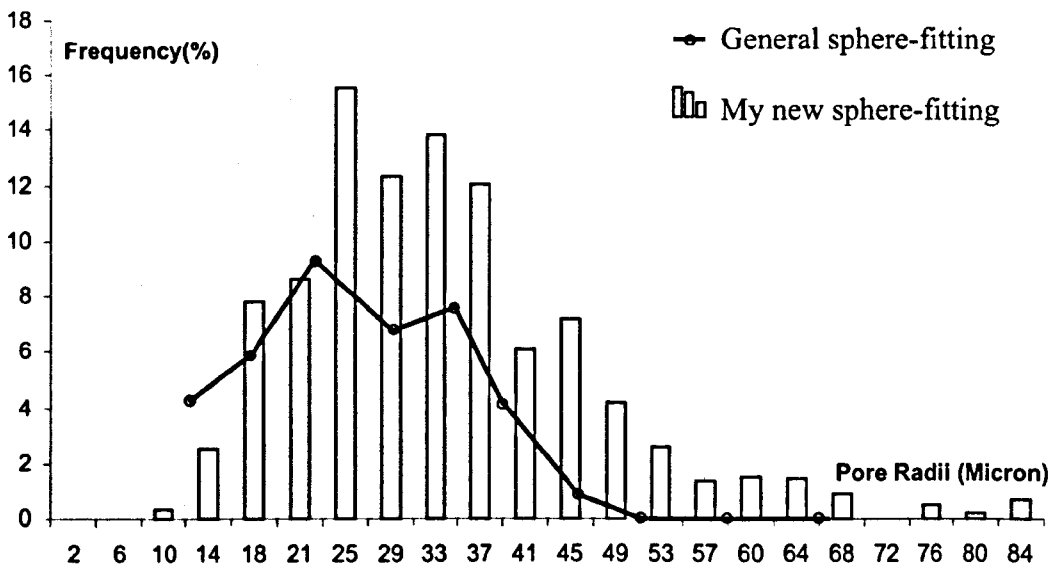


Figure 4-10: Two PSDs of the sandstone sample shown in Figure 4-9(a).

4.2 Calculation of Shape Factor

It is stated by Patzek and Silin (2001[124]) that the hydraulic resistance to flow is mostly in the narrow regions of the PS of a rock. Such a narrow region is commonly represented by a surface which is perpendicular to the flow direction at a point, called a cross section (CS). In a real rock, pore channels have complex and variable CSs. Often they are idealised by triangles of arbitrary shape, rectangles and ellipses in many network models. To quantify the PS or to construct a realistic network structure, however, the complex shapes of CSs need to be described in a much more accurate way.

Mason and Morrow (1991[103]) proposed a dimensionless quantity, the shape factor, to describe irregular shapes (e.g. CSs). The shape factor G of a shape S is defined as its area A divided by its squared perimeter P , i.e.

$$G = A/P^2 \quad (4.2)$$

Some regular shapes with constant shape factor are shown in Figure 4-11. Any square has the shape factor of $\frac{1}{16}$, and any circle has the shape factor of $\frac{1}{4\pi}$. For any triangle, the shape factor ranges from zero for a slit shaped triangle to $\frac{\sqrt{3}}{36}$ for an equilateral triangle.

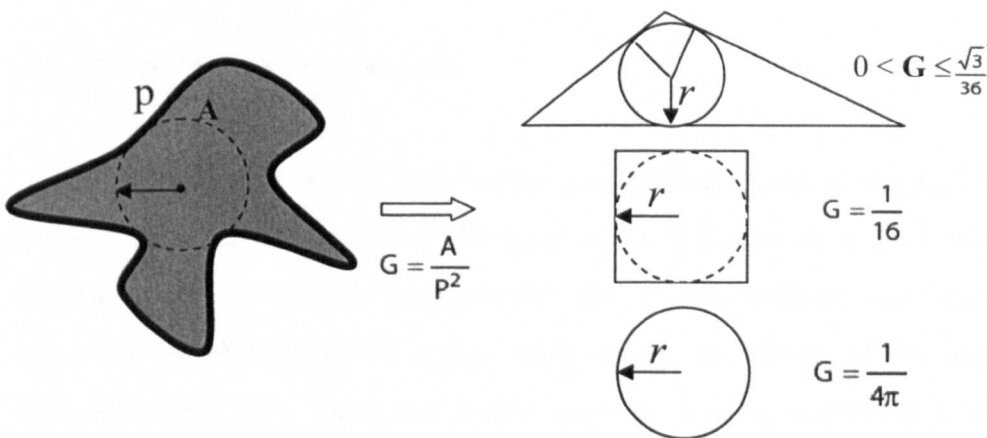


Figure 4-11: The definition of the shape factor and three regular shape factors (Valvatne and Blunt, 2004[170]).

In recent years, many properties and applications of the shape factor have been investigated by many researchers (e.g. Patzek and Kristensen, 2001[124]; Patzek and Silin, 2001[125]). Its computation in 3D discrete space, however, becomes an important

task in the pore quantification and network construction. To my knowledge, no one has given a systematic study about the computation of shape factor for arbitrary spatial shapes. In this section, I describe my efforts in pursuit of such a study.

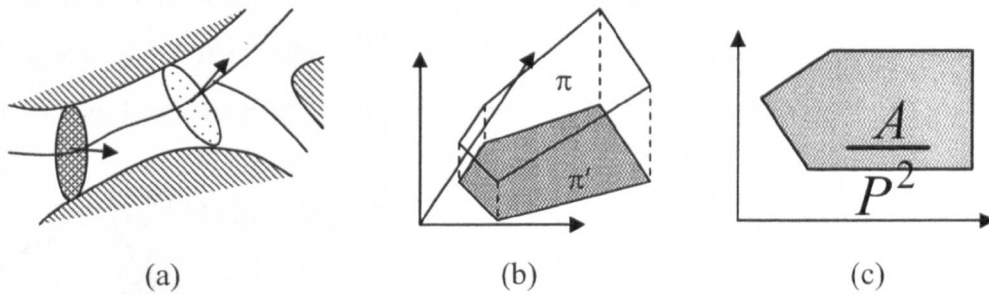


Figure 4-12: The computation of the shape factor. (a) Two CSs are extracted from the 3D PS; (b) a CS π is projected on XY plane and a 2D shape π' is then generated; (c) the cross sectional area A and perimeter P of π' is computed and transformed back to π .

With a 3D binary image of a porous medium, I propose three steps to compute the shape factor: The first step is to extract the CSs from the PS; the second step is to project those CSs to the coordinate planes (XY, YZ or XZ) in order to obtain the corresponding 2D shapes; in the final step the area and perimeter of 2D shapes are computed and transformed back to the original CSs. This process is demonstrated in Figure 4-12, and the details will be given in the following three subsections.

4.2.1 Extraction of Cross Sections

To obtain a CS that is related to the conductance of pore channels, I choose the planar region which is normal to the skeleton (i.e. GT network or the medial axis) of the pore system. As described in Chapter 3, the skeleton extracted using my algorithm has three important features which serve as the foundation of the shape factor computing algorithm. They are: central location, topology-preservation and single-voxel width. The first two features ensure that the extracted CSs are related to the fluid flow, and the third one provides a much more intuitive way to determine the orientations of the CSs. In this section, I present an efficient approach to determine the normal orientation for the partition of individual CSs.

Normal orientation of cross sections

Given a 3D binary image \mathcal{P} of a porous medium and its skeleton SkI , the CS from a skeleton point p is defined as the intersection of the PS with a plane which is normal at p . As described by Liang et al. (2000a[84]), in Figure 4-13, the dotted arrow (i.e. $(x_q - x_r, y_q - y_r, z_q - z_r)$) is used as the orientation of the perpendicular plane at p , which is normal to the skeleton at p . The equation of the plane is given by

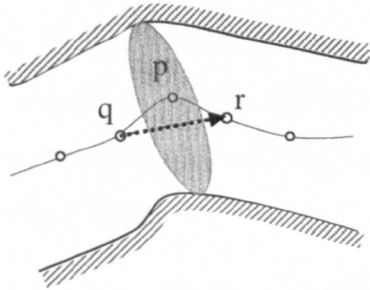


Figure 4-13: A cross section from p normal to the skeleton.

$$(x_q - x_r)(x - x_p) + (y_q - y_r)(y - y_p) + (z_q - z_r)(z - z_p) = 0. \tag{4.3}$$

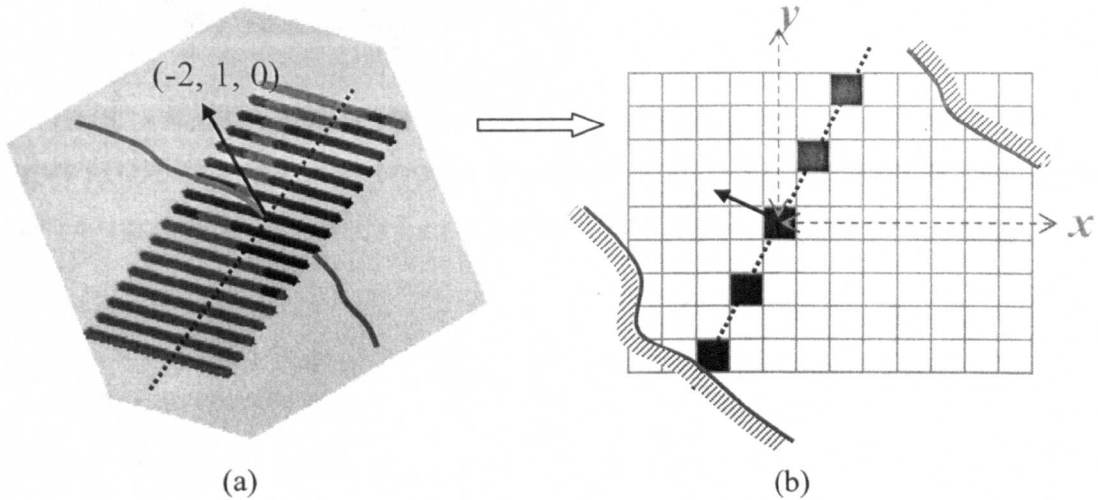


Figure 4-14: A discrete CS (i.e. the black region) is extracted using the plane of $y-2x = 0$. (a) The normal orientation (solid arrow) of the perpendicular plane through the origin of $(0, 0, 0)$ is $(-2, 1, 0)$ and the grey curve is the skeleton; (b) a part (the dashed line) of the perpendicular plane locating on the coordinate place of $Z = 0$ will generate a disconnected discrete line.

Using this equation, in 3D continuous Euclidean space E^3 , bounded CSs can be cut out from the PS. However, in Z^3 discrete CSs are much more complex: at some

points, the corresponding CSs may contain “holes”. For example, with the perpendicular plane (Figure 4-14(a)) of normal orientation $(-2, 1, 0)$ through the origin of $(0, 0, 0)$, a CS (the black region) and a plane are cut out from either the PS or the solid matrix. According to Equation (4.3), the plane can be represented by $y - 2x = 0$, and then the corresponding CS on the XY-coordinate plane must look like the region consisting of discrete lines shown in Figure 4-14(a). For the dashed line, its 2D visualization is showed in Figure 4-14(b), and such a 3D CS of grey voxels is illustrated in Figure 4-15. Apparently the CS plotted in Figure 4-15 is not a 26-connected component because it only contains grey voxels rather than includes the black voxels as well. Intuitively, a disconnected CS may lead to a significant error in the computation of shape factor.

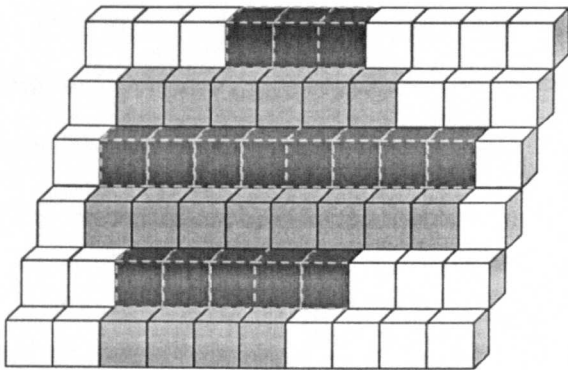


Figure 4-15: The cross section consisting of grey voxels is not 26-connected. It suggests that the region including grey and black voxels should be the desired cross section.

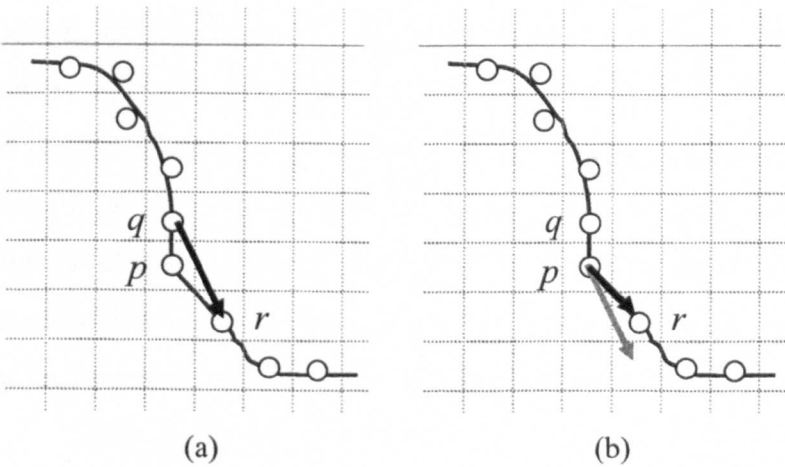


Figure 4-16: 2D illustration of a normal orientation and its approximated orientation. The direction (black arrow) in (a) will result in a disconnected CS, whereas its approximate direction (black arrow) in (b) leads to a connected CS.

The reason that the extracted CSs may be disconnected suggests the way how to choose the normal orientation. As shown in Figure 4-13, the normal orientation of the plane at point p is determined by the positions of its neighbours q and r because the skeleton can be interpolated to obtain the coordinates of any point (in continuous 3D space) around p . In this way, to some configurations in the neighbourhood of a point, the selected orientation at a point is bound to produce a disconnected region in 3D discrete space. For instance, the grey direction $(1, -2, 0)$ at p on the skeleton shown in Figure 4-16 must generate disconnected CSs using Equation (4.3).

To solve this problem (disconnected CSs), one of the thirteen possible orientations is used to approximate the normal orientation. The rule is that the angle between the selected direction and the normal orientation reaches to the minimum over the thirteen angles. The thirteen orientations, denoted by vectors $V_i = (x_i, y_i, z_i)$, $i = 1, 2 \dots 13$, are demonstrated in Figure 4-17 within the $3 \times 3 \times 3$ neighbourhood $\mathcal{N}(p)$ at a point p . Let V be a normal orientation determined by two neighbours q and r of p , i.e. $V \equiv (v_x, v_y, v_z) = (q_x - r_x, q_y - r_y, q_z - r_z)$, the angle between V_i and V is then defined as

$$\theta_i = \arccos\left(\frac{\langle V_i, V \rangle}{|V_i||V|}\right). \quad (4.4)$$

Where $\langle V_i, V \rangle = x_i v_x + y_i v_y + z_i v_z$, $|V| = \sqrt{v_x^2 + v_y^2 + v_z^2}$ and $|V_i| = \sqrt{x_i^2 + y_i^2 + z_i^2}$ for $i = 1, 2 \dots 13$. Thus, θ_i is used to approximate V if $\theta_i \leq \theta_j$ for all $j \in \{1, 2 \dots 13\}$ and $j \neq i$. Having approximated the normal orientations, connected perpendicular planes can be created using Equation (4.3). In other words, for each voxel in the PS, it is on the plane if its coordinates meet the equation. Apparently, this checking is very time-consuming if the PS is large. For this reason, a more efficient algorithm needs to be developed. Instead of checking each pore voxel in the PS, the proposed algorithm generates CSs by starting from skeleton points and keeps expanding the plane border layer by layer. This is implemented using thirteen templates which are shown in Figure 4-17.

Given a 3D rock image $\mathcal{P} = (\mathcal{V}, 26, 6, \mathcal{B})$, for each skeleton point p and an orientation V , we can choose a template \mathcal{T}_V from the thirteen templates in which only black voxels are on the plane (see Figure 4-18).

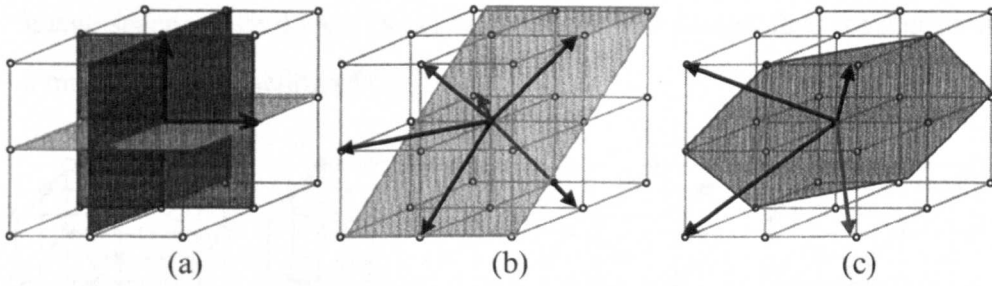


Figure 4-17: Thirteen normal orientation and perpendicular planes (templates). (a) Three orthogonal orientations and their corresponding perpendicular planes; (b) Six diagonal orientations and one of such perpendicular planes; (c) Four corner-to-corner orientations and one of such perpendicular planes.

Let *FrontQue*, *TmpQue* and *ResultSet* be three queues used for tracing the current front, temporary front and resultant perpendicular plane, respectively. In the very beginning, *FrontQue* is initialised with the skeleton point p , i.e. $FrontQue = \{p\}$ and $ResultSet = FrontQue$.

- a. *TmpQue* is emptied. For each point q in *FrontQue*, the template \mathcal{T}_V is virtually “placed” at q . If a voxel r at which a black point in \mathcal{T}_V appears locates in the PS, then r is pushed into *TmpQue* and *ResultSet*. This process stops and goes to step (2) until all points in *FrontQue* have been accessed in this way.
- b. If *TmpQue* is empty, i.e. no pore voxels in the image space \mathcal{V} can be found on the perpendicular place so that they are 26-connected with the original skeleton voxel p , then this algorithm terminates. Otherwise, *FrontQue* is swapped with *TmpQue*, and go to step (1).

The CS extracting algorithm can be further explained by an example shown in Figure 4-19. Figure 4-19(a) shows a slice of a 3D rock image on XY-plane where grey voxels belong to the PS. Using one of the templates shown in Figure 4-18, the red voxel is initialized into *FrontQue* and *ResultSet*. And then blue neighbours of the central voxel are added into *ResultSet*. The process continues until no more pore voxels can be found along the selected template. By the end of this process, purple voxels are finally identified. Therefore, the resultant CS *ResultSet* contains all coloured voxels (Figure 4-19(b)). In this way, I avoid checking a large number of voxels in the

image space which do not locate on perpendicular planes, thus the algorithm achieves a much faster extraction of CSs.

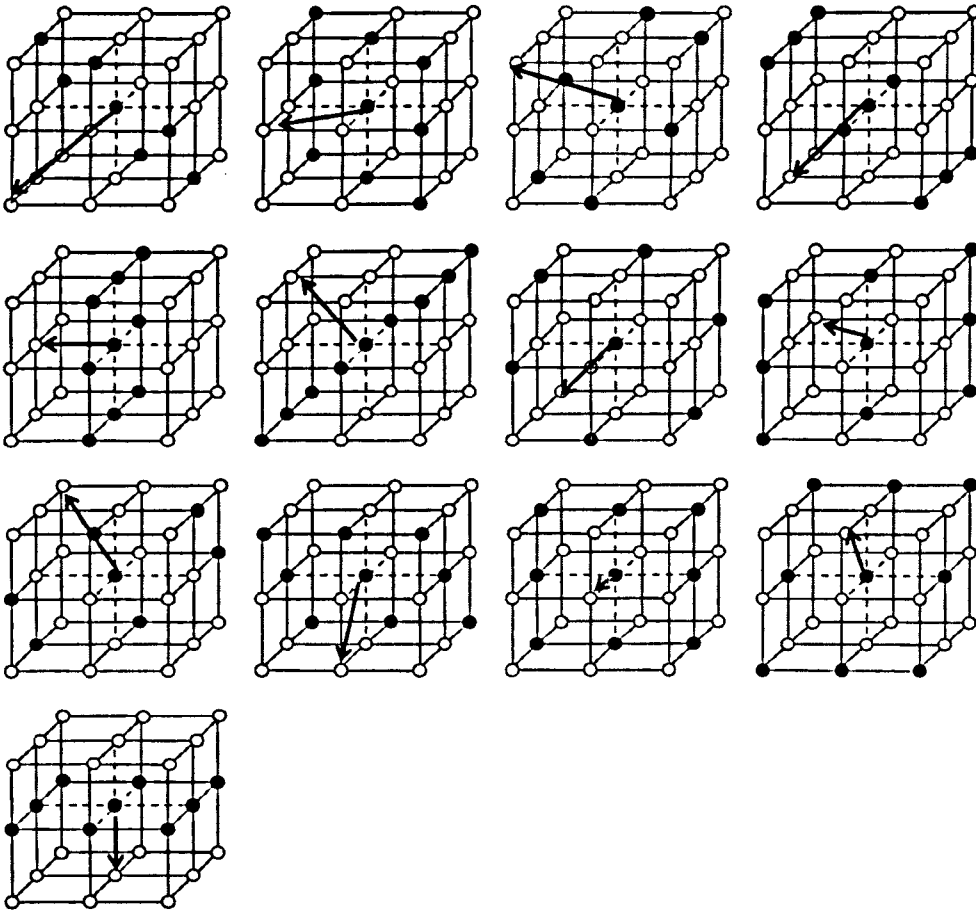


Figure 4-18: Thirteen orientations and their corresponding discrete perpendicular planes (templates) in the $3 \times 3 \times 3$ neighbourhoods of central points. Each grey arrow represents a normal orientation and each perpendicular plane consists of black voxels.

The Partition of Individual Cross Sections

Figure 4-20(a) shows that an orthogonal slice intersects with the skeleton (in red) of a sphere-packed image. Using the algorithm described above, in Figure 4-20(b), all CSs through any skeleton voxel of the same orientation will overlap each other and become an extremely irregular shape. This phenomenon can be found in unconsolidated sandstones.

To solve the problem, I simply assume that a CS should be equally shared by all the skeleton voxels on the plane if they have the same normal orientation. In Figure 4-21, the CS should be considered as two individual CSs (see Figure 4-21(b)) belonging

to two skeleton voxels. This can be done by clustering each voxel on the original CS into an appropriate CS associated with a skeleton voxel. For example, the white point in Figure 4-21(c) on the original CS will be clustered into the CS associated with the blue skeleton point, because it is closer to the blue point than to the black point. As usual, the geodesic chamfer DT is used to implement this kind of partitioning of individual CSs. For the CS shown in Figure 4-20(b), if we assume that all the skeleton voxels (red dots) have the same orientation, it can be partitioned into a set of individual CSs (in different colours) shown in Figure 4-20(c).

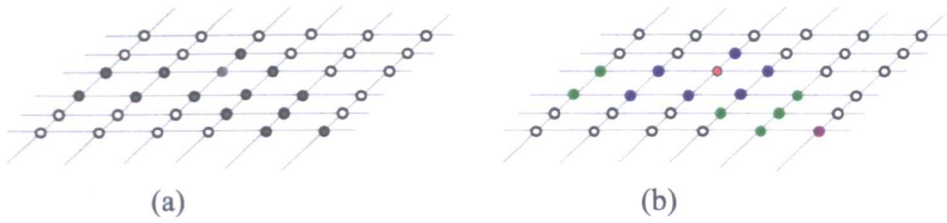


Figure 4-19: Illustration of the process how to extract a CS. (a) A slice of the PS in a rock image (pore voxels are coloured in grey and solid voxels are coloured in white); (b) using the template shown in Figure 4-18, starting from the red point, blue voxels are firstly identified, and then green voxels etc.

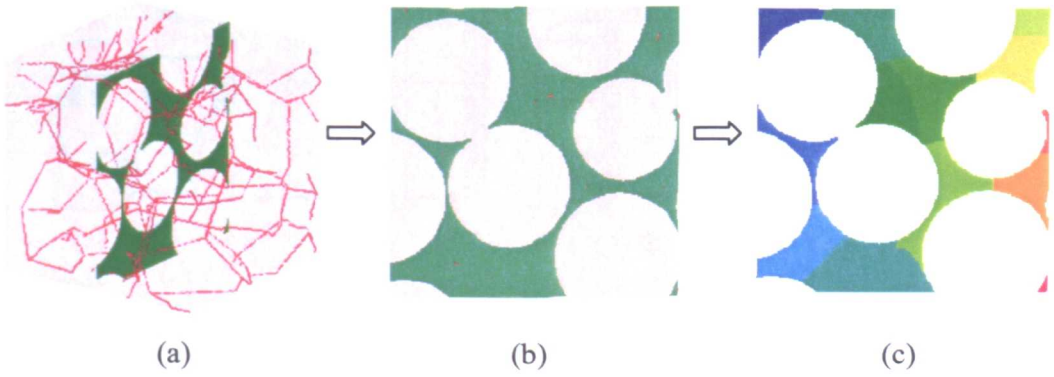


Figure 4-20: Illustration of the partition of individual CSs. (a) An orthogonal slice (green surface) intersected with the skeleton of a sphere-packed image; (b) the perpendicular plane (pore voxels in green, skeleton voxels in red and solid voxels in pink) at the corresponding position; (c) partition of individual CSs.

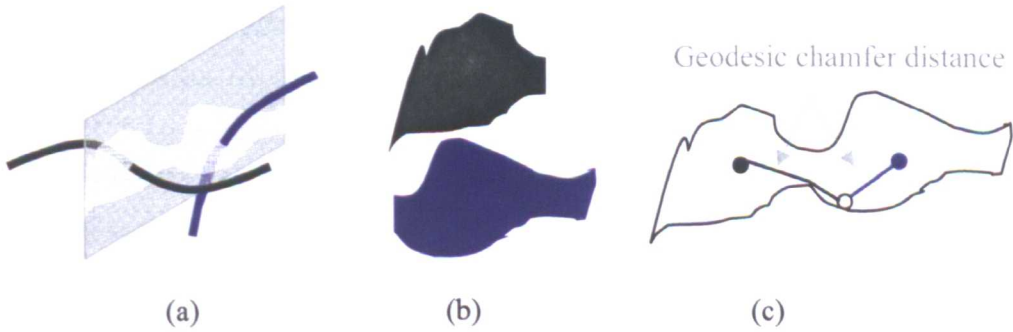


Figure 4-21: The partition of individual cross sections: (a) a CS (the white region) going through two skeleton voxels; (b) Two desired individual CSs; (c) each pore voxel on the CS is clustered either blue CS or the black one based on the comparison of the geodesic distances to the two skeleton voxels.

4.2.2 Projection of Cross Section

Considering a 3D discrete plane with one of the thirteen directions (Figure 4-18) as its normal orientation, only three types of the perpendicular planes can be obtained: edge-edge, face-face and edge-face (Figure 4-22). This classification is due to the relationship between two adjacent voxels. On the edge-edge (face-face) CS, any two voxels share at most one edge (face); and any two voxels on an edge-face share at most either one face or one edge.

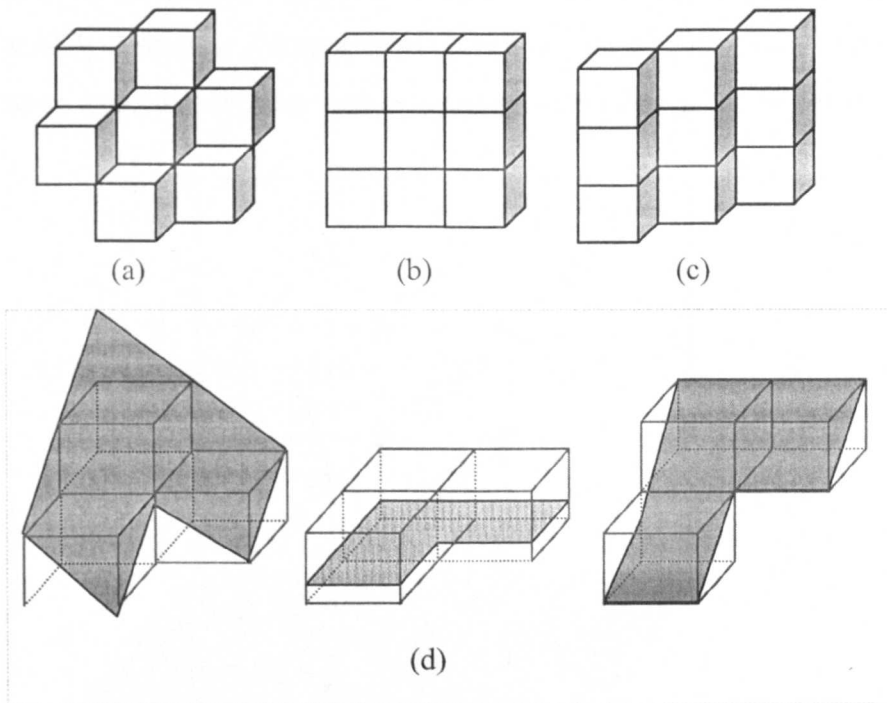


Figure 4-22: Three types of 3D discrete perpendicular planes. (a) Edge-edge; (b) face-face; (c) edge-face; (d) three kinds of spatial CSs (i.e. the grey surfaces).

Based on the classification of perpendicular planes, the spatial CSs can then be classified as three kinds of cross sections. Figure 4-22(d) shows three spatial CSs (grey surfaces) associated with only three voxels. In other words, the cross sectional area and perimeter of a spatial CS should be computed based on the 2D grey shapes shown in Figure 4-22(d). This coincides with the intuitive conception about a spatial planar shape but makes it difficult to calculate the area and perimeter directly from the spatial CSs. A simple way to solve this problem is to project CSs onto appropriate coordinate planes, the calculation of the area and perimeter of spatial CSs is then shifted to the

computation of the area and perimeter of corresponding 2D shapes on coordinate planes. From Figure 4-18, I note that the thirteen discrete planes should be projected on different coordinate planes. Some of them can be projected on any coordinate planes (i.e. XY, XZ or YZ-planes) such as the plane with the orientation of (1, 1, 1); others may be projected only on one or two coordinate planes. The requirement is that the number of black pixels in a projected shape must equal to the number of black voxels in the corresponding spatial CSs. In Figure 4-23, if the nine black voxels on the spatial plane are projected on XZ-plane (or XY-plane), we can obtain the same number of pixels (squares or triangles). However, only three pixels (rectangles) can be obtained by projecting the nine voxels on YZ-plane. In the following, I present an algorithm to quickly determine the appropriate projecting coordinate plane, in the case that there is more than one coordinate places available, any of them can be chosen.

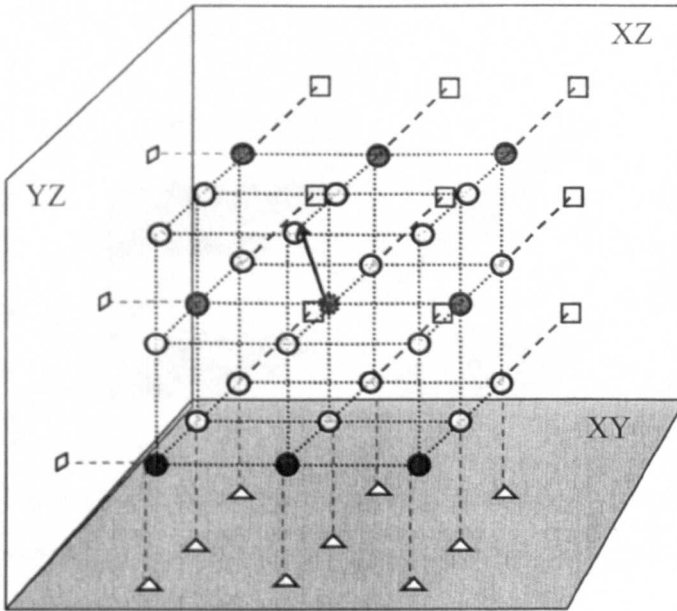


Figure 4-23: Projection of a spatial discrete plane consisting of only black voxels on XY-, XZ- or YZ-plane.

$V = (v_x, v_y, v_z)$ is a unit normal orientation.

$X_a = |v_x|$; $Y_a = |v_y|$; $Z_a = |v_z|$

$coord = 3$; // ignore z-coordinate i.e. XY-plane

if ($X_a > Y_a$) {

 if ($X_a > Z_a$) $coord = 1$; // ignore x-coordinate, i.e. YZ-plane

} else {

 if ($Y_a > Z_a$) $coord = 2$; // ignore y-coordinate, i.e. XZ-plane

}

At this stage, the area and perimeter of a projected shape on a coordinate plane can be efficiently computed, which will be discussed in the next section. From the point of view of analytical geometry, it is possible to obtain the corresponding values of spatial CSs by establishing an analytical relation between a spatial shape and its planar shape. Unfortunately, the conversion is of little practical value because the border of the CSs is quite irregular and the computation of the perimeter is much more complicated.

To simplify the conversion from 2D planar shapes to spatial shapes, I consider the unit element (i.e. voxel) which is commonly modelled as a cube. According to the classification of perpendicular planes shown in Figure 4-22, the unit shape of a voxel on the corresponding plane can also be classified as three general shapes, i.e. square, rectangle and diamond, shown in Figure 4-24, however, all these three spatial shapes are projected into the same shape – square.

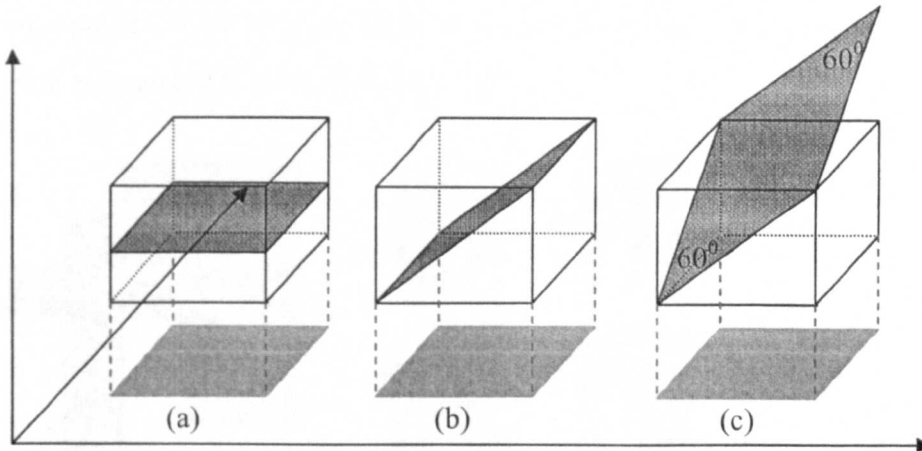


Figure 4-24: Three types of spatial shapes and their corresponding projected shapes of a voxel. (a) A square on a face-face plane; (b) a rectangle on an edge-face plane; (c) a diamond on an edge-edge plane.

Let A_c and P_c represent the area and average edge length of a unit shape, respectively, I can then compute three pairs of (A_c, P_c) , called a projecting coefficient, responding to the three types of unit shapes. The three projecting coefficients are given in Figure 4-25. Using these coefficients, an algorithm will be developed to compute the shape factor of spatial CSs.

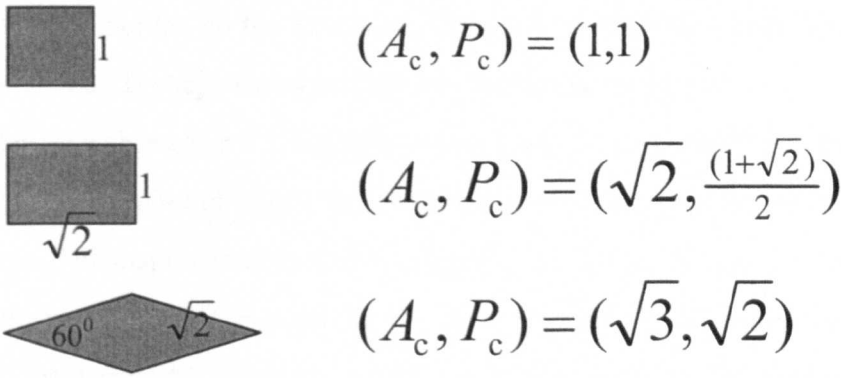


Figure 4-25: Projecting coefficients for three different types of unit shapes.

4.2.3 Computation of Shape Factor of 2D Shapes

From the discussion in the last section, we know that any unit shape of a voxel is projected into a square on a coordinate plane (see Figure 4-24). Thus the 2D shape of any spatial CS can be regarded as an 8-connected component consisting of only squares; such an example is given in Figure 4-26(a).

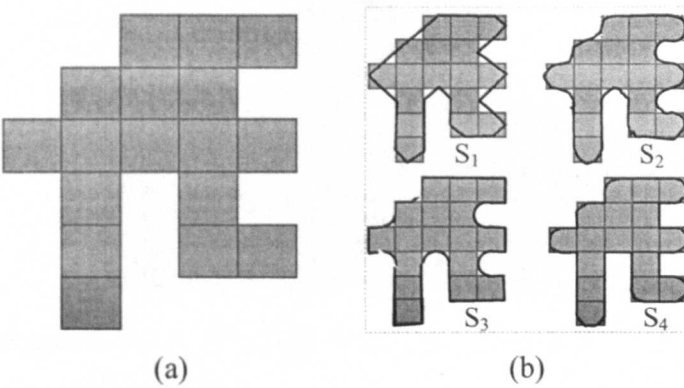


Figure 4-26: (a) A 2D shape on a coordinate plane; (b) four smoothing schemes.

In the computation of area and perimeter of a 2D shape, the key point is to determine the border of the shape in order to get a better approximation. For a 2D shape (e.g. Figure 4-26), its border's length being used to approximate its perimeter would be overestimated and result in much smaller shape factor due to the perimeter square-operation, which means that smoothing the borders of 2D shapes is necessary. In Figure 4-26(b), four smoothing schemes are illustrated, where the smoothed border is considered as the closed black curve and the corresponding shape is the region surrounded by the closed black curve. The perimeter of a 2D shape is then determined by the length of its smoothed border and its area is determined by the interior region of

the smoothed border. In the following, I present an algorithm to compute the area and perimeter of a 2D shape based on different smoothing schemes.

Given a shape S in Z^2 , I introduce four numbers to quantify the shape: the number of pixels; the number of edges; the number of corners and the number of vertices, which will be called shape numbers and are denoted by N_p , N_e , N_c and N_v respectively. The four relevant concepts (i.e. pixel, edge, corner and vertex) are illustrated in Figure 4-27.

Considering the 2D shape S shown in Figure 4-26(a), it is easy to obtain its four shape numbers: $N_p = 17$, $N_e = 30$, $N_c = 9$ and $N_v = 13$. Without smoothing the shape border, its area and perimeter are N_p and N_e respectively. According to the definition of shape factor (4.2), the shape factor of S can be computed by $G = N_p/(N_e)^2$ (i.e. 0.01889). In this simple computation of shape factor the outcome is not dependent on the other two shape numbers N_v and N_c , but they will be involved in the calculation if the smoothed borders of 2D shapes are used to calculate the area and perimeter.

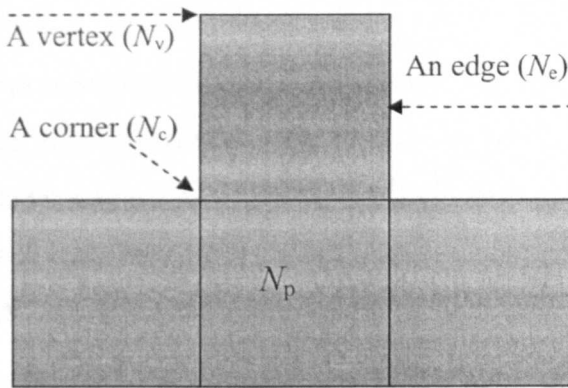


Figure 4-27: A 2D shape of four pixels (squares) and its four shape numbers: $N_p = 4$, $N_e = 10$, $N_c = 2$ and $N_v = 6$.

Let A_v , A_c , P_v and P_c be four coefficients which are related to each vertex and corner. A_v and A_c (P_v and P_c) are defined as the unit areas (perimeters) which need to be added or subtracted when a vertex or a corner is considered. Four basic smoothing schemes, denoted by S_1 , S_2 , S_3 and S_4 , are demonstrated in Figure 4-26(b). In the smoothing scheme S_2 , for example, for each vertex, A_v (P_v) is the quarter area (perimeter) of a unit circle which is the amount of area (perimeter) needed to be reduced from the resultant area A (perimeter P) of the shape shown in Figure 4-26(a); for each corner, A_c (P_c) is the quarter area (perimeter) of a unit circle needed to be added in the

resultant area A (perimeter P). Thus, for different smoothing schemes, the corresponding coefficients can be obtained and listed in Table 4-1.

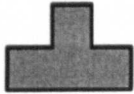
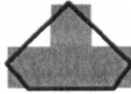
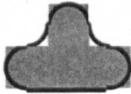
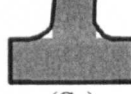

Smoothing schemes	 (S ₀)	 (S ₁)	 (S ₂)	 (S ₃)	 (S ₄)
A_v	0	-0.125	-0.0537	0	-0.0537
A_c	0	0.125	0.0537	0.0537	0
P_v	0	-0.2929	-0.2146	0	-0.2146
P_c	0	-0.2929	-0.2146	-0.2146	0

Table 4-1: Five smoothing schemes and their corresponding coefficients.

Therefore, for any 2D shape S with shape numbers (N_p, N_e, N_v, N_c), its area A and perimeter P can be estimated by

$$A = N_p + N_v A_v + N_c A_c, \tag{4.5a}$$

$$P = N_e + N_v P_v + N_c P_c. \tag{4.5b}$$

For example, I compute the shape factor of the 2D shape shown in Figure 4-26(a) under different smoothing schemes from S_0 to S_4 which are shown in Table 4-1, the computed result is listed in Table 4-2. Note that the shape factor error between S_0 and S_1 reaches to over 36% with respect to 0.02974. In general, for complex 2D shapes, i.e. if one of N_v and N_c is quite large, the shape factor error can not be ignored in that case.

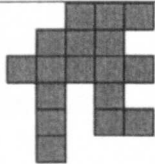
Smoothing schemes		S ₀	S ₁	S ₂	S ₃	S ₄
	A	17	16.5	16.7852	17.4833	16.3019
	P	30	23.5562	25.2788	28.0686	27.2102
	G	0.01889	0.02974	0.02627	0.02219	0.02202

Table 4-2: The computation of shape factor of the 2D shape shown in Figure 4-26(a), the shape numbers (N_p, N_e, N_v, N_c) = (17, 30, 13, 9).

At this stage, a question needs to be answered — which scheme is suitable for the computation of shape factor of projected shapes in porous media. In Table 4-2, both scheme S_3 and S_4 do not make much sense due to the different treatment for corners and vertices. Hence only two positive coefficients are sufficient to reach a good approximation, which are denoted by a and ρ , and called a smoothing area coefficient

and a smoothing perimeter coefficient, respectively. Equation (4.5) can then be adjusted as

$$A = N_p + a(N_e - N_v), \tag{4.6a}$$

$$P = N_e - \rho(N_v + N_c). \tag{4.6b}$$

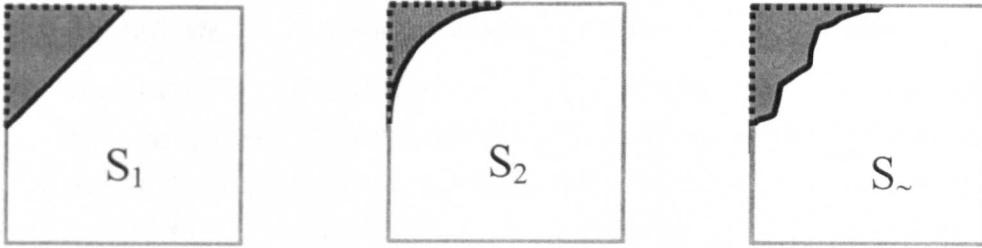


Figure 4-28: Geometrical explanation of the smoothing coefficients (a, ρ). S_{\sim} represents a general smoothing scheme.

In S_1 , $a = 0.125$ and $\rho = 0.2929$; in S_2 , $a = 0.0537$ and $\rho = 0.2146$.

Figure 4-28 gives a geometrical explanation of the smoothing coefficients: a is the area of the grey shape, and ρ equals to the length of the dotted curve minus the length of the black curve.

From the definition of shape factor (4.2), the shape factor is much more sensitive to the perimeter (ρ) than to the area (a) because of the square operation. For this reason, in order to search for an appropriate ρ , we can assume that $a = 0$ when Equation (4.6) is used to compute the shape factor of several regular shapes (Figure 4-29). In Figure 4-29, the shape factors G are computed analytically because of the regular shapes, and then in discrete space their shape numbers are counted. Using Equation (4.6b), the corresponding smoothing coefficients ρ can be estimated by

$$\rho = (N_e - \sqrt{\frac{N_p}{G}}) / (N_v + N_c). \tag{4.7}$$

Comparing the smoothing schemes in Table 4-1, the scheme S_2 seems to be an appropriate choice in the sense of minimal errors for computing the regular shapes shown in Figure 4-29.

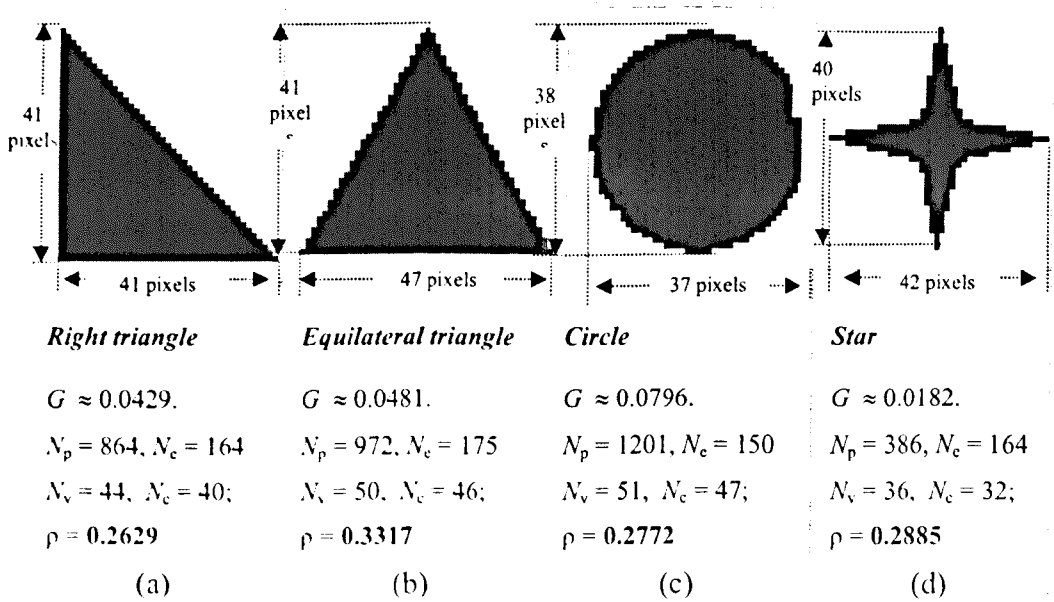


Figure 4-29: The selections of smoothing perimeter coefficients for approximating different regular shapes.

To end this section, I describe an algorithm to count the shape numbers (see Figure 4-27). Let $P = \{V, S\}$ be a 2D binary image which contains a 2D shape S , and is defined on a rectangle region V ; each pixel in S is called black, other pixels are called white. And we assume that any pixels beyond the image space V are white. For any two pixels p and q , they are said to be 4-adjacent (8-adjacent) if p and q share an edge (an edge or a face). Also q is said to be a 4-neighbour (4-neighbour) of p if p and q are 4-adjacent (8-adjacent but not 4-adjacent). In Figure 4-30, for example, q_2, q_4, q_5 and q_7 are 4 4-neighbours of p , and q_1, q_3, q_6 and q_8 are 4 8-neighbours of p .

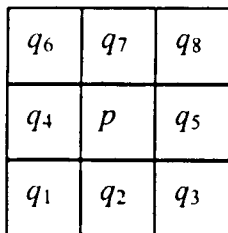


Figure 4-30: The 2x2 neighbourhood of a pixel p .

Algorithm for counting shape numbers

N_p, N_e, N_v and N_c are initialised as zeros.

For each pixel $p \in S$ {

$N_p ++$

For each 4-neighbour q of p (i.e. $q \in \{q_2, q_4, q_5, q_7\}$)
 if q is a white pixel, then N_e++
 For each 8-neighbour q of p (i.e. $q \in \{q_1, q_3, q_6, q_8\}$) {
 if q is a white pixel then {
 Let $S(p,q)$ be the 2×2 neighbourhood that contains p and q .
 If the other two pixels in $S(p,q) \setminus \{p,q\}$ are black then N_c++
 If the other two pixels in $S(p,q) \setminus \{p,q\}$ are white then N_v++ }
 } }

As an example, let us consider a CS extracted from a real rock image. In Figure 4-31, the 2D shape consisting of all pixels labelled by value 1 is created by projecting a spatial CS on the XZ-plane. Using the shape number counting algorithm, we have $(N_p, N_e, N_v, N_c) = (391, 148, 43, 39)$.

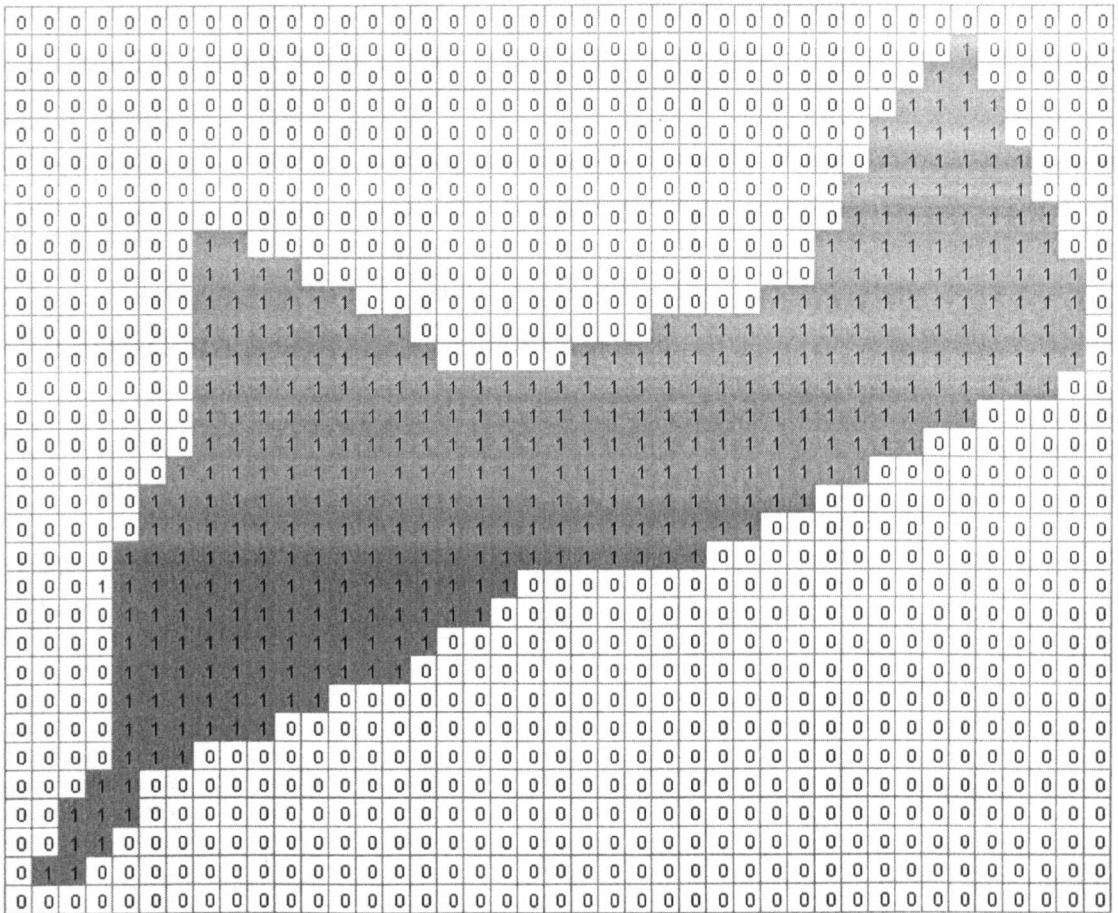


Figure 4-31: A cross section extracted from a rock image.

Using different smoothing schemes (Table 4-1) and Equations (4.6), the shape factors of the CS shown in Figure 4-31 are listed in Table 4-3.

Smoothing schemes	a	ρ	G
S_0	0	0	0.0178
S_1	0.125	0.2929	0.0254
S_2	0.0537	0.2146	0.0229
S^*	0.0894	0.2538	0.0241

Table 4-3: Shape factors of the cross section shown in Figure 4-31, where S^* is a new smoothing scheme by averaging their smoothing coefficients of S_1 and S_2 (i.e. $a = (0.125 + 0.0537)/2$ and $\rho = (0.2929 + 0.2146)/2$), G is the shape factor.

In a rock image, from a skeleton point p , we firstly determine the orientation of a discrete perpendicular plane based on its local configuration of skeleton voxels, and an individual spatial CS S' is then extracted from the perpendicular plane applying the partitioning approach. Secondly, the CS S' is projected onto a proper coordinate plane and a 2D shape S with shape factor of G is obtained. Using the algorithm and the projecting coefficients (Figure 4-25), finally, after the shape numbers are counted the area and perimeter of S' is given by

$$A(S') = [N_p + a(N_c - N_v)] A_c, \quad (4.8a)$$

$$P(S') = [N_c - \rho(N_c + N_v)] P_c. \quad (4.8b)$$

Therefore, we can compute the shape factor of a spatial CS S' by

$$Q(S) = \frac{N_p + a(N_c - N_v) A_c}{[N_c - \rho(N_c + N_v)]^2 P_c^2} = \frac{N_p + a(N_c - N_v)}{[N_c - \rho(N_c + N_v)]^2} G. \quad (4.9)$$

Projecting coefficients	$A_c = 1 \quad P_c = 1$	$A_c = 1.414 \quad P_c = 1.207$	$A_c = 1.732 \quad P_c = 1.414$
Shape factor	0.0229	0.0222	0.0198

Table 4-4: Shape factors of the spatial cross section which is projected into the 2D shape shown in Figure 4-31 for three projecting coefficients (Figure 4-25).

For the 2D shape shown in Figure 4-31, let us consider three cases in which the 2D shape may be generated by projecting a spatial CS with three different projecting

coefficients (see Figure 4-25). Using (4.9) and smoothing scheme S_2 , we can obtain the following result (Table 4-4).

4.3 Construction of Network Structure

With a 3D binary image of a porous medium at hand and a wealth of relevant image processing algorithms available, it is time to predict the flow properties. One simple method is to use a network flow model. We can construct a realistic network of nodes linked by bonds directly from a porous medium, and then feed the extracted network structure into one of the network models (e.g. Lopez et al. 2003[93]; van Dijke and Sorbie, 2002[171]). Network models can then predict some macroscopic properties of the porous system, such as capillary pressure or relative permeability, by applying rules that govern the transport and arrangement of fluids in nodes and bonds. Apart from being used in a network model, the extracted network from a 3D rock image can be also used to calculate some fluid transport properties based on averaging laws.

How to convert complex pore systems into node-bond network structures then becomes an important issue. The general procedure could contain two major steps. Firstly, the PS in rock images is partitioned into a network of individual nodes connected together by bonds. Secondly, some geometric and topological properties, which are necessary for and dependent on a specific network model, are assigned to each network element. This can be done by extracting the corresponding quantities (such as shape factor, radii, length, volumes, connecting list etc) from rock images. In this section, I discuss two relevant issues in order to facilitate the pore structure analysis technique: partitioning the PS into a network and characterising the network elements.

4.3.1 Partitioning the Pore Space into a Network

Having a Euclidean distance valued skeleton (see Figure 4-4), i.e. the GT network on which a squared Euclidean distance value is assigned to each skeleton voxel, of a rock 3D image, the identifying process of nodes and bonds can be summarised as three major steps: (1) to classify all skeleton voxels as either node-skeleton voxels or bond-skeleton voxels; (2) to merge node-skeleton voxels into various backbones of individual nodes; (3) to expand the skeleton voxels within the PS into individual nodes and bonds.

(1) Classification of Skeleton Voxels

According to Thover et al. (1993[167]), the skeleton voxels can be simply classified into two groups: edges and vertices, which are defined as composed of voxels with exactly two neighbours (16-adjacency) and three or more neighbours, respectively. This typical classification was analysed by Liang et al. (2000a[84]), and some drawbacks were pointed out such as the identification of only one vertex. To address these problems, based on the concept of λ -adjacency and using the corresponding rules a correct classification method was presented, and λ -adjacency will be also used in my approach.

In 3D discrete space, two distinct voxels p and q are said to be λ -adjacent if $d_E(p, q) = 1$, or if $d_E(p, q) = \sqrt{2}$ and no black (pore) voxels exist which are 6-adjacent to p and q , or if $d_E(p, q) = \sqrt{3}$ and no black voxels exist which are 18-adjacent to p and q , where $d_E(p, q)$ is the Euclidean distance function (i.e. $L_2(p, q)$ in (3.4)). Some examples of λ -adjacent are given in Figure 4-32.

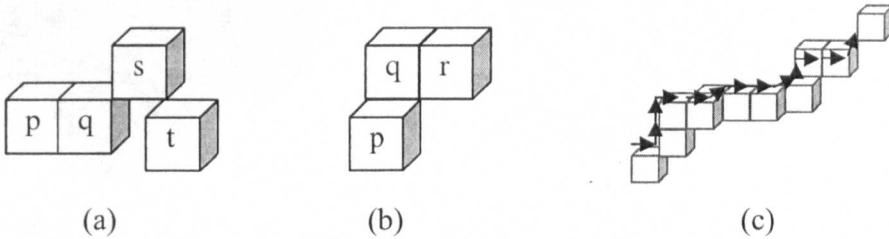


Figure 4-32: Illustration of λ -adjacency. (a) Three λ -adjacencies between p and q , q and s , s and t ; (b) p is λ -adjacent to q because they are 18-adjacent and no 6-neighbours between them, however, p is not λ -adjacent to r even though they are 26-adjacent because of the existence of q between them; (c) a λ -adjacent path (Liang et al. 2000a[84]).

Based on the concept of λ -adjacency, Liang et al. considered the following definition with regard to the classification of skeleton voxels as nodal or link points.

Definition 4.1: Skeleton points are classified as link points if they have exactly two λ -adjacent neighbours. Skeleton points are classified as nodal points if they have three or more λ -adjacent neighbours.

There are two drawbacks with this definition to classify skeleton voxels. The first one is that it ignores two cases when a skeleton point has no neighbour or only one λ -adjacent neighbour. In the generation of the GT network, an isolated pore would be shrunk to be a single voxels if it does not contain any cavities, and the boundary links and primary branches would result in the generation of endpoints in the resultant skeleton, which have only one neighbour. The second problem is that it may be unable to distinguish different pore channels. Figure 4-33(a) shows the case in which the four pore channels can not be obtained by identifying the central voxel as a nodal point because the skeleton excluding the central point is still 26-connected. However, the major drawback is that there is no consideration of inscribed spheres at skeleton voxels when the classification is being carried out. Apparently, the backbone of a nodal pore should contain all skeleton voxels in the PS which locate within its maximal inscribed sphere demonstrated in Figure 4-33(b).

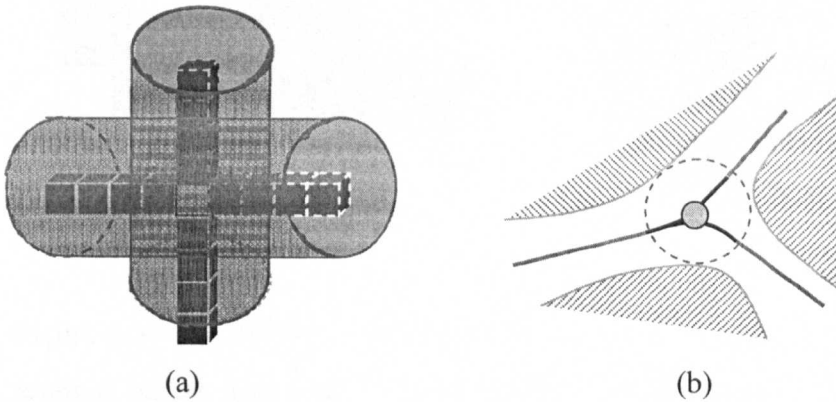


Figure 4-33: Illustration of partition issues. (a) Four pore channels (in 4 different patterns) which can not be distinguished by clustering the remaining skeleton voxels after removing the central voxel; (b) The backbone of a nodal pore should contain all skeleton voxels in the maximal inscribed sphere of the centre point.

To address the problem with Definition 4.1, I introduce the following definition and rule to classify skeleton voxels.

Definition 4.2: A skeleton point (voxel) is said to be an isolated, or terminal, or link or junction point if it has 0, or 1, or 2, or at least 3 λ -adjacent neighbours.

Rule 4.1: All link skeleton voxels are clustered as bond-skeleton voxels, and any other skeleton voxels are clustered as node-skeleton voxels.

Two examples of the classification of skeleton points according to Definition 4.2 are shown in Figure 4-34. In Figure 4-34(a), there are four junctions (in orange), four link points (in blue), three terminal points (in grey) and one isolated point (in turquoise).

After clustering the skeleton voxels using Rule 4.1, a set of original node-skeleton voxels can be obtained. To solve the second problem of Definition 4.1, I further expand the node-skeleton voxels. As suggested in Figure 4-33(b), all skeleton voxels within a maximal inscribed sphere centred at a node-skeleton voxel should be further identified as new node-skeleton voxels. The basic process is demonstrated in Figure 4-35, in which all skeleton voxels on the red curves are re-identified as node-skeleton voxels.

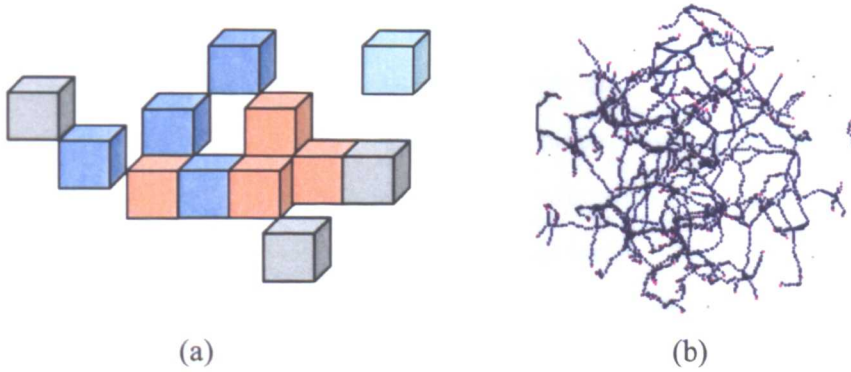


Figure 4-34: Classification of skeleton voxels: (a) an isolated point (light green), three terminal points (grey), four link points (light blue) and four junction points (orange, junctions); (b) a skeleton of the PS of a sandstone sample with four colours representing four types (i.e. isolated, terminal, link and junction) of skeleton voxels.

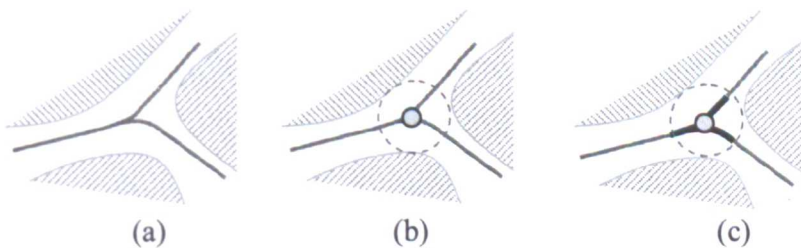


Figure 4-35: Illustration of expanding node-skeleton voxels: (a) a skeleton, (b) an original node-skeleton voxel, (c) newly expanded node-skeleton voxels (in black).

In the construction of the network structure, all node-skeleton voxels need to be grouped into the backbones of individual nodes. However, the extracted node-skeleton voxels are not separated naturally: most of them are 26-connected indeed. Hence, we need to develop a proper rule to merge node-skeleton voxels to find “real” backbones of nodes and bonds.

(2) Merging Node-Skeleton Voxels

Applying Definition 4.2 and Rule 4.1, any skeleton voxel can be clustered into either a bond-skeleton or a node-skeleton voxel. For convenience, these newly classified node-skeleton voxels are called original node-skeleton voxels. And then their spatial positions are used as the centres of maximal inscribed spheres and the Euclidean distance values at these centres in the coloured skeleton (e.g. Figure 4-4) are used the radii of the maximal inscribed spheres. Having carried out the classifying and expanding operations, a set of original and new node-skeleton voxels can be found in the coloured skeleton. In order to create individual nodes, we need to further merge some node-skeleton voxels together if they are connected and quite close, and then partition the PS based on the clustered skeleton voxels. In the following, I discuss some issues which are closely related to the correct merging of node-skeleton voxels and present rules to address these issues.

The first issue is that only very close original node-skeleton voxels should be merged together. In Figure 4-36, p and q are two original node-skeleton voxels and the skeleton voxels within the maximal inscribed circles (spheres) are new node-skeleton voxels by expanding p and q . Intuitively, all the node-skeleton voxels in Figure 4-36(a) should be merged into just one individual node-backbone (part of a resultant node on the skeleton). All the node-skeleton voxels in Figure 4-36(b), however, should be kept as two node-backbones because they are not close enough.

The second issue is that all node-skeleton voxels in a single node-backbone should be 26-connected within their maximal inscribed spheres. In Figure 4-37, p and q are very close but they are not 26-connected within their maximal inscribed spheres. Therefore, these node-skeleton voxels should not be merged into a single node-backbone.

The third issue is to ensure that not too many original node-skeleton voxels are merged into a single node-backbone, which is also called a “snowballing” phenomenon by Sheppard et al. (2005[153]). In Figure 4-38, all node-skeleton voxels should be merged into a single node-backbone when we only consider whether or not candidate node-skeleton voxels are close enough. This rule means that the so-called “snowballing” would occur. For some samples, without control of snowballing, a very large node could be found in the resultant network of nodes and bonds.

The last issue is that an individual node-backbone should be a 26-component without cavities and channels, in other words, the extracted network must be topology-preserving. Figure 4-39 shows the case when a tunnel appears nearby four very close original node-skeleton voxel.

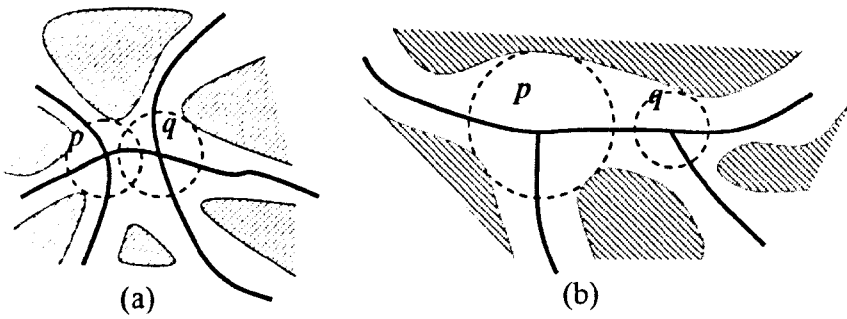


Figure 4-36: (a) Merging all node-skeleton voxels within the two spheres (circles) into one node-backbone or (b) keeping them as two individual node-backbones.

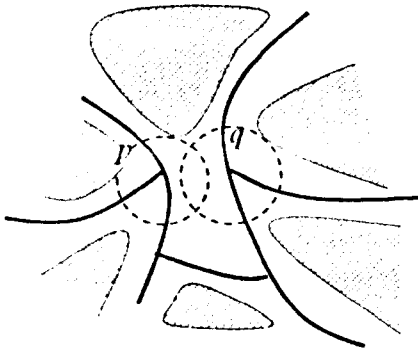


Figure 4-37: p is not 26-connected with q within the maximal inscribed spheres.

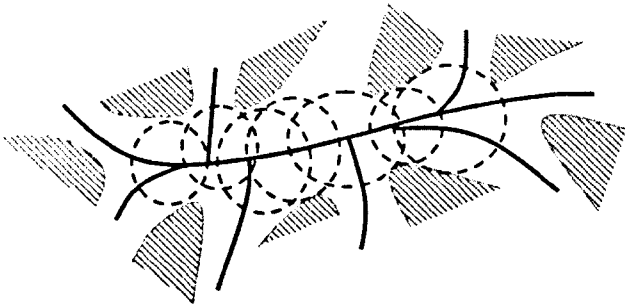


Figure 4-38: Too many node-skeleton voxels are merged into a single node-backbone.

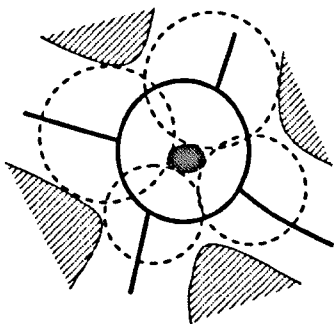


Figure 4-39: There is a tunnel (the central region) surrounded by four close original node-skeleton voxels.

Based on the distance values at original node-skeleton voxels, to tackle the four issues above, I introduce an algorithm for merging node-skeleton voxels into individual node-backbones.

Let $CSkl(\mathcal{P})$ (see Figure 4-4) be the Euclidean distance valued skeleton of a binary rock image $\mathcal{P} = \{\mathcal{V}, 26, 6, \mathcal{B}\}$. $CSkl(\mathcal{P})$ is generated by combining the GT network (skeleton) and distance map of \mathcal{P} together, i.e. each voxel p with $CSkl(p) > 0$ is a skeleton voxel and $CSkl(p)$ is the shortest squared Euclidean distance to the solid matrix. Applying Definition 4.2, all skeleton voxels are clustered as either original node-skeleton or bond-skeleton voxels. Let $NS(\mathcal{P})$ represent the set of original node-skeleton voxels. For any two voxels p and q in $NS(\mathcal{P})$ (Figure 4-40), r_p and r_q are the squared radii of their own maximal inscribed spheres, denoted by $IS(p)$ and $IS(q)$, respectively. It is clear that $r_p = CSkl(p)$ and $r_q = CSkl(q)$. Let $d(p, q)$ be the squared Euclidean distance between p and q , thus the two spheres can be described by $IS(p) = \{o \in \mathcal{B}: d(o, p) \leq r_p\}$ and $IS(q) = \{o \in \mathcal{B}: d(o, q) \leq r_q\}$. Let $\varepsilon > 0$ be a predefined coefficient used for avoiding the “snowballing”. The smaller ε is, and the less chance node-skeleton voxels are merged together. Therefore, for different porous media, different values can be used as ε to control the node size (avoiding generating too large individual pores).

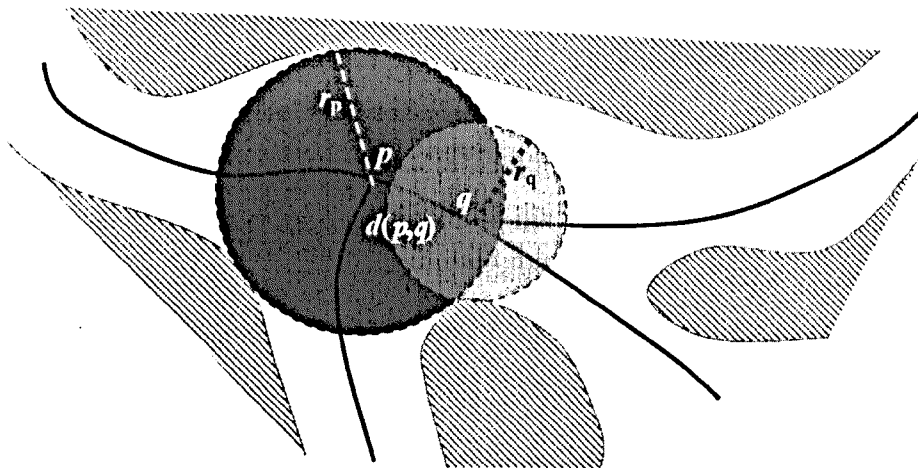


Figure 4-40: Two original node-skeleton voxels p and q , two squared inscribed radii r_p and r_q and the squared Euclidean distance $d(p, q)$ between p and q .

Algorithm for merging node-skeleton voxels

For each pair of two original node-skeleton voxels p and q in $NS(\mathcal{P})$ {
 Let $IS(p, q)$ be the set of skeleton voxels which locate within either $IS(p)$ or $IS(q)$, $IS(p, q) = \{ o \in \mathcal{B} : CSkl(q) > 0 \text{ and } o \in IS(p) \cup IS(q) \}$.
If p is not 26-connected to q in $IS(p, q)$, i.e. there is at least one 26-path in $IS(p, q)$ between these two voxels, **then** the procedure continues. Otherwise,
If $d(p, q) - \max(r_p, r_q) > \varepsilon \min(r_p, r_q)/2$, **then** the procedure continues.
 Otherwise,
If $IS(p, q)$ contains cavities (i.e. completely enclosed solid components) or tunnels, which can be simply determined by computing its Euler number, i.e. $\chi(IS(p, q)) = 1$ when all isolated solid particles have already been removed before generating GT network, **then** the procedure continues. **Otherwise**, merging all voxels in $IS(p, q)$ as an individual pore-bone.
 }

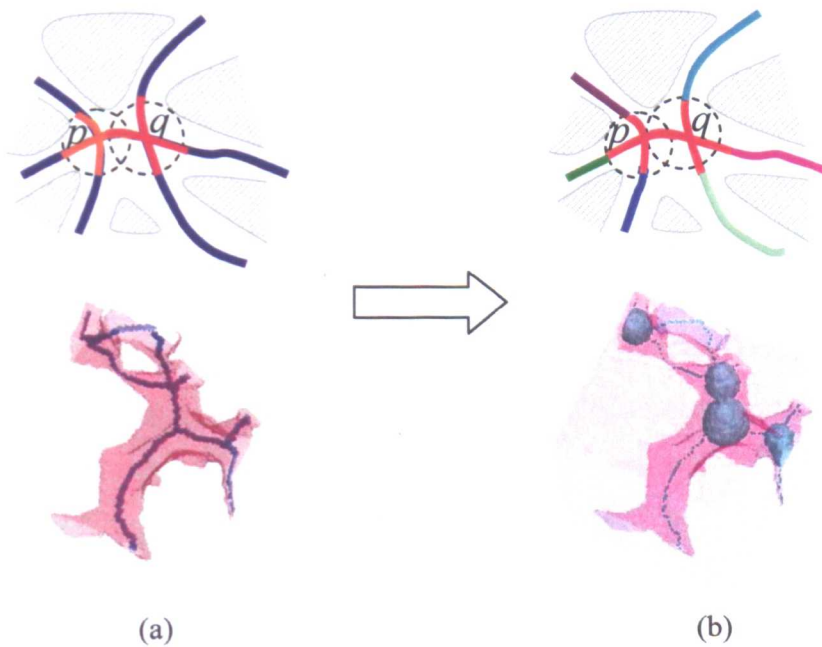


Figure 4-41: The node-skeleton voxels (in orange and red) in (a) are merged into one node-backbone (in red) in (b); and the remaining skeleton voxels (in blue) in (a) are clustered as six different bond-skeleton voxels (coded by different colours) because they are six components.

(3) Partitioning the Pore Space into Network of Nodes and Bonds

Based on the coloured skeleton of the PS in a porous medium, the skeleton voxels are firstly classified as four types of voxels applying Definition 4.2, and then are clustered as (original) node-skeleton and bond-skeleton voxels using Rule 4.1. Secondly, new node-skeleton voxels are generated by expanding the original node-

skeleton voxels along the skeleton within corresponding maximal inscribed spheres. The new and original node-skeleton voxels are then merged into individual node-backbones utilising the merging algorithm. Furthermore, by removing all node-backbones from the skeleton, the remaining skeleton voxels are clustered as different bond-skeleton voxels in terms of 26-connected components using our component labelling algorithm. The procedure end result is demonstrated in 2D and in 3D in Figure 4-41.

4.3.2 Characterising Network Elements

Having constructed the network of nodes and bonds from the PS in a porous media, apart from the shape factor which has already been discussed in section 4.2, more characteristics (e.g. volume, radii, length, connected relation etc.) are needed to assign to the network elements (nodes or bonds). These characteristics can be estimated to construct an ideal network based on experimental results to investigate some relationships between the permeability and the pore size distribution. However, the construction of realistic networks directly from 3D images of porous media is much more demanding. Hence, in the following, I explore how to modify the network structure to meet the requirements for different network models and how to measure most of the commonly used quantities from rock images.

Modifying the network structure

In essence network models usually simplify the realistic network elements to a less-rich representation, thus obtaining a regular network. For example, individual network elements are often regarded as uniform ducts with circular, triangular or square cross sectional shapes. Meanwhile some network models (e.g. Lopez et al. 2003[93]) are not limited to regular network lattices, and instead are based on the voxel representation of the pore space. Among these two types of network models, their network structures are significantly different. Therefore, for a specific network model, we need to transfer the extracted PS (as a GT network of nodes and bonds) to fulfil the specific structure requirements of the target application.

As an example, let us consider the Imperial College (IC) network model (Valvatne and Blunt, 2004[170]) to show some of the issues involved in modifying the realistic original network. In the following, I call the IC network structure an ideal network and the original GT network a realistic network (the GT network is extracted from rock images under no assumptions about the characteristics, which means that very complex structures may appear). In Figure 4-42, some unusual phenomena are demonstrated.

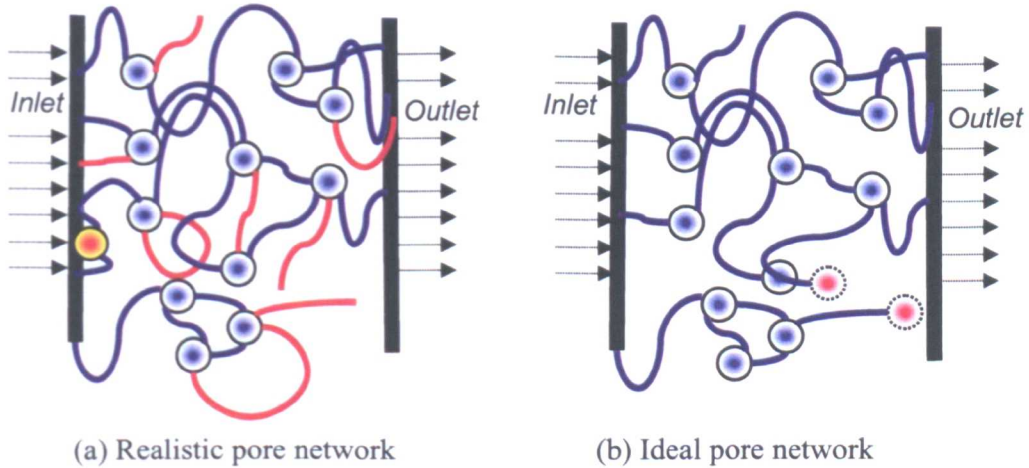


Figure 4-42: The transformation from a realistic pore network to ideal pore network, where discs represent nodes and curves represent bonds.

For a node in a realistic pore network, there may exist 0, 1, 2 or more bonds connected with this node, which correspond to isolated pore, dead-end pore, channel pore and nodal pores. In the IC network model, pores on the inlet/outlet of the system are not allowed. For a bond, it may connect with one, two and even more pores in a realistic network. This actual arrangement has to be adjusted to meet the model requirement, which specifies that a bond must link two and only two distinct nodes (pores), i.e. the red bonds in Figure 4-42 are not allowed to exist in the resultant ideal network structure. And note that the rules of the IC model state that a pore cannot be connected with itself by a bond, and two pores can be connected by only one bond. For this reason, the following rules are given to convert a realistic network structure to the IC network structure.

1. Create a virtual node (pore-body) at the terminal point of a bond if the bond is connected with only one node;

2. Remove all redundant bonds between two nodes where the inlet and outlet are virtually regarded as two nodes of infinite size;

It is not known what effects are introduced in this transformation (if any) by the removal of redundant/duplicate bonds, or whether certain bonds are critical, while others are not. These issues are relevant for the conversion to this specific network model, but it may not be necessary to address them if the target application does not have those restrictions and can represent the realistic GT network.

Measuring properties of network elements

There are two kinds of properties – connectivity and geometry. The topological property can be described by a graph in the IC network model. Using my approach, the network of volumetric nodes and bonds can be extracted from the PS. For a node in the extracted network, it is easy to determine the directly linked bonds by checking the neighbourhood of each voxel in the node volume. After finishing the check, all different bonds (different sequence numbers) can be identified and then a graph can be established. In my implementation, I use the node-backbones and bond-backbones rather than the volumetric nodes and bonds for the check. Doing so, most of the false links can be avoided.

The geometric properties of network elements include the shape factor, volume, radii and length in the IC network model. In the following, I introduce some skeleton-based techniques to measure the shape factor and radii of bonds and nodes or to establish the connection graph. As for volume and length, they can be simply derived by counting the number of voxels.

Shape factor of bonds and nodes

From each skeleton voxel, a CS can be cut off from the PS using the approaches described in Section 4.2 according to its local structure (neighbourhood). The number of CSs from a skeleton voxel is determined by the number of normal orientations. For example, only one normal orientation can be obtained if the skeleton voxel has only two 26-neighbours. And more than one normal orientation can be obtained if the skeleton voxel has more than two 26-neighbours. If only one neighbour of the skeleton voxel

exists, I use as the normal orientation the direction from the skeleton voxel to the neighbour. If a skeleton voxel has no 26-neighbour, any one of the thirteen orientations (see Figure 4-18) can be selected.

For a 3D rock image \mathcal{P} , we can extract a network of nodes and bonds from \mathcal{P} using the approach described above. Let $B_{\text{skl}}(\mathcal{P})$ be the set of all bond-skeleton voxels in the extracted network. Each 26-component in $B_{\text{skl}}(\mathcal{P})$ is then considered as the bond-backbone, $\{p_1, p_2 \dots p_m\}$, of an individual bond Bd . From each skeleton voxel p_i (black) of Bd , we can cut off n_i CSs, i.e. $Cs_1, Cs_2 \dots Cs_{n_i}$. For each CS $Cs_j, j = 1 \dots n_i$, further we can compute its shape factor $G(Cs_j)$ applying Equation (4.9). And the shape factor at p_i , denoted by G_i , is then defined as the harmonic (or arithmetic) mean of all $G(Cs_j)$ for $j = 1 \dots n_i$, i.e.

$$G_i = n_i / \sum_{j=1 \dots n_i} G(Cs_j). \quad (4.10)$$

Therefore, the shape factor of a bond Bd can be defined as

$$G(Bd) = m / \sum_{i=1 \dots m} G_i. \quad (4.11)$$

As for a node, the computation of its shape factor is similar to that of a bond. But the difference is that I only compute the shape factor for the origin of a node rather than for all node-skeleton voxels of the node. Applying Definition 4.2 and Rule 4.1, a set of original node-skeleton voxels can be identified, in which some original node-skeleton voxels generate independent node-backbones and others are merged together to become the node-backbones after invoking a merging operation. If the backbone of a node contains only one original node-skeleton voxel, then the original node-skeleton voxel is defined as the origin of the node, otherwise any one of original node-skeleton voxels in a node can be selected as the origin. For each node, the shape factor at its origin can then be computed using Equation (4.11).

Radii of bonds and nodes

There are two types of quantities that can be used to characterise the radii of nodes and bonds. The first one is the hydraulic radius which is defined as the cross sectional area divided by the corresponding perimeter. Obviously, the measure can be done in the same way for computing the shape factor described above. The second one is the radii

of maximal inscribed spheres, called inscribed radii for short. In the following, I focus on the computation of inscribed radii of nodes and bonds.

Given a rock image \mathcal{P} and its Euclidean distance valued skeleton $CSkl(\mathcal{P})$, let $Sk(Bd)$ represent the backbone of a bond Bd , i.e. for each $p \in Sk(Bd)$, we have $CSkl(p) > 0$. According to the definition of the distance map in $CSkl(\mathcal{P})$, the distance value at a pore voxel is defined as the squared Euclidean distance to the closest solid voxel. Therefore, the radius of the maximal inscribed sphere at a skeleton voxel p , denoted by $R(p)$, is equal to the square-root of the corresponding distance value, i.e.

$$R(p) = \sqrt{CSkl(p)}. \quad (4.12)$$

Therefore, for a bond Bd and backbone $Sk(Bd) = \{p_1, p_2 \dots p_m\}$, the inscribed radius of Bd can then be calculated by harmonic (or arithmetic) mean among p_i , $i=1, 2 \dots m$. i.e.

$$R(Bd) = m / \sum_{i=1}^m \sqrt{CSkl(p_i)}. \quad (4.13)$$

As for a node, its inscribed radius is simply defined as the square-root of the distance value at its origin.

4.4 Conclusion and Discussion

In this chapter, (1) an efficient skeleton-based sphere-fitting approach is introduced; (2) a comprehensive investigation on the computation of shape factor is carried out; and (3) an extraction of realistic network is developed based on the geodesic chamfer distance transformation using the pore skeleton as searching structure.

The new sphere-fitting method provides sphere equivalent pore sizes, which significantly differ from the cross sectional size (see Figure 5-6 and Figure 5-11) and in more detail (see Figure 4-10). The sphere equivalent size is used to quantify the pore volume while the cross sectional radii are utilized to characterize the pore-throat sizes, since the cross sectional radius is defined as the shortest Euclidean distance from a skeleton point to the pore solid surface.

Based on the central location and the SED values of the pore skeleton, an efficient and accurate computation of the shape factor has been developed. This computation

starts with extraction of spatial cross-sections by determining an optimal normal orientation and by using a fast template transporting algorithm. Then spatial cross-sections are projected onto coordinate planes to simplify the calculation of the areas and perimeters of the corresponding 2D shapes, which is done by introducing an optimal contour smoothing scheme. Finally, the shape factors of 2D shapes are converted back to the shape factors of the original spatial cross-sections using the projecting coefficients. For regular shapes, the computed shape factor coincides with analytical values. However the calculation of the shape factor is not sufficient to distinguish different rock samples (see Chapter 5), which are intrinsically different. One of the reasons may be the restriction of choosing only 13 discrete normal orientations of cross sections, which results in only 13 discrete perpendicular planes. To improve this, more discrete perpendicular planes should be introduced and the related disconnectedness of the discrete shapes should be resolved by new approaches such as interpolation techniques. Another reason may be in the optimal smoothing scheme. In Chapter 5 several smoothing schemes have been compared, but no conclusion can be made for the choice of a “best” smoothing scheme. The third reason may come from the vague relationship between a spatial shape and its projections on the coordinate planes. Based on three types of normal orientations, the conversion of area and perimeter from 2D shapes to spatial shape may produce some errors in certain cases.

The λ -adjacency and the clustering rule proposed by Liang et al. (2000a) have been adapted to classify skeleton voxels into four classes: isolated, terminal, link and junction voxels. This facilitates pruning of network structures according to the requirements of a specific network model and it determines the basic structure of the equivalent pore network. By incorporating skeleton voxels within the range of maximal inscribed sphere of junctions, an appropriate node-skeleton backbone is generated through a merging operation, which takes into account topological and spatial relation. In particular the so-called “snowballing” and topology-breaking are avoided. Most network parameters, such as average radii, shape factors, lengths of nodes and bonds and coordination numbers can be readily computed when the pore skeleton is extracted.

To assign volumetric parameters for the network elements, a new method based on the geodesic chamfer distance has been introduced to partition the pore space. Unfortunately, the accuracy of this method is still not satisfactory because some shared regions between two objects (node or bond) may be wrongly classified (see Figure 4-

20(c) and Section (4.3). One alternative is to use the level set method. Another way to improve the partition accuracy is to use geodesic Euclidean distance (GED) transformation instead of the GCD transformation. However, the major problem with the GED transformation is that its computational efficiency is unacceptably poor. To design a practical GED transformation, a more efficient algorithm for the determination of occlusion points and a discrete method for comparing two Euclidean distance values are required.

Chapter 5 Applications

In this chapter, the set of image processing and pore structure analysis techniques introduced in previous chapters is applied to three rock samples to explore their macroscopic properties based on the quantification of their basic geometric and topological features. Having microstructure information, pore network structures are constructed for network flow models to predict fluid flow properties through the porous media. In section 5.1, three sandstone samples are selected and pre-processed. The basic geometric properties, such as pore size, shape factor etc., of the three rocks are studied in section 5.2 with the additional numerical simulation of mercury injection. After pointing out the limitations of the Euler number and the coordination number, in section 5.3, a novel topological descriptor – the connectivity coefficient – is introduced in order to accurately describe the connectivity of the porous media. In section 5.4, I construct network structures from the three rock images as input to the IC network flow model and the predicted results are briefly analysed. As for a trial to build up the analytical correlation between microstructure and macroscopic properties, I design several numerical experiments aiming to establish the correlations between absolute permeability and connectivity coefficient, between absolute permeability and average cross sectional diameter (pore size), and among these three quantities.

5.1 Dataset and Pre-processing

5.1.1 Sandstone Samples

Fontainebleau sandstone is a natural sandstone of Oligocene age from France which has been widely used in texture studies (Arns et al., 2004[10]; Baldwin et al., 1996[13]; Blunt, 2001[21]; Ioannidis et al., 1996[63]; Knackstedt et al., 2001[73]; Lindquist et al., 2000[89]; Vogel and Roth, 2001[185] etc). Its composition is 100% quartz grains, with minor amounts of cement (dominantly silica). The variation of porosity ranges from 2% to 30% with constant grain size (around 250 μm). Because of its usual features, i.e. the uniformly constant composition, grain size and porosity

variation Fontainebleau sandstone allows for the study of effects of pore geometry independent of other parameters. Berea sandstone has also been used by the petroleum industry for many years as a standard material in core analysis research and in laboratory core flooding experiments. For example, Oak (1990[112]) studied a water-wet Berea sandstone to measure the relative permeability in the primary oil flooding and secondary water flooding, and provided an array of experimental results used widely as a good standard of comparison. Berea sandstone is relatively homogenous, and is made up of well-sorted and well-rounded predominately quartz grains. Berea sandstone also contains minor amounts of feldspar, dolomite, and clays (Churcher et al., 1991[33]).

In this chapter, I choose two Fontainebleau sandstone images and one Berea sandstone image, which are shown in Figure 5-1. For convenience, they will be called as FS-A, FS-B and BS, respectively, and their basic and quantified morphological (GT) properties are listed in Table 5-1.

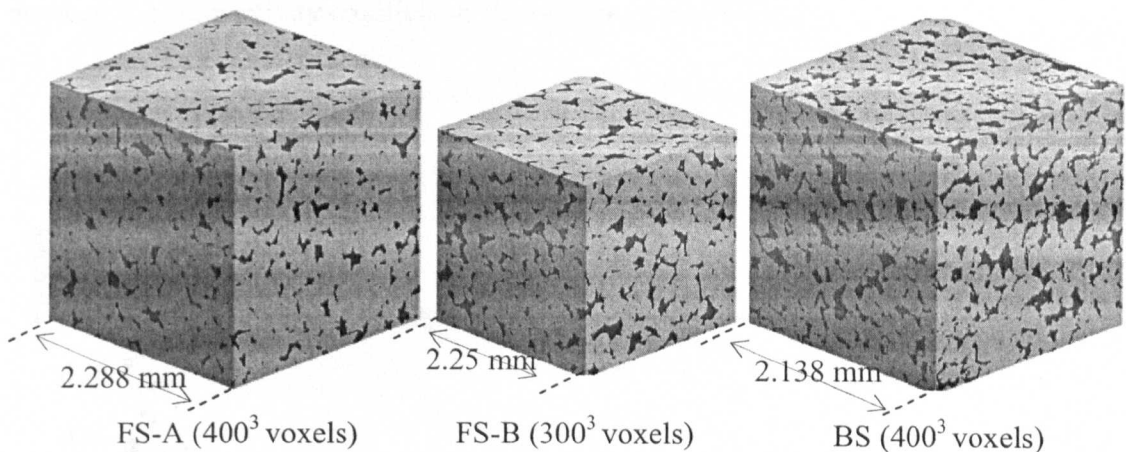


Figure 5-1: Three CT scanned sandstone 3D images consisting of the PS (in black) and the solid matrix (in grey). FS-A and FS-B are two Fontainebleau sandstone samples, and BS is a Berea sandstone sample.

These three sandstone images were acquired (by others, and made available to my study) via the scanning of cylindrical microplugs using a high resolution X-ray computer tomography process to produce digital images. Each voxel of these 3D images has a linear dimension of $5.72 \mu\text{m}$, $7.5 \mu\text{m}$ or $5.345 \mu\text{m}$ for FS-A, FS-B or BS, respectively, and takes on the value 0 (solid or grain) or 1 (pore or void). After the salt-and-pepper noise has been removed from the digital images, the measured porosities from the resultant images are 10.6252% (FS-A), 13.5527% (FS-B), and 19.6509% (BS) by counting the number of pore voxels.

Rock type	FS-A Fontainebleau sandstone	FS-B Fontainebleau sandstone	BS Berea sandstone
Dimension (voxels)	400×400×400	300×300×300	400×400×400
Resolution (μm)	5.720	7.500	5.345
Volume (mm ³)	11.98	11.39	9.77
Porosity φ (%)	10.6252	13.5527	19.6509
L_d (μm)	46.7	51.6	45.2
I_d (μm)	38.3	40.6	36.3
G	0.0425	0.0429	0.0447
C_n	3.0397	3.1109	3.0556
ζ_v (mm ⁻³)	110.65	203.74	687.15
K (mD)	425	1189	1805

Table 5-1: Basic (a) and quantified (b) morphological properties of the three sandstone samples shown in Figure 5-1 (L_d : average sphere equivalent pore diameter; I_d : average cross sectional pore diameter; G : average shape factor; C_n : average coordination number; ζ_v : connectivity coefficient; K : absolute permeability.)

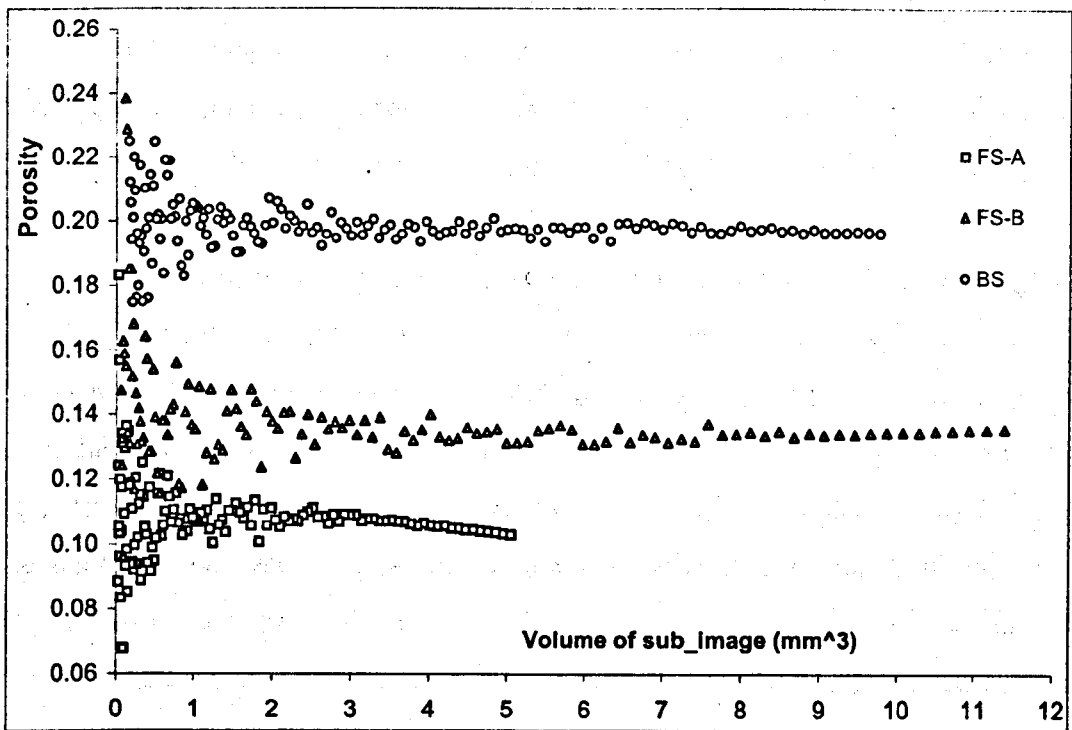


Figure 5-2: Representative elementary volume of the three rock images (i.e. FS-A, FS-B and BS) with regard to their porosities.

In order to efficiently handle and compare these samples, it is necessary to cut off sub-images from the original images such that they are quite small in volume of voxels

without losing the ability to represent the corresponding samples. This means that we need to determine a common REV (representative elementary volume) for these three samples. The simple way to do so is to find a minimum volume at which the porosities of sub-images of a rock image tend to be stable. And the volume is then used to minimise the size of our processed rock images. As indicated in Figure 5-2, the three REV volumes are $\sim 3.2 \text{ mm}^3$, $\sim 6.8 \text{ mm}^3$ and $\sim 8.1 \text{ mm}^3$ for FS-A, FS-B and BS, respectively. Therefore, we choose 10 mm^3 as the common REV for these three samples, and their corresponding dimensions (in voxels) are larger than the required REV.

5.1.2 Image Pre-processing

The original sandstone images contain a large number of floating solid particles and isolated pores due to artefacts of the CT scanning and digitalisation. In these images (26, 6) is used as the adjacency pair, so a so-called floating solid particle is actually a white (solid) 6-component which is completely enclosed within the PS, and an isolated pore is a black (pore) 26-component which is very small and is not connected to both of the inlet and outlet. The inlet and outlet are commonly chosen as two opposite coordinate planes on the boundaries of the image space.

The occurrence of floating solid particles and isolated pores in rock images has little impact on the computation of fluid flow properties, but has a significant effect on the quantification of morphological (i.e. GT) properties of the PS. For example, both of them have effect on the generation of skeleton (medial axis) of the PS. After skeletonization, each isolated pore is shrunk into a single isolated voxel while each of the floating solid particles produces a spherical surface in the resultant skeleton. In Figure 5-3(a), two spherical surfaces and a lot of dots (single voxels) remain in the resultant skeleton after the topology-preservation thinning has been carried out. As a direct result, they will jeopardize the identification of topological junctions on the skeleton and complicate the network structure when a network model is involved.

The Euler number is also an important quantity for describing the pore connectivity (see Section 2.2.1). But the object components would be outnumbered by a large number of isolated pores, and the cavities would be wrongly identified due to the existence of floating solid particles, thus making the Euler number less meaningful if

extracted from raw images. Table 5-2 shows an example for the three samples. In the PS of FS-A there are in total 1106 pores (object 26-components): only one is connected to both the inlet and outlet and occupies 97.16% of the PS; each of the other 1105 pores is either not connected to both the inlet and outlet, or only connected to one of them, and the accumulative volume of these 1105 pores is only 2.84% of the PS in FS-A. As shown in the table, the porosity in the original image of FS-A is 10.6252%, and it is reduced to 10.3231% after removing all the 1105 isolated pores. FS-A in total contains 402 solid particles, in which only one is the background (solid), but with 401 solid particles are floating in the PS. Converting the floating solids into pores increases the porosity of FS-A from 10.3231% to 10.3352. According to Equation (2.13), it is clear that the numbers of isolated pores and floating solid particles significantly amplify the influence of object components (h_0) and cavities (h_2) on the computation of the Euler number (see Table 5-5). Both the isolated pores and floating solid particles degrade the ability for the EPC to accurately describe the pore space. And it is the same for the other two samples. Therefore, it seems to be necessary to remove isolated pores and floating solid particles before initiating an analysis of the pore system.

Rocks	Numbers of pores		Numbers of solid particles		Porosities (%)		
	Total	Isolated	Total	Floating	Original	R-Pore	R-Solid
FS-A	1106	1105	402	401	10.6252	10.3231	10.3352
FS-B	680	679	33	32	13.5527	13.5001	13.5002
BS	2251	2250	388	387	19.6509	19.5399	19.5492

Table 5-2: Statistics of black 26-components (pores) and white 6-components (solid particles) from samples FS-A, FS-B and BS and the effect of pre-processing on porosity of the PS. In the column Original, R-Pore and R-Solid, three porosities are listed for each sample before and after removing isolated pores and removing floating solid particles.

In order to reduce the effect of such imaging noise, I carry out some pre-processing before any practical operation is undertaken. The pre-processing can be done by invoking morphological operations (e.g. opening or closing) to smooth original

images and removing isolated pores and floating solid particles from the smoothed images. Figure 5-3(b) shows the result of the removing operation: the spherical surfaces and single voxels in Figure 5-3(a) disappear in the resultant skeleton. The procedure can be summarised as three steps: (1) identifying all black 26-components and white 6-components using the component labelling algorithm described in Section 3.3; (2) removing all black 26-components (tiny isolated pores) which are disconnected from the inlet or outlet; (3) converting all floating solid particles except the background (the maximum white 6-component in voxels) into the PS.

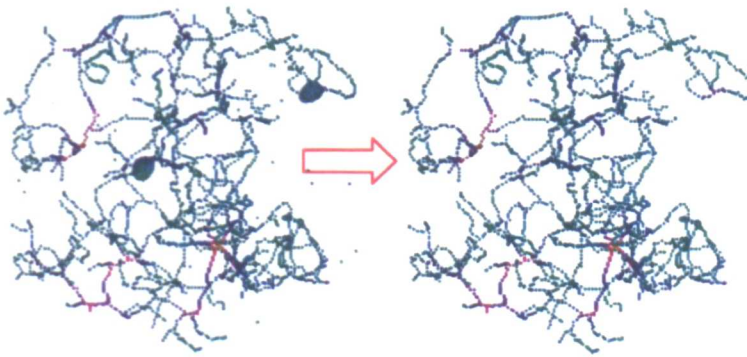


Figure 5-3: The effect of floating solid particles and isolated pores on the extraction of pore skeleton (a) before and (b) after removing floating solid particles and isolated pores.

5.2 Geometric Properties

In this section, some basic geometric properties of the three sandstone samples will be investigated, which includes pore size, cross sectional area and shape factor, and simulated mercury injection curves. As for the pore size, I introduce a new descriptor, cross section size (radii or diameter), which is different from the sphere equivalent size. The difference between these two pore sizes is demonstrated in Figure 5-4. In Figure 5-4(a), each pore pixel (voxel) is clustered into one of three different size pores, and the size (sphere equivalent size) is then determined by the radius of the corresponding inscribed sphere. A distinct value (grey level) is assigned to all pixels which belong to an individual pore. In Figure 5-4(b), from each pixel on the skeleton, a CS can be derived using the approach described in Chapter 4, and the radius of the corresponding inscribed circle in the CS is regarded as the size of the skeleton pixel, which is called its

cross sectional radius (size). Having determined all CSs on the pore skeleton, the area and the shape factor of these CSs can then be computed and analysed using the methods described in Chapter 4. Furthermore, numerical simulation of mercury injection can be easily carried out based on the cross sectional sizes of skeleton voxels.

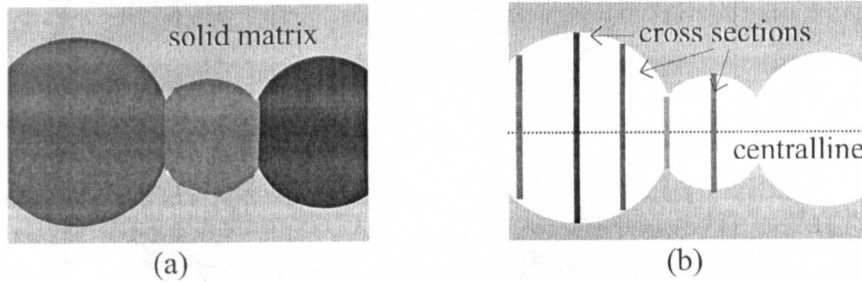


Figure 5-4: Comparison between sphere equivalent size and cross sectional radii (size). Each pore voxel is assigned (grey level) a value corresponding to a sphere equivalent radius while each skeleton voxel is assigned a value corresponding to a radius of an inscribed circle within a CS.

5.2.1 Sphere Equivalent Pore Size

Having the distance map and skeleton of the PS, i.e. a Euclidean distance valued skeleton (see Section 4.1.1), different sphere equivalent size pores can then be extracted from the PS. In my algorithm, firstly the skeleton voxels are sorted into a list in the descending order of skeleton voxels' SED in the coloured skeleton; secondly the backbones of individual pores are classified using maximal inscribed spheres, the pore size of an individual pore is determined by the corresponding SED on the skeleton; finally the backbones are expanded within the PS into individual pores using the geodesic chamfer DT described in Chapter 3 Algorithm 3.3. From rock images, I can obtain two kinds of images - the maximal inscribed sphere images and the resultant pores after partition (Figure 5-5), where distinct size pores are coded in different colours (rainbow-inverted colour scheme).

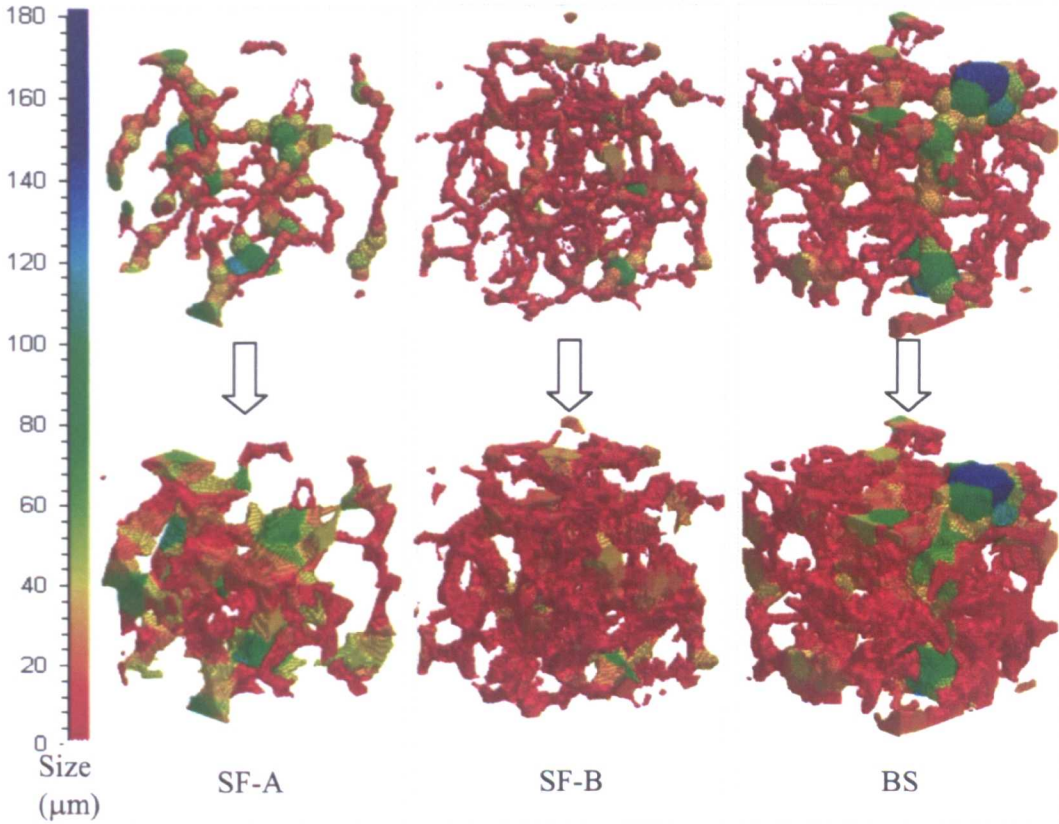


Figure 5-5: Individual pores of different sizes (i.e. sphere equivalent size) coded by rainbow-inverted colour scheme: the maximal inscribed spheres (top) and extracted pores (bottom) for sub-images of SF-A, SF-B and BS, respectively.

Pore size distribution (PSD) is an important characteristic of the PS. To obtain the PSD, let N be the total number of pore voxels and L_M represent the maximum pore size (SED) in a rock image, thus the pore size range can be equally divided into m sub-intervals: $[L_0, L_1), [L_1, L_2) \dots [L_{m-1}, L_m]$, where L_0 is the minimal pore size and $L_m = L_M$. Counting the number N_i of pore voxels that have been identified as belonging to the pores of size from L_{i-1} to L_i , I can then calculate the pore size distribution (volume percentage) by dividing N_i by N for all $i = 1, 2 \dots m$. The shapes of the PSDs for the three samples are shown in Figure 5-6, which indicates that there is significant difference among them. Table 5-3 lists four kinds of statistics about the pore sphere equivalent size, i.e. pore size variation, peak pore size, average pore size and the standard pore size deviation. The average pore sizes of FS-A, FS-B and BS are $46.7 \mu\text{m}$, $51.6 \mu\text{m}$ and $45.2 \mu\text{m}$, respectively. However, the three peak sizes are located at $36.7 \mu\text{m}$, $46.3 \mu\text{m}$ and $34 \mu\text{m}$ rather than in the middle of the pore size range, which are also

far away from the average pore sizes. From this analysis, the common feature of these three samples is that most of the pores are smaller than the average pores.

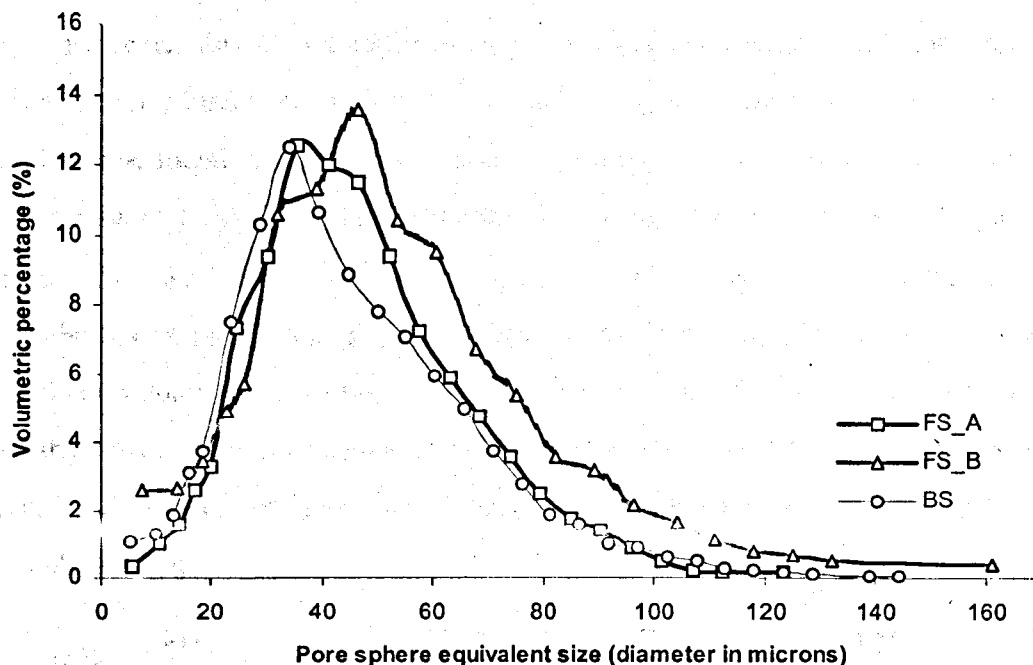


Figure 5-6: Pore Size Distribution of rock samples FS-A, FS-B and BS.

Samples	Pore size range (μm)	Peak pore size (μm)	Average pore size (μm)	Standard deviation (μm)
FS-A	5.72 ~ 116	36.7	46.7	20.17
FS-B	7.5 ~ 161	46.4	51.6	26.2
BS	5.345 ~ 144	34	45.2	21.9

Table 5-3: Statistics about the pore size of FS-A, FS-B and BS, where the pore size is described in terms of sphere equivalent size in diameter.

5.2.2 Cross Sectional Pore Size

The skeleton of the PS is the central path of fluid flowing through the PS of a rock, which is illustrated in Figure 5-7. According to the discussion in Chapter 4, the skeletonization ensures that the skeleton not only locates in the middle of the PS but also contains information about the maximum inscribed distance (SED) to the solid (grain) surface. Combining distance with the skeleton, a so-called Euclidean distance

valued (coloured) skeleton can be generated, which is shown in Figure 5-8. For each skeleton voxel, the distance from this voxel to its closest solid voxel is recorded and is used as the radius of the corresponding CS (cross sectional radius).

However, this measurement of cross sectional radii has a significant drawback when the PS is mainly connected by small pores (e.g. of radius of 1 or 2 in voxel). This issue can be found in many rock images if the imaging resolution is very coarse. And the measured radii for very narrow pore channels are certainly quite vague. For example, the SED of 1 could correspond to a lot of complex configurations in $3 \times 3 \times 3$ neighbourhood rather than a fixed pattern. Figure 5-9 highlights the problem when small pores dominate the pore connectivity. The minimum value is 1 voxel (pixel in 2D) but the corresponding configuration in its neighbourhood is complex: there exist more than 26 distinctive configurations in terms of different adjacent number in the $3 \times 3 \times 3$ neighbourhoods.

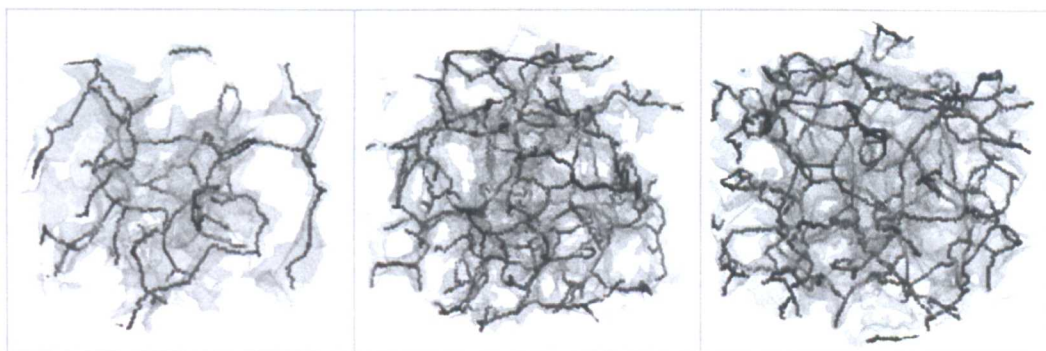


Figure 5-7: Skeleton's central location for sub-images of FS-A, FS-B and BS, respectively.

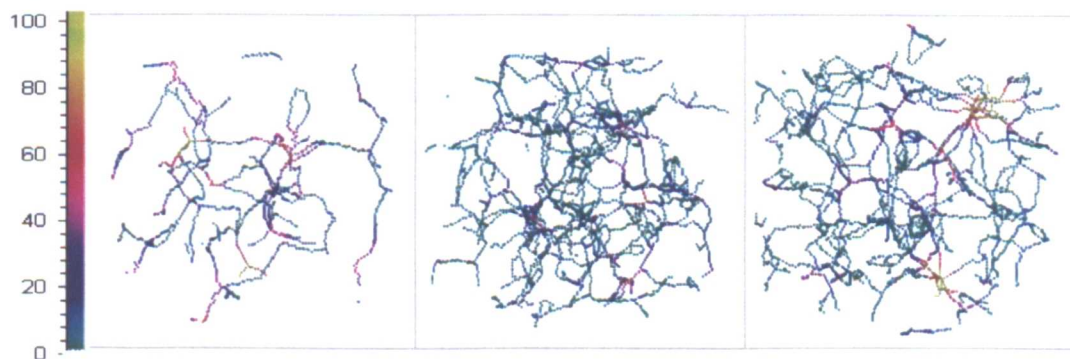


Figure 5-8: Small sub-images of the skeleton with SED values from FS-A, FS-B and BS, respectively. Voxels are supernova spectrum colour coded. Green represents skeleton pore voxels closest to the grain surface and yellow represents the skeleton voxels farthest from the grain surface.

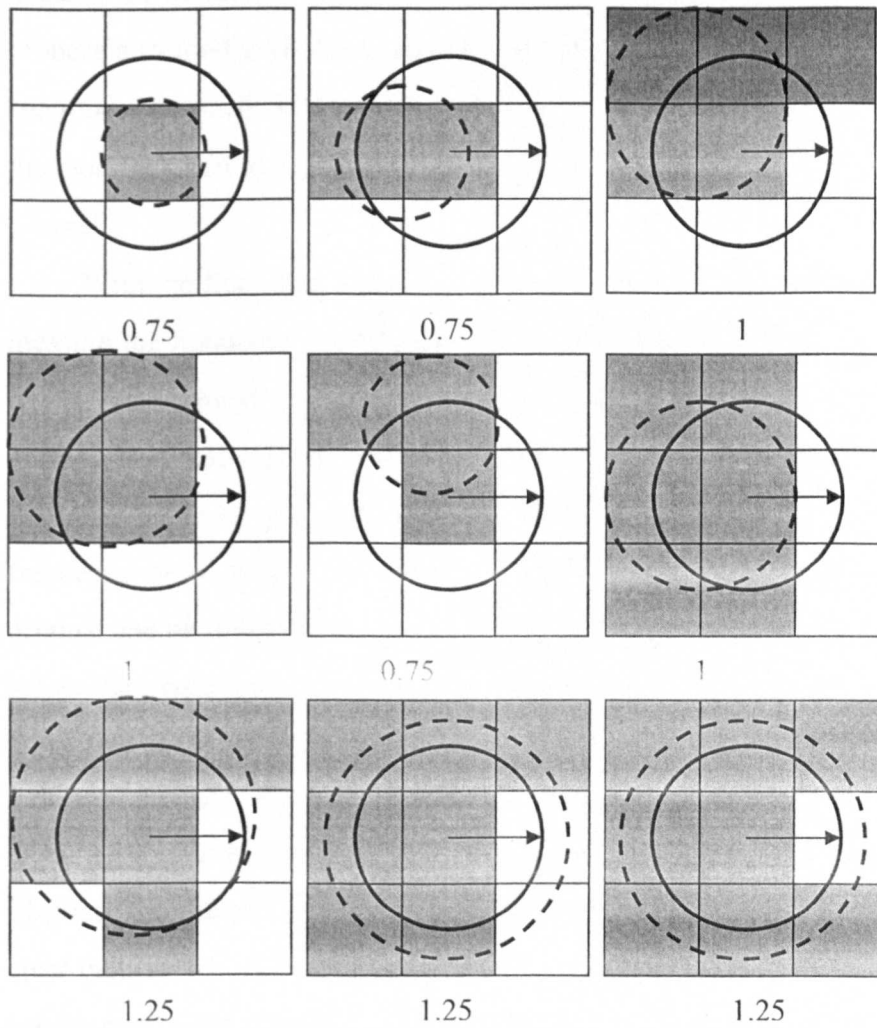


Figure 5-9: 2D illustration of some configurations in the neighbourhood of a pore voxel of radius 1 (in voxel): All the pixels centred at each 3×3 square have the same radius of 1 in pixel (voxel) but have different configurations in its neighbourhood. The solid circle shows the sphere (circle) associated with the initial radius (e.g. 1) measured through the distance transformation while the dotted circle shows the ideal sphere (circle) for a more accurate radius. The ideal radius is showed right below each figure. Grey squares represent pore pixel and white square solid pixel.

In Figure 5-9, only a few of the configurations in the $3 \times 3 \times 3$ neighbourhood of a skeleton voxel are given under the assumption that all omitted voxels belong to the PS. Besides different configurations, an example of the distribution (Figure 5-10) of the number of adjacent voxels in the $3 \times 3 \times 3$ neighbourhoods of skeleton voxels also suggest that it is not accurate when 1 is used to approximate the cross sectional radii at the central voxels (i.e. on the skeleton). This strongly suggests that the small pore size

needs to be modified carefully in order to provide much more detail. For this reason I propose a method to obtain a more accurate approximation to the cross sectional radii of small pore channels. In Figure 5-9, the dotted circles (spheres) are used to indicate how the modified radii are derived based on different configurations in the neighbourhood of a voxel.

With the Euclidean distance valued skeleton and the modified radii, we can then measure the frequency of skeleton voxels with regard to the cross sectional radii. This can be done through (1) the whole range of cross sectional diameter in a rock image is divided into many equal intervals, (2) the numbers of skeleton voxels whose cross sectional diameter fall within different intervals are counted, and finally (3) the frequency of cross sectional diameter of skeleton voxels is computed based on the original and modified SED value on skeletons. From the three rock images, Figure 5-11 shows the frequency of skeleton voxels against the cross sectional diameter. It should be noted that the distribution of FS-B is quite different from that of FS-A and BS, which indicates that the PS in FS-B has many more small CSs when the cross sectional diameter is used to measure pore size. In Table 5-4, some basic statistics are listed to illustrate the differences among these three samples. Comparing with Table 5-3, it is clear that the average cross sectional diameter is much smaller than the corresponding sphere equivalent diameter at the same position for the same sample. Peak pore size demonstrates greater differences in terms of sphere equivalent diameter than in cross sectional diameter.

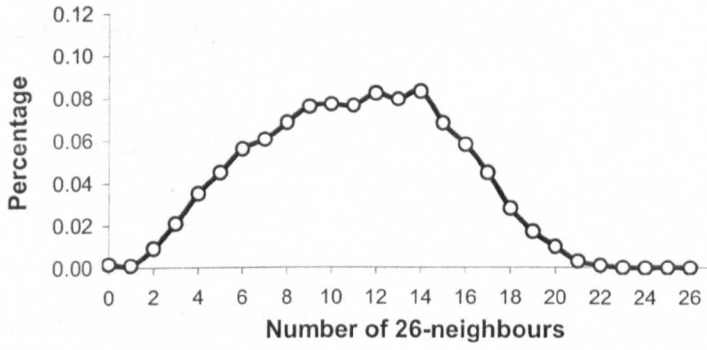


Figure 5-10: The distribution of the number of 26-neighbours at a skeleton voxel with SED of 1 for sample FS-B.

Samples	Pore size range (µm)	Peak pore size (µm)	Average pore size (µm)	Standard deviations (µm)
FS-A	6.95 ~ 110	33.2	38.3	18.3
FS-B	6.95 ~ 105	33.9	40.6	22.2
BS	6.95 ~ 127	32.6	36.3	18.2

Table 5-4: Statistics of pore sizes of skeleton voxels for sample FS-A, FS-B and BS, where the pore size are described in terms of cross sectional diameter.

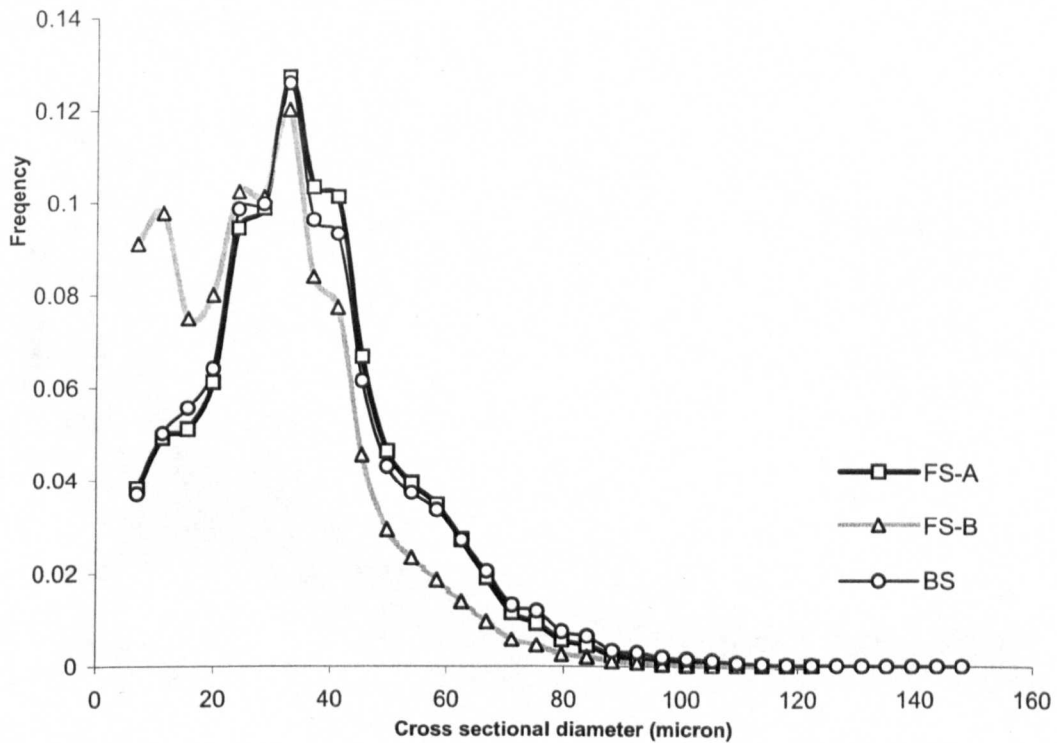


Figure 5-11: The distributions of cross sectional diameter of sample FS-A, FS-B and BS.

5.2.3 Cross Sectional Area and Shape Factor

For constructing a network structure or directly simulating the oil-flooding or water-flooding process, the morphological features of CSs need to be explored aiming to extract more quantities from the rock images. Many details associated with CSs have already been given in Chapter 4, such as the orientation, projection and computation etc. The orientation of a CS at a skeleton voxel is approximated by one of thirteen directions (see Figure 4-18) by considering the relative positions of its neighbours on skeleton. Using the extracting algorithm explained in Figure 4-19, CSs can be efficiently obtained and projected on an appropriate coordinate plane (XY, YZ, or XZ-plane). The area and perimeter of corresponding 2D shapes are calculated utilising Equation (4.6), and they are then transformed to the original spatial CSs using Equation (4.9).

To avoid under- or over-estimation of cross sectional area and perimeter, the basic ideas in the algorithm are: (1) smoothing sharp points or corners by replacing them with regular shapes such as circle, triangle or square (see Figure 4-26); (2) projecting spatial CSs on an appropriate coordinate plane in order to simplify the computation of area and perimeter; (3) readjusting the calculated area and perimeter based on the projection directions.

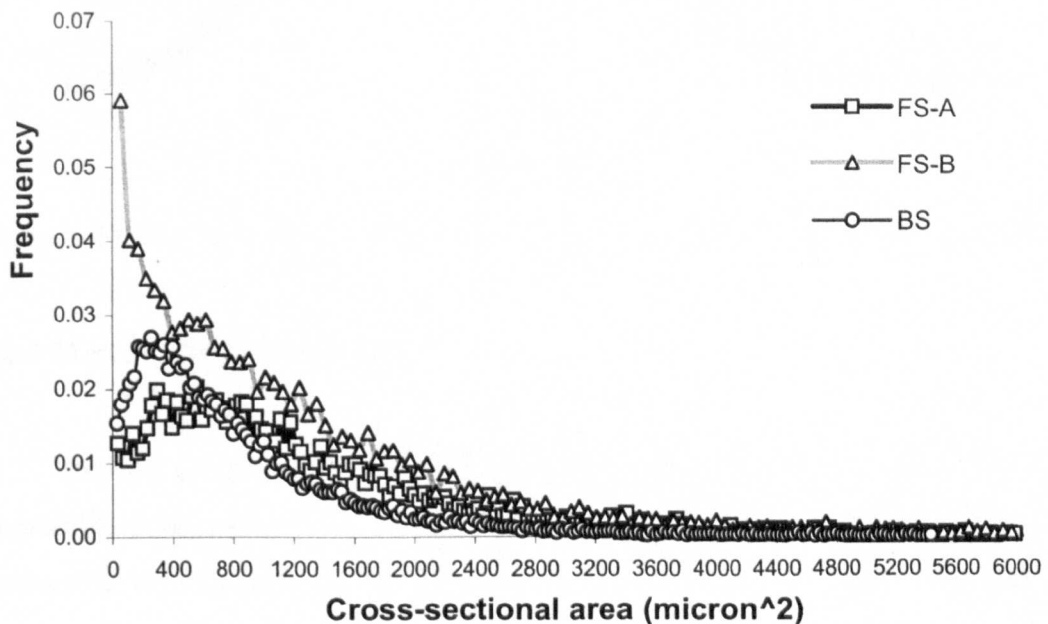


Figure 5-12: The distributions of cross sectional area of skeleton voxels.

To investigate the distributions of cross sectional area in the sandstone samples, the measured areas of CSs are firstly divided into a set of equal intervals, and then the numbers of CSs locating within different intervals are recorded to build up the frequency of cross sectional area. From Figure 5-12, I note that the distribution of FS-B's cross sectional area is significantly different from others. This indicates that the average cross sectional area of pores in FS-B is much smaller than that of other two samples.

Figure 5-13 illustrates the distributions of shape factors of the three samples. The average shape factors of FS-A, FS-B and BS are 0.0425, 0.0429 and 0.0447, respectively, which mean that shape of FS-A or FS-B tend to be more complex than that of BS but do not have significant differences among them.

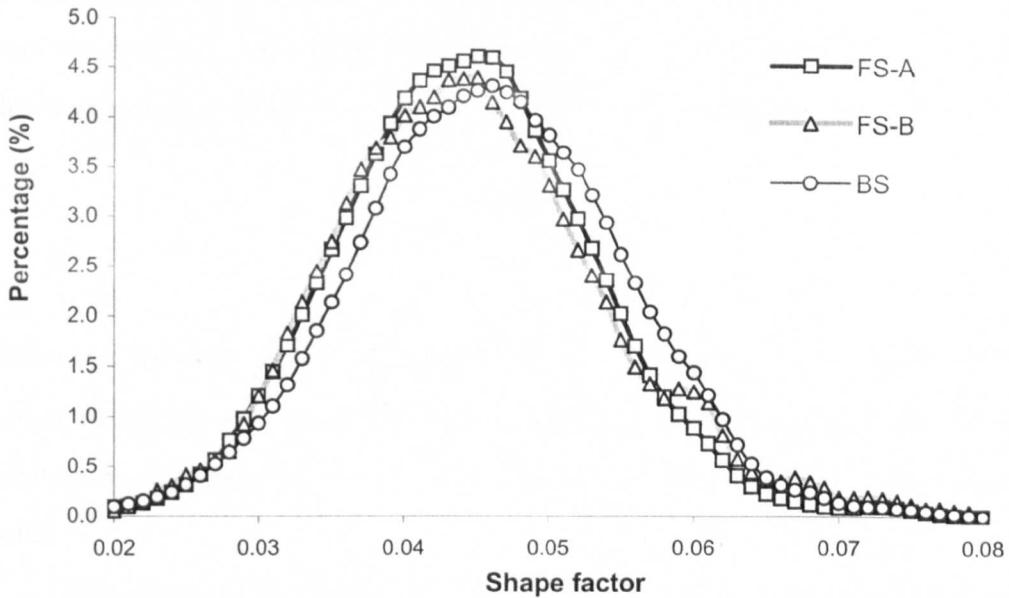


Figure 5-13: The distributions of shape factor of skeleton voxels for the three samples.

5.2.4 Mercury Injection Simulation

Invasion percolation is a dynamic flow process introduced to model the slow immiscible displacement of a wetting fluid by movement of a nonwetting fluid in a porous medium. Drainage is characterised by the movement of menisci through the porous medium and progressive invasion of the medium by the nonwetting fluid (Dias and Wilkinson, 1986[41]).

An invasion percolation algorithm simulating the process of mercury injection is given in the following. For a porous medium, which is originally completely saturated with wetting fluid (i.e. vacuum), a non-wetting fluid (e.g. mercury) is injected into one face (inlet) of the system and the fluids may escape through the opposite face (outlet). When the invading phase enters parts of the PS, the displaced fluid needs to escape. If the wetting fluid is continuous throughout the system, then at very low injected rates the wetting phase can escape from any pore or throat by flow in surface roughness to the outlet of the system. This means that no wetting phase is trapped, which coincides with the observation in mercury injection experiment.

During invasion of the non-wetting fluid, in a network of pores and throats, the throats and pores are filled one at a time. A throat is considered available if it contains no injected fluid, but is connected to a pore which does (i.e. contains injected fluid). At each stage the available throat with the largest radius is filled, together with any empty pore attached to it. The injection pressure associated with the filling at an infinitesimal flow rate is simply given by capillary equilibrium (the Young-Laplace equation)

$$P = \frac{-2\gamma \cos \theta}{r} \quad (5.1)$$

Where r is the mean radius of curvature. The capillary pressure P depends on the pore geometry (pore size), on the interaction between fluids, γ and on the amount and location of each phase in the PS, θ is the contact angle between the mercury and the solid.

The mercury injection simulation is image based, and no specific network structure is required. The extracted skeleton (GT network) of the PS is used to locate the central flow paths and the SED values on the skeleton are used to indicate the radii of CSs. Thus, the mercury injection algorithm can be described by the following.

Given a skeleton of the PS in a rock image \mathcal{P} , we regard it as the central line of flow paths. Let $\mathcal{V} = [0, L_x] \times [0, L_y] \times [0, L_z]$ be the image space of \mathcal{P} where L_x , L_y and L_z are the maxima of X-, Y- and Z-coordinates, respectively. Fluid flows along the skeleton of pore channels, and the break-through point depends on the corresponding cross sectional radius. To simulate this process, inlet and outlet are firstly selected, for example, X- (i.e. $X = 0$) is chosen as inlet and X+ (i.e. $X = L_x$) as outlet.

CSkl is a coloured skeleton, i.e. each skeleton voxel p has positive distance value i.e. $CSkl(p) > 0$ while any other non-skeleton voxels of distance value zero.

$ValNum = Max(CSkl)/2+1$; //Pre-set the number of intervals
 $UnitV = Max(CSkl)/ValNum$; //the length of an interval

Initialize queue Q_1 as all voxels on inlet and label. The accessed voxels indicate they have already been put in queue Q_1 , which are converted into negative value, i.e.

$CSkl(p) = - CSkl(p)$
 //Simulating the process of mercury invasion based on the skeleton *CSkl*
 //The direct result of this operation is to convert all distance value of skeleton voxels //into distinct label (negative value).

While $ValNum > 0$ {
 $CurVal = (ValNum-1) * UnitV$;
 $ExistLbl = false$
 Get a voxel p from queue Q_1 until Q_1 is empty
 If $abs(CSkl(p)) > CurVal$ then {
 $CSkl(p) = -ValNum$; //Label is negative integer
 $ExistLbl = true$; //indicate $-ValNum$ is a valid label
 //Insert all 26-neighbours q of $DMap(q) > 0$ into queue Q_2
 For each $q \in \mathcal{N}(p)$ { //the $3 \times 3 \times 3$ neighbourhood of p
 If $CSkl(p) > 0$ {
 Put q into queue Q_2
 $CSkl(q) = - CSkl(q)$
 }
 } else {
 Insert p into the queue of Q_2
 }
 If $ExistLbl$ is false { $ValNum--$ } //i.e. $-ValNum$ is not a valid label
 Empty Q_1 and swap Q_1 with Q_2
 }
}

Equation (5.1) expresses the relationship between the applied mercury pressure P (psi) and the radius r (μm) of the corresponding pore being invaded. The surface tension γ of mercury varies with purity, but the usually accepted value is 480 dynes/cm. The contact angle θ between the mercury and the solid, measured through the mercury, varies somewhat with solid composition, but is normally close to 140° . Thus, $r(\mu) = 107/P(\text{psia})$. Applying this to the sandstone samples, the simulated invasion processes are illustrated in Figure 5-14. At the beginning, only those pores, whose cross sectional size (radius) is very large and connected with the inlet, are occupied by mercury, and then the pressure is increased on non-wetting phase on the inlet face of the model to let smaller pores be invaded by that non-wetting phase. From the left to the right in Figure

5-14 smaller and smaller pores are invaded, the whole process is controlled by the radius of the largest cross sectional size of skeleton voxels at each pressure increment. At the end of primary drainage, all the pores are filled with mercury without traps, and the injection curve is then plotted in Figure 5-15.

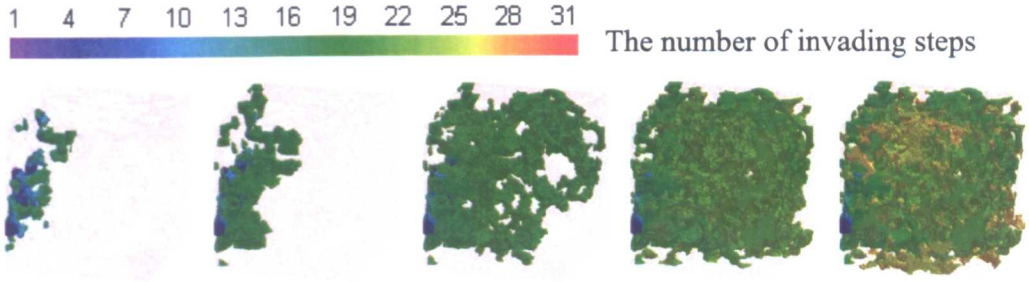


Figure 5-14: Illustration of invading process of mercury using our algorithm.

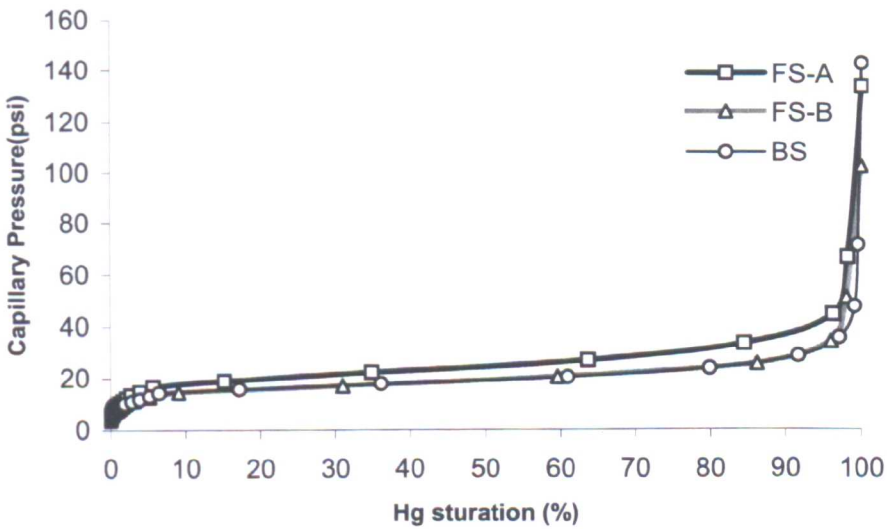


Figure 5-15: Simulated mercury injection curves of FS-A, FS-B and BS.

5.3 Topological Properties

5.3.1 Coordination Number

As discussed in Chapter 4, the PS can be referred to as the network of nodes connected by bonds. Thus the connectivity of such a pore network is often quantified by the coordination number. For each node, the coordination number is defined as the number of bonds connected with the specified node. The frequency of nodes of certain

coordination number in the whole pore network can be plotted as the coordination number distribution.

Figure 5-16 shows the coordination number distributions for the three sandstone samples. The maximum coordination number of Both FS-A and BS is 5, and this number is smaller than the maximum coordination number (i.e. 9) of FS-B. For all three samples, most of the nodes (more than 91%) are connected by three bonds. The average coordination numbers are 3.0397, 3.1109 and 3.0556 for FS-A, FS-B and BS (see Table 5-1), respectively.

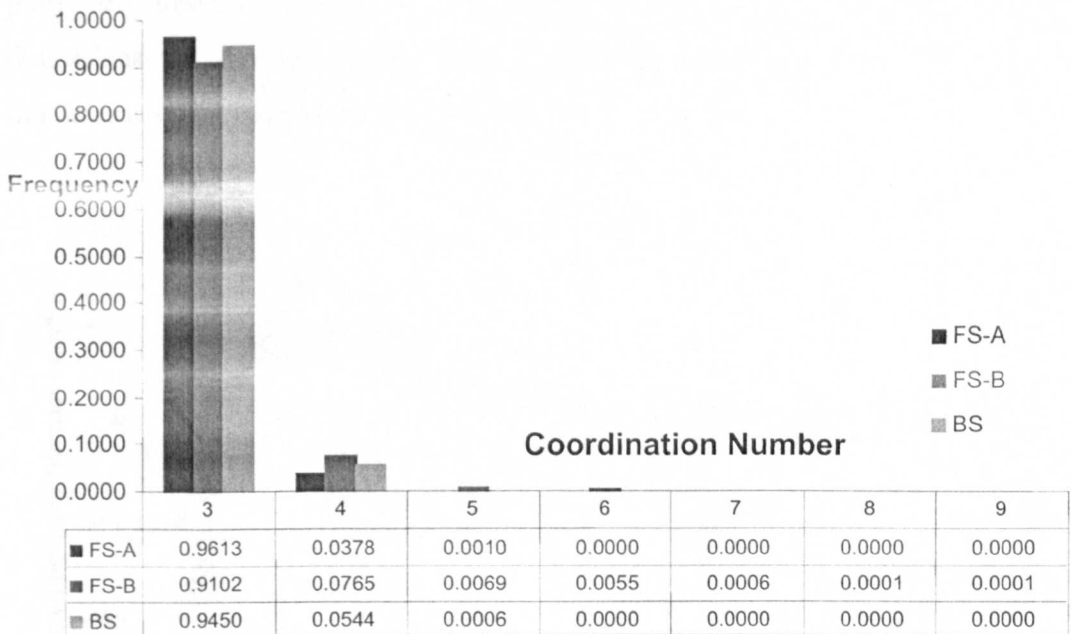


Figure 5-16: Distributions of the coordination number of pore networks extracted from FS-A, FS-B and BS.

5.3.2 The Euler Number and its Limitation

The Euler number (i.e. EPC) can be used to describe the connectivity of the components of a composite material or the PS of a porous medium (Ohser et al., 2003[115]; Levitz, 2007[83]). However, the Euler number does not lead to an unequivocal description of the topology, since the absolute values of h_0 , h_1 and h_2 (2.13) are often unknown. Moreover, the Euler number provides just a single number, describing the overall topology of the pore structure. Its value decreases with increasing connectivity. Aiming to overcome these drawbacks of the Euler number, Vogel and

Roth (2001[185]) introduced the concept of the connectivity function, which is defined as the specific Euler number in dependency of the minimum pore size being considered. The specific (volumetric) Euler number χ_v of the PS (i.e. all pores) is calculated as

$$\chi_v = \chi/V. \quad (5.2)$$

where χ is the Euler number of a rock image with volume V . This concept makes it possible for comparing the connectivity among rock images of different volume. Let d represent the sphere equivalent diameter when the PS of a porous medium has been partitioned into a set of different size pores, and the connectivity function $f(d)$ is then defined as the specific Euler number of the set of pores whose sphere-equivalent diameter is larger than d (see Section 2.4.1).

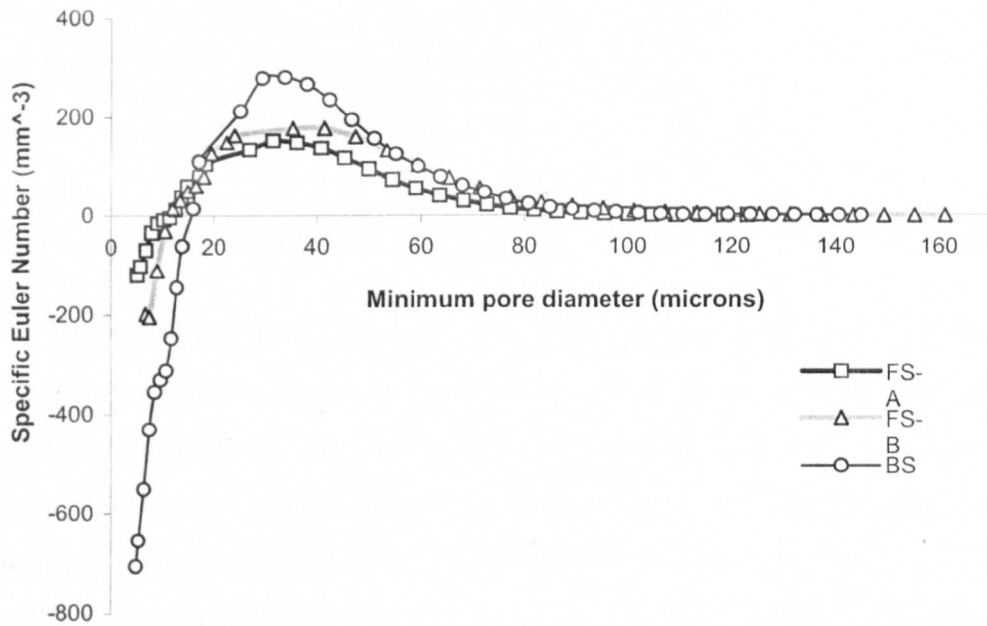


Figure 5-17: Connectivity functions of sample FS-A, FS-B and BS.

The connectivity function provides quantitative information about the pore connectivity against pore size. For BS its volume is $V = 9.77 \text{ mm}^3$ (see Table 5-1), thus the connectivity function of all pores, $f(5.345)$, is calculated as χ_v of the whole image of sample BS, i.e. $f(5.345) = -704.81 \text{ mm}^{-3}$ (see Figure 5-17). By removing all pores of diameter less than d from the original image, the χ_v of the new image is calculated again and $f(d)$ is obtained, where d is the minimum pore diameter of the new image. For the three samples, their connectivity functions are illustrated in Figure 5-17. We note

that for the whole PSs of FS-A, FS-B and BS, the χ_v of BS is about 3.46 times as the χ_v (204.64 mm⁻³) of FS-B and it is 6.86 times as that (-102.69 mm⁻³) of FS-A. Moreover, the three connectivity functions increase as the minimum diameter of pores considered increases, which means that the pore connectivity reduces after removing smaller pores from the original PS. However, the rate of reduction is different among the three samples. For FS-A and FS-B, when the minimum pore diameter reaches to about 12 μm , the χ_v at this point turns to be a positive value such that most of the remaining pores are not connected any more. For BS this phenomenon occurs when the minimum pore diameter is larger than 16 μm . Based on this observation, we can say that the pore connectivity of BS is better than that of both FS-A and FS-B.

Samples	Euler characteristic	Number of pores	Percentage in volume (%)	
FS-B	-1894	-2569	1	99.6117
		0	4	0.0295
		1	675	0.3587
BS	-4751	-6995	1	99.4355
		-1	1	0.01851
		0	4	0.0166
		1	2245	0.5293

Table 5-5: Statistics of the Euler number and the number of pores sample FS-B and BS.

Due to imaging noise, however, directly using such quantities associated with the Euler number as topological descriptors may jeopardize their ability for describing the overall pore topology. In fact, in the original rock images, there may be a large number of tiny isolated pores and floating solid particles as the result of imaging salt-and-pepper noise, which have an impact on the computation of the EPC (see Table 5-2). For FS-B and BS, the relevant statistical results are shown in Table 5-5. In FS-B, there are in total 680 pores and 3659228 pore voxels, in which only one pore is connected to both of the inlet and outlet and its volume occupies more than 99.6117% of the PS. The largest pore in FS-B has no cavities but has 2570 tunnels, i.e. its EPC is -2569. Unfortunately, the overall EPC is -1894 by directly computing it from the original image of sample FS-B. As indicated in Table 5-5, all other pores in FS-B are very small (0.3883%) and should have no contribution for fluid flow in the PS. The connectivity of the PS is underestimated by these tiny isolated pores from -2569 to -1894, i.e. its negative impact counts more than 26.275%. For the other samples, the same observation can be found. This suggests that all quantities associated with the EPC seem to reflect the false pore

connectivity if we ignore the effect of tiny isolated pores. Thus, there is a need to introduce another robust topological descriptor to overcome this limitation.

5.3.3 Connectivity Coefficient

Given a rock image \mathcal{P} , suppose that it has m pore components denoted by $P_1, P_2 \dots P_m$ with volumes (number of pore voxels) of $N_1, N_2 \dots N_m$, respectively. For each pore component P_i , let χ_i be its Euler number, and then we define the weighted Euler number χ_w as

$$\chi_w = \frac{\sum_{i=1}^m \chi_i N_i}{\sum_{i=1}^m N_i} \quad (5.3)$$

Where $\sum N_i$ is actually the total number of pore voxels in the image \mathcal{P} . Taking into account the effect of volume of pore components on the calculation of Euler number, we further compute a so-called volumetric weighted Euler number as

$$\chi_{wv} = \chi_w / V, \quad (5.4)$$

Where V is the volume of \mathcal{P} in unit of mm^3 . For example, the volume of FS-B is 11.39 mm^3 and the volume of BS is 9.11 mm^3 . Based on the data shown in Table 5-5, for FS-B χ_w is -2559.02 , and then χ_{wv} is -224.67 . It is clear that the value of the weighted Euler number is dominated by the volume of the biggest pore component with 99.61% pore voxels of the PS in FS-B. For BS (see Table 5-5), χ_w is -6955.51 and χ_{wv} is -711.93 .

The volumetric weighted Euler number provides more accurate information about the pore connectivity by reducing the effect of image noise (tiny pores). In Table 5-5, I note that most of the small pore components have no tunnels or a very small number of tunnels (redundant connections). Notionally, the number of tunnels is important for the pore connectivity because tunnels correspond to the pore flow channels. Moreover, it seems unnatural for a smaller negative integer to represent better connectivity. Therefore it is necessary to introduce another more explicit measure to quantify the connectivity of porous media.

For a rock image \mathcal{P} of volume V , let χ be its overall Euler number and h_0 be the number of pore components and h_2 be the number of cavities. Therefore the number of tunnels, h_1 , can be computed by the following formula:

$$h_1 = h_0 + h_2 - \chi \tag{5.5}$$

As discussed before, floating solid particles (cavities) are removed to obtain the curve-skeleton, which means that $h_2 = 0$. Having a rock image without any cavities, we simply use the tunnels derived by the number h_0 of pore components minus the Euler number χ . For comparison between different samples, we need the volumetric number of tunnels, i.e.

$$\zeta_V = \frac{h_0 - \chi}{V} \tag{5.6}$$

This quantity will be called the connectivity coefficient in the following. The connectivity coefficient provides explicit information about pore connectivity. The larger the connectivity coefficient, the better is the connectivity of the PS.

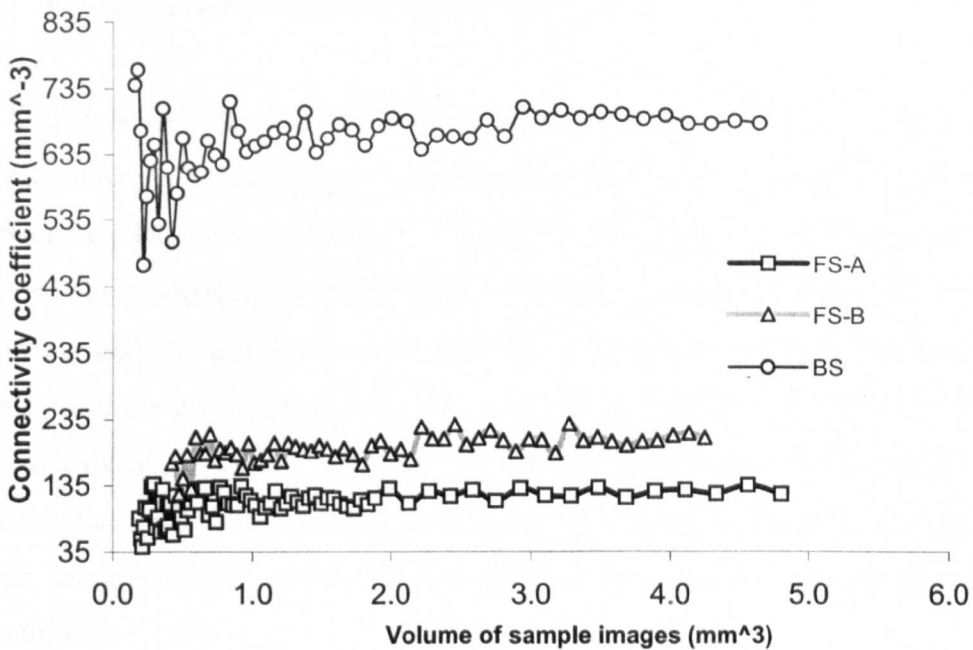


Figure 5-18: The stable trend of connectivity coefficients of FS-A, FS-B and BS as the volume of sub-images increase from about 0.1 mm³ to 5.0 mm³.

To explore the representative elementary volume with regard to the connectivity coefficient (ζ_v), we need to ensure that ζ_v tends toward a stable value when the sample volume is large enough. In my numerical experiment, a series of sub-images are taken from the original images of FS-A, FS-B and BS of dimensions of 400^3 , 300^3 and 400^3 , respectively. And then for each of these sub-images the corresponding connectivity coefficient and the number of pore components are calculated. The three curves of connectivity coefficient against their volume of the underlying sub-image are plotted in Figure 5-18.

According to Figure 5-18, we can say that ζ_{vs} of FS-A, FS-B and BS tend to be stable (110.65 mm^{-3} , 203.74 mm^{-3} , and 687.15 mm^{-3}) when the volume of the sub-images reaches to about 2.1 mm^3 , 3.25 mm^3 and 3.0 mm^3 , respectively. Based on the definition of ζ_v these three values can be explained in the following way. There are about 111, 204 and 687 tunnels for a single pore component in the sense of average quantity per unit volume. Obviously the connectivity of FS-A is the worst, but is close to that of FS-B. The BS has much higher ζ_v , which means that the PS of BS provides many more pore channels (tunnels) for fluid to flow through than that of FS-A or FS-B.

5.4 Extracted Network for Network Flow Model

In this section, to predict flow properties of porous media, I describe how to extract network structures from rock images to cope with the specific requirements of network models. This includes (1) partitioning the PS into a network of nodes and bonds, (2) assigning quantified geometric and topological properties to network elements, and (3) using the extracted network as input of network flow model to predict some macroscopic properties. In this section, the Valvatne and Blunt (2004[170]) network model is selected to predict absolute and relative permeabilities based on the extracted network data. Additionally, I also try to do some preliminary investigations on cross sectional radii, connectivity coefficient and absolute permeability in ideal conditions.

5.4.1 IC Network Model

The Valvatne and Blunt's (2004[170]) network model, i.e. the Imperial College network model (IC network for short), was designed to predict single and multiphase flow properties. It is not limited to regular network lattices. It was successfully applied to predict relative permeability and oil recovery for water wet, oil wet, and mixed wet data sets. In their network, the individual network elements are uniform ducts with circular, triangular or square cross sectional shapes. Microporosity and water saturated clays will typically not be drained during core analysis. This effect is included in the network representation by assigning a constant volume to each pore or throat that always remains water saturated. All the throats along the inlet face of the network model are assumed to be connected to a reservoir of oil. The pressure in the oil phase P_o is then increased while the water phase pressure P_w is kept constant throughout the network, resulting in increased capillary pressure P_c . The network elements are filled in order of increasing capillary entry pressure (assuming they have an oil-filled neighbour). This process continues until some predefined saturation is reached or all elements have been filled by oil. Once a polygonal element has been filled by oil, water still remains in the corners. This will ensure that water, as the wetting phase, will remain connected throughout primary oil flooding, since escape to the outlet is always possible through wetting layers.

In order to use this model, it is necessary to edit the networks of nodes and bonds that have been extracted from the 3D rock images. To map the GT networks onto the network structure of the IC network model, some factors must be considered very carefully. In Figure 4-42 a realistic pore structure and an ideal network are illustrated. The realistic structure may be extracted directly from the original image, but the ideal structure is required by the IC network model. The ideal structure illustrates two major characteristics required by the IC network structure: (1) each bond (pore-throat) must connect with two and only two distinct nodes (inlet/outlet is referred as two nodes of infinite size); (2) for any two connected nodes there is only one bond between them. Therefore some redundant branches (bonds, links) need to be removed and some virtual nodes need to be created.

For the three samples, their network structures are demonstrated in Figure 5-19, in which all the nodes are represented by regions with volumes but only the "backbones" of the bonds are plotted for a better visualization. Note that most of the nodes have more than 2 adjacent bonds while others have just one or two adjacent bonds. The nodes with

one or two adjacent bonds are virtual nodes which are created in order to meet the specific requirement of the IC network model. Also a few of the existing bonds in the original pore network, which have a single node as their two terminals, have been removed (i.e. combining the bond and node into a new single node). As for other geometrical and topological parameters of the network, much more detail can be found in the algorithm introduced in Chapter 4. In the following, I will present the calculation of some transport properties using the network flow model for the three rock sample images.

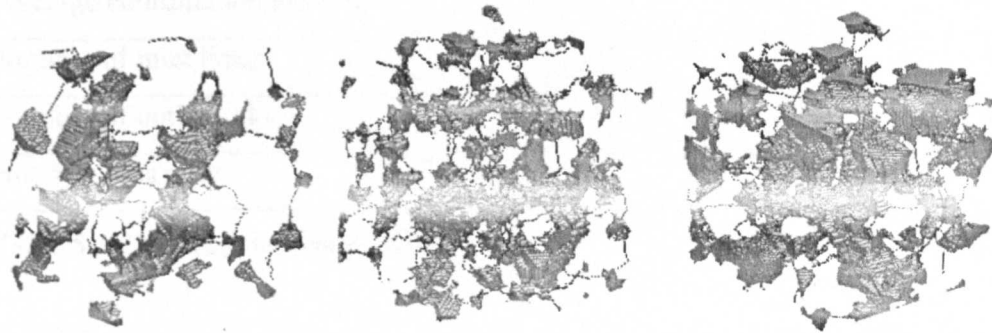


Figure 5-19: Network structures of (100^3) sub-samples of FS-A (left), FS-B (middle) and BS (right). The regions with volumes represent nodes and the grey lines bonds without volume. In IC network model, both of them are assigned with volume.

5.4.2 Analysis of Network Structure

In order to use the IC network flow model, I need to create three network structures for analysis and prediction for the three samples. The main network parameters are listed in Table 5-6.

(i) Node size and bond size distributions

For the three samples, Figure 5-20 shows all size distributions of nodes and bonds in the extracted networks. The node size is described by the cross sectional diameter at the centre of each node, and the bond size is represented by the average cross sectional diameter along the corresponding skeleton voxels. From Table 5-6, it can be seen that

the average size of bonds is always smaller than the according average node size. And both node and node sizes of BS are much less than that of FS-A and FS-B

Samples	FS-A	FS-B	BS
Number of nodes	2890	3811	8147
Average node size (μm)	41.93	39.62	34.67
Number of bonds	4054	5546	11961
Average bond size (μm)	28.70	28.94	25.37
Average coordination number	3.0397	3.1109	3.0556
Number of inlet links	79	80	121
Number of outlet links	74	87	136
Bonds/radius ratio	8.32	7.45	6.96

Table 5-6: Network structure properties.

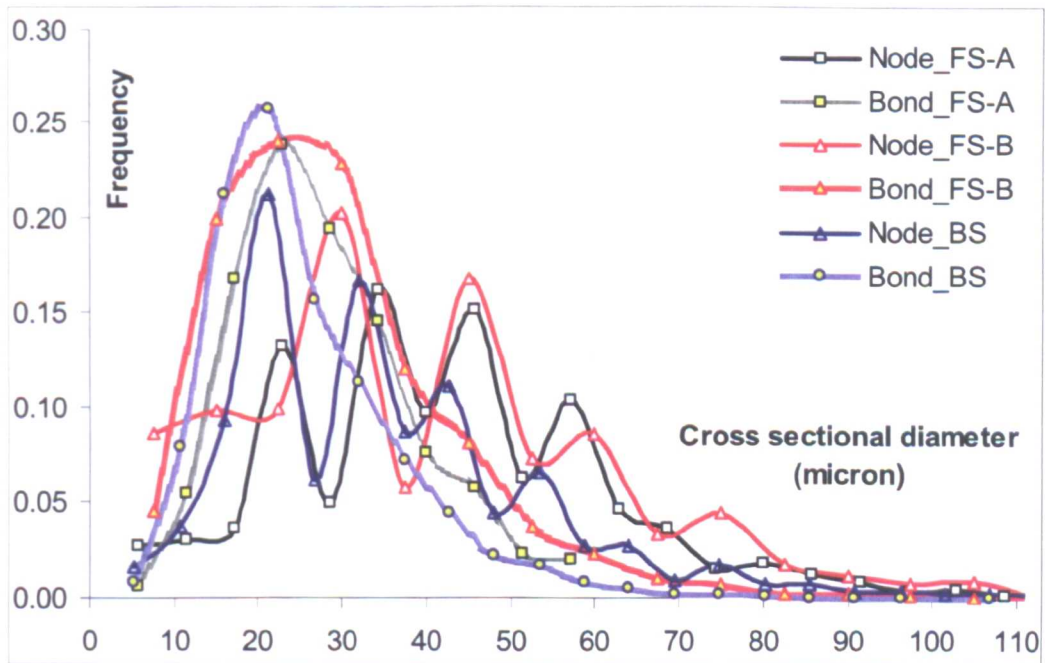


Figure 5-20: Node and bond size distributions of FS-A, FS-B and BS.

(ii) Node size versus bond connection

Figure 5-21 shows the correlation between node size and the corresponding average coordination number. The cross sectional diameter at the centre of a node is used to describe the size of the node, and the coordination number of a node is the

number of bonds that are connected with the node. From Figure 5-21, three correlations between node cross sectional diameter and the number of adjacent bonds have linear trends with similar slopes (about 0.04) but different intercepts (i.e. 2.92, 1.33 and 1.15). The slopes reveal an inherent attribute of these sandstone materials while the intercepts distinguish their connectivities from each other. This coincides with their connectivity coefficients (ζ_V : 687.15 mm^{-3} , 203.74 mm^{-3} and 110.65 mm^{-3}) shown in Table 5-1.

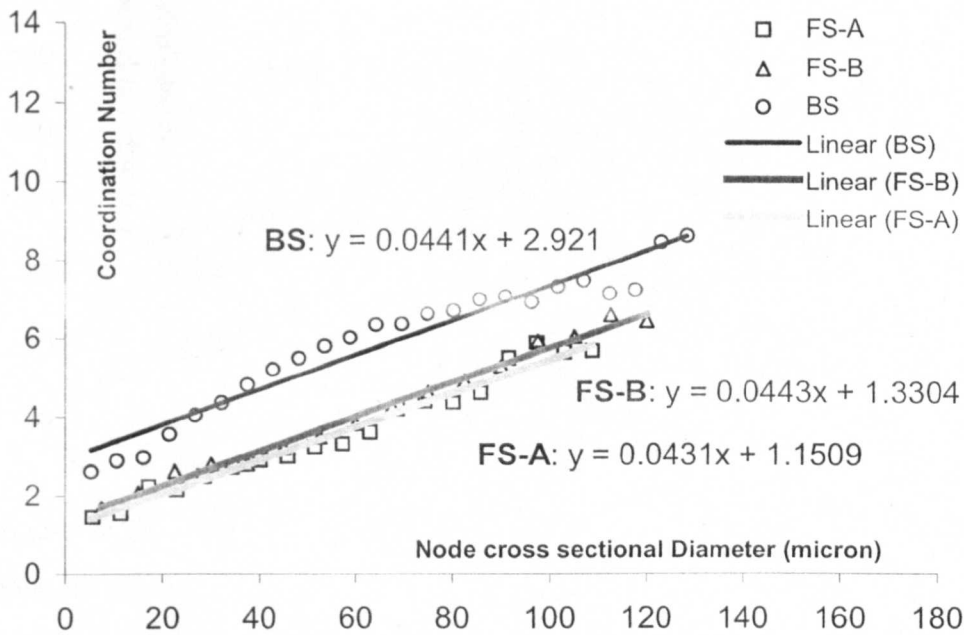


Figure 5-21: The correlation between node size (cross sectional diameter at the centre of each node) and the corresponding coordination number.

(iii) Node size versus bond length

Considering node size and adjacent bond length, for the three samples, we can obtain the following data illustrated in Figure 5-22. The X-coordinate represents the cross sectional diameter of nodes, and the Y-coordinate the average length of their adjacent bonds. Figure 5-22 indicates that adjacent node length tends to linearly increase at a similar rate (slopes: 0.34, 0.37 and 0.28) for the three samples as the corresponding node's size increases. The intercepts (64, 51 and 34) of the three linear regression lines are significantly different and can be used to recognize the three different sandstones. The average length of all bonds adjacent to a node in BS is shorter than that in FS-A and FS-B, which coincide to the average node size shown in Table 5-6. The longer the length of adjacent bonds of a node is, the larger the coordination

number of the node is. From Figure 5-22, the connectivity of BS seems to be the best among them, because for the same size pores the length of the connected bonds of BS is much shorter than that of FS-A and FS-B.

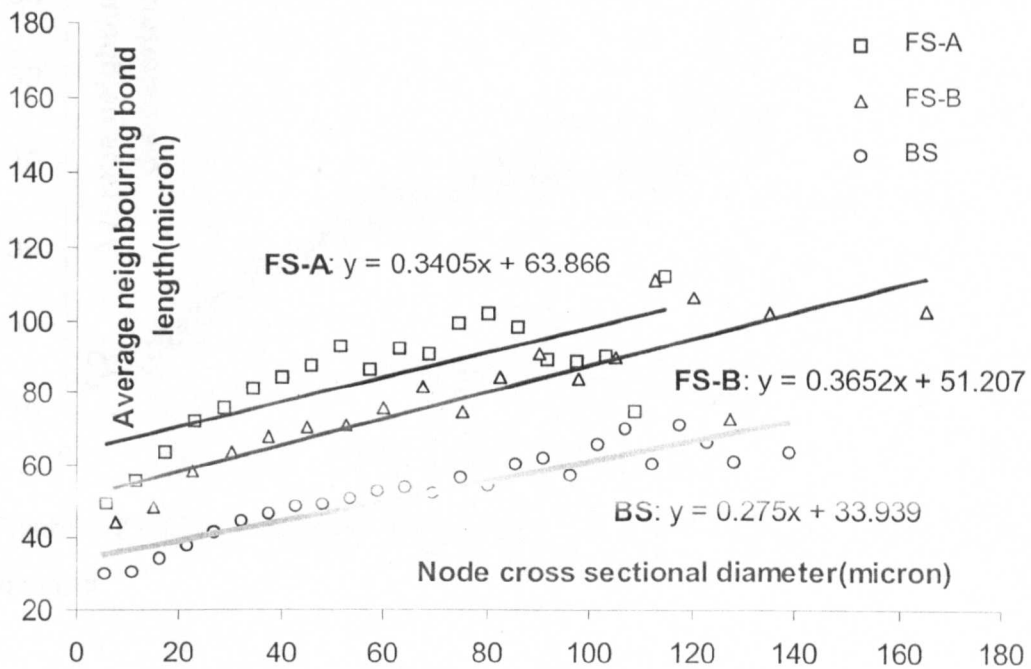


Figure 5-22: The correlation between node size and the corresponding length of adjacent bonds.

(iv) Node size versus neighbouring node size

In terms of the correlation between node size and the neighbouring node size, for the three samples, the measured data is shown in Figure 5-23. It is clear that there is no significant difference between the three samples in this correlation. Note that a smaller node seems to be more likely connected with smaller nodes. For instance, for a node of diameter of 60 μm the average diameter of nodes connected by some bonds with that node is about 32 μm .

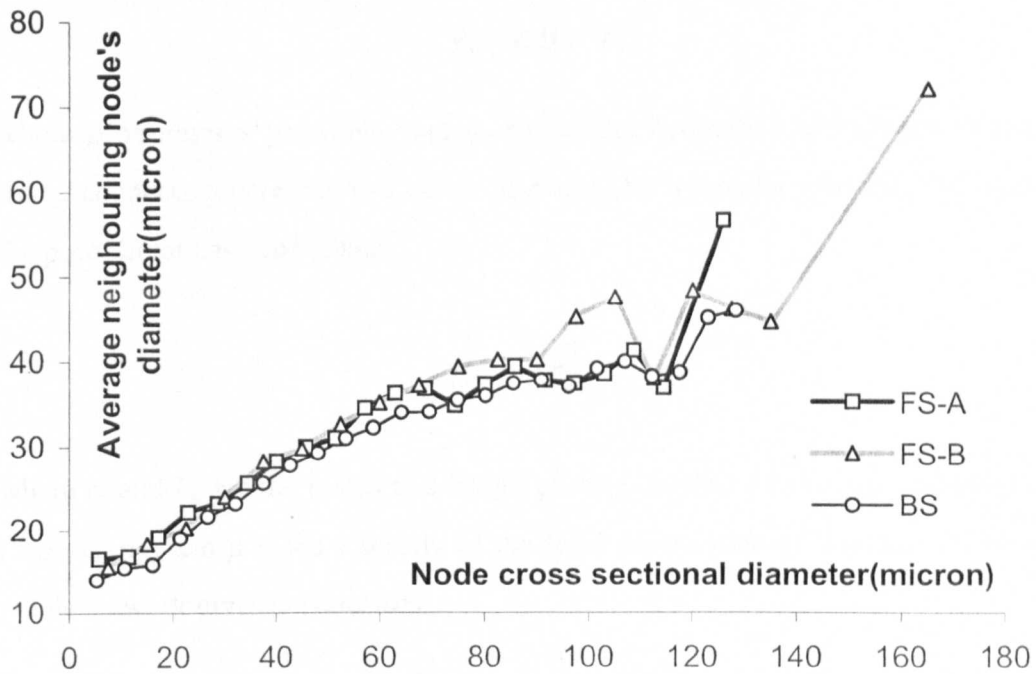


Figure 5-23: The correlation between node and their adjacent node cross sectional diameter.

5.4.3 Calculation of Conductance

According to Blunt and King (1992[23]), single-phase fluid flow through a porous medium system can be modelled as a simplified network of pore-bodies and pore-throats with some basic assumptions: (1) local capillary pressure in the pore-bodies can be negligible; (2) the radius and volume of a pore throat is assumed to be small relative to volumes of pore-bodies; (3) flow within pore-throats is assumed to be laminar and given by Poiseuille's law; (4) the fluid is assumed to be incompressible. With these assumptions, the fluid phase must obey volume conservation within each pore-body, such that

$$V_i \frac{\partial S_i}{\partial t} + \sum_{j \in N_i} q_{ij} = 0 \quad i = 1, 2 \dots N \quad (5.7)$$

Where N is the number of pore-bodies, V_i represents the volume of pore-body i , S_i represents local saturation of the fluid, q_{ij} is the volumetric flux from pore-body i to its neighbour j , and N_i is a list of all neighbour pore-bodies for pore-body i . The volumetric flux is related to pressures at the pore-bodies by Poiseuille's law,

$$q_{ij} = g_{ij}(p_i - p_j), \quad (5.8)$$

where p_i represents pressures, and g_{ij} represents hydraulic conductance in the pore-throat connecting pore-bodies i and j . Therefore, for a circular tube the fluid occupying the pore-throat has conductance

$$g_{ij} = \frac{\pi r_{ij}^4}{8\mu L_{ij}}, \quad (5.9)$$

where r_{ij} and L_{ij} are the radius and length of the pore-throat linking pore-bodies i and j , respectively, and μ is the viscosity of the fluid. Summation of Equation (5.7) over the whole network gives the equation

$$\sum_{j \in N_i} q_{ij} = 0. \quad (5.10)$$

When using networks extracted from rock images one would like to relate the network pore shapes to those observed in the rock images. Since the real pore space is highly irregular it is not feasible to reproduce it exactly, but one can describe the observed shapes through the use of a dimensionless shape factor G , as suggested by Mason and Morrow (1991[103]). In the IC network models (Valvatne and Blunt, 2004[170]), once the shape factor has been measured, an equivalent irregular triangle can be defined that characterises the irregular pore/throat, where G varies from 0 for a slit shaped pore to $\sqrt{3}/36$ for an equilateral triangle. In other cases where pore shapes are quite regular one can use other equivalent pore shapes like squares ($G = 0.0625$) or circles ($G = 0.0796$). It is assumed that the wetting fluid residing in corners is connected to that in adjacent pores and throats, with the result that the wetting fluid generally spans the entire network.

The conductance g_{ij} of a circular cross section in Equation (5.9) is associated with the shape factor G by Poiseuille's law: $g_{ij} = kA^2G$ ($k = 0.5$). Similar analytical expressions for equilateral triangles and squares can also be developed (Patzek and Silin, 2001[125]) with k being $3/5$ and 0.5623 respectively. Using square or triangular shaped pore throats allows for the explicit modelling of wetting layers (water or oil depending on the wetting state), whereby non-wetting phase occupies the centre of the

element and wetting phase remains in the corners. The pore space in real rock is highly irregular with water remaining in grooves and crevices after primary oil flooding, due to capillary forces. This behaviour has been observed in micromodel experiments where flow channels typically have a square cross-section (Lenormand et al., 1983[82]). The wetting layers may not be more than a few microns in thickness, with little effect on the overall saturation or flow but their contribution to the wetting phase connectivity is of vital importance, as they ensure low residual wetting phase saturation by preventing trapping.

Substitution of Equation (5.8) for the fluid fluxes q_{ij} provides a set of algebraic equations with the pore-body pressures as unknowns. These can be solved using standard matrix solution methods. When the network is fully saturated with a single phase, the overall absolute permeability K of the network is found from Darcy's law,

$$K = \frac{\mu qL}{A \Delta p} \quad (5.11)$$

The total single-phase flow rate q through the network is determined by imposing a pressure drop Δp across its length L , with A being the cross sectional area of the model. According to Poiseuille's law, i.e. $g = kA^2G$, g strongly depends on the cross sectional area and shape factor G . Thus, K is strongly influenced by the cross sectional radii (diameter) of pores and their shapes.

The three rock samples' permeabilities are predicted using the IC network model based on the extracted network structures (see Table 5-6) from the three rock images. The predicted absolute permeabilities are listed in the last row in Table 5-1.

Taking into account the heterogeneity of sandstones, we need to investigate the absolute permeabilities (K) at the dimensions (400^3 , 300^3 , and 400^3). Hence, from the three original images, a series of sub-images of different volumes from 0.5 mm^3 to 9 mm^3 are randomly cut out, and based on each of such sub-images, a network structure is then extracted to feed into the IC network model from which some transport properties are predicted. In Figure 5-24, three predicted absolute permeabilities (K) are plotted to show the stability of these values against the volumes of sub-images. The blue curve corresponds to the result coming from sample BS, which is the maximum permeability among the three stable values and the black from sample FS-A is the minimum. It is quite clear that the variation of the calculated K intends to be smaller and smaller when

the volume of sub-images under consideration becomes larger for every rock sample. This indicates that the minimal dimension of sub-images of FS-B should be larger than 240^3 voxels in the sense of the error to stable value (1188 mD) less than 5%. Similarly, the stabilities of absolute permeabilities computed for FS-A and BS can also be observed by constructing IC network for each sub-image of these two samples, the result is shown in Table 5-6. Figure 5-24 shows the trends of absolute permeability K when the volume of sub-images increases, they are 450, 1188 and 1871 mD for FS-A, FS-B and BS, respectively, and the corresponding minimal volumes are 5.58 mm^3 (310^3 voxels), 6.59 mm^3 (250^3 voxels), and 3.5 mm^3 (285^3 voxels), respectively.

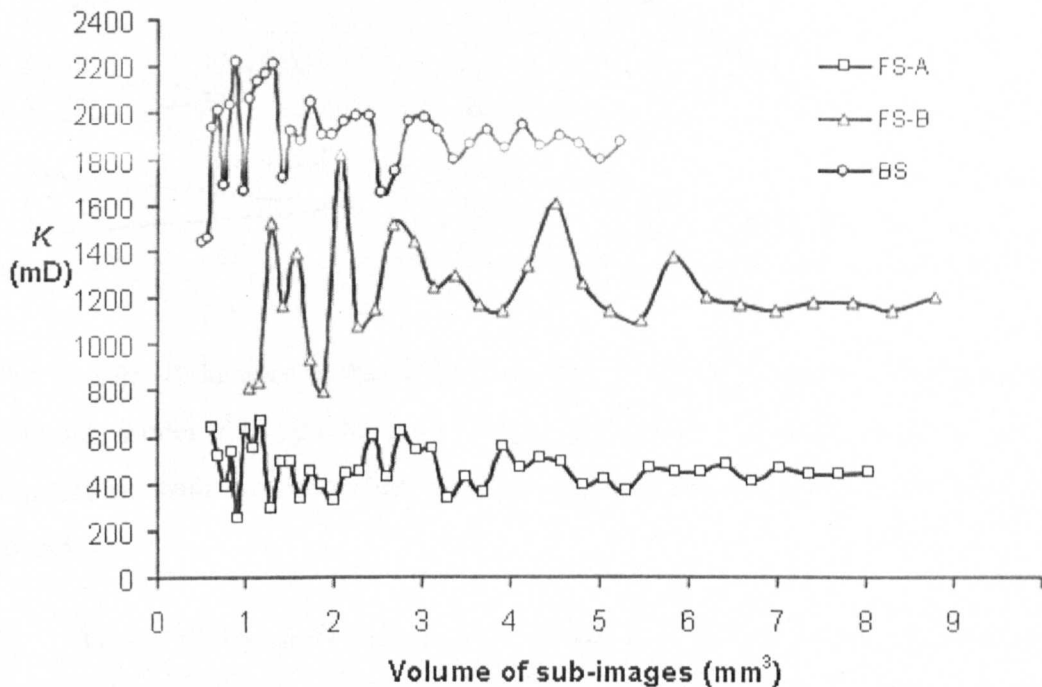


Figure 5-24: The stable trend of absolute permeabilities when the volume of sub-image becomes larger and larger.

In the IC network model, the shape factor is an important network parameter. Given a shape factor G , if G ranges from 0 to 0.048 (equilateral triangle), then the corresponding bond is idealized as a duct of triangular cross section; otherwise the cross section is regarded as being either square-shaped or circle-shaped. For sandstone samples, however, the latter (e.g. $G > 0.048$) is rather rare and can be ignored in the computation of absolute permeability using the IC network model.

To have an insight in the relevance of the shape factor for the permeability, I designed a simple numerical experiment in three steps: (1) constructing network

structures from a sub-image of FS-A; (2) keeping all network parameters the same (including inscribed radii), except for the shape factor, which is decreased the factor by 5%; (3) feeding modified network structure into the IC network model to predict absolute permeability and then go back to (2). The result is shown in Figure 5-25(a). Note that the absolute permeability (K) decreases as the shape factor increases. From Figure 5-25 (b) follows that the cross sectional area increases as the shape factor decreases because the inscribed radii remains unchanged. Therefore, we can see that the shape factor strongly affects the permeability.

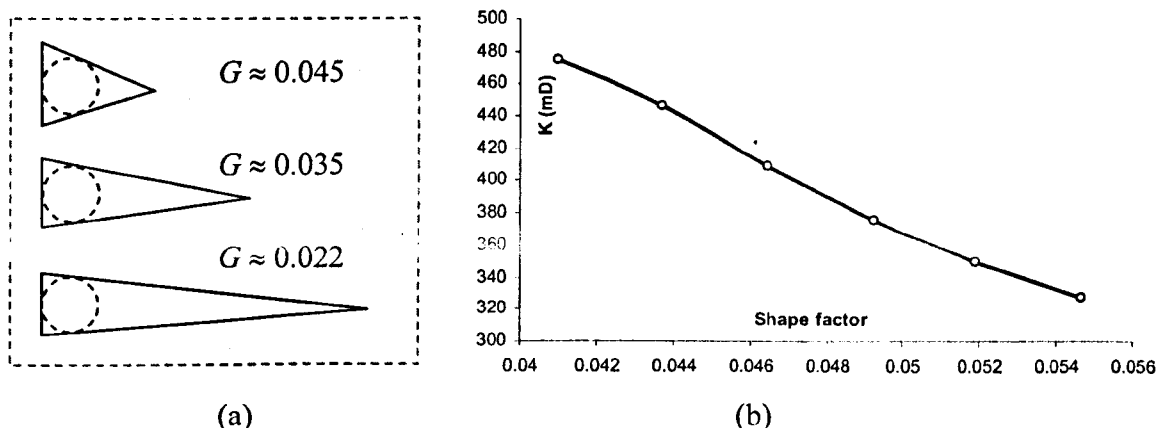


Figure 5-25: Relevance of the shape factor for the absolute permeability using the IC network model for sample FS-A. This result uses the same network for each experiment, with the difference being the assigned shape factor for all pores in that model.

When multi-phase fluid flow is considered in a network model, if flow rates are computed using the same pressure drop as for single-phase flow, then the relative-permeability is simply obtained by

$$K_r = Q_{tm}/Q_{ts}. \quad (5.12)$$

Where Q_{tm} is the flow rate of a phase and Q_{ts} is the total flow rate for all phases. For FS-A, FS-B and BS, the relative permeabilities (Figure 5-26) for primary drainage and waterflooding are computed by finding the pressure field in the oil and water phases assuming that each phase occupies a separate non-communicating sub-network and that the oil and water are both Newtonian fluids. During primary drainage the network is assumed to be strongly water-wet with a receding contact angle of 0 degrees. There are no other parameters to adjust, with all geometric network properties (connection

numbers, radii, shape factors etc) defined in the sandstone reconstruction process. Though the network is still water-wet during waterflooding the advancing contact angles will be larger, due to roughness of the surface and minor intrinsic wettability alteration.

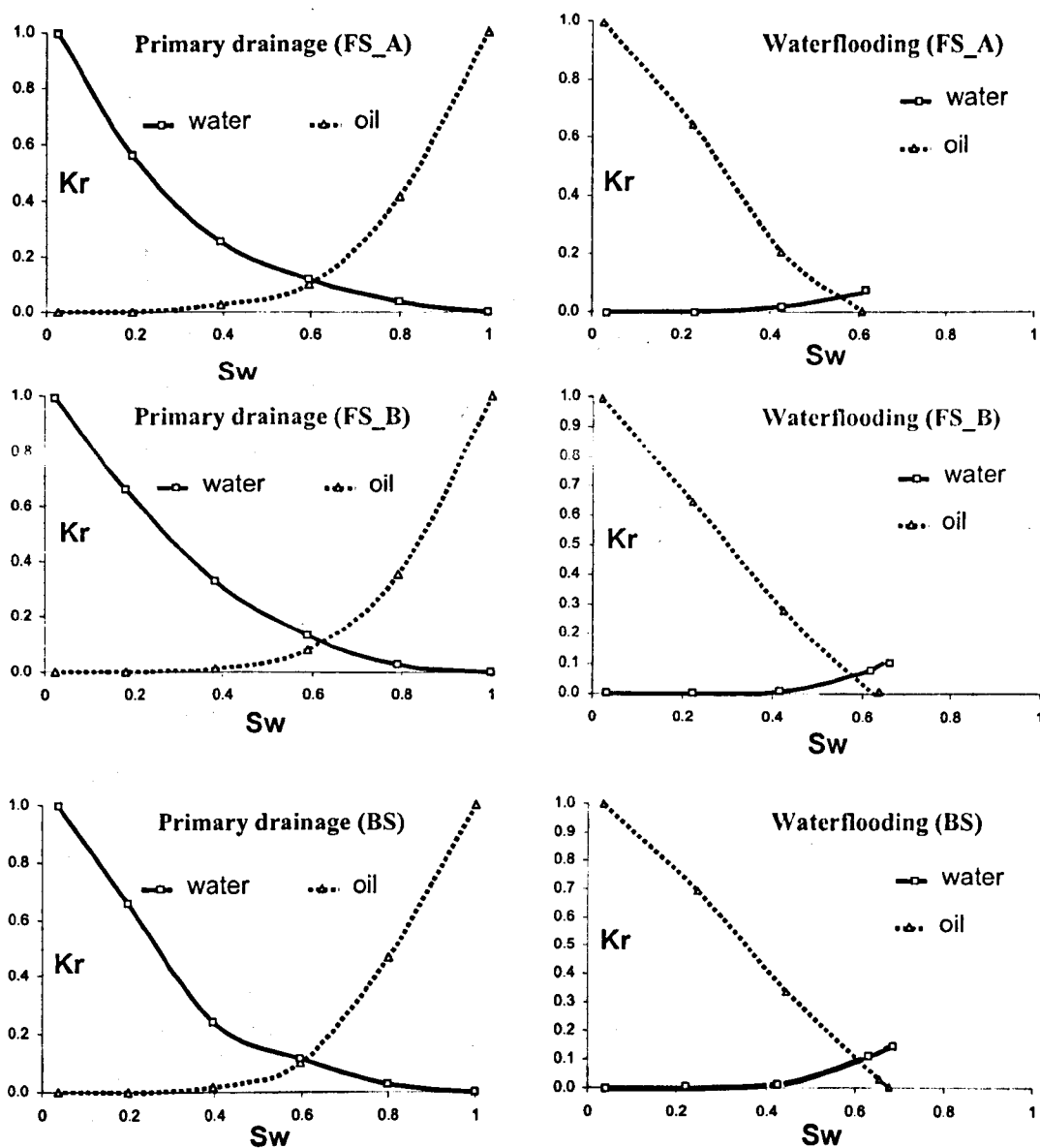


Figure 5-26: Predicted oil/water relative permeabilities by IC network model for FS-A (top row), FS-B (middle row) and BS (bottom row). The primary drainage relative permeabilities illustrated in the left, secondary imbibition (waterflooding) relative permeabilities in the right.

5.4.4 The correlation between Absolute Permeability and Inscribed Diameter

As discussed before, there are many microscopic morphological (geometric and topological) features which affect the macroscopic properties. Among them, the pore size and the pore connectivity are two major factors. The former is quantified by cross sectional radii and the latter by the connectivity coefficient. In order to study the correlation between absolute permeability and the pore size, I test an array of rock images, which are created by keeping their connectivities but imposing different pore sizes onto the three rock images.

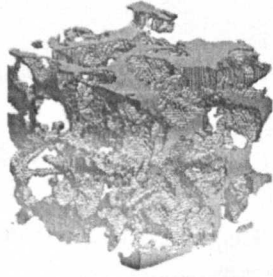
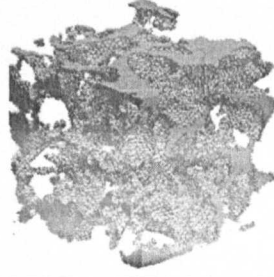
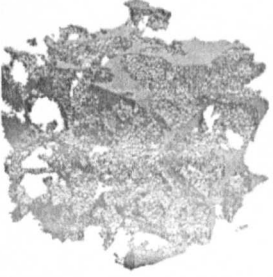
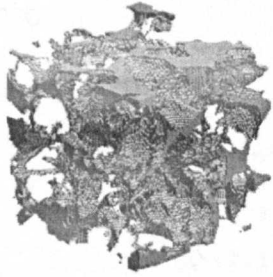
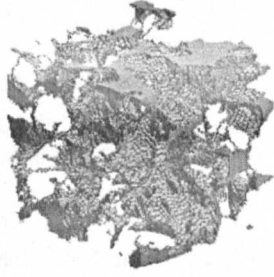
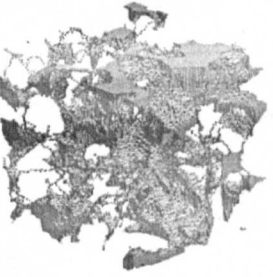
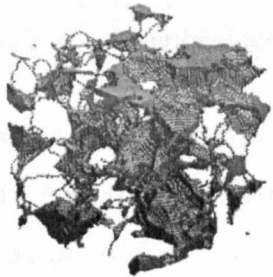
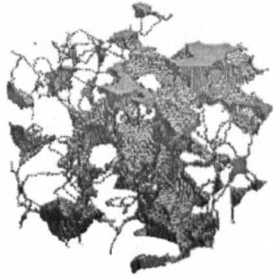
			
K	1805	917	743
I_d	36.32	29.09	28.12
			
K	542	127	90
I_d	27.18	23.53	21.56
			
K	80	27	
I_d	19.17	15.83	

Table 5-7: Creation of a series of images of different average pore size but the same topology ($\zeta_V = 687\text{mm}^{-3}$) from the original image of BS.

In the construction of network structures, the general procedure can be described as follows: For a rock image \mathcal{P} , removing all current simple border pore voxels (see

Chapter 3) leads to the creation of a new image. The newly created image contains the shrunk PS, in other words, the average pore size is smaller than that of the original image \mathcal{P} . Based on this new image, the corresponding network structure can be constructed and then the absolute permeability can be predicted using the IC network model. This procedure continues by removing more and more border simple points until the skeleton remains. At each step, an amount of pore voxels have been removed and a new image is created based on its previous image. Therefore, an array of the permeabilities against the pore size can be computed for a given PS topology.

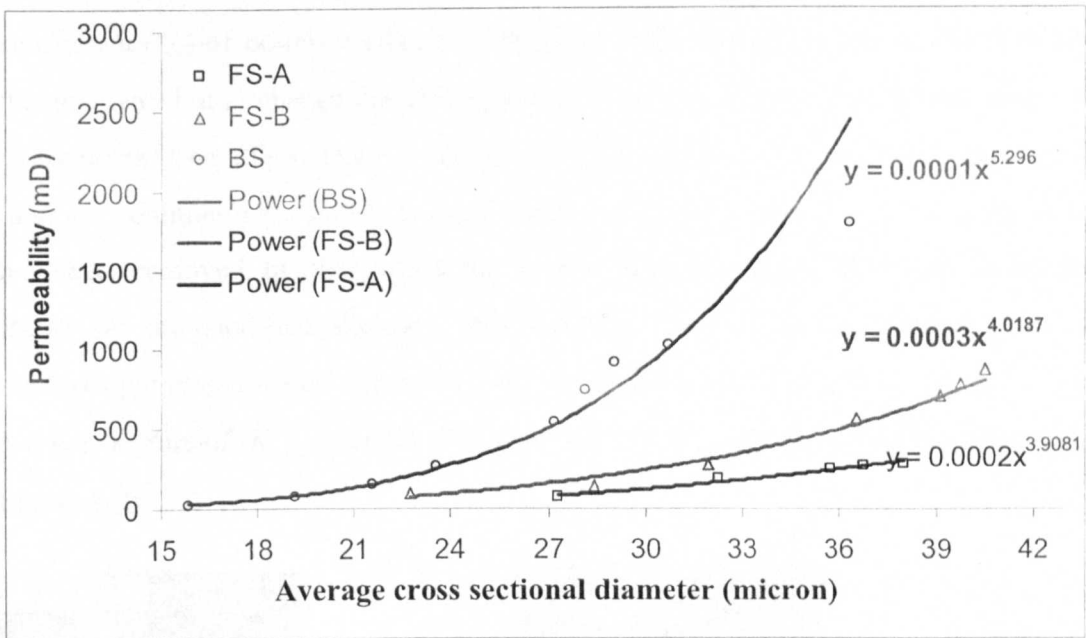


Figure 5-27: Measured data and their trend-lines of absolute permeability (K) against the average cross sectional inscribed diameter (I_d) for FS-A, FS-B and BS.

For BS, I create a series of images from its original image illustrated in Table 5-7. There are 8 newly created images of different average pore size I_d , which decreases from $36.32 \mu\text{m}$ to $15.83 \mu\text{m}$. The corresponding absolute permeability (K) predicted by the IC network model decreases from 1805 mD to 27 mD . The process of removing pore voxels can be imagined as peeling off the outmost boundary of the PS layer by layer. In a similar way, for FS-A and FS-B the (K, I_d) curves are plotted in Figure 5-27. If one imagines that the PS of a rock had been infilled by cement in such a way as to mimic the layer-by-layer shrinking described here, we start to see a potential method for predicting the influence of diagenesis on flow properties in the absence of a complete suite of samples.

In Figure 5-27, three sets of data correspond to the permeabilities plotted against the average pore size for the three rock samples. The absolute permeability increases exponentially with the increase of the average cross sectional diameter in each case, but the rate of increase differs. The three trend-lines are illustrated in Figure 5-27 along the scattered data.

5.4.5 The correlation between Absolute Permeability and Connectivity Coefficient

To explore the correlation between absolute permeability (K) and the connectivity coefficient (ζ_V) of porous media, the key point in the reconstruction of PSs is to keep the geometry but to change the topology of the original image. Given a rock image and its skeleton (see 2D schematic picture in Figure 5-28), I change the topology by randomly eliminating a set of skeleton voxels. Note that in this process no pore voxels have been removed. In other words, the shape and the size of the PS remain unchanged. Based on the modified skeleton, new network structure is re-constructed and its macroscopic properties are predicted using the IC network model. As an example, Table 5-8 lists 8 pairs of (K , ζ_V) for BS. The ultimate result for the three samples is plotted in Figure 5-29.

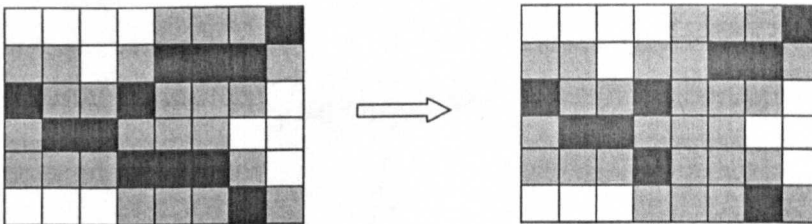


Figure 5-28: 2D schematic pictures demonstrate the idea for changing the topology by removing skeleton voxels.

In Figure 5-29, the range of connectivity coefficient ζ_V of FS-A goes from 25 mm^{-3} to 127 mm^{-3} while the one of FS-B goes from 41 mm^{-3} to 226 mm^{-3} , the maximum range of ζ_V is achieved by BS from 214 mm^{-3} to 716 mm^{-3} . Note that these ranges are used to compute the absolute permeabilities shown, but that the result may be incomplete since ζ_V should range from 0 to its maximum value, theoretically. Even with this caveat, we can roughly say that the correlation between K and ζ_V looks to be power

function. The parameters of the regression lines (trendlines in Figure 5-29) seem to be correlated to the average pore size due to the removal of skeleton voxels.

Sub-image of BS (100×100×100)	$K(mD)$	$\zeta_V(mm^{-3})$
	1805	715.86
	1497	655.69
	1247	600.23
	1023	548.86
	837	500.67
	537	412.86
	345	334.09
	183	268.29
	81	214.37

Table 5-8: The predicted absolute permeabilities for images of different connectivity but the same average pore size for BS.

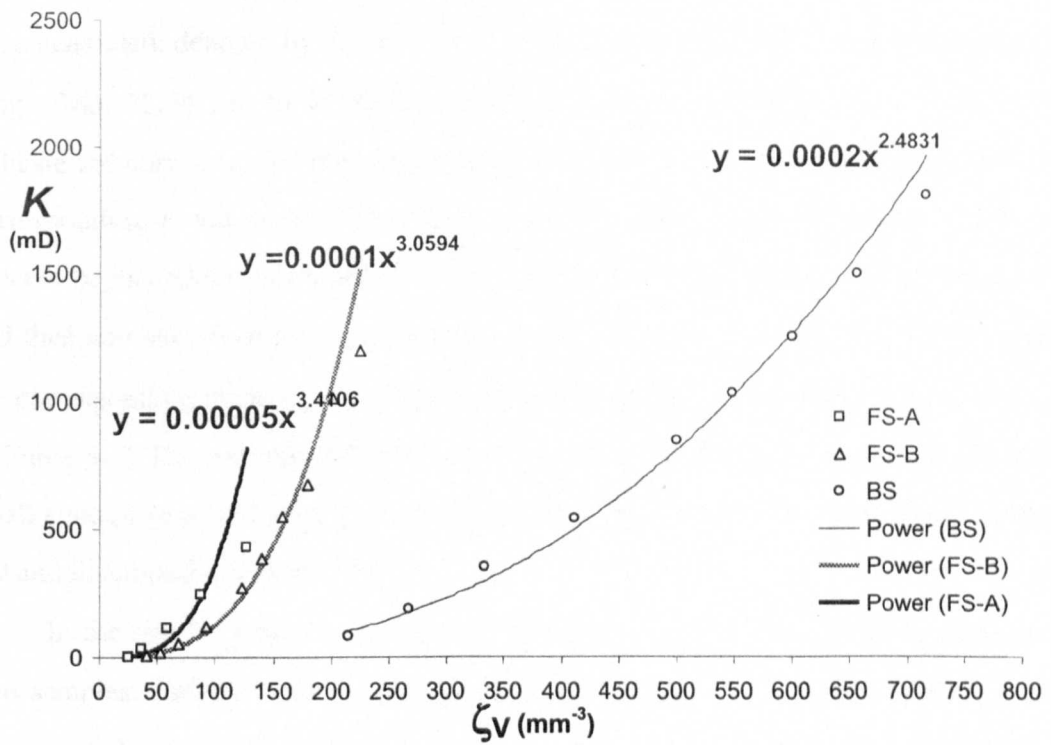


Figure 5-29: The correlation curves between absolute permeability K and connectivity coefficients ζ_V with trend-lines of slopes of 4.18, 6.38, and 3.39 for FS-A, FS-B and BS, respectively.

5.4.6 Comprehensive Correlation

Combing the two kinds of numerical experiments discussed above, I can investigate the comprehensive correlation among absolute permeability (K), average pore size (cross sectional diameter I_d), and connectivity coefficient (ζ_v). For an input rock image \mathcal{P} , the numerical experiment is carried out in the following way.

From the skeleton of \mathcal{P} (e.g. BS), I randomly remove a number of skeleton voxels, such as m skeleton voxels, and obtain a new image \mathcal{P}_1^1 with a modified skeleton. For this newly generated image \mathcal{P}_1^1 , its average cross sectional diameter I_d and the connectivity coefficient ζ_v are determined. Then the absolute permeability K is predicted using the IC network model based on the extracted network structure from \mathcal{P}_1^1 . Further, removing the outmost layer of border simple voxels from \mathcal{P}_1^1 , an image \mathcal{P}_2^1 of smaller pore size is generated and the corresponding triple of (I_d , ζ_v , K) is determined or computed based on \mathcal{P}_2^1 . The removing of border simple voxels continues until only the skeleton remains. In this way, seven rock images with the same topology but different average pore size have been generated, denoted by \mathcal{P}_1^1 , \mathcal{P}_2^1 , \mathcal{P}_3^1 ... \mathcal{P}_7^1 . Their average cross sectional diameter I_d range from 22.74 μm to 40.48 μm , which is listed as the first row in Table 5-9 to indicate the pore size, and the connectivity coefficient is the same value 226 mm^{-3} . The corresponding K values are listed in the row with entry mark 226 in Table 5-9. The process begins again by randomly remove $2m$ skeleton voxels from the skeleton of \mathcal{P} , and then another seven reconstructed rock image \mathcal{P}_1^2 , \mathcal{P}_2^2 , \mathcal{P}_3^2 ... \mathcal{P}_7^2 . For these images, the corresponding triple (I_d , ζ_v , K) is computed and listed in the row of entry mark 217 in Table 5-9. The process described above repeats until the connectivity coefficient is small enough (e.g. 145 mm^{-3}). From sample BS, the computed result is listed in Table 5-9 and illustrated in Figure 5-30.

In the similar way, I calculate the three quantities (i.e. K , ζ_v and I_d) from other two samples, and the ultimate result is plotted in Figure 5-31. The X-coordinate axis represents the connectivity coefficient ζ_v . For an array of reconstructed rock images, which have the same average pore size (I_d) but their connectivity coefficients (ζ_v) decrease, the predicted absolute permeabilities (K) are represented by the Y-coordinate. Each curve in Figure 5-31 corresponds to an array of reconstructed images of a single

average pore size. For example, the curve of mark BS (33.70) indicates that the absolute permeability K increases as the connectivity coefficient ζ_v increases based on the extracted images by removing skeleton voxels continuously. Due to the different connectivity of the three samples, the ζ_v locates within three distinct regions on the X-coordinate axis in Figure 5-31. The ζ_{vs} of FS-A range from 0 to 120 mm^{-3} , FS-B from 145 to 220 mm^{-3} and BS from 270 to 700 mm^{-3} , respectively.

$\zeta_v \setminus I_d$	22.74	28.43	31.96	36.53	39.12	39.75	40.48
145	72	101	200	340	370	425	533
166	87	125	243	401	472	550	664
187	103	147	291	538	666	688	844
195	109	154	308	613	716	735	889
202	117	160	322	640	770	856	934
209	124	168	345	678	837	885	1014
217	129	178	359	715	906	957	1110
226	137	188	378	764	970	1071	1189

Table 5-9: Triples of absolute permeability (K), connectivity coefficient (ζ_v) and cross sectional diameter (I_d).

Based on this observation, it is clear that the absolute permeability is strongly related to both the pore size and to the connectivity. In my data, the trend between K and I_d seems to be exponential, also the trend between K and ζ_v look to be exponential with different power coefficients. According to Figure 5-30 and Figure 5-31, more suggestions can be made in the following.

For Fontainebleau sandstone, the connectivity (ζ_v) is more important than the pore size (I_d), whereas I_d is critical for Berea sandstone. In Figure 5-31, the slopes of most curves of both FS-A and FS-B are larger than that of BS, which means that a slight enhancement of the connectivity of Fontainebleau sandstone would result in much better permeability than would a similar change to Berea sandstone. For BS, a small change of the pore size leads a big change of the conductivity. From Table 5-1, BS has smallest cross sectional diameter (36.3 μm) but largest porosity (19.65%), which is why it has highest connectivity.

The functional dependence of K on ζ_v and I_d is significantly different between the two Fontainebleau sandstones and the Berea sandstone, but there seems to be a set of relationships that appear to transcend the differences between the individual rocks. It seems that a set of curves could be fitted to these results that would predict permeability as a function of ζ_v and some normalisation of I_d . At this time, I have not attempted to

identify how to normalise the pore size, but this seems to be a useful avenue for further work.

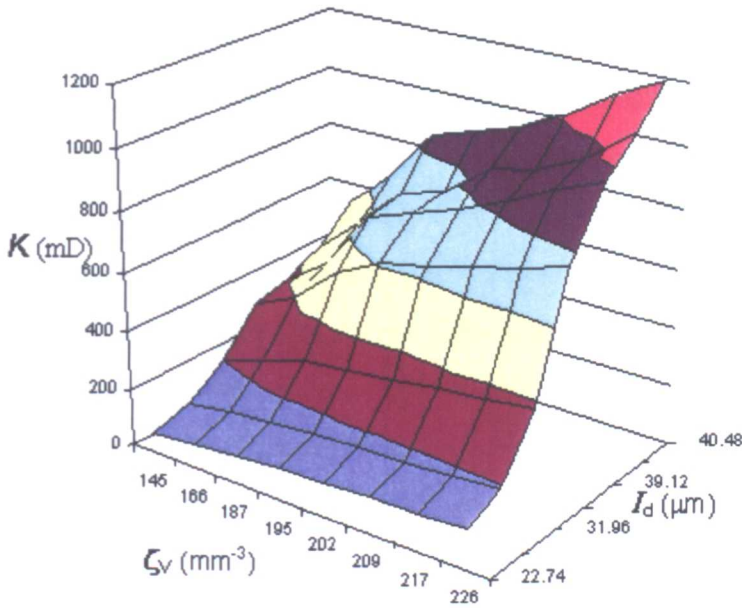


Figure 5-30: The correlation among absolute permeability (K), connectivity coefficient (ζ_V) and average cross sectional diameter (I_d) for sample FS-B.

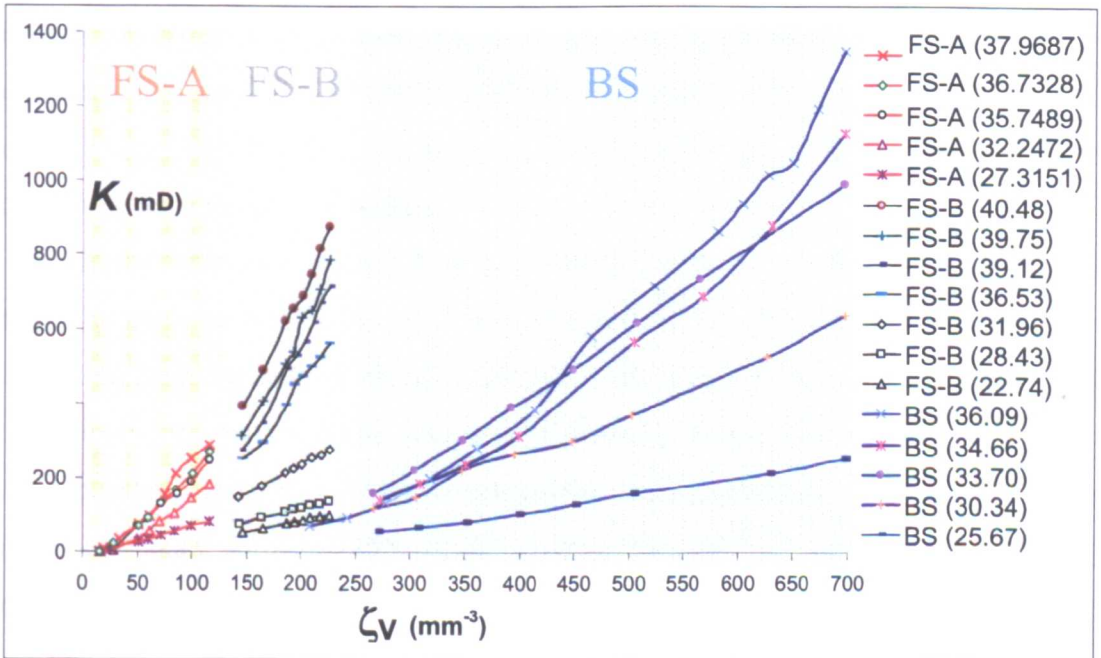


Figure 5-31: Each curve corresponds to an array of reconstructed rock images with the same average pore size after removing amount of skeleton voxels. It shows the change of absolute permeability K against the connectivity coefficient ζ_V without changing the pore size.

5.5 Conclusion

In this chapter I have studied two Fontainebleau sandstone samples (FS-A and FS-B) and one Berea sandstone sample (BS) with respect to their microstructure and macroscopic flow behaviour. Using the C++ codes for image processing and pore structure analysis, many pore geometric and topological properties have been extracted from the three rock images. After combination with the pore partitioning technique, network structures for the IC network flow model have been constructed. Subsequently, single-/multi-phase flow properties have been predicted using this network model. Using all these techniques, a series of numerical experiments on the three rocks have been performed and many interesting correlations between network element properties or among permeability, pore size and pore connectivity have been studied.

From Figure 5-2 and Figure 5-18, the stable porosities and connectivities can be obtained when the volumes of the sub-images of the three rock image are larger than certain threshold volumes (e.g. $\sim 4 \text{ mm}^3$ for FS-A, $\sim 7 \text{ mm}^3$ for FS-B and $\sim 8 \text{ mm}^3$ for BS). Naturally, the absolute permeabilities also become stable when the volumes of sub-images are large enough (see Figure 5-24). All three rocks have representative elementary volumes (11.98 mm^3 , 11.39 and 9.77 mm^3) with respect to porosity and connectivity, therefore the network predicted results are reliable and useful for describing macroscopic properties.

In the three rock images there are a large number of separate pore components and solid particles (see Table 5-2). Only a very small number of pore components are connected from one side of the pore systems to the other, but they occupy almost 98% of the total pore space volume, which any other pore components are tiny and isolated. Also, besides the single background component (solid matrix) for each sample, a huge number of small solid particles “float” in the pore space. The reason is the imaging noise from CT-scan or digitalizing. The existence of tiny isolated pores and floating solid particles in the pore space considerably degrades the quality of the Euler number for describing pore connectivity (see Table 5-5). This highlights the importance of image pre-processing or the introduction of a new topological descriptor, such as the connectivity coefficient (5.6).

According to Table 5-1, there are no significant differences in terms of average pore size (I_d), average shape factor (G), average coordination number (C_n) between the

three samples. Some descriptors (e.g. I_d and G) reveal intrinsic structural variations of the different rocks, but for others properties (e.g. C_n), the differences stem from the descriptors themselves. The coordination number represents the level of local pore connectivity, which is dependent on the construction of the network structure, but it cannot reveal the global connectivity (see Figure 5-16). However, the connectivity coefficients clearly quantify the global pore connectivities. From the data shown in Table 5-2, we conclude that the connectivities (ζ_v) and pore volumes (porosities) identify the differences between the three rock samples with similar pore sizes (also see Figure 5-15). From Figure 5-25 follows that as the average shape factors decrease, the cross sectional areas, hence the conductance, of the idealized equivalent triangles increases.

Using the network construction technique and the IC network flow model, I have predicted many characteristics (absolute permeabilities, see Figure 5-24; relative permeabilities, see Figure 5-26 and correlations of pore elements such as node size against number of connected bonds, see Figure 5-21) and correlations of pore elements, such as node size against number of connected bonds (Figure 5-22) as well as node size against average adjacent node size (Figure 5-23). Also, the correlation between absolute permeability, pore size and pore connectivity has been explored and preliminary analysis are given.

Chapter 6 Discussion, Conclusions and Future Research

In this chapter, I firstly present a discussion about the issues examined in this thesis, and then I summarise and conclude my study. Finally, I propose some areas for further research. In brief, this thesis presented a suite of newly improved methods for characterising porous materials, and described the development of a set of pore analysis tools (PAT). The original objectives of this thesis, as described in Chapter 1, have been achieved.

6.1 Discussion

With high quality 3D rock images available, in this research I have focused on the characterisation of the extremely irregular PSs in terms of their geometric and topological descriptions. The quantification techniques can be used either to provide realistic network structures for network flow models or to carry out some numerical simulations. The basic targets mainly include three topics: (1) description of the morphological (GT) properties of the PS; (2) algorithm efficiency and robustness; (3) construction of network structures.

My skeleton-based algorithms and techniques range from basic distance transformations, component labelling, skeletonization, and region partition to network construction. I am mainly concerned about how much detail can be derived directly from rock images while achieving certain accuracy in a very efficient way on a PC. Without efficient algorithms, the thinning operation, GED transformation and pore partitioning would be prohibitive for large 3D consolidated rock images using a desktop PC. For skeletonization, although the resultant skeleton is certainly topology-preserving if the corresponding thinning algorithm is based on the concept of a simple point, the skeletonization still needs to be improved by some so-called multi-orientation or parallel approaches. In this thesis, a new concept and its thinning algorithm were presented to greatly improve the normal distance-based thinning. With the consideration

of fluid flow in porous media, specific geometric constraints in the thinning method have also taken into account.

In the geometric description of the PS, the pore size is commonly represented by the pore equivalent spherical radius, i.e. the radius of the corresponding maximum inscribed discrete sphere. The inscribed radii cannot give much detail about the real pore size in relative to its irregularity in rock images, which means that an accurate descriptor of pore size was needed. Meanwhile, current topological descriptions of the PS cannot meet the requirement for explaining complicated fluid flow properties among homogenous pore media. Due to the inherent noise in rock images, the Euler number does not tend to be stable even though the considered image is very large (e.g., 512^3 voxels). For this reason, the Euler number itself and its derived quantities (e.g. the specific Euler number and the connectivity function) are not good enough to distinguish some porous systems that have very similar geometric features but different connectivities. In this thesis, an analytical relationship between topological numbers and the numbers of tunnels and cavities in a local neighbourhood is introduced and an accurate computation of the EPC is then developed for 3D images. In the comparison with Vogel's approximation of the EPC, the result can be summarised as follows (see Section 3.4.2).

Calculation of the EPC	Vogel's method	My method
Existing error?	Yes	No
Efficient	High	low
Leading to the determination of three numbers of component, tunnels and cavities.	No	Yes
Dependent on the choice of slices (number of serial sections and coordinate directions)?	Yes	No

In the construction of network structures for network flow models, I find that the network extracted directly from rock images is much more complicated than any simplified network. The major issues are: (1) the definition of node (pore-body); (2) the partition of the pore space; (3) the calculations of geometric and topological properties; and (4) tailoring the extracted network for a specific network model. With distinct definitions of node, the extracted network illustrates a significant difference. To

investigate single- or multi-phase flow, it is necessary to take into account the hydraulic features of fluid flow through pore channels. Therefore, the flow network consisting of nodes and bonds becomes the favoured choice because the nodes and bonds can be rigorously identified based on the determination of skeleton junctions. For the network geometric parameters, the irregular shapes of spatial objects such as nodes, bonds and cross sections need to be smoothed and approximated in digital space because of their zigzagged edges. The morphological quantities (e.g. radius, volume, length, shape factor and coordination number etc.) are calculated in the way of either arithmetic average or harmonic average. To feed a realistic network into a network flow model, some virtual network elements (nodes and bonds) may need to be added into the realistic network while some real network elements may need to be removed from the network. Over Øren and Bakke's method (2003[119]), my GT network has several significant advantages, which are listed in the following table.

Atributes	Øren and Bakke method	My GT network extraction
Central location	not clear; it may depend on the shape of structuring elements for dilating the grain space	guaranteed according to the 2D and 3D Euclidean distance
Single-Voxel Width (Curve)	surface skeleton may occur, and multi-voxels are common	guaranteed at nonjunction skeleton voxels, curve skeleton can be assured.
Topology Preservation	no	yes
Identification of Branches and Dead-end pores	not clear	yes

In order to make a comparison about the network construction from different research groups, two sets of data are collected from Imperial College of London (ICL) and Øren's group – and my network structure parameters (HWU) are also calculated using the PAT codes. All the network structure data come from the exact same sample (a Fontainebleau sandstone with porosity of 13.83% and with similar microstructure to the FS-B sample in Chapter 5, whose experimental permeability in lab is 1300 mD).

After the networks are extracted, the IC network model is used to predict the permeability. The basic network parameters and network predicted permeabilities are listed in the table below.

Network structure and permeabilities	Øren	ICL	HWU
Number of pores (nodes)	4997	3101	4480
Number of throats (bonds)	8192	6112	7185
Average Coordination number	3.19	3.85	3.16
Network perm (mD)	582	380	923

My extracted network structure is close to that of Øren but quite different from ICL. The reason is that both Øren's and my methods are skeleton-based but the ICL approach is a type of sphere-fitting. The difference between Øren's and mine is the skeletonization and the resultant skeleton, my methodology has several advantages: (1) topology-preservation; (2) no false junctions are identified as centres of pores because I use Liang's λ -adjacency; (3) the range of a node on the skeleton is determined by its cross sectional radii (squared Euclidean value); (4) reasonable volume partitioning based on the geodesic distance chamfer transformation. For this sample, my network predicted permeability is closest to the lab test result. As for the ICL method, due to its artificial operations to adjust pore and throat volume the result is not as close to the lab permeability.

6.2 Summary and Conclusions

In this thesis, I have developed a suite of image processing algorithms and pore structure analysis techniques (PAT), which has been coded in C++. According to Lindquist and Venkatarangan (1999[88]), my methods can be classified as skeleton-based and they mainly include distance transformations, component clustering, MA transformation (skeletonization), pore space partitioning, geometrical and topological quantification and network structure construction. Aiming to accurately and efficiently characterise the geometric and topological features and predict the macroscopic properties of porous media systems, I extended and improved existing approaches in different ways such as from lower to higher dimensions, from complicated to simple implementations, from slow to fast handling, and from narrow to wide range of

applications. Meanwhile, I developed algorithms to meet the specific need in the pore structure analysis if no suitable techniques can be found, such as keeping the links with inlet and outlet and branches under control of parameters. From the applications in the three sandstone samples in this thesis, the PAT techniques have been verified to be very useful in the network structure construction and the pore structure analysis.

The main conclusions and findings are as follows:

1. The relationship between Euclidean and chamfer distance in 2D or 3D has been established (see (3.12) and (3.13)), which provides a rigorous mathematical base to develop efficient algorithms for region partition. And I also gave a condition for the 3D chamfer distance metric (3.10).
2. Motivated by Shih and Wu's (2004a[154]) approach, I extended and improved their algorithm by propagating relative coordinates and distance values in neighbourhoods without their complicated decomposition. Through the two-scans (forward and backward), for any foreground voxel its nearest background voxel is obtained by comparing the SED of its neighbours. In this way, not only the algorithm efficiency has been improved, but also the algorithm (Algorithm 3.1 and Algorithm 3.2) can be used to cluster foreground voxels based on minimum distance criterion. Furthermore, the three targets, i.e. 1) to simplify the comparison of SED values in a $3 \times 3 \times 3$ neighbourhood, (2) to avoid the complex decomposition of the SED structure and (3) to make algorithm easy to implement and to understand, have been achieved in the design of the algorithms.
3. To avoid floating-point calculations, chamfer and geodesic chamfer distances are used to approximate the Euclidean and geodesic Euclidean distance, respectively. Similar to Cárdenes et al.'s (2003[31]) method, a geodesic chamfer distance transformation (Algorithm 3.3) has been proposed for the GCD with CDC of (3, 4, 5). The GCD transformation is used to assist with the geodesic Euclidean distance transformation, to partition the PS, to cluster

individual CSs, to determine primary branches on skeleton or to plan route for robot.

4. In order to compute the Euler number, to extract a skeleton from the object, and to conduct cluster analysis, I extended the classical HK algorithm into 3D with a consideration of diverse adjacencies (6-, 18-, 26- and λ -adjacencies) and a more efficient algorithm for counting the number of components. The method is based on the HK (Hoshen and Kopelman, 1976[59]) algorithm and its extensions (Hoshen, 1998[58]; Al-Futaisi and Patzek, 2003[2]).
5. The analytical relationship among the topological number (Bertrand, 1994[14]), the number of tunnels and the number of cavities in the $3 \times 3 \times 3$ neighbourhood of any voxel has been found and proved (Theorem 3.1). This is then used to efficiently compute the Euler number (3.29) because only a component counting and one-way scanning are involved in the new algorithm, and it also provides a theoretical foundation for topological thinning and counting global redundant connections in the PS.
6. A sufficiency condition (Theorem 3.2) of a simple set has been presented and proved in order to identify whether or not a pure 6-component is a simple set. This theorem can be considered as being the extension of the local characterization of a simple point (Bertrand, 1994[14]) because when a pure 6-component contains only one point, these two theorems are the same. Based on this theorem, a more efficient and robust skeletonization algorithm has been developed. The extracted skeleton can be used to quantify cross sectional radii and the coordination number, to cluster a set of individual pores, and to construct a network of nodes and bonds etc. To meet the four requirements (Section 3.5.1) and to give an efficient implementation, my thinning algorithm peels off object border voxels in the order controlled by their SED values layer by layer. The efficiency is mainly achieved by introducing a concept of pure 6-component (Definition 8) and the local characterization of a simple pure 6-component (Theorem 3.2). In addition, special strategies (e.g. symmetry and interval deletion) have been introduced

in order that: (a) far fewer voxels need to be checked in an iteration; and (b) the position of the skeleton voxels is located in the middle as much as possible even when they have same Euclidean distance values.

7. Based on Theorem 3.2, an efficient and flexible thinning algorithm has been developed to extract the GT network from rock images. The algorithm efficiency is achieved by (1) checking the simplicity of a pure 6-component rather than a single point, (2) avoiding redundant checking between two iterations and (3) introducing queues storing candidate set or points. The algorithm flexibility is obtained by: (1) introducing different parameters for retaining boundary, branch and anchor points and (2) designing specific routines for retaining 6-, 18-, 26- or λ -skeletons. The extracted GT network (skeleton) has the four properties required in pore structure analysis: topology-preservation, single voxel width, central location and integration of geometry.

8. Based on the Euclidean distance valued skeleton of porous media, a novel sphere-fitting approach is introduced to solve the drawbacks of general sphere-fitting:
 - Avoiding using discrete spheres, my approach can derive much detail about the pore size;
 - Dead-end pores may not be regarded as individual pores;
 - Natural irregular pores can be kept in the resultant partition;
 - Algorithm efficiency is significantly improved.

9. A comprehensive set of approaches is explored aiming to compute the shape factor in a more accurate and efficient way. It includes three aspects in particular:
 - The extraction of CSs from rock images;
 - The generation of 2D shapes by projecting spatial CSs into coordinate planes;
 - The computation of shape factor of 2D shapes;

- The convert of shape factor from 2D shapes to spatial CSs.
10. A method for extracting a network of nodes and bonds from 3D rock images is presented to address four issues (close enough, 26-connected, not snowballing and topology-preserving). The extracted networks are constructed to meet specific network structure requirement, and are then fed in network flow models, such as the IC (Imperial College) network flow model, to predict some macroscopic transport properties of porous media.
 11. Apart from the commonly used relationship between the pore size – sphere equivalent pore size, in the analysis of pore geometric properties, I present a new measure, called cross sectional size (radius or diameter), to characterise the pore channel size based on the SEDs at skeleton voxels. The complication of neighbour configurations of skeleton voxels with small SEDs (e.g. 1 in voxel) is explored, and much more accurate cross sectional sizes can then be measured from rock images. This new pore size measure facilitates our numerical simulation of mercury injection and improves the predicted result of network model by assigning average cross sectional radii for pore-throats (bonds).
 12. In the application for studying sandstone samples, I study the pore connectivity through measuring the coordination number distribution and computing specific (volumetric) Euler number. The limitations of the Euler number for describing the global pore connectivity are investigated, thus a robust and accurate topological descriptor, connectivity coefficient, is introduced because the effect of tiny isolated pores are weakened and the pore volume are taken into account.
 13. Based on three sandstone samples and using the IC network flow model, I have done some preliminary studies of morphological properties, single/multi-phase fluid flow properties and the correlations among absolute permeability, average pore size (cross sectional diameter) and connectivity coefficient by

reconstructing a series of images from the three original rock images. Some major results are obtained in the pore analysis:

- The morphological statistics and permeability of the three sandstone samples can be summarised in Table 5-1.
- The correlation between node cross sectional diameter and coordination number can be approximated by linear equations with almost same slope but different intercepts (Figure 5-21).
- The correlation between node and adjacent node sizes (cross sectional diameter) seems to be linear with different slope but similar intercepts (Figure 5-23).
- The correlation between absolute permeability and pore size (average cross sectional diameter) tends to be exponential with distinct powers (Figure 5-28).
- The correlation between absolute permeability and connectivity coefficient seems to be exponential with distinct powers (Figure 5-30).
- The comprehensive correlation among permeability, pore size and connectivity indicates that the permeability is more sensitive to the pore size than to the connectivity of the PS in porous media (Figure 5-31).

6.3 Future Research

As shown in this thesis, the PAT provides a series of efficient algorithms and state of the art techniques for 3D image processing and pore structure analysis. From the analysis of the three sandstone samples, the efficiency, accuracy and robustness of the approaches have been verified. However, it should be noted that the techniques are not perfect and there are still issues in some cases as discussed before. In future, more research needs to be done in order to improve the capabilities of the PAT tool.

In PAT, some techniques need to be refined. Using GCD transformation-based pore partitioning would solve the challenge that arises when two individual bonds share a large number of voxels. This method would produce systematic biases from its middle surface between two bonds, hence the exact GED transformation needs to be developed in the future in a very efficient way. For the calculation of shape factor, the optimal smoothing scheme dependent on types of material should be explored and more than 13

normal orientations and non-planar cross sections are also critical for idealizing pore throats.

In this thesis, only preliminary correlations between pore sizes, connectivity and absolute permeability have been explored. The next stage of this research will be investigating the correlations among pore geometry, topology and multiphase flow property (e.g. relative permeability), as well as the effect of wettability of porous media. Therefore, we need to design more effective algorithms to extract relevant GT elements and validate the correlation hypothesis using experimental data and introduce new techniques to extend this study. Apparently a good explanation of these correlations is very important for better understanding of pore microstructures from rock images or reconstructed models.

In Chapter 5, only three well consolidated sandstone samples are studied, and some quantitative characterisations of geometric and topological properties of the pore space and some good predictions have been reported. For unconsolidated materials, related techniques (e.g. *equal-distance pore partitioning*; *computation of shape factor and λ -adjacency-based skeleton clustering*) have already been successfully developed, and some preliminary research has also been done (but is not included here). However, there are three major problems which are totally different from consolidated samples: (1) from any pore voxel and at any orientation, it is not possible to cut off such a cross section that it has rigorous limited solid contour, which means one cannot identify any limited cross section as a narrow surface (throat); (2) the possibility of any two inscribed spheres touching or overlapping centred at two skeleton junctions is very high, thus certainly it is very difficult to cluster the pore skeleton into a network of node-skeleton backbones and bond-skeleton backbones without “snowballing”; and (3) the volume assignment for network elements is very sensitive to the scanning direction when the partitioning algorithm is applied. Aiming to solve such problems which occur in unconsolidated samples, some key techniques are in demand: (1) partitioning of planar regions or 3D domains; (2) good merging rule of node-skeleton voxels; (3) determination of flow-relevant flow paths. The extracted network structure should coincide with experimentally intuitive observations of the fluid flow porous media, and it should be independent of the scanning direction. The most important feature must be having reasonable predictions of macroscopic properties with regard to the observation in labs. For unconsolidated materials, I have not yet obtained ideal results due to two

reasons: short of relevant techniques and datasets. Therefore my future research will focus on the study of unconsolidated material and related techniques.

Bibliography

- [1] Aktouf, Z., Bertrand, G. and Perroton, L., 2002. "A three-dimensional holes closing algorithm", *Pattern Recognition Letters*, **23**, 523-531.
- [2] Al-Futaisi, A. and Patzek, T.W., 2003. "Extension of Hoshen-Kopelman algorithm to non-lattice environments", *Physica A*, **321**, 665-678.
- [3] Al-Kharusi, A.S. and Blunt, M.J., 2007. "Network extraction from sandstone and carbonate pore space images", *Journal of Petroleum Science and Engineering*, **56**, 219-231.
- [4] Al-Raoush, R.I. and Alshibli, K.A., 2006. "Distribution of local void ratio in porous media systems from 3D X-ray microtomography images", *Physica A*, **361**, 441-456.
- [5] Al-Raoush, R.I., Clinton, S. and Willson, C.S., 2005. "A pore-scale investigation of a multiphase porous media system", *Journal of Contaminant Hydrology*, **77**, 67-89.
- [6] Al-Raoush, R.I., Thompson, K. and Willson, C.S., 2003. "Comparison of Network Generation Techniques for Unconsolidated Porous Media", *Soil Science Society of America*, **67**, 1687-1700.
- [7] Al-Raoush, R.I. and Willson, C.S., 2005. "Extraction of physically realistic pore network properties from three-dimensional synchrotron X-ray microtomography images of unconsolidated porous media systems", *Journal of Hydrology*, **300**, 44-64.
- [8] Arcelli, C., Sanniti di Baja, G. and Svensson, S., 2005. "Computing and analysing convex deficiencies to characterise 3D complex objects", *Image and Vision Computing*, **23**, 203-211.
- [9] Arns, C.H., 1996. "The influence of morphology physical properties of reservoir rocks", PhD thesis, School of Petroleum Engineering, University of New South Wales, Sydney, Australia.

- [10] Arns, C.H., Knackstedt, M.A. and Mecke, K.R., 2004. "Characterisation of irregular spatial structures by parallel sets and integral geometric measures", *Colloids and Surfaces A: Physicochem. Eng. Aspects*, **241**, 351-372.
- [11] Arns, C.H., Knackstedt, M.A., Pinczewski, W.V. and Mecke, K.R., 2001. "Euler-Poincaré characteristics of classes of disordered media", *Physical Review E*, **63**(31112), 1-13.
- [12] Arns, J.Y., Arns, C.H., Sheppard, A.P., Sok, R.M., Knackstedt, M.A. and Pinczewski, W.V., 2003. "Relative permeability from tomographic images; effect of correlated heterogeneity", *Journal of Petroleum Science and Engineering*, **39**, 247-259.
- [13] Baldwin, C.A., Sederman, A.J, Mantle, M.D., Alexander, P. and Gladden, L.F., 1996. "Determination and characterization of the structure of a pore space from 3D volume images", *Journal of Colloid Interface Science*, **181**, 79-92.
- [14] Bertrand, G., 1994. "Simple points, topological numbers and geodesic neighbourhoods in cubic grids", *Pattern Recognition Letters*, **15**, 1003-1011.
- [15] Bertrand, G., 1995. "On P-simple points", in: *Comptes Rendus de l'Académie des Sciences de Paris (Computer Science/Theory of Signal), Série Math.*, **I(321)**, 1077-1084.
- [16] Bertrand, G., 1996. "A Boolean characterization of three-dimensional simple points", *Pattern Recognition Letters*, **17**, 115-124.
- [17] Bertrand G. and Aktouf, Z., 1994. "A three-dimensional thinning algorithm using subfields", *SPIE Vision Geometry III*, **2356**, 113-124.
- [18] Bertrand, G. and Malandain, G., 1994. "A new characterization of 3d simple points", *Pattern Recognition Letters*, **15**, 169-175.
- [19] Bitter, I., Kaufman, A.E. and Sato, M., 2001. "Penalized-Distance Volumetric Skeleton Algorithm", *IEEE TVCG (Transactions on Visualization and Computer Graphics)*, **7(3)**, 195-206.
- [20] Blum, H., 1967. "A transformation for extracting new descriptors of shape", in: W. Wathen-Dunn, W.(Ed.), *Models for the Perception of Speech and Visual Forms*, MIT Press, Cambridge, 362-380.
- [21] Blunt, M.J., 2001. "Flow in porous media – pore-network models and multiphase flow", *Current Opinion in Colloid and Interface Science*, **6**, 197-207.

- [22] Blunt, M.J., Jackson, M.D., Piri, M. and Valvatne, P.H., 2002. "Detailed physics, predictive capabilities and macroscopic consequences for pore-network models of multiphase flow", *Advances in Water Resources*, **25**, 1069-1089.
- [23] Blunt, M.J. and King, M.J., 1992. "Simulation and theory of two-phase flow in porous media", *Physical Review A*, **46**(12), 7680-7698.
- [24] Borgefors, G., 1984. "Distance transformations in arbitrary dimensions", *Computer Vision Graphics Image Processing*, **27**, 1984, 321-345.
- [25] Borgefors, G., 1996. "On digital distance transforms in three dimensions", *Computer Vision and Image Understanding*, **64**(3), 368-376
- [26] Borgefors, G., Nyström, I. and Sanniti di Baja, G., 1999. "Computing skeletons in three dimensions", *Pattern Recognition*, **32**(7), 1225-1236.
- [27] Bouix, S. and Siddiqi, K., 2000. "Divergence-Based Medial Surfaces", in *ECCV (European Conference on Computer Vision)*, **1842**, 603-618, Dublin, Ireland, Springer.
- [28] Boyce, R.W., Eber, D.C., Youngs, T.A., Paddock, C.L., Mosekilde, L., Stevens, L. and Gundersen, H.J., 1995. "Unbiased estimation of vertebral trabecular connectivity in calcium-restricted ovariectomized minipigs", *Bone*, **16**(6), 637-642.
- [29] Bykov, A.I., Zerkalov, L.G. and Rodríguez Pineda, M.A., 1999. "Index of a point of 3-D digital binary image and algorithm for computing its Euler characteristic", *Pattern Recognition*, **32**, 845-850.
- [30] Calabi, L. and Harnett, W.E., 1968, "Shape recognition, prairies fires, convex deficiencies and skeletons", *AMM (American Mathematical Monthly)*, **75**, 335-342.
- [31] Cárdenes, R., Warfield, S.K., Macias, E. and Ruiz-Alzola, J., 2003. "Occlusion points propagation geodesic distance transformation", in: *Image Processing, ICIP2003, 2003 International Conference*, **1**, 1-36.
- [32] Chang, D. and Ioannidis, M.A., 2002. "Magnetization Evolution in Network Models of Porous Rock under Conditions of Drainage and Imbibition", *Journal of Colloid and Interface Science*, **253**, 159-200.
- [33] Churcher, P.L., French, P.R., Shaw, J.C., and Schramm, L.L., 1991. "Rock properties of Berea sandstone, Baker dolomite, and Indiane limestone", *paper SPE*

21044. *Proceedings of the 1991 SPE International Symposium on Oilfield Chemistry*, Anaheim, Feb. 20-22.

[34] Coeurjolly, D., Miguet, S. and Tougne, L., 2004. "2D and 3D visibility in discrete geometry: an application to discrete geodesic paths", *Pattern Recognition Letters*, **25**, 561-570.

[35] Couprie, M. and Zour, R., 2005, "Discrete Bisector Function and Euclidean Skeleton", *DGCI2005 (Discrete Geometry for Computer Imagery)*, 216-227.

[36] Cuisenaire, O., 1999. "Distance Transformations: Fast Algorithms and Applications to Medical Image Processing", PhD thesis, Universite Catholique de Louvain.

[37] DeHoff, R.T., Aigeltinger, E.H. and Graig, K.R., 1972. "Experimental determination of the topological properties of three-dimensional microstructures", *Journal of Microscopy*, **95**, 69-91.

[38] Delerue, J.F. and Perrier, E., 2002. "DXSoil, a library for 3D image analysis in soil science", *Computer & Geosciences*, **28**, 1041-1050.

[39] Delerue, J.F., Perrier, E., Timmerman, A. and Rieu, M., 1999a. "New computer tools to quantify 3D porous structures in relation with hydraulic properties", In: Feyen, J. & Wiyo, K. (eds), *Modelling of Transport Processes in Soil*, Wageningen Press, Wageningen, The Netherlands, 153-163.

[40] Delerue, J.F., Perrier, E., Yu, Z.Y. and Velde, B., 1999b. "New algorithms in 3D image analysis and their application to the measurement of a spatialized pore size distribution in soils", *Physics and Chemistry of the Earth (A)*, **24(7)**, 639-644.

[41] Dias, M.M. and Wilkinson, D., 1986. "Percolation with trapping", *Journal of Physics A: Mathematical and General*, **19**, 3131-3146.

[42] Dijkstra, E.W., 1959. "A note on two problems in connection with graphs", *Numerical Mathematics*, **1**, 269-271.

[43] Dillard, L.A. and Blunt, M.J., 2000. "Development of a pore network simulation model to study nonaqueous phase liquid dissolution", *Water Resource Research*, **36**, 449-454.

- [44] Dullien, F.A.L., 1992. "Porous Media: Fluid Transport and Pore Structure", 2nd, Academic Press, San Diego.
- [45] Fatt, I., 1956a. "The network model of porous media I. Capillary characteristics", *Pet. Trans. AIME.*, 207, 144-159.
- [46] Fatt, I., 1956b. "The network model of porous media II. Dynamic properties of a single size tube network, *Pet. Trans. AIME.*, 207, 160-163.
- [47] Fatt, I., 1956c. "The network model of porous media III. Dynamic properties of networks with tube radius distribution", *Pet. Trans. AIME.*, 207, 164-181.
- [48] Forchhammer, S., 1989. "Euclidean distances from chamfer distances for limited distances", in *Proceedings of Sixth Scandinavian Conference on Image Analysis, Oulu, Finland*, 393-400
- [49] Gagvani, N. and Silver, D., 2001. "Animating volumetric models", *Academic Press Professional*, 63(6), 443-458.
- [50] Gau, C.J., Yung, T. and Kong, T.Y., 2003. "Minimal non-simple sets in 4D binary images", *Graphical Models*, 65(1-3), 112-130.
- [51] Golland, P. and Grimson, E.L., 2000. "Fixed Topology Skeletons", *In Proc. IEEE CVPR (Computer Vision and Pattern Recognition)*, 1, 10-17.
- [52] Gong, W. and Bertrand, G., 1990. "A simple parallel 3D thinning algorithm", in: *International Conference on Pattern Recognition*, Atlantic City, NJ, USA, 188-190.
- [53] Gonzalez, R.C. and Woods, R.E., 1993. "Digital Image Processing", Addison-Wesley, Reading, Massachusetts.
- [54] Gundersen, H.J., Boyce, R.W., Nyengaard, J.R. and Odgaard, A., 1993. "The ConnEuler: unbiased estimation of connectivity using physical dissectors under projection", *Bone*, 14, 217-222.
- [55] Hadwiger, H. 1957. *Vorlesung über Inhalt, Oberfläche und Isoperimetrie*. Springer-Verlag, Berlin.
- [56] He, T.S., Hong, L.C., Chen, D.Q. and Liang, Z.R., 2001. "Reliable Path for Virtual Endoscopy: Ensuring Complete Examination of Human Organs", *IEEE Transactions on Visualization and Comp. Graphics*, 7(4), 333-342.

- [57] Hirata, T., 1996. "A unified linear-time algorithm for computing distance maps", *Information Processing Letters*, **58**, 129-133.
- [58] Hoshen, J., 1998. "On the application of the enhanced Hoshen-Kopelman algorithm for image analysis", *Pattern Recognition Letters*, **19**, 575-584.
- [59] Hoshen, J. and Kopelman, R., 1976. "Percolation and cluster distribution. I. Cluster multiple labeling technique and critical concentration algorithm", *Physical Review B*, **4**, 3438-3444.
- [60] Ioannidis, M.A. and Chatzis, I., 1993. "Network modelling of pore structure and transport properties of porous media", *Chemistry Engineering Sciences*, **48**, 951-972.
- [61] Ioannidis, M.A. and Chatzis, I., 2000. "On the geometry and topology of 3D stochastic porous media", *Journal of Colloid and Interface Science*, **229**, 322-334.
- [62] Ioannidis, M.A., Chatzis, I. and Kwiecien, M.J., 1999. "Computer enhanced core analysis for petrophysical properties", *Journal of Canadian Petroleum Technology*, **38**, 18-25.
- [63] Ioannidis, M.A., Kwiecien, M.J. and Chatzis, I., 1996. "Statistical analysis of the porous microstructure as a method for estimating reservoir permeability", *Journal of Petroleum Science and Engineering*, **16**, 251-261.
- [64] Jackson, M.D., Valvatne, P.H. and Blunt, M.J., 2003. "Prediction of wettability variation and its impact on flow using pore- to reservoir-scale simulations", *Journal of Petroleum Science and Engineering*, **39**, 231-246.
- [65] Jerauld, G.R. and Salter, S.J., 1990. "The effect of pore-structure on hysteresis in relative permeability and capillary pressure: Porelevel modeling", *Transport in Porous Media*, **5**, 103-151.
- [66] Jones, A.C., Sheppard, A.P., Sok, R.M., Arns, C.H., Limaye, A., Averdunk, H., Brandwood, A. Sakellariou, A. Senden, T.J., Milthorpe, B.K. and Knackstedt, M.A. , 2004. "Three-dimensional analysis of cortical bone structure using X-ray micro-computed tomography", *Physica A* **339**, 125-130.
- [67] Jones, K.W., Feng, H., Stanmire Tomov, S., Winters, W.J., Prodanović, M. and Mahajian, D., 2007. "Characterization of methane hydrate host sediments using

synchrotron-computed microtomography (CMT)", *Journal of Petroleum Science and Engineering*, **56**, 136-145.

[68] Jones, M.W., Bærentzen, J.A. and Sramek, M., 2006. "3D Distance Fields: A Survey of Techniques and Applications", *IEEE Transactions on Visualization and Computer Graphics*, **12**(4), 581-599.

[69] Jonker, P.P., 2000. "Morphological operations on 3D and 4D images: From shape primitive deletion to skeletonization", in *DGCI (Discrete Geometry for Computer Imagery)*, **953**, 371-391.

[70] Kantzas, A. and Chatzis, I., 1988. "Network simulation of relative permeability curves using a bond correlated-site percolation model of pore structure", *Chemical Engineering Communications*, **69**, 191-214.

[71] Knackstedt, M.A., Arns, C.H., Limaye, A., Sakellariou, A., Senden, T.J., Sheppard, A.P., Sok, P.M., Pinczewski, W.V. and Bunn, G.F., 2004. "Digital Core Laboratory: Properties of reservoir core derived from 3D images", *2004 Asia Pacific Conference on Intergrated Modelling for Asset Management*, Kuala Lumpur, March 2004, SPE 87009:1-14.

[72] Knackstedt, M.A., Arns, C.H., Senden, T.J. and Gross, K., 2006. "Structure and properties of clinical coralline implants measured via 3D imaging and analysis", *Biomaterials*, **27**, 2776-2786.

[73] Knackstedt, M.A., Sheppard, A.P. and Sahimi, M., 2001. "Pore network modelling of two-phase flow in porous rock- the effect of correlated heterogeneity", *Advances in Water Resources*, **24**, 257-277.

[74] Kong, T.Y., 1993. "On the problem of determining whether a parallel reduction operator for n-dimensional binary image always preserves topology", in *Proceedings, 1993 SPIE Conference on Vision Geometry, Boston, MA*, 69-77.

[75] Kong, T.Y., Roscoe, A.W. and Rosenfeld, A., 1992. "Concepts of digital topology", *Topology and its Application*, **46**, 219-262.

[76] Kong, T.Y. and Rosenfeld, A., 1989. "Digital Topology: Introduction and survey", *Computer Graphics and Image Process*, **48**, 358-393.

- [77] Koplik, J., 1982. "Creeping flow in two-dimensional networks", *Journal of Fluid Mechanics*, **19**, 219-247.
- [78] Kwiecien, M.J., 1994. "Comprehensive Characterization of Porous Media via Computer Reconstruction and Stochastic Modelling", PhD thesis, University of Waterloo.
- [79] Kwiecien, M.J., Macdonald, I.F. and Dullien, F.A.L., 1990. "Three-Dimensional Reconstruction of Porous Media from Serial Section Data", *Journal of Microscopy*, **159**, 343-359.
- [80] Larson, R., Scriven, L.E. and Davis, H.T., 1977. "Percolation theory of residual phases in porous media", *Nature*, **268**, No. 5619, 409.
- [81] Lee, T.C and Kashyap, R.L., 1994. "Building skeleton models via 3-D medial surface/axis thinning algorithms", *CVGIP: Graphical Models and Image Processing*, **56(6)**, 462-478.
- [82] Lenormand, R., Zarconend, C., Sarr, A., 1983. "Mechanisms of the displacement of one fluid by another in a network of capillar ducts", *Journal of Fluid Mechanics*, **135**, 337-353.
- [83] Levitz, P.E., 2007, "Toolbox for 3D imaging and modelling of porous media", *Osteoporosis International*, **18**, 837-843.
- [84] Liang, Z., Ioannidis, M.A. and Chatzis, I., 2000a. "Geometric and Topological Analysis of Three-Dimensional Porous Media: Pore Space Partitioning Based on Morphological Skeletonization", *Journal of Colloid and Interface Science*, **221**, 13-24.
- [85] Liang, Z., Ioannidis, M.A. and Chatzis, I., 2000b. "Permeability and electrical conductivity of porous media from 3D stochastic replicas of the microstructure", *Chemical Engineering Science*, **55**, 5247-5262.
- [86] Lindquist, W.B., 2006. "The geometry of primary drainage", *Journal of Colloid and Interface Science*, **296**, 655-668.
- [87] Lindquist, W.B. and Lee, S., 1996. "Medial Axis Analysis of void structure in 3D tomographic images of porous media", *Journal of Geophysical Research*, **101(B4)**, 8297-8310.

- [88] Lindquist, W.B. and Venkatarangan, A., 1999. "Investigating 3D geometry of porous media from high resolution images", *Physics and Chemistry of the Earth (A)*, **25**(7), 593-599.
- [89] Lindquist, W.B., Venkatarangan, A., Dunsmuir, J. and Wong, T.F., 2000. "Pore and throat size distributions measured from synchrotron X-ray tomographic images of fontainbleau sandstones", *Journal of Geophysical Research*, **105B**, 21508-21528.
- [90] Lobregt, S., W. Verbeek, W. and Groen, F.C.A., 1980. "Three-dimensional skeletonization: Principle and algorithm", *IEEE Transaction on PATTERN Analysis and Machine Intelligence*, **2**, 75-77.
- [91] Lohou, C. and Bertrand, G., 2004. "A 3D 12-subiteration thinning algorithm based on P-simple points", *Discrete Applied Mathematics*, **139**, 171-195.
- [92] Lohou, C. and Bertrand, G., 2005. "A 3D 6-subiteration curve thinning algorithm based on P-simple points", *Discrete Applied Mathematics* (www.sciencedirect.com, www.elsevier.com/locate/dam), **151**(1-3), 198-228.
- [93] Lopez, X., Valvatne, P.H. and Blunt, M.J., 2003. "Predictive network modeling of single-phase non-Newtonian flow in porous media", *Journal of Colloid and Interface Science*, **264**, 256-265.
- [94] Lymberopoulos, D.P. and Payatakes, A.C., 1992. "Derivation of topological, geometrical, and correlational properties of porous media from pore-chart analysis of serial section data", *Journal of Colloid and Interface Science*, **150**, 61-80.
- [95] Ma, C.M., 1994. "On topology preservation in 3D thinning", *CVGIP: Image Understanding*, **59**(3), 328-339.
- [96] Ma, C.M. and Sonka, M., 1996. "A Fully Parallel 3D Thinning Algorithm and Its Applications", *Computer Vision and Image Understanding*, **64**(3), 420-433.
- [97] Macdonald, I.F., Kaufmann, P.M. and Dullien, F.A.L., 1986. "Quantitative Image Analysis of Finite Porous Media. I. Development of Genus and Pore Map Software", *Journal of Microscopy*, **144**, 277-296.
- [98] Malandain, G. and Bertrand, G., 1992. "Fast characterization of 3D simple points", in *IEEE International Conference on Pattern Recognition*, 232-235.

- [99] Malandain, G. and Vidal, S.F., 1998. "Euclidean Skeletons", *Image and Vision Computing*, 16, 317-327.
- [100] Manzanera, A., Bernard, T., Preteux, F. and Longuet, B., 1999. "A unified mathematical framework for a compact and fully parallel n-D skeletonization procedure", *Vision Geometry VIII*, 3811, 57-68.
- [101] Marchand-Maillet, S. and Sharaiha, Y.M., 1999. "Euclidean Ordering via Chamfer Distance Calculations", *Computer Vision and Image Understanding*, 73(3), 404-413.
- [102] Mason, G. and Mellor, D.W., 1995. "Simulation of Drainage and Imbibition in a Random Packing of Equal Spheres", *Journal of Colloid and Interface Science*, 176, 214-225.
- [103] Mason, G. and Morrow, N.R., 1991. "Capillary behaviour of a perfectly wetting liquid in irregular triangular tubes", *Journal of Colloid and Interface Sciences*, 141(1), 262-274.
- [104] Matheron, G., 1975. "Random sets and integral geometry", John Wiley & Sons Inc, New York.
- [105] Maurer, J., Calvin, R., Qi, R. and Raghavan, V., 2003. "A Linear Time Algorithm for Computing Exact Euclidean Distance Transforms of Binary Images in Arbitrary Dimensions", *IEEE Transaction On Pattern Analysis and Machine Intelligence*, 25(2), 265-270.
- [106] Meijster, A., Roerdink, J.B.T.M. and Hesselink, W.H., 2000. "A general algorithm for computing distance transforms in linear time," in: *Mathematical Morphology and its Applications to Image and Signal processing*; J. Goutsias, L. Vincent, and D. S. Bloomberg (Eds.), Kluwer, 331-340.
- [107] Meyer, F., 1977. "Contrast feature extraction", in *Quantitative Analysis of Microstructures in Material Science, Biology, and Medicine*, J.L. Charmont, ed. Stuttgart, Germany:Riedner-Verlag.
- [108] Michielsen, K. and Raedt, H.De., 2001. "Integral-Geometry Morphological Image Analysis", *Physics Reports*, 347, 461-538.

- [109] Michielsen, K., Raedt, H.De. and Hosson, J. Th.M.De., 2002. "Aspects of Mathematical Morphology", *Advances in Imaging and Electron Physics*, **125**, 199-195.
- [110] Morgenthaler, D.G., 1981. "Three-dimensional simple points: Serial erosion, parallel thinning and skeletonization", *Technical Report TR-1005, Computer Vision Laboratory, Computer Science Center, University of Maryland, Colledge Park, MD*.
- [111] Nagel, W., Ohser, J. and Pischang, K., 2000. "An integral-geometric approach for the Euler-Poincaré characteristic of spatial images", *Journal of Microscopy*, **198**(1), 54-62.
- [112] Oak, M.J., 1990. "Three-phase relative permeability of water-wet Berea", *proceedings of the SPE/DOE Seventh Symposium on Enhanced Oil Recovery*, SPE 20183, Soc. Of Petroleum Engineers, Tulsa.
- [113] Ohser, J. and McKlich, F., 2000. "Statistical Analysis of Materials Structures", J. Wiley & Sons, Chichester, New York.
- [114] Ohser, J., Nagel, W. and Schladitz, K., 2002. "The Euler number of discretised sets – on the choice of adjacency in homogeneous lattices", *Lecture Notes in Physics*, **600**, 275-298.
- [115] Ohser, J., Nagel, W. and Schladitz, K., 2003, "The Euler number of discretised sets – surprising results in three dimensions", *Image Analysis Stereology*, **22**, 11-19.
- [116] Okabe, A. Boots, B., Sugihara, K. and Chiu, S., 2000. "Spatial Tessellation: Concepts and Applications of Voronoi Diagrams", John Wiley, New York, NY.
- [117] Okabe, H. and Blunt, M.J., 2005, "Pore space reconstruction using multiple-point statistics", *Journal of Petroleum Science and Engineering*, **46**, 121-137.
- [118] Okun, B.L., 1990, "Euler characteristic in percolation theory", *Journal of Statistical Physics*, **59**, 523.
- [119] Øren, P. and Bakke, S., 2003. "Reconstruction of Berea sandstone and pore-scale modelling of wettability effects", *Journal of Petroleum Science and Engineering*, **39**, 177-199.
- [120] Palágyi, K. and Kuba, A., 1997. "A parallel 12-subiteration 3D thinning algorithm to extract medial lines", In: *Proceedings of the 7th International conference*

on computer analysis of images processing (CAIP'97), *Lecture Notes in Computer Science*, Vol. 1296. Springer, Berlin, 400-407.

[121] Palágyi, K. and Kuba, A., 1998. "A 3D 6-subiteration thinning algorithm for extracting medial lines", *Pattern Recognition Letters*, **19**,613-627.

[122] Palágyi, K. and Kuba, A., 1999. "Directional 3d thinning using 8 subiterations", *In: Proceedings of the 8th International conference on computer analysis of images processing, Lecture Notes on Computer Science*, Vol. 1568, Springer-Verlag, 325-336.

[123] Park, C.M. and Rosenfeld, A., 1971. "Connectivity and genus in three dimensions", TR-156, Computer Science Centre, University of Maryland, College Park.

[124] Patzck, T.W. and Kristensen, J.G., 2001. "Shape Factor Correlations of Hydraulic Conductance in Noncircular Capillaries II. Two-Phase Creeping Flow", *Journal of Colloid and Interface Science*, **236**, 305-317.

[125] Patzek, T.W. and Silin, D.B., 2001. "Shape Factor and Hydraulic Conductance in Noncircular Capillaries 1. One-Phase Creeping Flow", *Journal of Colloid and Interface Science*, **236**, 295-304.

[126] Perchet, D., Fetita, C.I. and Preteux, F., 2004. "Advanced navigation tools for virtual bronchoscopy", *Proc. SPIE Conf. on Image Processing: Algorithms and Systems III*, vol. 5298, 147-158.

[127] Piper, J. and Granum, E., 1987. "Computing distance transformations in convex and non-convex domains", *Pattern Recognition*, **20**(6), 599-6156.

[128] Piri, M. and Blunt, M.J., 2005. "Three-dimensional mixed-wet random pore-scale network modeling of two- and three-phase flow in porous media. I. Model description", *Physical Review E*, **71**, 026301.

[129] Prodanović, M., Lindquist, W.B. and Serigh, R.S., 2006. "Porous structure and fluid partitioning in polyethylene cores from 3D X-ray microtomographic imaging", *Journal of Colloid and Interface Science*, **298**, 282-297.

[130] Prodanović, M., Lindquist, W.B. and Seright, R.S., 2007. "3D image-based characterization of fluid displacement in a Berea core", *Advances in Water Resources*, **30**, 214-226.

- [131] Pudney, C., 1996. "Distance-Based Skeletonization of 3D images", *IEEE Trncon-Digital Signal Processing Applications*, 1(26-29), 209-214.
- [132] Pudney, C., 1998. "Distance-Ordered Homotopic Thinning: A Skeletonization Algorithm for 3D Digital Images", *Computer Vision and Image Understanding*, 72, 404-413.
- [133] Ragnemalm, I., 1993. "The Euclidean distance transform in arbitrary dimensions", *Pattern Recognition Letters*, 14, 883-888.
- [134] Reeves, P.C. and Celia, M.A., 1996. "A functional relationship between capillary pressure, saturation, and interfacial areas as revealed by a pore-scale network model", *Water Resources Research*, 32(8), 2345-2358.
- [135] Remy, E. and Thiel, E., 2005. "Exact medial axis with euclidean distance", *Image and Vision Computing*, 23, 167-175.
- [136] Remy, E. and Thiel, E., 2002. "Medial axis for chamfer distances - computing look-up tables and neighbourhoods in 2D or 3D", *Pattern Recognition Letters*, 23(6), 649-661.
- [137] Rosenfeld, A., 1979. "Digital topology", *American Mathematical Monthly*, 86, 621-630.
- [138] Rosenfeld, A. and Pfalz, J.L., 1966. "Sequential operations in digital picture processing," *Journal of the Association for Computer Machinery (ACM)*, 13, 471-494.
- [139] Saha, P.K. and Chaudhuri, B.B., 1995. "A new approach to computing the Euler Characteristic", *Pattern Recognition*, 28(12), 1955-1963.
- [140] Saha, P.K. and Chaudhuri, B.B., 1996. "3D Digital Topology under Binary Transformation with Applications", *Computer Vision and Image Understanding*, 63 (3), 418-429.
- [141] Saha, P.K., Chaudhuri, B.B. and Majumder, D.D., 1997. "A new shape preserving parallel thinning algorithm for 3D digital images", *Pattern Recognition*, 30, 1939-1955.
- [142] Sahimi, M., 1988. "On the determination of transport properties of disordered systems", *Chemical Engineering Communications*, 64:177.

- [143] Sahimi, M., 1998. "Non-linear and non-local transport processes in heterogeneous media: from long-range correlated percolation to fracture and materials breakdown", *Physics Reports*, 306, 213-395.
- [144] Saito, T. and Toriwaki, J., 1994. "New algorithms for euclidean distance transformation of an n-dimensional digitized picture with applications", *Pattern Recognition*, 27(11) 1551-1565.
- [145] Saito, T. and Toriwaki, J., 1995. "A sequential thinning algorithm for three dimensional digital pictures using the Euclidean distance transformation", in Proceedings, *9th Scandinavian Conference on Image Analysis (SCIA'95)*, Uppsala, Sweden, IAPR, 507-516.
- [146] Schirmacher, H., Zöckler, M., Stalling, D. and Hege, H., 1998. "Boundary Surface Shrinking - a Continuous Approach to 3D Center Line Extraction", *Proc. of IMDSP (Image and Multidimensional Signal Processing)*, 25-28.
- [147] Schneider, R., 1993. "Convex Bodies: The Brunn-Minkowski Theory", *Encyclopedia of Mathematics and Its Application 44*, Cambridge University Press, Cambridge.
- [148] Schneider, R. and Wei, W., 2000, "Stochastische Geometric", Teubner, Stuttgart, 2000.
- [149] Serra, J., 1982. "Image Analysis and Mathematical Morphology", Vol. 1: Academic Press, New York.
- [150] Sethian, J.A., 1999. "Fast Marching Methods", *SIAM (Society for Industrial and Applied Mathematics) Review*, 41(2), 199-235.
- [151] Sheppard, A.P., Knackstedt, M.A., Pinczewski, W.V. and Sahimi, M., 1999. "Invasion percolation: new algorithms and universality classes", *Journal of Physics A*, 32, L521-L529.
- [152] Sheppard, A.P., Sok, R.M. and Averdunk, H., 2004. "Techniques for image enhancement and segmentation of tomographic images of porous materials", *Physica A*, 339, 145-151.

- [153] Sheppard, A.P., Sok, R.M. and Averdunk, H., 2005. "Improved pore network extraction methods", in: Proceedings of the international Symposium of the Society of Core Analysts, Toronto, Canada.
- [154] Shih, F.Y. and Wu, Y.T., 2004a. "Fast Euclidean distance transformation in two scans using a 3x3 neighbourhood", *Computer Vision and Image Understanding*, **93**, 195-205.
- [155] Shih, F.Y. and Wu, Y.T., 2004b. "Three-dimensional Euclidean distance transformation and its application to shortest path planning", *Pattern Recognition*, **37**, 79-92.
- [156] Silin, D. B., Jin, G. and Patzek, T.W., 2004. "Robust determination of the pore space morphology in sedimentary rocks", *Journal of Petroleum Technology*, 69-70.
- [157] Silin, D.B. and Patzek, T.W., 2006. "Pore space morphology analysis using maximal inscribed spheres", *Physica A*, **371**, 336-360.
- [158] Shin, H., Lindquist, W.B., Sahagian, D.L. and Song, S.-R., 2005. "Analysis of the vesicular structure of basalts", *Computer & Geoscience*, **31**, 473-487.
- [159] Shin, K., 2002. "A Throat Finding Algorithm for Medial Axis Analysis of 3D Images of Vesiculated Basalts", PhD thesis, 2002, Department of Applied Mathematics and Statistics, Stony Brook University.
- [160] Sok, R.M., Knackstedt, M.A., Sheppard, A.P., Pinczewski, W., Lindquist, W.B., Ventatarangan, A. and Paterson, L., 2000. "Direct and stochastic generation of network models from tomographic images", *Transport in Porous Media*, **46**(2-3), 345-372.
- [161] Stauffer, D., 1985, "Introduction to Percolation Theory", *Taylor and Francis, London*, 1985.
- [162] Sundar, H., Silver, D., Gagvani, N. and Dickinson, S., 2003. "Skeleton Based Shape Matching and Retrieval", *Proceedings, Shape Modeling and Applications Conference*, SMI 2003, Seoul, Korea, May 2003, 130-142.
- [163] Svensson, S., Arcelli, C. and Sanniti di Baja, G., 2003. "Finding cavities and tunnels in 3D complex objects", in: *Proceedings of the 12th International Conference on Image Analysis and Processing, IEEE CS*, 342-347.

- [164] Svensson, S., Nyström, I., Sanniti di Baja, G., 2002. "Curve skeletonization of surface-like objects in 3D images guided by voxel classification", *Pattern Recognition Letters*, **23**, 1419-1426.
- [165] Telea, A. and Vilanova, A., 2003. "A robust level-set algorithm for centerline extraction", in *Symposium on Visualization (VisSym '03)*, 185–194.
- [166] Thiel E. and Montanvert, A., 1992. "Chamfer masks: Discrete distance functions, geometrical properties and optimization", in *Proceedings, 11th International Conference on Pattern Recognition, The Hague, The Netherlands*, 244–247.
- [167] Thovert, J.F., Salles, S. and Adler, P.M., 1993. "Computerized characterization of the geometry of real porous-media - their discretization, analysis and interpretation", *J. Microscopy-Oxford.*, **170**, 65-79.
- [168] Tsao, Y.F. and Fu, K.S., 1981, "A parallel thinning algorithm for 3D pictures", *Computer Vision Graphics Image Process*, **17**, 315-331.
- [169] Turner, M.L., Knüfing, L., Arns, C.H., Sakellariou, A., Senden, T.J., Sheppard, A.P., Sok, R.M., Limaye, A., Pinczeski, W.V. and Knackstedt, M.A., 2004. "Three-dimensional imaging of multiphase flow in porous media", *Physica A*, **339**, 166-172.
- [170] Valvatne, P.H. and Blunt, M.J., 2004. "Predictive pore-scale modeling of two-phase flow in mixed wet media", *Water Resources Research*, Vol. 40, W07406, doi: 10.1029/2003WR002627.
- [171] van Dijke, M.I.J. and Sorbie, K.S., 2002, "Pore-scale network model for three-phase flow in mixed-wet porous media", *Physical Review E.*, **66**(4), 046302.
- [172] van Dijke, M.I.J. and Sorbie, K.S., 2003a. "Three-phase capillary entry conditions in pores of noncircular cross-section", *Journal of Colloid and Interface Science*, **260**, 385-397.
- [173] van Dijke, M.I.J. and Sorbie, K.S., 2003b. "Pore-scale modelling of three-phase flow in mixed-wet porous media: multiple displacement chains", *Journal of Petroleum Science and Engineering*, **39**, 201-216.
- [174] van Dijke, M.I.J. and Sorbie, K.S., 2006. "Existence of Fluid Layers in Corners of a Capillary with Non-uniform Wettability", *Journal of Colloid and Interface Science*, **293**, 455-463.

- [175] van Dijke, M.I.J. and Sorbie, K.S., 2007. "Consistency of three-phase capillary entry pressures and pore phase occupancies", *Proceedings of the 15th International Conference on Computational Methods in Water Resources*, **20**, 182-198.
- [176] van Dijke, M.I.J., Sorbie, K.S. Sohrabi, M. and Danesh, A., 2006. "Simulation of WAG floods in an oil-wet micromodel using a 2-D pore-scale network model", *Journal of Petroleum Science and Engineering*, **52**, 71-86.
- [177] Venkatarangan, A.B., 2000. "Geometric and Statistical Analysis of Porous Media", PhD Dissertation, Department of Applied Mathematics and Statistics, State University of New York at Stony Brook, NY.
- [178] Verwer, B.H., Verbeek, P.W. and Dekker, S.T., 1989. "An efficient uniform cost algorithm applied to distance transforms", *IEEE Transactions on Pattern Analysis and Machine Intelligence*, **11**(4), 425-429.
- [179] Verwer, J.H. 1991. "Local distance for distance transformations in two and three dimensions", *Pattern Recognition Letter* **12**, 671-682.
- [180] Vincent, L. M., 1991. "Efficient computation of various types of skeletons", in *Proceedings, SPIE Image Processing*, **1445**, 297-311.
- [181] Vogel, H.J., 1997a. "Digital unbiased estimation of the Euler-Poincaré characteristic in different dimensions", *Acta Stereol*, **16**(2), 97-104.
- [182] Vogel, H.J., 1997b. "Morphological determination of pore connectivity as a function of pore size using serial sections", *European Journal of Soil Sciences*, **48**, 365-377.
- [183] Vogel H.J., 2000. "A numerical experiment on pore size, pore connectivity, water retention, permeability, and solute transport using network models", *European Journal of Soil Science*, **51**, 99-105.
- [184] Vogel, H.J. and Kretzschmar, A., 1996. "Topological characterization of pore space in soil-sample preparation and digital image-processing", *Geoderma*, **73**, 23-38.
- [185] Vogel, H.J. and Roth, K., 2001. "Quantitative morphology and network representation of soil pore structure", *Advances in Water Resources*, **24**, 233-242.
- [186] Wan, M., Dachille, F. and Kaufman, A., 2001. "Distance-Field Based Skeletons for Virtual Navigation", *IEEE Visualization 2001, San Diego, CA*.

- [187] Wilkinson, D. and Willemsen, J.F., 1983. "Invasion percolation: a new form of percolation theory", *Journal of Physics, A*, **16**, 3365-3370.
- [188] Wu, K., van Dijke, M.I.J., Couples, G.D., Jiang, Z., Ma, J., Sorbie, K.S., Crawford, J., Young, I. and Zhang, X., 2006. "3D stochastic modelling of heterogeneous porous media – applications to reservoir rocks", *Transport in Porous Media*, **65**, 443-467.
- [189] Xie, W., Thompson, R.P. and Perucchio, R., 2003. "A topology-preserving parallel 3D thinning algorithm for exacting the curve skeleton", *Pattern Recognition* **36**, 1529-1544.
- [190] Yang, X., 2005. "Three-Dimensional Characterization of Inherent and Induced sand microstructure", PhD thesis, Civil & Environmental Engineering, University of Dongguk.
- [191] Yu, Z.Y., Delerue, J.F. and Ma, S.D., 1998. "3D Euclidean distance transformation", In: *Proceedings of the International Symposium on Image, Speech, Signal Processing and Robotics*, Hong Kong, 67-72.
- [192] Zallen, R., 1983, "*The Physics of Amorphous Solids*", J. Wiley and Sons, New York, 1983.
- [193] Zhao, H.Q., Macdonald, I.F. and Kwiecien, M.J., 1994. "Multiorientation scanning: a necessity in the identification of pore necks in porous media by 3-D computer reconstruction from serial section data", *Journal of Colloid and Interface Science*, **162**(2), 390-401.
- [194] Zhou, Y., Kaufman, A. and Toga, A.W., 1998. "Three-dimensional Skeleton and Centerline Generation Based on an Approximate Minimum Distance Field", *The Visual Computer*, **14**, 303-314.